CHEMICAL PHYSICS AND ASTROCHEMISTRY OF H_3^+ AND SUB DOPPLER MID INFRARED SPECTROSCOPY OF MOLECULAR IONS

BY

KYLE NICHOLAS CRABTREE

DISSERTATION

Submitted in partial fulfillment of the requirements
for the degree of Doctor of Philosophy in Chemistry
in the Graduate College of the
University of Illinois at Urbana-Champaign, 2012

Urbana, Illinois

Doctoral Committee:

Professor Benjamin J. McCall, Chair
Professor Martin Gruebele
Professor So Hirata
Professor Alexander Scheeline

Abstract

Molecular ions are known to be key reactive intermediates in interstellar environments, and H_3^+ in particular is responsible for initiating a network of chemical reactions that ultimately results in the formation of the ∼170 molecules detected so far in space. Yet fundamental questions about the interstellar abundances of the two nuclear spin configurations of H_3^+ (*ortho*-H_3^+, $I = 3/2$; and *para*-H_3^+, $I = 1/2$) remain. In this thesis, experiments to measure the nuclear spin dependence of the chemical reactions of H_3^+ with electrons and with molecular hydrogen at astronomically relevant temperatures are described. The results of these laboratory measurements are included into a model of the hydrogenic chemistry of diffuse molecular clouds, in which an excess of *para*-H_3^+ is observed relative to its expected abundance at the measured cloud temperature. The model suggests that the *ortho*:*para* ratio is likely controlled by a competition between the aforementioned chemical reactions of H_3^+ with electrons and molecular hydrogen.

Other molecular ions may similarly be useful for constraining the physical and chemical conditions of astronomical environments, but such insight can only be derived if laboratory spectroscopy of these ions has been performed. However, for many ionic species, insufficient laboratory data are available, and this is primarily because of difficulties in producing sufficient quantities of ions for traditional spectroscopic techniques. This thesis discusses the development of instrumentation to overcome the challenge of ion production. First, a continuous supersonic expansion discharge source is described that allows for the production of internally cold molecular ions in modest abundance, thereby maximizing population in the lowest-lying energy states relevant for astronomical spectroscopy. Then, an instrument for performing sub-Doppler spectroscopy of molecular ions in a liquid nitrogen cooled plasma is discussed. This instrument offers ultra high sensitivity, and sufficient accuracy and precision that rotational frequencies suitable for observational astronomy can be inferred. As a case study of the performance and capabilities of this instrument, the high resolution sub-Doppler spectrum of H_3^+ is presented.

To Debra, Kolt, and Kenton, for giving me motivation, perspective, and love.

Acknowledgments

I'd first like to thank my advisor, Ben McCall, for his immeasurable support and guidance during my years in graduate school. His enthusiasm for science is infectious, and countless times has been responsible for providing a much-needed lift when faced with some of the daunting challenges inherent in these experiments. I'm grateful for the opportunities to help write NSF and NASA proposals for our group's funding, and also for Ben pointing me towards competitive external fellowships for which I had to write proposals. From those experiences I learned a great deal about how to present research and ideas in a proposal format, and have already been fruitful in helping me to secure a postdoctoral fellowship. The list of opportunities for which I owe Ben my gratitude goes on: international conferences, experiments with collaborators in Germany, independence in the lab, the opportunity to mentor younger graduate students, and much more of which I would not have originally thought myself capable.

Thanks also to my committee members, Alexander Scheeline, So Hirata, and Martin Gruebele, for numerous insightful and supportive conversations over the years. I'd also like to acknowlegde Jim Lisy, who was on my preliminary exam committee before retiring.

I want to thank the people who are responsible for sparking my interest in science in general (and chemistry in particular). My high school chemistry teacher Darla Hoover is largely responsible for starting me on a career in chemistry. She allowed me to take a special class in which I served as a lab assistant, preparing the needed reagents and solutions for the upcoming chemistry lab experiments and also seeking out relevant chemistry demonstrations to accompany lectures. More importantly, she gave me free reign in the lab to conduct my own "experiments," which cemented my interest in pursuing research in chemistry. After leaving high school, I was fortunate to work with James Poole at Ball State University. It was in his laboratory that I performed my first research project, and my first exposure to the thought process that goes into science. He also took me to my first research conference and allowed me to present a poster, and that was probably the defining experience of my undergraduate career.

I've been very fortunate to work with a group of talented, intelligent, quirky, and humorous labmates; I will greatly miss the group camaraderie and interpersonal dynamics. Brian Brumfield showed great ded-

ication to science, and a patient, thorough, and analytical approach toward his work that was inspiring, and coupled that with a dry, macabre sense of humor that brought levity to difficult times. Brian Tom laid the foundation for most of the work I did with H_3^+, and was a mentor to me in my early days in the group, demonstrating the highest levels of commitment, integrity, and sacrifice that I've ever seen in a person. I also owe thanks to Brian Siller for a number of reasons: we've worked on home improvement projects together at both of our houses; he first introduced me to Linux, which has been instrumental in improving my facility with computers and programming; and he has been a great help in setting up the OPO-NICE-OHVMS instrument. I've also been inspired and motivated by his approach at solving practical, hands-on problems, whether involving electronics, optics, construction, or programming, Siller dispatches them with almost casual ease, and I've drawn on this expertise many times and tried to learn from it. It was also a privilege to work with Holger Kreckel on the dissociative recombination of H_3^+; our trip to the Test Storage ring in Heidelberg, Germany for a two-week experiment was one of the highlights of my time in graduate school, and his methodical, details-oriented approach to science was very influential. I will always have fond memories of playing softball with Nick Indriolo and Adam Perry, and brewing beer with Brian Siller and Jamie Hodges. The rest of the McCall group members have, with their witty banter, insight, and commiseration at times, made graduate school a memorable and special experience.

Special thanks also go out to those with whom I've worked on various experiments and with whom I've co-authored papers. The work on the supersonic expansion source was done with the assistance of Carrie Kauffman, who humorously earned the title "Destroyer of Sources" after breaking some components during the challenging and delicate assembly process. She was a great help during the lead-up to my preliminary examination, when she had to carry on the experiments herself while I abandoned her in preparation for the exam. The $H_3^+ + H_2$ experiment was made possible in part due to contributions by her, Brian Tom, Brett McGuire, and the very talented undergraduate student Eftalda Beçka. I also owe thanks to the OPO team, Brian Siller, Jamie Hodges, Joe Kelly, Adam Perry, and Paul Jenkins II. Nick Indriolo helped me learn a great deal about astronomy and observations as we coauthored a paper on H_3^+ in diffuse molecular clouds, and also successful observing proposal with the Very Large Telescope. Jessica Pearson has very recently been of great help in reducing the observational data we obtained from that successful proposal while I've been working on this dissertation, and I look forward to continuing my collaboration with her and with Nick in the future.

Most of all, I'd like to thank my wife Debra for her support during this time. When I came to Illinois, we already had our first son, and we've since added another son while I was in graduate school. Debra has put her goals and dreams on hold for the past five years to care for our children while I pursued my own goal of

earning my doctorate. Without her sacrifice and nurturing care, I would not have been able to complete this program. She has endured weeks alone with the children while I've been off to do experiments and attend conferences around the world, and has spent countless nights alone as I've been furiously working on one project or another. My children, Kolt and Kenton, in their own way have shown me love and support, giving me both the motivation to go out and succeed, but also to come back home to try not to miss any special moments. Together, they have helped me to maintain a balance between work and family, preventing me from becoming burned out, and also keeping me focused and productive.

Finally, I'd like to acknowledge the financial support I have received over the years: the Lebus Graduate Scholar Award, the James P. Beck Fellowship, the Buhrke Fellowship, the NASA Earth and Space Science fellowship, as well as a few departmental fellowships.

Table of Contents

List of Tables

List of Figures

Chapter 1

Introduction

The overarching motivation for the work presented in this dissertation is studying molecular ions and chemical processes of relevance for astrochemistry using high resolution spectroscopy. While sharing the same broad motivation, the chapters that follow are not all directly related to one another in a manner that can be simply explained. Rather, each chapter differs substantially from the others in its specific motivation, methods, and analysis. The structure of this document reflects this: each chapter stands mostly independent of the others, containing its own introduction, description of experimental techniques, results, and conclusions. Thus, the aim of this introduction is to provide the broader context for how the work described in the later chapters contributes to astrochemistry, and the reader is referred to the introductory sections of each chapter for its respective scientific background.

Molecular ions have long been known to be important reactive intermediates in interstellar clouds, the birthplaces of stars. [1, 2] In these cold (temperature < 100 K), diffuse (density $< 10^4$ cm^{-3}) environments, only chemical reactions that are both exothermic and barrierless proceed at any significant rate. Ion-molecule reactions generally satisfy these conditions, and after the formation of primary ions through cosmic ray ionization, these types of reactions are responsible for driving the formation of larger, more complex molecules. Because of their heavy involvement with the chemistry, ions serve as key tracers of the physical and chemical conditions of interstellar clouds.

In order to extract information about any molecule in interstellar space, its spectroscopic signature must be investigated in the laboratory. High resolution laboratory spectroscopy reveals the frequencies at which a molecule absorbs and/or emits light, and can give information that relates the intensity of an absorption or emission feature to the abundance of a particular quantum state of the molecule. When these frequencies of light are observed using astronomical telescopes, the laboratory information can be used to identify and quantify the molecule, and to possibly give insight into the physical environment in which it is found (temperature, density, photon flux, ionization rate, etc.). For many stable neutral molecules, high-quality detailed spectroscopic information is readily available, but this is not always the case for ions. Measuring such high-quality spectra of molecular ions is the broad motivation for Chapters 2 and 3.

Acquiring the high resolution laboratory spectrum of an ion presents several challenges. First, ions are difficult to produce, requiring a source of energy sufficient to effect ionization, such as an electric discharge or a high energy photon. Once made, ions are generally quite reactive, and so production rates must be high to balance the destruction rates in order to accumulate a significant population for spectroscopy. High production rates require yet even more energy input into the system, and much of this goes into heating, both kinetic (resulting in larger linewidths from Doppler broadening) and internal (resulting in spectral dilution from an increased partition function). Even under favorable production circumstances, the peak ion abundance is often several orders of magnitude lower than that of neutral molecules, and the spectroscopic signals of neutrals can overwhelm the weaker ion signals. All of these factors, as well as electronic and optical interference from the production process, contribute to the technical difficulty of ion spectroscopy.

To overcome such challenges requires the use of specialized ion sources and sensitive spectroscopic techniques. In the McCall laboratory, a long-term goal has been to develop an instrument called SCRIBES (Sensitive, Cooled, Resolved Ion BEam Spectroscopy). The heart of the instrument is a fast ion beam formed by extracting and accelerating ions out of a plasma source. After acceleration, ions are steered electrostatically by 90 degrees into a drift region in which they can be interrogated by laser spectroscopy. The ions are therefore spatially separated from neutral molecules, providing selectivity in spectroscopic detection, and the acceleration results in velocity narrowing from kinematic compression, giving sub-Doppler spectroscopic linewidths. After being probed spectroscopically, the ions are turned again and sent into a mass spectrometer, yielding mass identification for all constituents of the ion beam. The primary disadvantage of SCRIBES is that the density of ions in the drift region is a few orders of magnitude lower than other commonly used ion sources. This instrument is now operational, and a more detailed and extensive description of its performance, advantages, and capabilities has been published. [3]

In the implementation described in [3], the SCRIBES instrument is not yet "Cooled." The ion beam is extracted from an uncooled cold cathode dc discharge source, and the internal temperature of the ions in the beam is high ($\sim$750 K). Because of the low ion density in the drift region, the increase in partition function is highly detrimental to the technique, even moreso than other methods. Rotational cooling would dramatically improve the performance of the instrument by reducing the partition function. Rotational temperatures below 20 K for some ions can be achieved by use of a supersonic expansion, in which gas at high pressure is forced through a narrow aperture into vacuum, resulting in an adiabatic expansion that converts internal energy into translational energy. In Chapter 2, an ion source suitable for use with SCRIBES is presented: a continuous supersonic expansion coupled to a dc discharge. The performance of the source– its lifetime and the generated ions' internal temperature and density– is characterized by cavity

ringdown spectroscopy of the ν_2 fundamental band of the molecular ion H_3^+. With the use of an appropriate skimmer [4, 5], an internally cooled ion beam can be produced. The integration of the supersonic expansion discharge source with the ion beam instrument is envisioned in the near future.

Another consideration not yet discussed is the region of the electromagnetic spectrum in which to search for an ion's transitions. Design of a spectrometer requires analyzing the tradeoffs that come with the various regions. The visible region is attractive because of the availability of broadly tunable light sources, as well as inexpensive, fast, and sensitive silicon-based detectors, and in this region rovibronic transitions can be measured. However, not all ions have stable electronically excited states, and it is often difficult to predict where a particular ion's electronic spectrum will be located in frequency space. On the other side of the spectrum, in the microwave/millimeterwave region rotational transitions can be directly observed with extremely high accuracy, and light sources and detectors are readily available. Rotational spectroscopy is also the main tool used in detection of molecules in interstellar space, so the rotational spectrum of a molecule can be directly used to enable an astronomical search. There are two main limitations to laboratory rotational spectroscopy: first, only molecules with a permanent dipole moment can be detected; and second, when rotational frequencies are not approximately known from theoretical calculations, the spectral features are difficult to locate. In between, the mid-infrared (particularly between 3-5 μm) contains fundamental vibrational transitions, and the vast majority of molecular ions have at least one transition in this region. The downsides traditionally have been twofold: fast, low-noise detectors have been difficult to realize, and the linewidths of the observed transitions preclude determination of rotational energy level spacings with sufficient precision to enable interstellar searches. Increasingly, low-noise detectors are becoming available, as well as high-power cw broadly tunable lasers that can cover this spectral region, leaving the linewidth issue as the only remaining challenge.

In Chapter 3, a general-purpose instrument for sub-Doppler mid-infrared spectroscopy of molecular ions is presented. Narrow linewidths are achieved by using a high-power cw optical parametric oscillator (OPO) source combined with an enhancement cavity. The high intracavity power saturates rovibrational transitions, leading to narrow Lamb dip features at the line center that can be measured with sub-MHz precision, about 2-3 orders of magnitude better than traditional mid-infrared spectroscopy. The OPO is in principle tunable over the entire 3-5 μm range, enabling its use to detect a wide variety of molecular ions. With the high line center frequency precision that can be achieved for each rovibrational transition, this technique is capable of extracting the underlying rotational energy level spacings well enough for astronomical purposes. The primary benefit of this approach is to extract rotational transitions in the sub-millimeter/THz portion of the electromagnetic spectrum, which was omitted in the above discussion. This region features low-lying

rotational transitions of light molecules and higher-energy rotational transitions of larger molecules, and is very difficult to probe experimentally owing to a dearth of readily available radiation sources and detectors. Measurements of appropriate transition frequencies is critical for the success of THz/sub-mm telescopes such as the Herschel Observatory, the Atacama Large Millimeter/sub-millimeter Array, and the Stratospheric Observatory for Far Infrared Astronomy.

While Chapters 2 and 3 focus broadly on the development of instruments that enable state-of-the-art spectroscopy, the remaining chapters together highlight the interplay between astronomical observations, theory, and experiment in the field of astrochemistry, using the nuclear spin dependence of the reaction of H_3^+ with H_2 as a case study. As mentioned before, molecules often serve as probes of physical conditions in astronomical environments. For instance, the relative populations of two rotational levels of a molecule by absorption spectroscopy give a measure of temperature. In diffuse molecular clouds, UV absorption measurements of H_2 rovibronic transitions gives a measure of the relative populations of $J = 0$ and $J = 1$, and this is a reliable measure of such a cloud's kinetic temperature (see section 4.3 for details). Chapter 4 presents astronomical observations that show a discrepancy between the nuclear spin temperatures of H_2 and H_3^+ (i.e., their *ortho*:*para* ratios), the latter derived from infrared rovibrational transitions. Such a temperature difference is surprising because H_2 is efficiently thermalized by reactions with abundant protons, and H_3^+ was thought to be efficiently thermalized by reactions with H_2. Understanding the origin of the discrepancy would possibly enable H_3^+ to be used as an astrophysical temperature probe in other environments in which UV radiation is highly attenuated, precluding measurement of H_2 directly. On a more fundamental level, diffuse molecular clouds feature some of the simplest chemistry in space, and thus serve as an ideal testbed for ensuring that physical and chemical models are reliable in more complicated environments.

Chapter 4 also discusses a chemical model for the relationship between the *ortho*:*para* ratios of H_3^+ and H_2. Central to the model is the reaction $H_3^+ + H_2 \rightarrow H_2 + H_3^+$, which is capable of interconverting the nuclear spin modifications of H_3^+ and H_2. The reaction has three possible outcomes: the identity, hop, and exchange (these are explained in more detail in Chapters 5 and 6), and the ratio of the rates of the hop and exchange reactions can be used to determine how this reaction influences the nuclear spin states of the products. Experimental measurement of the hop:exchange ratio is challenging: while mass spectrometry is a powerful tool for measuring reaction rates, it is not effective when the masses of the reactants and products are equal. Spectroscopy is required for measuring the internal state distribution. By monitoring the populations of several low-lying rotational states of *ortho* and *para*-H_3^+ and controlling the *ortho*:*para* ratio of H_2, the hop:exchange ratio of the $H_3^+ + H_2$ reaction can be inferred. The detailed kinetics and

nuclear spin statistical weights required for the analysis of such an experiment are presented in Chapter 5 (some additional notes are given in Appendix E). Then, in Chapter 6, experimental results on the H_3^+ + H_2 reaction are presented at 350 K and 135 K, and are analyzed in the context of the results of Chapter 5. The experimental work is the most detailed investigation of this process to date, and is the first such study at low temperature.

The hop:exchange ratio for the H_3^+ + H_2 reaction at low temperatures derived from the theoretical and experimental studies can be used to refine the aforementioned astrochemical model (Chapter 4). The synthesis of theory, experiment, and observation is presented in Appendix D. By way of summary, good agreement between the observations and the chemical model are obtained under certain conditions, but there remain two major unknowns. The first of these is the branching fraction of the identity outcome of the H_3^+ + H_2 reaction, which could not be determined from the experiments in Chapter 6. The identity branching fraction influences how many reactive (i.e., proton-scrambling) reactions H_3^+ experiences during its lifetime in a diffuse molecular cloud prior to its destruction by dissociative recombination (DR) with electrons. Good agreement is achieved only when this identity branching fraction is larger than expected, although additional measurements of the H_3^+ + H_2 reaction are needed to constrain this quantity.

The other major unknown remaining in the chemical model is the nuclear spin dependence of H_3^+ DR at low temperature. DR of H_3^+ has a long and controversial history, which is discussed in detail in Appendix C. Recently, theory and experiment have generally come into agreement regarding the temperature dependent rate, but the nuclear spin dependence at low temperature is still under investigation. Appendices A, B, and C describe experimental work aimed at measuring the DR rates of *ortho*- and *para*-H_3^+ at temperatures on the order of 100 K. H_3^+ is produced in a supersonic expansion discharge source, and the rotational temperature and *ortho*:*para* ratio is measured spectroscopically. The H_3^+ ions are extracted from the source, accelerated to MeV energies, and guided into a storage ring in which they are overlapped with a velocity-matched electron beam. The ions recombine with the electrons, and the resultant neutral fragments (which are no longer steered by the storage ring) are measured. The combination of internally cold ions with a velocity-matched, translationally cold electron beam gives the reaction rate under conditions similar to those found in the interstellar medium.

In order to assess the nuclear spin dependence, the supersonic expansion ion source is fed with enriched *para*-H_2, and as a consequence the H_3^+ generated is enriched in its *para* form as measured spectroscopically. When storage ring experiments are performed with enriched *para*-H_3^+, the low-temperature DR rate coefficient is enhanced relative to that measured with non-enriched H_3^+. By performing measurements with two different known enrichments of *para*-H_3^+, the rate coefficients for pure *para*- and *ortho*-H_3^+ can be ex-

trapolated. The experiments presented in Appendix A were the first such measurements made, and the spectroscopic characterization of the ion source utilized in the storage ring measurements are presented in Appendix B. Later, the measurements were repeated with a more reliable ion source at a different storage ring with higher resolution (Appendix C). A similar enhancement in the DR rate for *para*-H_3^+ was observed, but for the first time a technique for *in situ* determination of the rotational temperature of H_3^+ in the storage ring was employed. The results of the temperature measurement indicate that at some point after their production but prior to their measurement in the ring, the H_3^+ ions are internally heated. It is hypothesized that the heating is a result of collisions of H_3^+ with the carrier gas from the supersonic expansion during acceleration, and that all previous storage ring measurements of H_3^+ DR involving a supersonic expansion source may have been affected as well. Other researchers have attempted to perform plasma-based measurements of H_3^+ DR, but are beset by complicated data analysis arising from competing plasma processes. [6, 7] In all, the low-temperature nuclear spin dependent DR rates of H_3^+ still have not been definitively measured, and this remains an unknown quantity in the astrochemical model.

This dissertation presents numerous ways in which high resolution spectroscopy can be employed in support of astrochemistry. It can be used to characterize the ions produced by plasma sources (Chapter 2 and Appendix B) intended to be used for other studies (e.g. an ion beam spectrometer, or DR measurements such as those in Appendices A and C). Alternatively, it can be used directly to record spectra of yet-unobserved molecules in space, or to better understand their spectroscopic properties (see Chapter 3). High resolution spectroscopy can also directly measure astrochemically relevant reaction rates, as discussed extensively in Chapters 4, 5, and 6. While the details differ greatly among these applications, they all demonstrate examples of how high resolution spectroscopy provides data that can further our understanding of processes occurring in space.

Chapter 2

Supersonic Expansion Discharge Source

High-resolution spectroscopy of gas-phase molecular ions provides information of both fundamental and astrochemical importance. The observed transition frequencies in a high resolution spectrum serve as useful benchmarks for improving *ab initio* theory. [8] In the low-temperature and low-density conditions of the interstellar medium, molecular ions are key intermediates that drive chemical evolution because of fast ion-neutral reaction rates. [1] High-resolution spectroscopy is a critical tool for observing the presence and abundances of various species in space, leading to an understanding of the chemistry that occurs around us in the universe.

For these reasons, high-resolution gas-phase spectroscopy of molecular ions in the laboratory has been a highly active field during the past three decades. A persistent challenge, however, is the production of these transient species in enough abundance to be observable. While a number of ionization techniques have been developed, an electrical discharge has been most widely used for spectroscopic purposes owing to the higher ion densities produced. Two particularly effective and widely-used ionization techniques have been the positive column glow discharge [9] in conjunction with velocity modulation spectroscopy [10] and the negative glow of a hollow cathode. [11, 12] However, even when the walls of these ion sources are cryogenically cooled, the ions produced exhibit translational and rotational temperatures upwards of 150 K. For larger ions, the spectral congestion and intensity dilution at these high temperatures poses a challenge for understanding the spectra of more complex ions.

Supersonic expansions have been coupled with electrical discharges to produce ions and radicals at low temperatures. As the plasma expands into vacuum, the transient species produced in the discharge are adiabatically cooled, resulting in rotational temperatures as low as 2-3 K for molecules that cool efficiently. [13] The earliest of these were the "corona-excited" supersonic expansion discharge sources [14], consisting of a drawn glass or quartz capillary containing a long needle electrode. As gas passes through a small orifice at the end of the capillary, it is discharged between the needle electrode and a second electrode located outside of the source and further downstream. This source design, however, suffers from limited discharge stability

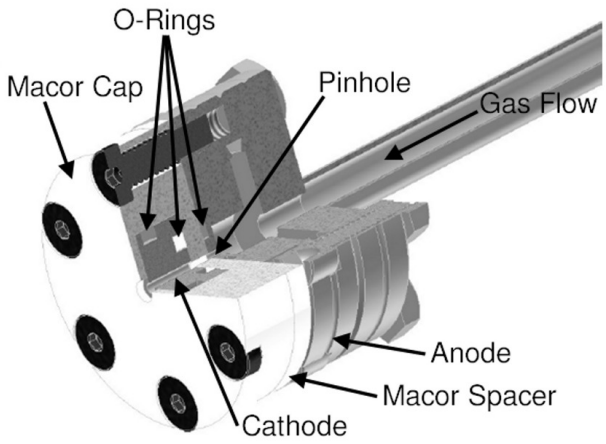

Figure 2.1: Cutaway view of the supersonic expansion discharge source. Dimensions are listed in Table 2.1.

Component	Material	ID (mm)[1]	Thickness (mm)
Anode	Stainless Steel	0.5	2.5
Spacer	Macor	1.0	2.5
Cathode	Stainless Steel	1.0/2.5	6.4
Cap	Macor	2.5/4.1	1.0

Table 2.1: Dimensions of source components.

and nozzle clogging. [15] Pulsed supersonic expansion discharge sources have been preferred in recent years owing to less-demanding pumping requirements, and have proved to be reliable sources of a variety of cold radicals and ions. [16, 17] However, such pulsed sources have intrinsic properties undesirable for achieving the highest spectral sensitivity, namely, limited duty cycle and shot-to-shot intensity fluctuations. To overcome these limitations, we have constructed a continuous supersonic expansion discharge source based on the design of the pulsed sources referenced above.

The continuous supersonic expansion discharge nozzle designed in our laboratory is illustrated in Fig. 2.1. Gas enters the system through a 1/4 in. stainless steel tube welded to a 1-1/3 in. Conflat flange. A pinhole is drilled into a second Conflat flange, which acts as the grounded anode of the discharge. The stainless steel cathode is separated from the anode by a Macor spacer, and is enclosed in a Macor cap. The assembly is sealed by means of three high-temperature silicone o-rings, and is held together by six screws which provide compression from the cap to the anode. The modularity of the various components allows for easy replacement of individual components in the case of failure, and also gives a very flexible design. The parameters of the source used in this particular experiment are listed in Table 2.1.

The supersonic expansion was formed in a chamber evacuated by a Roots blower (Leybold WS-2001,

[1]The cathode and cap inner diameters are flared like the bell of a trumpet. The listed dimensions are the beginning and ending inner diameters.

pumping speed 2460 m^3/h) backed by a rotary vane pump (Leybold SV-630, pumping speed 840 m^3/h). Hydrogen gas at pressures ranging from 2-3 bar was passed through the source, which resulted in a chamber pressure of 300-400 mTorr. A discharge was struck by applying negative high voltage to the cathode through a 10 kΩ ballast resistor and grounding the anode. The discharge current was varied between 10 mA (-500 V) and 130 mA (-1300 V). The reported voltages were the voltages at the power supply, and do not include the voltage drop across the ballast resistor.

To assess the performance of the source, the R(1,0), R(1,1)^u and R(2,2)^l transitions within the ν_2 fundamental band of H_3^+ at $\sim$3.67 μm were probed to determine the rotational temperature of this ion in the free-jet zone of silence. This molecular ion, whose high-resolution spectrum was first recorded by Oka in 1980 [18], has been well-studied in the laboratory [19] as well as in dense [20] and diffuse [21, 22] interstellar clouds, planetary atmospheres [23–25] and the galactic center. [26] It was chosen for this study because the R(1,0) and R(1,1)^u transitions are separated by only 0.32 cm^{-1}, allowing for spectra to be rapidly acquired under a variety of conditions. The R(2,2)^l line was measured on occasion to verify the temperature inferred from the relative intensities of the R(1,0) and R(1,1)^u lines.

A difference frequency generation laser was employed to perform continuous-wave cavity ringdown spectroscopy in a setup similar to that described in [27]. Briefly, a 532 nm Nd:YVO_4 laser (Coherent Verdi V-10) was split into two beams. One beam (7.5 W) was used to pump a tunable cw ring dye laser (Coherent 899-29) using Rhodamine 640 dye to produce 622 nm single-frequency radiation. The other 532 nm beam (2.5 W) was sent through an acousto-optical modulator (AOM), and the first-order beam was combined with the 622 nm beam on a dichroic beamsplitter and focused into a MgO-doped periodically-poled $LiNbO_3$ crystal. The 500 μW of tunable 3.67 μm light was coupled into a high-finesse cavity defined by two high-reflectivity mirrors (R $\sim$99.98%, Los Gatos Research), which surrounded the expansion jet. A piezoelectric transducer attached to one of the mirrors dithered the length of the cavity, causing it to move in and out of resonance with the laser. The light leaking out of the cavity was collected by a cryogenically-cooled InSb detector. When the detector output reached a predetermined threshold, the AOM was turned off, and the decay trace was recorded on a computer for analysis.

The operation of the source over its lifetime can be roughly divided into two regimes: the "low current" regime ($I < 50$ mA) and the "high current" regime ($I \geq 50$ mA). Sample spectra of the R(1,0) and R(1,1)^u lines are shown in Fig. 2.2. For the first 150 hours, the source was operated entirely in the low current regime. At a current of 25 mA and backing pressure of 2 bar H_2, the rotational temperature of the H_3^+ ions was 80 K. As the current was raised from 10 to 50 mA, the ion density noticeably increased. The rotational temperature also appeared to increase in the range of 50-100 K; however, the signal-to-noise ratio was quite

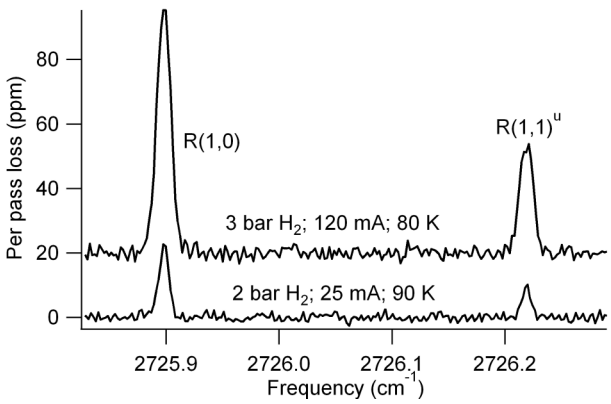

Figure 2.2: Sample H_3^+ spectra acquired at different pressures and currents. The top trace has been offset for clarity.

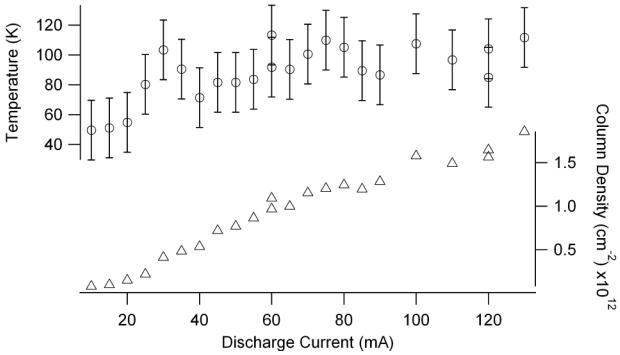

Figure 2.3: Temperature and column density of H_3^+ as a function of discharge current at 3 bar backing pressure. The error bars are representative of typical scatter in the temperature measurements.

low at the lowest currents. Operation in the high current regime was sustained for around 50 hours. The ion density increased with increasing current, but the rotational temperature was constant throughout this regime, varying between 80-110 K. After 50 hours of runtime at high current, the o-rings in direct contact with the cathode failed.

The performance of the source is summarized in Fig. 2.3. In the low current regime, the source was able to produce spectroscopically detectable quantities of ions for an extended period of time (> 150 hours). No indication of source failure was observed when operating at low current. Operation at high current offered a greater ion density without a significant increase in temperature; however, operation could not be sustained for the same duration of time. At present, it is unclear whether damage to the o-rings was induced slowly over the entire operation period or if the source temperature at high current increased beyond the thermal tolerance of the o-rings. To prevent this failure mode, it might be possible to braze the cap and spacer to the cathode, thereby sacrificing design modularity in exchange for a longer lifetime.

The most critical aspect of the performance of this supersonic expansion source is the rotational cooling it offers. H_3^+ was cooled to temperatures ranging from 50-110 K. These results are in agreement with the temperatures observed in a pulsed supersonic expansion source by Tom *et al.* (60-100 K) [28], and in a continuous slit-jet corona source by Xu *et al.* (77 K). [29] Due to its large rotational constant (B = 43.56 cm^{-1}) [19], H_3^+ does not cool as efficiently in an expansion as larger molecules. Future measurements with this ion source will be performed on the ν_1 fundamental band of HN_2^+ (B = 1.554 cm^{-1}) [30], which cools much more efficiently in a supersonic expansion environment. [16, 29]

The ion density produced is another important facet of the source performance. The observed H_3^+ column density (probed 1 cm downstream of the source exit) ranged between 8×10^{10} and 2×10^{12} cm^{-2} as a function of the discharge current. By visually observing emission from the discharge plume through a glass viewport, the plasma diameter appeared to be approximately 1 cm. Although the density across the plasma is not expected to be homogeneous, using that diameter the observed column densities indicate that the H_3^+ ion density 1 cm downstream is on the order of $10^{10} - 10^{12}$ cm^{-3}, which is similar to the observed ion densities produced in pulsed slit jet discharge sources. [16, 31] With a comparable number density and higher operating duty cycle, this source should provide greater spectroscopic sensitivity in an equal integration time in comparison with pulsed sources. Compared with other continuous sources, this source avoids the stability issues associated with the source of Xu *et al.* [29], and has a longer lifetime than continuous electron impact sources. [32]

In summary, we have constructed a continuous supersonic expansion discharge source and performed initial performance characterization by measuring the temperature and density of H_3^+ ions produced as a function of discharge current. These ions are generated with temperatures in the range of 50-110 K, and the source is capable of sustaining this operation for at minimum 50 hours. Ion densities produced are comparable to the densities afforded by pulsed sources, but with a high duty cycle which further enables sensitive spectroscopy. Improvements to the design will be tested by observing the ν_1 fundamental band of HN_2^+.

The authors would like to thank Prof. Susanna Widicus Weaver and Brian Pohrte for their early work on continuous supersonic expansion discharge sources in our laboratory. We also thank James Hodges for his work on the difference frequency generation laser system and Christopher Neese for his CFN-899 Autoscan dye laser control software. This work has been supported by an NSF CAREER award (CHE-0449592), by an Air Force Young Investigator Award (FA 9550-07-1-0128), and by the David and Lucile Packard Foundation.

Chapter 3

Sub-Doppler Mid-Infrared Spectroscopy of Molecular Ions

3.1 Introduction

Molecular ions play a key role as intermediates in chemical reactions, and a detailed understanding of their structure and intramolecular dynamics in the gas phase, generally obtained by spectroscopy, is a critical first step toward understanding their behavior in more complicated systems. The primary technique used for ion spectroscopy over the past 30 years has been velocity modulation spectroscopy (VMS). [30, 33] In VMS, ions are produced in an AC positive column plasma whose polarity is alternated at frequency f_{vm}. The average drift velocity of the ions in the plasma is shifted in the direction of the cathode from the applied electric field, while neutral molecules are generally unaffected. As the polarity is reversed, the average ion drift velocity also reverses, resulting in a periodic oscillation in ion velocity at f_{vm}. By interrogating the ions with a laser beam passing in one direction through the plasma, the absorption profiles are red- and blue-shifted with respect to their rest frequencies, and phase-sensitive detection at f_{vm} allows for selective retrieval of ionic signals. VMS therefore addresses one of the main challenges of ion spectroscopy, i.e., detection of ionic species that are only $\sim 10^{-5}$-10^{-6} as abundant as neutral molecules. Well over 40 unique molecular ions (not counting isotopologues) have been detected with VMS; these have been extensively reviewed by Stephenson and Saykally. [10]

Recently, the use of a Fabry-Perot optical cavity to enhance the optical path length was demonstrated by Siller et al. (cavity-enhanced velocity modulation spectroscopy, CEVMS), who locked a Ti:Sapphire laser to an optical cavity surrounding a velocity modulated positive column cell and detected the transmitted light. [34] Because the light in the cavity is bidirectional, red and blue Doppler shifts are simultaneously superimposed, encoding the velocity modulation signal at $2f_{vm}$. Initially, this was believed to be problematic because any neutral molecules excited by the discharge are concentration modulated at $2f_{vm}$; that is, the population of the excited species varies with the magnitude of the applied voltage, but not the sign of the voltage. By also encoding the ion signal at $2f_{vm}$, it was thought the concentration modulation signal of

This chapter is a preprint of a manuscript to be submitted to Chemical Physics Letters, authored by K. N. Crabtree, J. N. Hodges, B. M. Siller, A. J. Perry, J. Kelly, P. A. Jenkins II, and B. J. McCall

neutral molecules would overwhelm the ion velocity modulation signal. Siller et al. showed that the ion and neutral signals occurred at different phases with respect to the plasma voltage, thereby preserving ion-neutral discrimination. Additionally, the power enhancement from the optical cavity enables saturation spectroscopy and precision line-center determination. [35] CEVMS has also been employed using an optical frequency comb as the light source and a unidirectional ring cavity surrounding a plasma cell, effectively converting VMS to a broadband technique while preserving the high resolution of laser spectroscopy. [36]

Cavity enhanced absorption spectroscopy suffers from the fact that frequency noise in the laser is directly converted into intensity noise as a result of reduced cavity transmission. This limitation was overcome by Ye et al. with noise-immune cavity-enhanced optical heterodyne molecular spectroscopy (NICE-OHMS). [37] In this technique, the laser is phase modulated at f_h (typically ∼100s of MHz), effectively generating an FM triplet consisting of a carrier (at the optical frequency f_o) and a pair of sidebands with opposite phase at $f_o \pm f_h$. The triplet is coupled into the optical cavity by setting f_h equal to an integer multiple of the cavity free spectral range (FSR). Detection is accomplished by comparing the beat notes of each sideband with the carrier; in the presence of an intracavity absorber or disperser, the beat notes are unbalanced in amplitude or phase, yielding a net signal. By encoding absorption/dispersion information at a high frequency, $1/f$ technical noise is reduced. Another advantage is that any laser frequency noise affects the beat note of the carrier with each sideband equally, which eliminates direct conversion of laser frequency noise to noise in the final spectrum. The disadvantages are the complexity of the technique, particularly the demands of maintaining the laser-cavity lock, and the requirement of a detector whose bandwidth is at least f_h. An extensive review of the NICE-OHMS technique has been published by Foltynowicz et al. [38]

CEVMS and NICE-OHMS have been combined into a technique called noise-immune cavity enhanced optical heterodyne velocity modulation spectroscopy (NICE-OHVMS) in the near-infrared with a Ti:Sapphire laser. [39] Because f_h and f_{vm} are at significantly different frequencies (typically ∼100 MHz and ∼10 kHz, respectively), the detector signal is first demodulated at f_h, and then sent on to further phase-sensitive detection at $2f_{vm}$. NICE-OHVMS preserves the ion-neutral discrimination afforded by VMS, and takes advantage of the ultra-high sensitivity, saturation, and noise immunity of NICE-OHMS.

However, the technical demands of the NICE-OHMS technique have largely precluded its use in the mid-infrared spectral region in which VMS has been successfully exploited. The high bandwidth detectors and phase modulators required for NICE-OHMS are not as readily available in the mid-IR compared with the visible/near-IR. The only published mid-IR NICE-OHMS work was done with a quantum cascade laser near 8.5 μm, and was limited by the detector bandwidth and the phase modulation characteristics of the device. [40] In particular, the 3-5 μm region is particularly attractive for a general-purpose ion spectrometer

because the vast majority of molecules have at least one fundamental vibrational band in that portion of the spectrum.

We have implemented NICE-OHVMS in the mid-IR for the first time using a commercially available cw-optical parametric oscillator (OPO) laser tunable from 3.2-3.9 μm. The high optical power of the OPO ($\sim$1 W) allows for use of higher-bandwidth mid-IR detectors, which have sensitivities too low to be used with many other lower-power cw lasers in this region. This technique enables all of the advantages of the NICE-OHVMS technique to be brought to bear on fundamental vibrational transitions of molecular ions, including high precision sub-Doppler spectroscopy. As a demonstration of the capabilities of this instrument, we present in this paper spectra of H_3^+ at 3.67 μm. In section 3.2 we describe the instrumental details, including a brief discussion of NICE-OHVMS lineshapes, and in section 3.3 we present spectra acquired with the instrument. Finally, in section 3.4, the performance of the instrument is assessed, and future directions discussed.

3.2 Experimental Details

Our OPO-NICE-OHVMS instrument is outlined in Figure 3.1. A Ytterbium-doped fiber laser (YDFL, Koheras Adjustik Y-10) is sent through a fiber EOM (EOSPACE PM-0K5-00-PFU-PFU-106-S), amplified (IPG Photonics YAR-10K-1064-LP-SF), and used to pump a singly-resonant OPO (Aculight Argos 2400 SF). The pump (1064 nm) and signal (1.5-1.6 μm) beams are sent to a wavemeter (Burleigh WA-1500) for frequency calibration. The idler (3.2-3.9 μm) is locked with the Pound-Drever-Hall (PDH) technique to a 1.9-m-long optical cavity consisting of two 1 m radius of curvature concave Si mirrors dielectric coated for 99.7% reflectivity over 3.1-3.4 μm surrounding a plasma cell. Cavity reflection and transmission are monitored by photodiodes (Boston Electronics Vigo PVM-10.6-1x1) with an effective bandwidth of $\sim$125 MHz.

Heterodyne and PDH sidebands are generated by applying voltages at their respective frequencies to the fiber EOM on the seed laser simultaneously. The resultant frequency spectrum of the pump laser is imprinted on the idler beam. A PDH error signal used for cavity locking is generated by demodulating the cavity reflection signal at the frequency RF1 (typically 2-20 MHz). The error signal is sent to feedback electronics which stabilize the length of the cavity on slow timescales via a piezoelectric transducer (PZT) attached to one of the cavity mirrors, and apply fast corrections to the idler frequency by a PZT mounted to one of the resonant signal cavity mirrors inside the OPO head. The cavity transmission detector signal is sent to a pair of mixers 90° out of phase with one another, and each is demodulated at frequency RF2

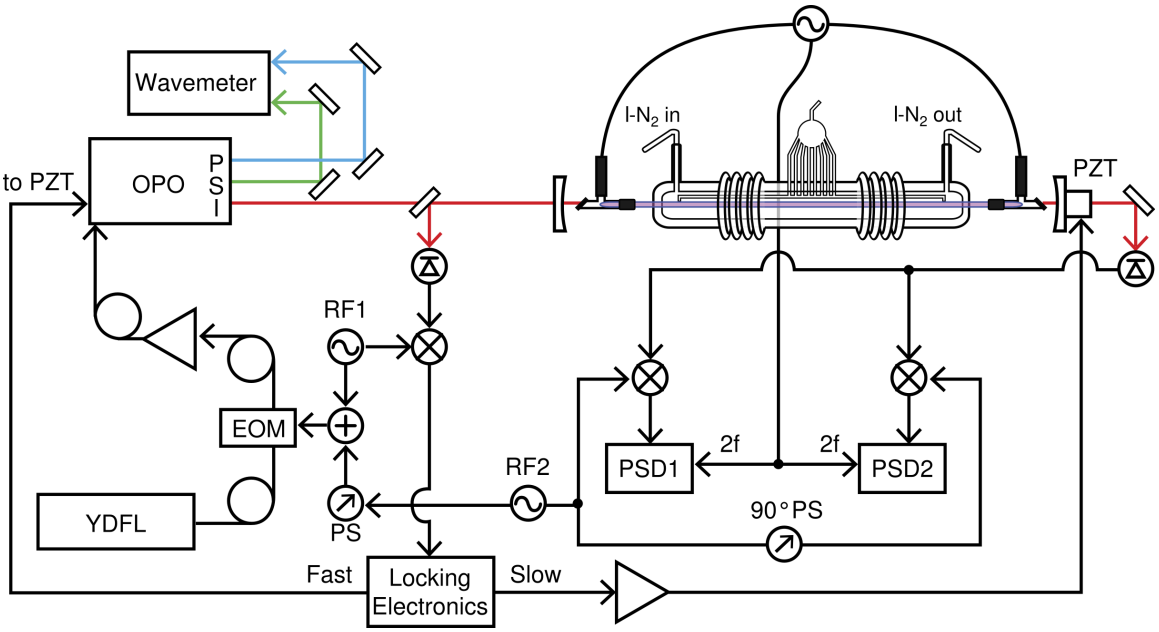

Figure 3.1: Block diagram of OPO-NICE-OHVMS instrument. Details of its operation are given in the main text. YDFL: Ytterbium-doped fiber laser; EOM: electro-optic modulator; OPO: optical parametric oscillator with pump (P, blue), signal (S, green) and idler (I, red) beams; PZT: piezoelectric transducer, PS: phase shifter; PSD: phase sensitive detector; •: signal splitter.

(equal to the cavity FSR of 79.12 MHz). The overall phase of the heterodyne detection is adjusted by phase shifting the RF signal driving the EOM using cables of appropriate lengths. The demodulated signal from each mixer is then sent to a lock-in amplifier referenced to twice the frequency used to drive the plasma, and the in-phase and quadrature outputs of each amplifier are digitized and stored on a computer.

Ions are produced in a liquid-nitrogen-cooled multi-inlet multi-outlet positive column discharge cell, which is placed between the two free-standing mirrors of the optical cavity. [41] Intracavity radiation is admitted into the cell by means of CaF_2 windows aligned at Brewster's angle. The plasma is driven by an AC voltage produced by amplifying the output of an arbitrary waveform generator with an audio amplifier (Techron 7780) and a step-up transformer. The exact gas mixtures, pressures, discharge currents, and frequencies used vary; the specific conditions employed are described in the results section.

Typical operation begins by filling the cooling jacket of the cell with liquid nitrogen and igniting the plasma. The cavity length is adjusted to bring it into resonance with the laser, and the laser-cavity lock is established. The idler frequency is tuned by applying a voltage to an internal PZT on the YDFL, and the cavity length is controlled with the locking electronics to maintain the resonance condition. When the PZT reaches the end of its travel, the laser-cavity lock is electronically interrupted, the cavity length is reset to the other end of its travel, a new resonance is found, and the lock is reestablished. In this manner,

the spectrometer can scan without manual intervention over the entire range of the YDFL PZT (around 100 GHz), although in practice a scan is generally much shorter. It is in principle possible to extend the automated tuning range further by electronic control of the intracavity etalon of the OPO and the nonlinear crystal position/temperature, but the practical utility of such efforts would likely be minimal.

3.3 Results and Analysis

3.3.1 Lineshapes

The overall Doppler lineshape for NICE-OHVMS in both absorption and dispersion has odd symmetry, and qualitatively appears similar to the third derivative of a Gaussian, Lorentzian, or Voigt profile. A detailed analysis of the lineshape is beyond the scope of this paper and will be the subject of a future work, but a qualitative description follows. Consider a general NICE-OHMS lineshape, such as that shown in panels a and b of Figure 2 in Ref. [38]. If the signal belongs to an ion, then the ac voltage of the plasma causes velocity modulation (VM), Doppler shifting the lineshape at the plasma frequency. As a result of the bidirectional nature of light in our optical cavity, the lineshape is simultaneously Doppler shifted to the red and to the blue by the same amount at each point in time along the plasma voltage cycle. Consequently, the time-dependent signal repeats itself every plasma half-cycle, or at twice the ac plasma frequency ($2f$). In addition to VM, an ion also experiences concentration modulation (CM) at $2f$, and CM may be phase shifted with respect to VM. Thus, in addition to a periodic Doppler shift at $2f$ from VM, the lineshape amplitude varies at $2f$ from CM. The net signal observed comes in 4 channels corresponding to the even and odd second order Fourier coefficients of the absorption and dispersion profiles affected by VM and CM.

The sub-Doppler lineshape is more straightforward. As has been discussed in regard to previous NICE-OHMS setups [39, 42, 43], the carrier and sidebands can all act as pumps and probes for saturation spectroscopy. The spectroscopic Lamb dips arising from the Bennet holes burned in the population appear at half-integer multiples of the carrier-sideband spacing f_h, i.e. at all frequencies at which forward- and reverse-propagating beams sample the same velocity component. At the line center ν_0, when the zero-velocity distribution is both pumped and probed by the carrier, a signal only appears in dispersion as the heterodyne detection scheme employed by NICE-OHMS is insensitive to absorption of the carrier. The dispersion signal therefore contains Lamb dips at $\nu_0 \pm (nf_h/2)$ with $(n \geq 0)$, and the absorption signal contains them at $\nu_0 \pm (nf_h/2)$ with $(n > 0)$. The relative strengths of the Lamb dips with increasing n depend on the modulation index of the laser frequency modulation; at sufficiently low modulation index, higher order Lamb dips are not observable.

While VM and CM have a strong influence on the lineshape of the Doppler profile, they do not affect the sub-Doppler features in the same way. Because Bennet holes are only burned in the population at or spaced evenly around the zero-velocity component of the ion distribution, VM effectively changes the abundance of ions with the appropriate velocity. In that way, VM effectively behaves like CM, and the net effect is to influence the amplitude of the Lamb dip lineshape and the relationship between the amplitudes of the even and odd Fourier coefficients within absorption or dispersion. Neglecting any change of ion's collision rate with changing velocity, VM and CM do not affect the sub-Doppler profile beyond its amplitude. The sub-Doppler lineshape function [39] is

$$\begin{aligned}\chi(\nu_d) =& \sum_{n>0}\left(A_n\left[\chi_a\left(\nu_d-\frac{nf_h}{2}\right)-\chi_a\left(\nu_d+\frac{nf_h}{2}\right)\right]\right)\sin\theta_h \\ &+\left\{-2A_0\chi_d(\nu_d)+\sum_{n>0}\left(A_n\left[\chi_d\left(\nu_d-\frac{nf_h}{2}\right)+\chi_d\left(\nu_d+\frac{nf_h}{2}\right)\right]\right)\right\}\cos\theta_h, \qquad (3.1)\end{aligned}$$

where ν_d is the frequency detuning $\nu-\nu_0$, θ_h is the heterodyne detection phase, and A_n are effective amplitudes of the nth order Lamb dips for absorption and dispersion. $\chi_a(\omega)$ is a Lorentzian lineshape function for absorption, and $\chi_d(\omega)$ is a lineshape function for dispersion related to $\chi_a(\omega)$ by the Kramers-Kronig relations. These are defined as

$$\begin{aligned}\chi_a(\omega) =& \frac{1}{1+\gamma^2(\omega-\omega_0)^2} \quad \text{and} \\ \chi_d(\omega) =& \frac{-(\omega-\omega_0)\gamma}{1+\gamma^2(\omega-\omega_0)^2},\end{aligned}$$

where ω_0 is the center and γ is the inverse of the half-width at half-maximum. When using this fit function, f_h is held at the cavity FSR (79.12 MHz), the amplitudes are constrained such that $A_n > A_{n+1}$, and the Doppler profile near the line center is approximated by a third-order polynomial with the quadratic term set to 0. The maximum index of n used in the fit depends on the modulation index and saturation parameter; in this work, only $n=1$ terms are used.

3.3.2 H_3^+

H_3^+ is the simplest polyatomic molecular ion, and serves as the primary initiator of ion-molecule chemistry in interstellar clouds. [1, 2] Its infrared spectrum was first observed by Oka in 1980, [18] and since then it has been extensively studied spectroscopically (see, for instance, the review in Ref. [19]). More recent research on H_3^+ focuses on spectroscopy above the so-called "barrier to linearity," at which point the molecule adopts a linear geometry that induces a singularity in the Hamiltonian, complicating its theoretical treatment. [8]

Nevertheless, for the lowest-lying energy levels, the agreement between experiment and ab initio theory is good to spectroscopic accuracy. [44] Measuring the energy level spacings experimentally with greater precision and accuracy would present a greater challenge for ab initio theory, possibly spurring new developments. The OPO-NICE-OHVMS technique opens the possibility of measuring such energy level spacings in H_3^+.

H_3^+ was produced in a liquid-nitrogen-cooled 40 kHz AC plasma at a pressure of 200 mTorr. The outputs of the two mixers were each demodulated at 80 kHz with a lock-in amplifier set to a 10 ms time constant, and each amplifier's detection phase was set at 40° relative to the plasma reference signal. A sample spectrum of the $R(1,0)$ and $R(1,1)^u$ transitions of the ν_2 fundamental band of H_3^+ acquired with a discharge current of 100 mA is shown in Figure 3.2. The signals in the top panel are the demodulated in-phase (black) and quadrature (red, offset) components of the mixer nominally set to the absorption phase, and the corresponding traces in the bottom panel are those of the dispersion phase (see below for more detail about absorption vs. dispersion phases). A scan over just the $R(1,0)$ transition at a current of 175 mA is shown in Figure 3.3, in which the in-phase absorption (black) and dispersion (red) signals are shown. The dispersion signal has been inverted relative to Figure 3.2 for clarity.

A fit of the sub-Doppler portion of the traces shown in Figure 3.3 to Equation 3.1 is shown in Figure 3.4. Both data sets were fit simultaneously subject to the constraints that ω_0, γ, and all A_n are equal for both sets. The phase difference between the two mixers, nominally 90°, was allowed to float during the fit. The overall quality of the fit is quite good; the residuals are composed primarily of fringing evident on top of the spectrum. The line center derived from the fit is $2725.9011918 \pm 0.0000098$ cm^{-1}, but the absolute accuracy is limited by the 2×10^{-3} cm^{-1} accuracy of the wavemeter. The value of θ_h for mixer 1 was found to be ∼123°, and ∼50° for mixer 2; thus, the two mixers are ∼70° out of phase with one another rather than 90°. Typically, dispersion can be isolated from absorption by minimizing the central Lamb dip feature in one of the two detection phases; however, the full width at half maximum of the Lamb dips (as derived from our fit) is ∼100 MHz. The spacing between the first-order absorption Lamb dips is equal to the heterodyne sideband spacing of 79.12 MHz, so even if absorption were isolated, the features would be blended into a single central feature. Thus, proper isolation of absorption and dispersion is not possible simply by inspection in this case; with narrower Lamb dips or a larger heterodyne frequency, isolation would be much easier.

3.4 Discussion

The most interesting aspect of the OPO-NICE-OHVMS technique is the presence of Lamb dips which enables high precision measurements of line center frequencies. As demonstrated above with H_3^+, the precision of

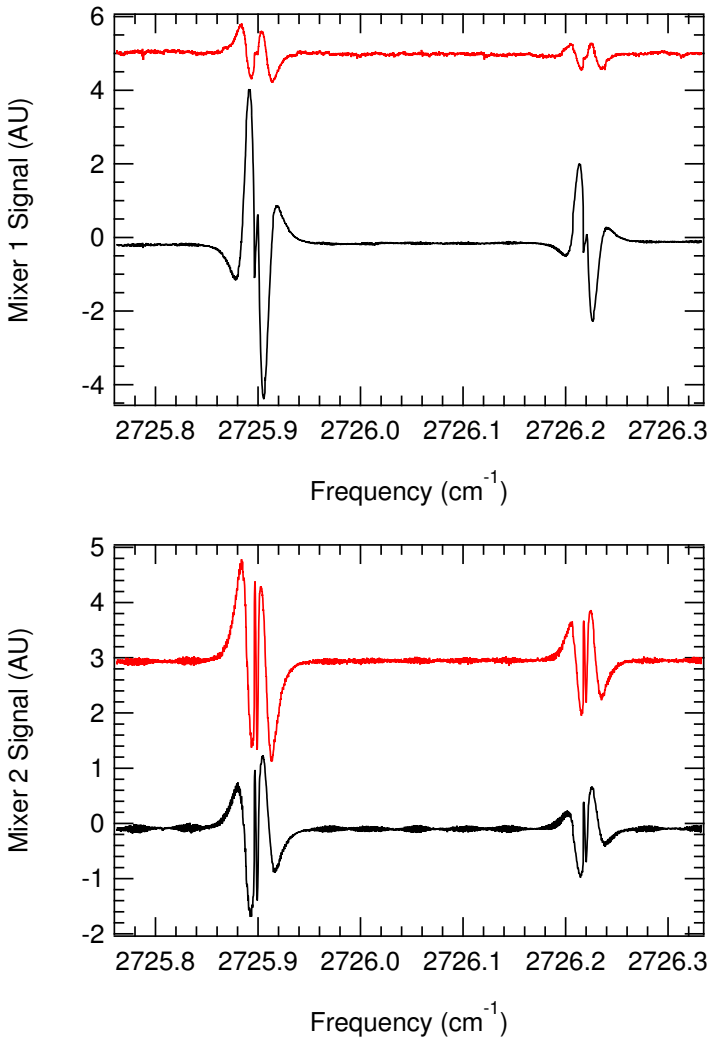

Figure 3.2: OPO-NICE-OHVMS spectrum of the $R(1,0)$ and $R(1,1)^u$ transitions of the ν_2 fundamental band of H_3^+. Each panel shows the in-phase (black, bottom) and quadrature (red, top) outputs of a lock-in amplifier demodulating the indicated mixer's signal.

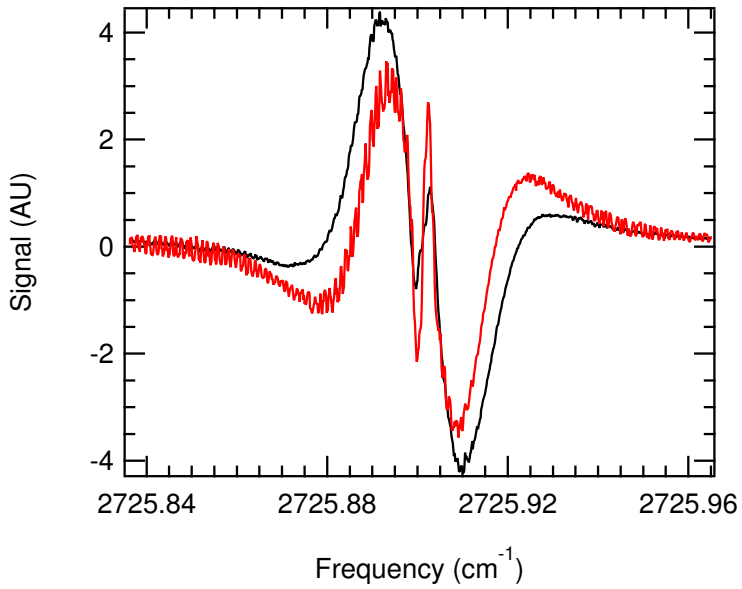

Figure 3.3: OPO-NICE-OHVMS spectrum of the $R(1,0)$ transition of the ν_2 fundamental band of H_3^+. The black trace is the in-phase output of mixer 1, and the red is the in-phase output of mixer 2.

the line center determination is on the order of 0.3 MHz. In its present implementation, the technique's accuracy is limited by the wavemeter, and also by slow drifts in the frequency of the signal beam caused by thermal fluctuations of the OPO cavity. Use of an optical frequency comb to stabilize and measure the frequencies of the pump and signal beams would reduce the accuracy uncertainty to < 100 kHz, and thus the total uncertainty on line center measurements would be limited primarily by the width of the Lamb dips.

The width of the Lamb dips ($\sim$100 MHz from the fitting) is fairly broad. We have varied the intracavity laser power and the cell pressure, but any differences in the linewidth were not observable. However, the ranges of the power and pressure measurements were limited: the intracavity power could only be changed by a factor of 2 before the laser-cavity lock was adversely affected, and the plasma could only give stable operation over 200-600 mTorr. Such wide Lamb dips were also observed in the NICE-OHVMS experiment performed in the near-IR [39]; in that study, the authors were able to observe a change in linewidth with pressure, but extrapolating to zero pressure still gave a linewidth of $\sim$30 MHz. Assuming that the linewidth is related to the time an ion spends at zero velocity, it is perhaps unsurprising that a light ion like H_3^+ has a broader linewidth than N_2^+, as its velocity may be more easily altered by weak long-range collisions.

The fringing apparent in the figures above limits the sensitivity of the present measurements. The origin of the fringing is not fully understood; however, it appears to have a definite phase with respect to the heterodyne detection. When the plasma is turned off, the fringing does not appear in a scan, and if the cavity transmission detector is blocked while a fringe is present on a lock-in channel, the signal returns to

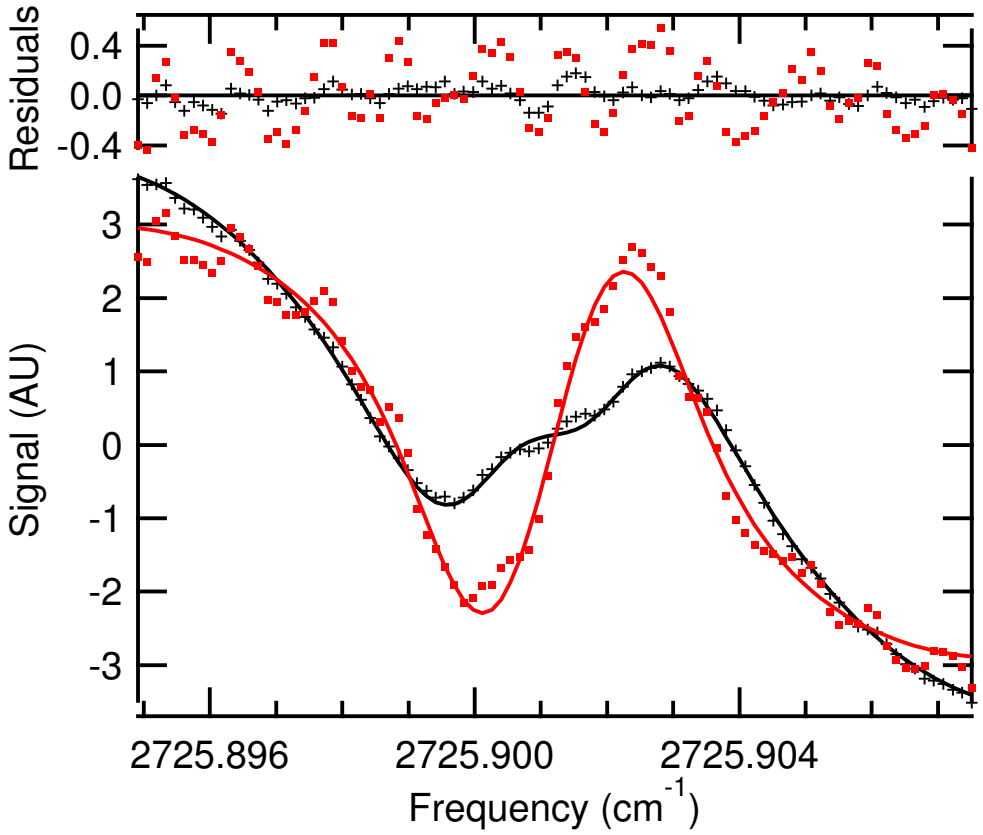

Figure 3.4: A fit of the central sub-Doppler region of the traces shown in Figure 3.3 to Equation 3.1. The red dots are the data points corresponding to mixer 2, and the black crosses correspond to mixer 1. The red and black curves are the fitted lineshapes, and the residuals for each fit are shown above, with symbols corresponding to the appropriate trace.

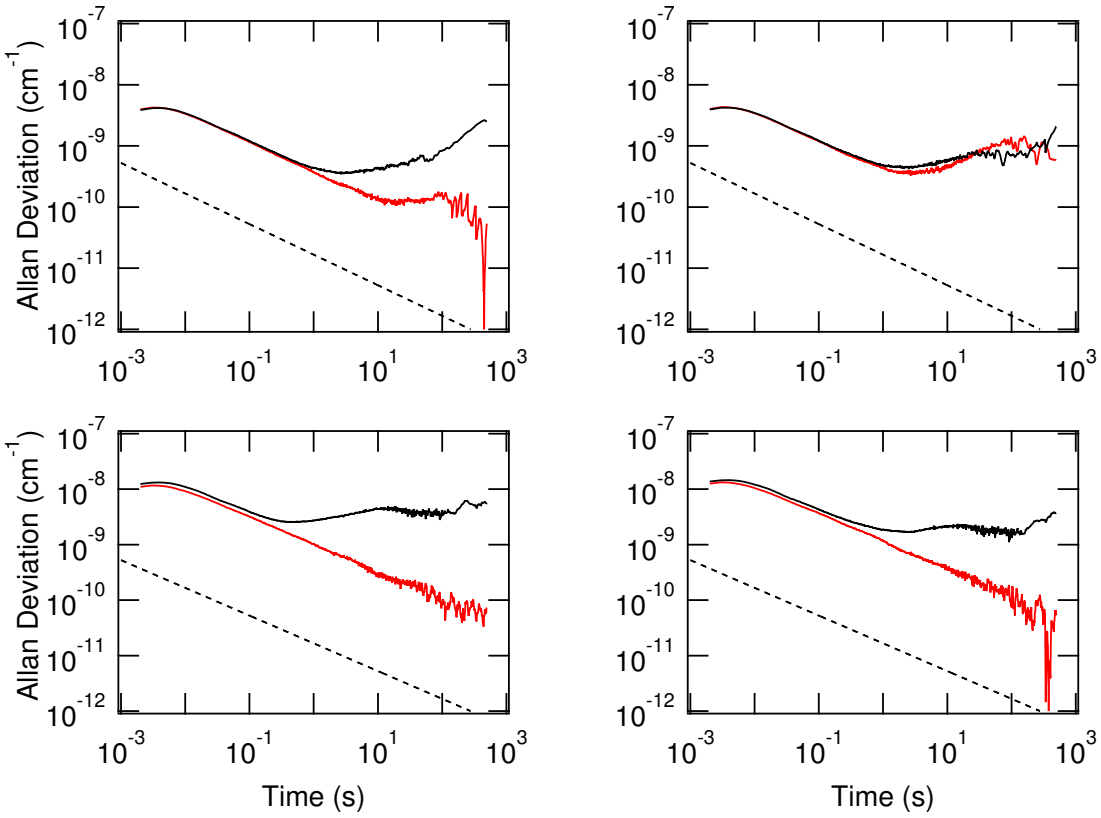

Figure 3.5: Plots of Allan deviation of the noise equivalent fractional absorption in the four detection channels. The red traces were recorded with the plasma off, and the black traces with the plasma on. The dashed line is the shot noise limit. The upper left and right panels correspond to the in-phase and quadrature components respectively of the signal from mixer 1, and the lower panels to mixer 2.

zero. Thus, it appears that the fringing is the result of the plasma interacting with the laser light. One possibility is that residual amplitude modulation (RAM) in the heterodyne sidebands is being modulated by the plasma. RAM is an imbalance in the amplitude and/or phase of the sidebands with respect to one another. When demodulated, RAM appears as a DC offset in the heterodyne signal; because of our detection scheme using velocity modulation and $2f$ detection, the NICE-OHVMS would ordinarily be insensitive to such an offset. However, if the refractive index of the plasma varies at $2f$, the DC signal from RAM will be modulated at $2f$ as well, resulting in a net NICE-OHVMS signal. Because RAM is also affected by the presence of etalons in the optical system and the optical frequency, a fringing pattern could possibly result as a function of laser frequency. Testing whether this is truly the origin of the fringing is difficult; however, initial experiments performed at a heterodyne frequency of ∼240 MHz (three times the cavity FSR) do not appear to show the same fringing. It is probable that the fringing would be reduced by employing a RAM compensation scheme via temperature and voltage control of the fiber EOM. [45]

The sensitivity of the technique is illustrated by the Allan deviation plots of noise-equivalent fractional absorption in Figure 3.5. With a 10 ms integration time on the lock-in amplifiers (as shown in Figures 3.2, 3.3, and 3.4), the noise-equivalent fractional absorption α_{min} is $\sim 3 \times 10^{-9}$ cm^{-1} in mixer 1, and $\sim 1 \times 10^{-8}$ cm^{-1} in mixer 2. This difference is likely electronic in origin; when the plasma is off, there is no appreciable difference in the Allan deviation at such short timescales. Both of these values are well above the shot-noise limit of 1.66×10^{-10} cm^{-1}, which for NICE-OHMS (and NICE-OHVMS) is given in terms of equivalent fractional absorption by:

$$\alpha_{min} = \frac{\pi}{2F}\sqrt{\frac{eB}{\eta P_0}}\frac{1}{J_0(\beta)J_1(\beta)L}, \tag{3.2}$$

where F is the cavity finesse, e the electric charge, B the detection bandwidth, η the detector responsivity, P_0 the power incident on the detector, $J_n(\beta)$ the nth order Bessel function for modulation index β ($\beta = 0.63$ in our instrument), and L the cavity length. While NICE-OHMS has been able to achieve a noise level within a factor of 2 of the shot noise limit in one implementation [37], the performance achieved by OPO-NICE-OHVMS relative to the shot noise limit is already comparable to a number of other NICE-OHMS setups (see the extensive discussion in section 4 of [38]).

Ultimately, the absolute sensitivity can be improved by identifying and eliminating noise sources and by increasing the cavity finesse. An increase in cavity finesse leads to additional technical challenge in maintaining the laser-cavity lock, and may increase the sensitivity of the system toward the fringing effects that have already been observed. Such challenges can likely be overcome by improving the bandwidth of the laser frequency corrections (currently limited to the 10 kHz bandwidth of the signal cavity PZT), and correcting for RAM as discussed above.

3.5 Conclusions

In this paper, we have demonstrated sub-Doppler spectroscopy of molecular ions in the mid-infrared spectral region using the NICE-OHVMS technique with a cw-OPO laser. By phase modulating a 1064 nm seed laser with a fiber EOM prior to amplification and optical parametric oscillation, frequency modulation of the infrared idler beam is effected without requiring a mid-IR EOM. The high optical power of the idler beam allows use of high-bandwidth detectors, which in turn makes ultra-sensitive spectroscopy via NICE-OHMS possible. Velocity modulation spectroscopy is then combined with NICE-OHMS to afford ion-neutral discrimination, and the intracavity laser power is sufficient for saturating fundamental rovibrational transitions as demonstrated by spectroscopy of H_3^+. By fitting the sub-Doppler spectral features, the center frequencies of individual rovibrational lines can be measured with a precision of 0.3 MHz, and the achieved

sensitivity is within a factor of 20-50 of the shot noise limit, likely limited by electronic noise in the system. Improvements to the technique, such as addition of an optical frequency comb for accurate wavelength calibration, technical modifications to improve its sensitivity, and expanding the frequency coverage of the OPO from 3.2-3.9 μm to 2.8-4.8 μm are envisioned.

The authors would like to thank Takeshi Oka for providing us with the liquid nitrogen cooled plasma cell and its associated pumps and plasma electronics. KNC acknowledges support from a NASA Earth and Space Science Fellowship. JNH acknowledges support from a Springborn Fellowship. This work has been supported by the National Science Foundation (PHY 08-55633), the NASA Laboratory Astrophysics program (NNX08AN82G), and a David and Lucile Packard Fellowship.

Chapter 4

On the Ortho:Para Ratio of H_3^+ in Diffuse Molecular Clouds

4.1 Introduction

Observations of H_3^+ in diffuse molecular clouds—diffuse clouds in which a significant fraction of the hydrogen is in molecular form [46]—have led to various unexpected discoveries. The very first detection of H_3^+ along a diffuse molecular cloud sight line (toward Cyg OB2 12) showed an abundance about 10 times greater than expected for the environment [21]. This surprising overabundance, also found toward several more diffuse cloud sight lines, led to the eventual conclusion that the ionization rate of H_2 due to cosmic rays, ζ_2, must be about 1 order of magnitude larger than previously thought [22, 47]. Another puzzling outcome from H_3^+ observations is that the average excitation temperature derived from the two lowest energy states ($\langle T(H_3^+)\rangle \approx 30$ K [22]) differs significantly from the average excitation temperature derived from the two lowest rotational states of H_2 ($\langle T_{01}\rangle \approx 70$ K [48–50]). Given that both species are expected to be thermalized to the cloud kinetic temperature by collisions, such a discrepancy is unexpected.

Despite the fact that the $J = 0$ and $J = 1$ levels of H_2 are essentially different "species"—conversion between the even–J *para* and odd–J *ortho* nuclear spin states is only possible through reactive collisions—it has long been assumed that T_{01} is a good approximation for the kinetic temperature, T_{kin}, in diffuse molecular clouds. This is because H_2 molecules are expected to experience many reactive collisions with protons during their lifetimes. As a result, the *ortho* and *para* populations of H_2 should be brought into thermal equilibrium with the proton kinetic temperature [51].

Similarly, H_3^+ also has *ortho* and *para* nuclear spin states ($(J, K) = (1, 1)$ is the lowest lying *para* state, and $(J, K) = (1, 0)$ the lowest lying *ortho* state). For H_3^+ though, the relative population between the two states has been expected to be thermalized by reactive collisions with H_2 [47, 52, 53]. As the average values of T_{01} and $T(H_3^+)$ do not agree, this does not seem to be the case.

However, out of the 66 and 18 sight lines used to compute $\langle T_{01}\rangle$ and $\langle T(H_3^+)\rangle$, respectively, only 2 are

This chapter is adapted with permission from K. N. Crabtree, N. Indriolo, H. Kreckel, B. A. Tom, and B. J. McCall, Astrophysical Journal 729 (2011) 15, Copyright 2011, American Astronomical Society. The astronomical observations and associated spectra and tables in this chapter were made by N. Indriolo. Based in part on observations made with ESO Telescopes at the La Silla or Paranal Observatories under programme ID 384.C-0618

shared between both samples. While previously reported values of T_{01} and $T(H_3^+)$ do differ for these sight lines toward ζ Per and X Per by about 30 K [22, 48, 49], such a small sample does not provide particularly meaningful results. In order to increase the number of sight lines with *ortho* and *para* column densities determined for both H_2 and H_3^+, we have made observations searching for H_3^+ absorption features along sight lines with measured H_2 column densities. These observations and our data reduction procedures are described in Section 2. Section 3 discusses and justifies many of the assumptions made concerning molecular hydrogen and T_{01} in diffuse molecular clouds. In Section 4, we examine the $H_3^+ + H_2$ reaction and present steady state models to explore the temperature discrepancy between T_{01} and $T(H_3^+)$. Section 5 reviews the observations and modeling, and presents our conclusions from the work.

4.2 Observations & Data Reduction

Target sight lines were selected based on H_2 column densities [48–50] and L-band magnitudes. We required that the $J = 0$ and $J = 1$ column densities of H_2 ($N(0)$ and $N(1)$, respectively) both be known, and that the total H_2 column density ($N(H_2)$) be greater than 10^{20} cm^{-2}. The L-band magnitude was required to be brighter than 6 mag so that the necessary integration times would be relatively short. Observations focused on the $R(1,1)^u$, $R(1,0)$, and $R(1,1)^l$ transitions (at 3.668083 μm, 3.668516 μm, and 3.715479 μm, respectively) which arise from the $(J,K) = (1,1)$ and $(1,0)$ levels of the ground vibrational state of H_3^+, the only levels expected to be significantly populated at average diffuse cloud temperatures ($T \sim 70$ K).

Spectra in support of this project were obtained using the Phoenix spectrometer [54] at the Gemini South Telescope and the Cryogenic High-resolution Infrared Echelle Spectrograph (CRIRES) [55] at the Very Large Telescope (VLT). Observations at Gemini South were made in queue mode, and the Phoenix spectrometer was used with its echelle grating and 0.17" slit to produce a resolving power of about 70,000, and with the L2734 filter to select the order containing the $R(1,1)^u$ and $R(1,0)$ transitions. Observations at the VLT were made in service mode, and CRIRES was used with its 0.2" slit to provide a resolving power of about 100,000, and a reference wavelength of 3715.0 nm to cover the $R(1,1)^u$ and $R(1,0)$ transitions on detector 1 and the $R(1,1)^l$ transition on detector 3. The adaptive optics system was used with CRIRES to maximize starlight passing through the narrow slit. In addition to the science targets, bright, early-type stars were observed for use as telluric standards. For all observations, the star was nodded along the slit in an ABBA pattern in order to facilitate the removal of atmospheric emission lines and dark current via the subtraction of neighboring images. A log containing the observed sight lines and respective integration times is given in Table 4.1.

Object	Date(s) of Observation	Telescope	Integration Time (min)	Standard
HD 149404	2009 Aug 05	Gemini South	32	λ Sco
χ Oph	2009 Aug 30	Gemini South	12	λ Sco
HD 152236	2009 Aug 30	Gemini South	16	λ Sco
HD 154368	2009 Aug 30	Gemini South	32	λ Sco
HD 53367	2009 Dec 03	VLT	30	κ Ori
HD 73882	2009 Dec 03	VLT	30	ζ Pup
	2010 Jan 17	VLT	30	ζ Pup
HD 110432	2010 Jan 27	VLT	10	η Cen
	2010 Feb 28	VLT	20	η Cen
	2010 Mar 02	VLT	40	η Cen
μ Nor	2010 Apr 05	Gemini South	72	λ Sco

Table 4.1: Observations

Various standard IRAF[1] procedures were used in the data reduction process. Given the different state of data available from Phoenix versus CRIRES, different amounts of processing were required for data from the 2 telescopes. For each night of Phoenix observations, a bad pixel map was created from the average of several dark frames, and these pixels were interpolated over in the object and flat frames. Flats were then combined to create a normalized flat field which was divided out of the object frames. Neighboring AB image pairs were subtracted from each other to remove atmospheric emission and dark current. Finally, one-dimensional spectra were extracted using *apall*. In the case of CRIRES observations, data were processed through the CRIRES specific pipeline, resulting in fully reduced two-dimensional spectral images for each target (given the product codes SCOM and PCOM by the pipeline). One-dimensional spectra were extracted from these images. All such spectra from both telescopes were then imported to IGOR Pro[2] where the remainder of reduction was performed.

Individual Phoenix spectra within an exposure sequence for a given target were then added together. Science target spectra from both telescopes were divided by telluric standard spectra to remove atmospheric absorption features and to normalize each spectrum. These normalized spectra were wavelength calibrated with a typical accuracy of ~ 2 km s^{-1} using the vacuum wavelengths of the atmospheric absorption lines. Calibrated spectra were then shifted into the local standard of rest (LSR) frame, and spectra of the same target from different nights were combined using a variance-weighted mean. For each sight line the continuum surrounding the absorption features was then fit with an $n^{\rm th}$ order polynomial ($n = 7-9$) and the spectrum was divided by the fit to re-normalize the continuum level. The resulting spectra for sight lines with H_3^+ absorption features—HD 154368, HD 73882, and HD 110432—are shown in Figure 4.1. Although H_3^+ spectra for ζ Per and X Per (the other 2 sight lines with both H_2 and H_3^+ data) are reported in Indriolo et al. [22],

[1] http://iraf.noao.edu/
[2] http://www.wavemetrics.com/

the reduction process utilized in that study did not combine spectra using a variance-weighted mean, nor did it fit fluctuations in the continuum level with a polynomial function. For the purpose of consistency, we have reprocessed the data from both sight lines. No new data have been added, but differences in the method of processing have resulted in output spectra with slightly better signal-to-noise ratios (S/N). These spectra are also shown in Figure 4.1.

Absorption features due to H_3^+ were fit with Gaussian functions in order to determine equivalent widths, velocity full-width at half-maxima (FWHM), and interstellar gas velocities. Our fitting procedure uses the functional form of a Gaussian where area (as opposed to amplitude) is a free parameter, and includes a fit to the continuum level, y_0. In the case of the $R(1,1)^u$ and $R(1,0)$ lines, both absorption features are fit simultaneously and a single best-fit continuum level is found. Uncertainties on the equivalent widths (δW_λ) and continuum level (δy)—both at the 1σ level—were output by the fitting process. To estimate the systematic uncertainties due to continuum placement, we forced the continuum level to $y_0 + \delta y$ and $y_0 - \delta y$ and re-fit the absorption lines. Variations in the equivalent widths due to this shift are small compared to those reported by the fitting procedure and so are not included in our analysis (i.e., $\sigma(W_\lambda)$=δW_λ). Assuming optically thin absorption lines and taking transition dipole moments and wavelengths from Goto et al. [56] and references therein, column densities were derived from equivalent widths using the standard relation. All of these results are shown in Table 4.2.

These observations increase the total number of sight lines with both H_3^+ and H_2 detections from 2 to 5. Column densities, *para*-fractions, and excitation temperatures for both species along all 5 sight lines are collected in Table 4.3. H_2 data come from Savage et al. [48] and Rachford et al. [49]. Uncertainties on all values are 1σ. The excitation temperatures inferred from the $R(1,0)$, $R(1,1)^u$, and $R(1,1)^l$ absorption lines of H_3^+ range from $20 \leq T(H_3^+) \leq 46$ K, while those reported for H_2 vary from $51 \leq T(H_2) \leq 68$ K. In 4 sight lines T_{01} is greater than $T(H_3^+)$ by about 30 K, while for X Per T_{01} and $T(H_3^+)$ are consistent within uncertainties. Still, these observations clearly show that for the same interstellar material along 4 different diffuse molecular cloud sight lines the excitation temperatures derived from H_3^+ and H_2 do not agree.

4.3 H_2 Thermalization

Given the large discrepancies between T_{01} inferred from H_2 and the excitation temperature of H_3^+, it is important to re-examine the assumption that the inferred T_{01} accurately reflects the kinetic temperature of the diffuse molecular clouds. If this assumption were incorrect, it would be conceivable that H_3^+ provides the true (lower) temperature of diffuse molecular clouds. There are at least 4 reasons this assumption could

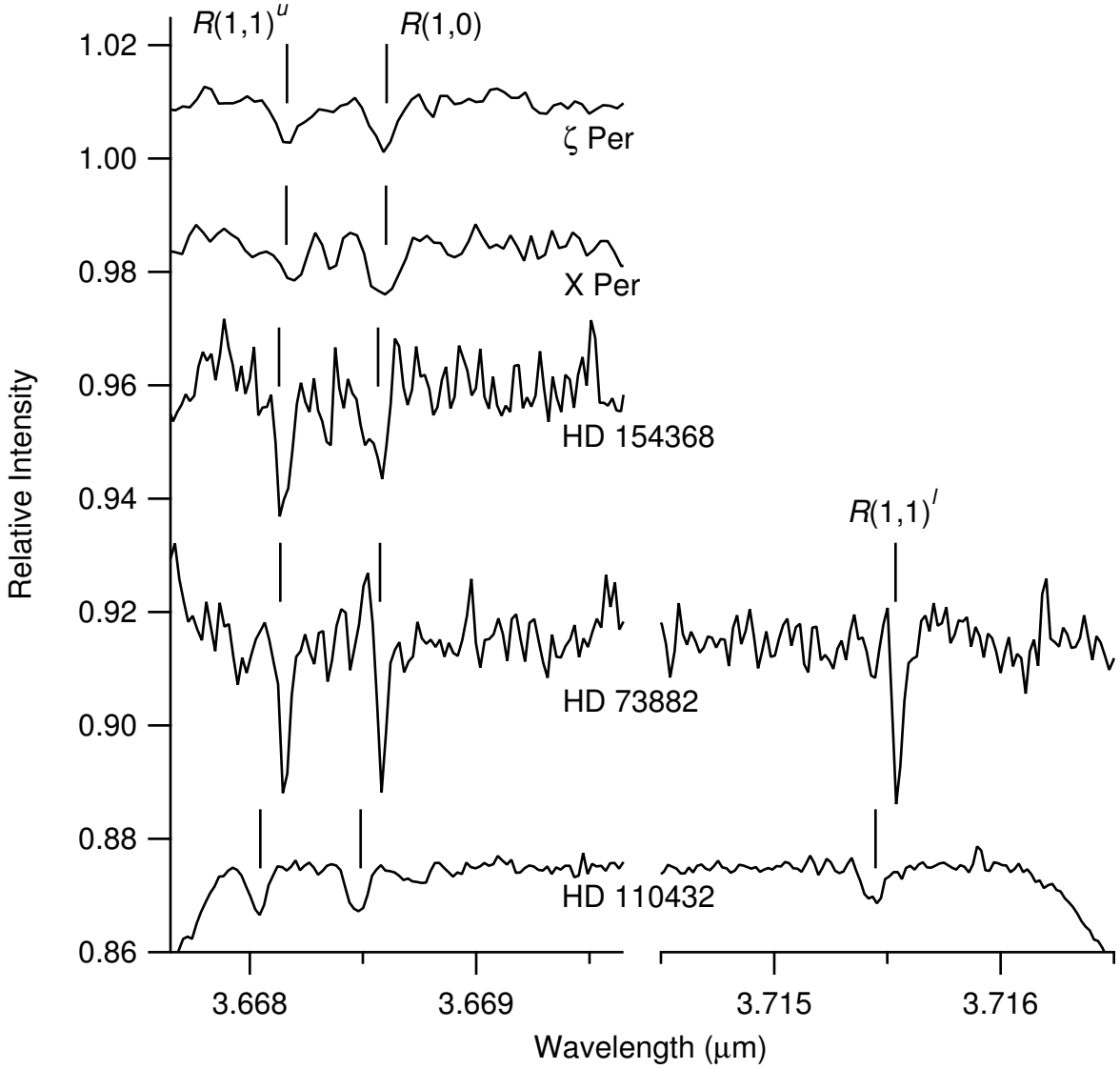

Figure 4.1: Spectra showing absorption lines from the $(J, K) = (1, 1)$ and $(1, 0)$ states of H_3^+. Spectra for ζ Per and X Per were taken at UKIRT and are reprocessed versions of the data previously reported in Indriolo et al. [22]. The spectrum for HD 154368 was taken at Gemini South, while those for HD 73882 and HD 110432 were taken at the VLT. Large deviations from flat continuum levels in the spectra for HD 154368, HD 73882, and HD 110432 are the combination of 2 effects: (1) artifacts due to continuum fitting at wavelengths far away from the H_3^+ absorption lines; (2) inability to remove the strong atmospheric methane line immediately shortward of the $R(1, 1)^u$ line. Vertical lines mark the expected positions of the H_3^+ absorption lines given previously determined interstellar gas velocities along each sight line.

Object	Transition	$v_{\rm LSR}$ (km s^{-1})	FWHM (km s^{-1})	W_λ (10^{-6} μm)	$\sigma(W_\lambda)$ (10^{-6} μm)	$N(J,K)$ (10^{13} cm^{-2})	$\sigma(N)$ (10^{13} cm^{-2})
ζ Per	$R(1,1)^u$	7.7	11.0	0.99	0.13	4.09	0.53
	$R(1,0)$	6.1	9.0	1.00	0.11	2.53	0.29
X Per	$R(1,1)^u$	8.2	9.1	0.80	0.17	3.34	0.69
	$R(1,0)$	6.3	10.2	1.30	0.18	3.29	0.45
HD 154368	$R(1,1)^u$	5.4	6.0	1.79	0.30	7.43	1.24
	$R(1,0)$	5.2	5.6	1.12	0.29	2.83	0.74
HD 73882	$R(1,1)^u$	5.9	3.9	1.44	0.21	5.97	0.86
	$R(1,0)$	5.7	3.2	1.16	0.19	2.94	0.48
	$R(1,1)^l$	5.4	3.5	1.34	0.15	6.15	0.69
HD 110432	$R(1,1)^u$	-3.8	6.9	0.74	0.06	3.08	0.24
	$R(1,0)$	-3.3	7.5	0.83	0.07	2.11	0.17
	$R(1,1)^l$	-3.1	8.1	0.69	0.06	3.15	0.28

Table 4.2: Absorption line parameters. Column 3 ($v_{\rm LSR}$) gives the interstellar gas velocity in the local standard of rest frame. Column 4 (FWHM) gives the full width at half-maximum of the absorption features. Columns 5 and 6 show the equivalent width, W_λ, and its 1σ uncertainty, $\sigma(W_\lambda)$, respectively. Columns 7 and 8 give the column density of H_3^+ in the state each transition probes, $N(J,K)$, and its uncertainty, $\sigma(N)$, respectively. Values for these parameters in the ζ Per and X Per sight lines were previously reported in Indriolo et al. [22]. The new values for both absorption lines toward ζ Per and the $R(1,0)$ line toward X Per are consistent with the previously published results within uncertainties. However, the new and old results for the $R(1,1)^u$ line toward X Per are inconsistent. Upon inspection, we found this to be due to a bad fit to that line during the 2007 analysis. In all cases, the values published herein should be taken to supersede those from Indriolo et al. [22].

		ζ Per[a,b]	X Per[a,c]	HD 154368[c]	HD 73882[c]	HD 110432[c,d]
			H_3^+ Results			
$N(1,1)$	(10^{13} cm^{-2})	4.09 ± 0.53	3.34 ± 0.69	7.43 ± 1.24	6.08 ± 0.12	3.11 ± 0.05
$N(1,0)$	(10^{13} cm^{-2})	2.53 ± 0.29	3.29 ± 0.45	2.83 ± 0.74	2.94 ± 0.48	2.11 ± 0.17
$p_3^{\rm e}$		0.62 ± 0.04	0.50 ± 0.06	0.72 ± 0.06	0.67 ± 0.04	0.60 ± 0.02
$T(H_3^+)$	(K)	28 ± 4	46^{+21}_{-13}	20 ± 4	23 ± 3	30 ± 2
			H_2 Results			
$\log[N(0)]$	(cm^{-2})	20.51 ± 0.09	20.76 ± 0.03	21.04 ± 0.05	20.99 ± 0.08	20.40 ± 0.03
$\log[N(1)]$	(cm^{-2})	20.18 ± 0.09	20.42 ± 0.06	20.54 ± 0.15	20.50 ± 0.07	20.27 ± 0.04
$p_2^{\rm f}$		0.68 ± 0.06	0.69 ± 0.04	0.76 ± 0.07	0.76 ± 0.05	0.57 ± 0.03
T_{01}	(K)	58 ± 6	57 ± 4	51 ± 8	51 ± 6	68 ± 5

Table 4.3: Measured column densities for the lowest lying *ortho* and *para* states of H_2 and H_3^+ are shown for the 5 sight lines with all such data available. Also shown are the *para*-fractions for each species and the rotational temperatures derived from a simple 2-state system analysis. a) Updated analysis of H_3^+ data originally presented in Indriolo et al. [22]. b) H_2 data from Savage et al. [48]. c) H_2 data from Rachford et al. [49]. d) May be affected by multiple velocity components [57]. e) *p*-H_3^+ fraction: $N(1,1)/(N(1,0)+N(1,1))$. f) *p*-H_2 fraction: $N(1)/(N(0)+N(1))$.

be invalid: (1) observational errors in the determination of the $J = 0$ and $J = 1$ column densities of H_2; (2) an insufficient frequency of $H^+ + H_2$ collisions to achieve steady state; (3) the steady state of this reaction being different from the thermodynamic equilibrium; and (4) errors caused by a varying $J = 0 : 1$ ratio along the line of sight. In the following subsections, we investigate each of these possibilities in turn.

4.3.1 Observational Determination of H_2 Columns

The measurement of the column densities of $J = 0$ and $J = 1$ of H_2 is performed by profile fitting to spectra of the Lyman (A-X) band in the ultraviolet, recorded with Copernicus or FUSE. The H_2 transitions are optically thick, and are completely opaque in the line cores. Given the difficulties in accurately retrieving column densities from optically thick transitions, one might worry that the inferred T_{01} is contaminated by uncertainties caused by radiative transfer.

According to B. L. Rachford (private communication, 2010), the detailed shape of the combined profile of the $J = 0$ line and the two $J = 1$ lines is quite sensitive to the ratio of the column densities of these two rotational levels, and thus provides a very useful probe of T_{01}. Because multiple vibronic bands of H_2, which are known to be relatively free of contamination by stellar lines, are used in the determination of T_{01}, it is difficult to envision any systematic errors that could affect the measurements. The statistical errors in the column density measurements are typically $\sim$0.1 dex, and we can therefore conclude that the ultraviolet measurements provide an accurate and fairly precise measure of the ratio of $N(0)$ to $N(1)$ for H_2.

4.3.2 Frequency of $H^+ + H_2$ Reactions

The $J = 0$ and $J = 1$ rotational levels of H_2 belong to different spin modifications (*para* and *ortho*, respectively) and are therefore not thermalized by non-reactive collisions or radiative transitions. Only chemical reactions, in which the protons are exchanged, can affect the nuclear spin modification of H_2.[3]

Since H_2 is formed in a highly exothermic reaction on grain surfaces, its nascent rotational (and spin) distribution is presumed to represent a high temperature [58]. In the high temperature limit, H_2 should be formed with an *ortho*:*para* ratio of 3:1. If an insufficient number of reactive collisions occur between the formation of an H_2 molecule and its subsequent destruction (by photodissociation or cosmic-ray ionization), then the average *ortho*:*para* ratio of H_2 may lie somewhere between the nascent value (3:1) and the thermalized value (1:2 at 60 K, for example). This could lead to T_{01} overestimating the true cloud kinetic temperature.

[3]Strictly speaking, large inhomogeneous magnetic fields, such as found on the surface of paramagnetic catalysts, can also affect the nuclear spin modification of H_2, but we assume that such effects are negligible in interstellar conditions.

The number of reactive collisions suffered by an average H_2 molecule in its lifetime can be expressed as $\mathcal{N}_{rxn} \equiv \tau_{life}/\tau_{rxn}$, where τ_{life} is the average lifetime of an H_2 molecule and τ_{rxn} is the average time between reactive collisions. If $\mathcal{N}_{rxn} \gg 1$, then the *ortho*:*para* ratio of H_2 should reflect the steady-state of the reaction in question.

In diffuse molecular clouds, H_2 is formed on grains at a rate of $Rn_{\rm H}n({\rm H})$, where R is the grain formation rate (typically taken to be about 3×10^{-17} cm^3 s^{-1}; e.g. [59, 60]), $n_{\rm H} \equiv n({\rm H}) + 2n(H_2)$ is the total number density of hydrogen nuclei, and $n({\rm H})$ is the number density of atomic hydrogen. The destruction of H_2 is dominated by cosmic-ray ionization and photodissociation (following absorption in the Lyman bands), and has a rate of $(\zeta_2 + \Gamma)n(H_2)$, where Γ is the photodissociation rate. In steady state, these two rates are equal, and we can solve for $\tau_{life} = (\zeta_2 + \Gamma)^{-1} = n(H_2)/[Rn_{\rm H}n({\rm H})]$. By using the definition of the local molecular fraction $f^n_{H_2} \equiv 2n(H_2)/n_{\rm H}$ (which we will simply call f), we can rewrite this expression as $\tau_{life} = f/[2Rn_{\rm H}(1-f)]$.

Assuming that the reaction of $H^+ + H_2$ dominates the interconversion of o-H_2 and p-H_2(*ortho*- and *para*-H_2, respectively), we can write $\tau_{rxn} = [k_{ic}n({\rm H}^+)]^{-1}$, where k_{ic} is the rate coefficient for the interconversion reaction. Substituting into the equation for $\mathcal{N}_{rxn}$, we find

$$\mathcal{N}_{rxn} = \frac{k_{ic}}{R}\frac{n({\rm H}^+)}{n_{\rm H}}\frac{f}{2(1-f)}.$$

To estimate the number density of H^+, we consider the steady state of its formation and destruction. H^+ is formed by cosmic-ray ionization of H atoms, at a rate of $\zeta_{\rm H}n({\rm H})$, where $\zeta_{\rm H}$ is the cosmic-ray ionization rate of H ($2.3\zeta_{\rm H} \approx 1.5\zeta_2$ [61]). Given the abundances of various species in diffuse clouds and the rate coefficients for reactions between H^+ and such species, chemical models predict that H^+ is destroyed predominantly by charge transfer to atomic oxygen, with a rate of $k_{ct}n({\rm H}^+)n({\rm O})$. [62] Equating these rates of formation and destruction and solving for $n(H^+)$, we find $n({\rm H}^+) = \zeta_{\rm H}(1-f)/[k_{ct}x({\rm O})]$, where $x({\rm O}) \equiv n({\rm O})/n_{\rm H}$. Finally, substituting this into the expression for $\mathcal{N}_{rxn}$ gives

$$\mathcal{N}_{rxn} = \frac{k_{ic}}{R}\frac{\zeta_{\rm H}}{k_{ct}}\frac{f}{2n_{\rm H}}\frac{1}{x({\rm O})}.$$

Adopting values of $k_{ic} = 2.2 \times 10^{-10}$ cm^3 s^{-1} [63], $R = 3 \times 10^{-17}$ cm^3 s^{-1}, $\zeta_2 = 4 \times 10^{-16}$ s^{-1} [22], $k_{ct} = 7.31 \times 10^{-10}(T/300)^{0.23}e^{-225.9/T}$ cm^3 s^{-1} [62], $x({\rm O}) \approx 3 \times 10^{-4}$ [64, 65], and typical diffuse cloud values of $f = 0.9$[4] and $n_{\rm H} = 100$ cm^{-3} [46], we find that at $T \sim 70$ K, $\mathcal{N}_{rxn} \sim 1400$. Thus, the typical H_2 molecule will experience over 1000 reactive collisions during its lifetime, and we can safely assume that the

[4]While the line-of-sight molecular fraction is lower, that quantity integrates over atomic gas not associated with the diffuse molecular cloud. We are therefore using the local molecular fraction typical of diffuse molecular clouds.

initial *ortho*:*para* ratio of H_2 is irrelevant; instead, the observed *ortho*:*para* ratio should reflect the steady state of the reactive collisions.

4.3.3 Steady State of $H^+ + H_2$ Reactions

From a thermodynamic perspective, one would expect that the steady state of the $H^+ + H_2$ reaction would represent a thermal distribution of o-H_2 and p-H_2, if no other processes influence the spin modifications. This expectation has been confirmed by a phase space theoretical calculation by Gerlich [63], who found that the *ortho*:*para* ratio could be expressed at low temperatures (30–80 K) by the expression $9.35\exp(-169.4/T)$, quite close to the thermodynamic expectation of $9\exp(-170.4/T)$. Evidently the nuclear spin selection rules for this chemical reaction, which suppress the *ortho*-to-*para* conversion by a factor of 6, do not significantly impact the final distribution.

4.3.4 Line of Sight Integration Effects

One remaining concern regards the estimation of T_{01} in a diffuse molecular cloud from the column densities of $J = 0$ and $J = 1$, which are integrated quantities along the line of sight. If some of the H_2 resides in hotter, mostly atomic gas where H_3^+ is not abundant, that hot H_2 would cause the observed line-of-sight T_{01} to exceed T_{01} in the molecular cloud. We expect that such contamination would not be a major effect, as H_2 is known to self-shield very effectively from the interstellar radiation field; thus, the amount of H_2 in primarily atomic (and presumably warmer) gas is likely to be quite small compared to the amount of H_2 in the molecular cloud itself.

To estimate the magnitude of this effect more quantitatively, we take a simple cloud model with a hotter outer region and cooler inner region. Assuming that $T_{01} = 100$ K in the outer region (based on Copernicus observations of diffuse atomic clouds [66]), we varied T_{01} in the inner region between 10 K and 100 K for a set of models where the outer region contained 1/2, 1/4, 1/8, and 1/16 of the material in the cloud. We then computed the line-of-sight T_{01} that would be derived considering both regions of gas. The result of this analysis is shown in Figure 4.2.

Taking the diffuse cloud model of Neufeld et al. [67] with a constant density ($n_{\rm H} = 100$ cm^{-3}) and standard UV radiation field ($\chi_{\rm UV} = 1$) illuminating the cloud from one side, we then determined the amount of H_2 expected to be in the outer region for comparison with observed H_2 column densities in diffuse clouds. We define the transition from the outer to inner regions to be at $E(B-V) = 0.04$ ($N_{\rm H} \approx 2.3 \times 10^{20}$ cm^{-2}), about half of the total color excess (hydrogen column density) found to supply self-shielding effects in H_2 [48, 68]. Integrating $n(H_2)$ in the outer region gives $N_{outer}(H_2) = 6 \times 10^{19}$ cm^{-2}. Because this model

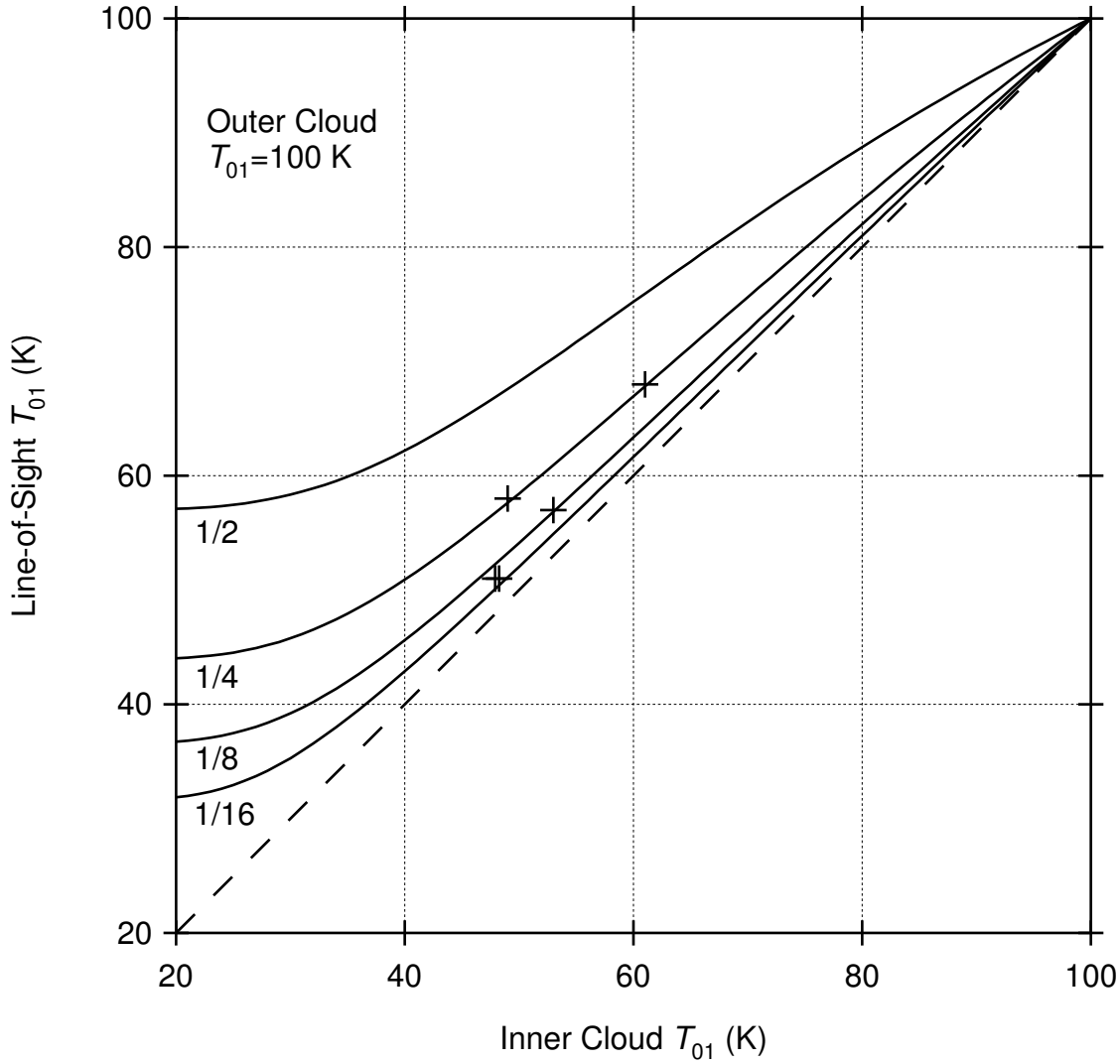

Figure 4.2: The line-of-sight rotational temperature, T_{01}, is determined for a cloud containing both a warm and cold component. The cold, inner component is varied between 10 K and 100 K, while the warm, outer component is set at 100 K. Different curves show the results for cases where the warm component contains 1/2, 1/4, 1/8, and 1/16 of the total material in the cloud, and are labeled accordingly. Cross hairs mark the inferred inner cloud values of T_{01} given the observed line-of-sight values of T_{01} and estimated fractions of H_2 in a 100 K cloud component for the 5 sight lines considered herein. From left to right the cross hairs mark HD 73882, HD 154368, ζ Per, X Per, and HD 110432.

effectively only treats one side of a cloud, we compare this value to half of the total H_2 column densities reported in Table 4.3. The two extreme cases are HD 110432 and HD 154368, where the outer region accounts for about 1/4 and 1/12 of the total cloud, respectively. Taking the observed values of T_{01} and using the appropriate curves on Figure 2, we estimate the temperature of the inner cloud region for each of the 5 sight lines considered herein. The results are marked in Figure 2 as cross hairs, and show that the line-of-sight values of T_{01} overestimate the inferred inner cloud values of T_{01} by only about 5–10 K. As such, the observed values of T_{01} should be relatively close to the true values of T_{01} in molecular clouds. We therefore assume for the remainder of this paper that the line of sight T_{01} does represent the diffuse molecular cloud kinetic temperature.

4.3.5 Summary on H_2 Temperature

From the preceding discussions, we conclude that UV measurements accurately measure the column densities of $J = 0$ and $J = 1$ of H_2 in diffuse clouds, that the chemical reaction between H^+ and H_2 occurs $\sim 10^3$ times during the life of an average H_2, and that the steady state of this chemical reaction leads to an *ortho*:*para* ratio that closely reflects the kinetic temperature of the gas. Furthermore, we conclude that it is unlikely that the integration along the line of sight introduces significant contamination of the inferred T_{01}. In summary, then, measured values of T_{01} in diffuse molecular clouds should accurately reflect the cloud kinetic temperature. Consequently, the excitation temperature of H_3^+, which is significantly lower than T_{01}, must not always reflect the kinetic temperature.

4.4 *Ortho* And *Para* H_3^+

Having shown that the temperature discrepancy between T_{01} and $T(H_3^+)$ in diffuse molecular clouds is real and that T_{01} accurately reflects the cloud kinetic temperature, we now consider the processes related to H_3^+ thermalization in diffuse molecular clouds to examine why $T(H_3^+)$ might not match the kinetic temperature.

4.4.1 Nascent and Thermalized *Para*-H_3^+ Fractions

H_3^+ is produced by the reaction

$$H_2 + H_2^+ \rightarrow H_3^+ + H, \tag{4.1}$$

which follows the cosmic-ray ionization of H_2 to form H_2^+. The nuclear spin modification of the product H_3^+ depends on the nuclear spin modifications of the reactant H_2 and H_2^+ according to the selection rules given by [69]. It is most convenient to express the nuclear spin modifications in terms of the *para*-fractions, rather

Reaction	Collision Fraction	Branching Fraction	p-H_3^+ Fraction
p-H_2^+ + p-H_2	$(p_2)^2$	1	p_2^2
p-H_2^+ + o-H_2	$p_2(1-p_2)$	2/3	$(2/3)(1-p_2)p_2$
o-H_2^+ + p-H_2	$(1-p_2)p_2$	2/3	$(2/3)(1-p_2)p_2$
o-H_2^+ + o-H_2	$(1-p_2)^2$	1/3	$(1/3)(1-p_2)^2$
Total	–	–	$(1/3)+(2/3)p_2$

Table 4.4: This table presents the calculation of the nascent p-H_3^+ fraction formed in diffuse molecular clouds from the $H_2^+ + H_2$ reaction, assuming that cosmic ray ionization of H_2 to form H_2^+ does not affect its nuclear spin configuration. The collision fraction represents the fraction of total $H_2^+ + H_2$ collisions with the specified nuclear spin configurations. The branching fractions are for p-H_3^+ formation, and are derived from nuclear spin selection rules [69, 72]. The final column presents the calculation of the nascent p-H_3^+ fraction.

than the *ortho*:*para* ratios, so we define

$$p_2 \equiv \frac{n(p\text{-}H_2)}{n(p\text{-}H_2)+n(o\text{-}H_2)}$$

and

$$p_3 \equiv \frac{n(p\text{-}H_3^+)}{n(p\text{-}H_3^+)+n(o\text{-}H_3^+)}.$$

As the cosmic-ray ionization of H_2 is not expected to affect the nuclear spin modification, we can further assume that the *para*-fraction of H_2^+ is also given by p_2. Table 4.4 demonstrates, using these reactant fractions and the nuclear spin branching fractions, that the *para*-fraction of newly formed H_3^+ is $p_3 = (1/3)+(2/3)p_2$, assuming that the rate for the $H_2^+ + H_2$ reaction is independent of nuclear spin configuration.

In diffuse molecular clouds, the vast majority of the H_2 population lies in the lowest *ortho* and *para* states, as the temperature of 70 K is well below the energy of the next states (the $J = 2$ state lies 510 K above $J = 0$, and $J = 3$ lies 844 K above $J = 1$). Therefore, to derive p_2 from astronomical observations we use the formula $p_2 = N(0)/[N(0)+N(1)]$. H_3^+ on the other hand does have energetically accessible *para* states, as the (2,2) and (2,1) states lie only 151.3 and 249.2 K above the (1,1) ground state. However, the (2,2) and (2,1) states are expected to quickly undergo radiative decay to the (1,1) state at the temperatures and densities of the diffuse molecular clouds [70]. Furthermore, population in the next *ortho* state, (3,3) has not been observed in these environments [71], so the vast majority of o-H_3^+ is in the (1,0) state. Consequently, to calculate p_3 from the astronomical observations, we use $p_3 = N(1,1)/[N(1,1)+N(1,0)]$.

Figure 4.3 shows the nascent p_3 distribution as a function of p_2. This figure also shows the total *para*-fraction of a thermalized sample of H_3^+ at various temperatures, calculated using the energy levels $E(J,K)$ from Lindsay and McCall [19]. Also plotted in the figure are the results of the astronomical observations presented in Table 4.3. In diffuse molecular clouds, p_3 generally appears to lie between the nascent p_3 and

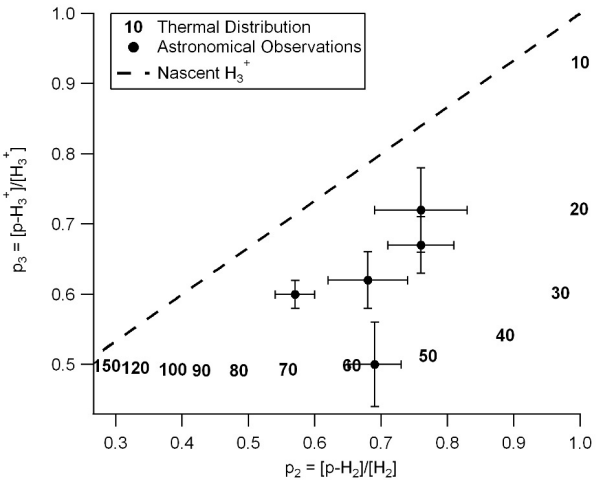

Figure 4.3: The nascent (dashed line) and thermalized (numbers, in K) p-H_3^+ fraction as a function of the p-H_2 fraction. The circles represent the observations of diffuse molecular clouds summarized in Table 4.3 with 1σ uncertainties.

the thermal p_3 values, suggesting an incomplete thermalization of the nuclear spin modifications of H_3^+.

As discussed by Oka and Epp [70], the aforementioned spontaneous emission from the (2,2) and (2,1) states decreases $T(H_3^+)$ relative to T_{01}. They show that for a cloud density of 100 cm^{-3} and $60 \leq T_{01} \leq 120$ K, $T(H_3^+)$ should fall in the range of 40-50 K, and this accounts for a $\sim 40-80$ K difference between T_{01} and $T(H_3^+)$. However, in the temperature ranges discussed here, the *para*-fractions of H_3^+ and H_2 are nonlinear with respect to these excitation temperatures. In terms of p_3, all $T(H_3^+)$ above about 40 K should have about the same p_3, while p_3 changes substantially when $T(H_3^+)$ falls below 40 K, as can be seen in Figure 4.3. Spontaneous emission will raise the apparent p_3 [as derived from the N(1,1):N(1,0) ratio] relative to the thermalized p_3 and consequently lower $T(H_3^+)$ with respect to T_{01}. However, Figure 4.3 illustrates that the magnitude of this effect cannot account for the discrepancy observed in the astronomical observations in these environments in terms of the *para*-fractions, with the possible exception of X Per.

4.4.2 The Reaction of H_3^+ with H_2

As in the case of H_2, the nuclear spin modifications of H_3^+ cannot effectively be changed by radiative transitions or by non-reactive collisions; only chemical reactions can do so. In this case, the reaction $H_3^+ + H_2 \rightarrow (H_5^+)^* \rightarrow H_2 + H_3^+$ is the most efficient mechanism for interconverting o-H_3^+ and p-H_3^+. When H_3^+ and H_2 collide, there are three possible reaction outcomes:

$$\tilde{H}_3^+ + H_2 \rightarrow \quad \tilde{H}_3^+ + H_2 \quad \text{(identity)}, \tag{4.2}$$

$$\tilde{H}_3^+ + H_2 \rightarrow \quad H_2\tilde{H}^+ + \tilde{H}_2 \quad \text{(hop), and} \tag{4.3}$$

$$\tilde{H}_3^+ + H_2 \rightarrow \quad H\tilde{H}_2^+ + H\tilde{H} \quad \text{(exchange)}. \tag{4.4}$$

In the case of reaction 4.2, the nuclear spin configurations of the H_3^+ and H_2 remain unchanged, while in reactions 4.3 and 4.4 the configuration may change. However, like reaction 4.1, the hop and exchange pathways must obey nuclear spin selection rules [69, 72]. For instance, in order for a reaction between p-H_3^+ and p-H_2 to form o-H_3^+ the reaction must be an exchange, and o-H_2 must also be formed to conserve the total nuclear spin angular momentum.

A potential energy surface based on high-level *ab initio* calculations is available for the H_5^+ system [73]. Based on the surface stationary points, a barrier of 52.2 cm^{-1} must be overcome for a hop reaction (5.2) to occur, and a barrier of 1565.9 cm^{-1} for an exchange reaction (5.3) to occur. The dissociation energy D_e is calculated to be 2903 cm^{-1}; therefore $(H_5^+)^*$ formed from association of H_3^+ with H_2 has sufficient energy to overcome these barriers. As such, the complex may undergo many hop and exchange processes over its lifetime, and given sufficient time, the product distribution may approach a statistical limit. As the statistical weights for the hop and exchange reactions are 3 and 6, respectively, the branching ratio $\alpha \equiv k_{5.2}/k_{5.3}$ is 0.5 in the statistical limit. Quantum reactive scattering calculations are presently unavailable on this potential energy surface, so experimental data are necessary for determining the value of α, as well as its temperature dependence.

The only experimental determination of α for the $H_3^+ + H_2$ system was performed by [74]. This study was done by spectroscopically measuring the *ortho*-to-*para* ratio of H_3^+ formed in a discharge of pure p-H_2 at 400 K, and under these conditions, the value $\alpha = 2.4$ was derived. No measurements at lower temperatures have been reported for this system, but the isotopically-substituted reaction $D_3^+ + H_2$ has been studied at a variety of collision energies using an ion trap/guided beam technique [75]. It was observed that α varies substantially with the D_3^+-H_2 collision energy. As this energy decreases, α approaches the statistical value of 0.5, and the value 2.4 is reached at an energy corresponding to the average collision energy at ∼440 K, in general agreement with the study by [74]. However, a direct comparison of these results to H_3^+ in the interstellar medium is problematic owing to the endothermicity of the reaction channel and the nonthermal reactant internal state distribution in the experimental measurement.

The final consideration for this reaction is the fraction of reactions that lead to no change in the nuclear

spin modification, S^{id}. A large value for S^{id} would indicate that nuclear-spin-changing collisions are a small fraction of the total number of $H_3^+ + H_2$ collisions, and the thermalization process would be slower than the collision rate. In fact, there is experimental evidence for this, as studies of the $H_3^+ + HD \rightarrow H_2D^+ + H_2$ reaction give a rate coefficient of 3.5×10^{-10} cm^3 s^{-1} [76], much slower than the Langevin rate coefficient 1.7×10^{-9} cm^3 s^{-1}. These results lead to $S^{id} \sim 0.8$, but it is possible that S^{id} could be different for the purely hydrogenic system, which is thermoneutral rather than exothermic.

4.4.3 Steady State *Para*-H_3^+ Fraction from $H_3^+ + H_2$: "Bimolecular Reactive Equilibrium"

After taking into account its chemical physics, does the steady state of the $H_3^+ + H_2$ chemical reaction lead to a completely thermalized p_3 in the interstellar medium? To consider this question, we have constructed a simple steady-state model for *ortho* and *para*-H_3^+, in terms of nuclear-spin-dependent rate coefficients k_{xxxx} for each potential sub-reaction (e.g., k_{oppo}: o-$H_3^+ + p$-$H_2 \rightarrow p$-$H_3^+ + o$-H_2). The derivation of this model, which we shall call the "bimolecular reactive equilibrium" (BRE) model, is presented in section 4.7, and the resulting expression for p_3 is given as equation (4.8).

The rate coefficients themselves were computed using the prescription of [77], which takes into account both the nuclear spin branching fractions as well as energetic considerations at the state-to-state level, using a microcanonical approach. This work has since been extended by [78] to deuterated versions of this chemical reaction, and the latter authors report quantitative agreement between the two sets of calculations. We therefore judge these rate coefficients to be reliable within the context of this theoretical approach.

The Park & Light code (provided by K. Park, private communication 2009) requires five input parameters: the kinetic temperature, the rotational temperature of H_3^+ and H_2, and the three branching fractions S^{id}, S^{hop}, and S^{exch}. For these calculations, the rotational temperature was held at 10 K in each nuclear spin manifold in order to have the vast majority of o-H_3^+ in (1,0) and p-H_3^+ in (1,1). Therefore, we express the inputs to the model in terms of only three parameters: $T \equiv T_{kin}$, S^{id}, and α, as $S^{id} + S^{hop} + S^{exch} = 1$ and $\alpha = S^{hop}/S^{exch}$. The code then outputs all of the rate coefficients required in equation (4.8). For a single set of branching fraction values, the rate coefficients were calculated for $10 \leq T \leq 160$ K in steps of 10 K, and p_2 was set to its thermal value for each calculation.

Figure 4.4 shows the results of the BRE model for a fixed value of $\alpha = 0.5$ for various values of S^{id} ranging from 0.1-0.9; similarly, Figure 4.5 shows results for fixed $S^{id} = 0.5$ and various α ranging from 0-∞. The results of the calculation are not particularly sensitive to the fraction of collisions that are reactive (as traced by S^{id}) or the ratio of the hop to exchange outcomes (α). Since in all cases p_3 falls near its thermal

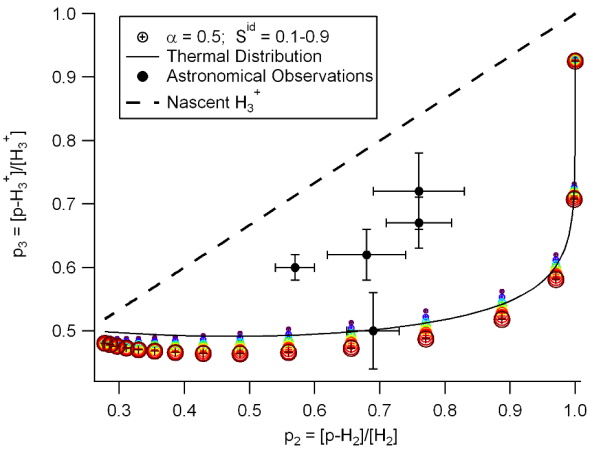

Figure 4.4: BRE calculations of the *para*-H_3^+ fraction as a function of the *para*-H_2 fraction, under the influence of the $H_3^+ + H_2$ reaction. The thin solid line represents the thermal limit (as in Figure 4.3), and the circled crosses represent the results of our calculations (based on Park & Light's model) for $\alpha = 0.5$ and various values of S^{id} ranging from 0.1 (small purple) to 0.9 (large brown). Each cluster of crosses represents a calculation at a single temperature, ranging from 10 K (upper right) to 160 K (lower left) in steps of 10 K. Also plotted are the nascent H_3^+ distribution and the astronomical observations.

value, these results suggest that regardless of the values of α or S^{id}, the $H_3^+ + H_2$ reaction should essentially thermalize the H_3^+ nuclear spin species. This stands in clear contradiction to the reported astronomical observations in diffuse molecular clouds, with the exception of X Per. The discrepancy between T_{01} and $T(H_3^+)$ cannot be explained by the BRE model, and must then be explained by a lack of equilibration via this chemical reaction.

An interesting aspect of these results is that the steady state p_3 at some temperatures is actually *below* the value of 0.5 expected based on statistical weights alone (often called the "high-temperature limit"). This appears to be a robust result for $\alpha > 0.5$, at least in the range of S^{id} explored here. This effect may have been observed experimentally in our group's recent measurements of supersonically expanding hydrogen plasmas. [79] reported $p_3 = 0.491 \pm 0.024$ for a normal hydrogen ($p_2 = 0.25$) plasma at ~ 80 K, and [80] reported $p_3 = 0.479 \pm 0.02$ in a warmer (~ 200 K) normal hydrogen and argon plasma.[5] Finally, in work outside our laboratory, [81] have reported $p_3 = 0.4$ in a low-temperature ion trap. All of these measurements suggest that it is in fact possible to achieve $p_3 < 0.5$, and lend some evidence to support the calculated results.

[5]Recent measurements in our laboratory have confirmed, with higher statistical significance, $p_3 < 0.5$ in hollow cathode plasmas containing normal hydrogen. These results will be reported elsewhere, but it should be noted that p_3 in these plasmas may be influenced by three-body collisions due to the higher number densities.

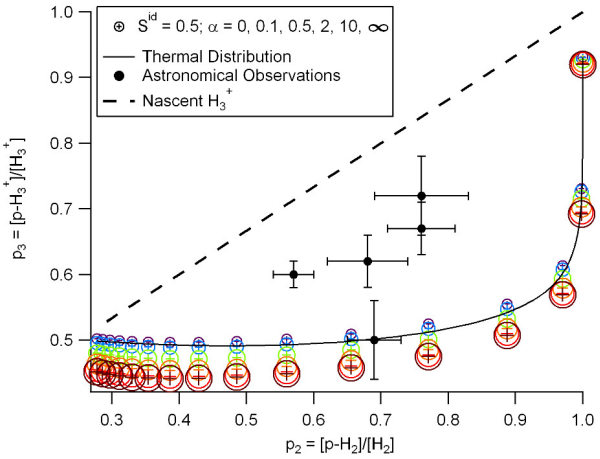

Figure 4.5: Same as Figure 4.4, except that S^{id} is held at 0.5 and α varies between 0 (small purple) and ∞ (large brown).

4.4.4 Steady State *Para*-H_3^+ Fraction from $H_3^+ + H_2$ and $H_3^+ + e^-$

We now consider whether there are enough reactive collisions within the lifetime of an average H_3^+ in diffuse molecular clouds to bring the spin modifications into BRE. The destruction of H_3^+ in such clouds is dominated by dissociative recombination (DR) with electrons, and the lifetime is simply $\tau_{life} = (k_{DR} n(e^-))^{-1}$ (the reciprocal of the destruction rate), where k_{DR} is the dissociative recombination rate coefficient. The average time between reactive collisions can be expressed as $\tau_{rxn} = (k_{rc} n(H_2))^{-1}$, where k_{rc} is the reactive collision rate for $H_3^+ + H_2$. The average number of collisions an H_3^+ will experience is then $\mathcal{N}_{rxn} = \tau_{life}/\tau_{rxn} = [k_{rc}/k_{DR}][n(H_2)/n(e^-)]$.

Assuming for the moment that k_{DR} is independent of the nuclear spin modification, we adopt a typical value (for $T \sim 70$ K) of $k_{DR} = 2 \times 10^{-7}$ cm^3 s^{-1} [82]. The ratio $n(H_2)/n(e^-)$ can be rewritten as $f/2x_e$, where x_e is the electron fraction, typically 1.5×10^{-4} assuming charge neutrality and that C^+ is the dominant ionic species [83, 84]. If we adopt $f = 0.9$, and take k_{rc} to be the full collision rate of $H_3^+ + H_2$ (1.5×10^{-9} cm^3 s^{-1} [85]), we find that $\mathcal{N}_{rxn} \sim 20$. However, if we instead adopt the smaller reactive rate coefficient $\sim 3 \times 10^{-10}$ cm^3 s^{-1} of [76], we find that $\mathcal{N}_{rxn} \sim 5$. With such a small number of collisions in the lifetime of H_3^+, p_3 may not reach the value predicted by equation 4.8. In the section 4.8 we derive a more complete steady state expression (equation 4.15) including the effects of both the $H_3^+ + H_2$ reaction and nuclear-spin-dependent DR rates ($k_{e,p}$ and $k_{e,o}$ for *p*-H_3^+ and *o*-H_3^+).

We call this model simply the "steady state" model, and we adopt the values $f = 0.9$ and $x_e = 1.5 \times 10^{-4}$ as before. Figure 4.6 shows the results of this steady state model if we assume that the DR rate coefficient is the same for both nuclear spin modifications (we have adopted the temperature-dependent value of McCall

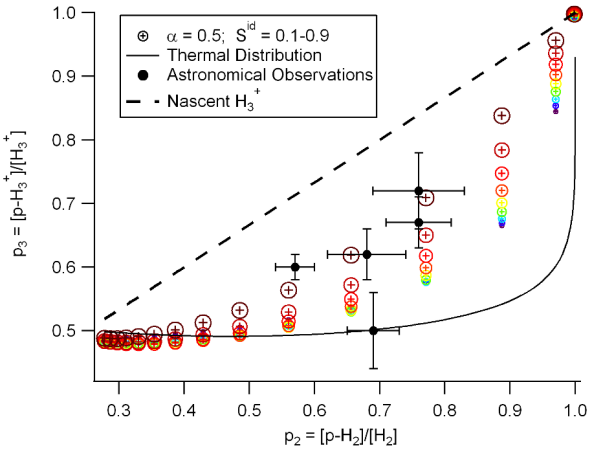

Figure 4.6: Steady state calculations of the *para*-H_3^+ fraction as a function of the *para*-H_2 fraction, under the influence of both the $H_3^+ + H_2$ reaction and dissociative recombination. The plotted quantities are analogous to those in Figure 4.4. In this case, the *o*-H_3^+ and *p*-H_3^+ DR rate coefficients $k_{e,o}$ and $k_{e,p}$ are assumed to be equal and taken from [82]. Each vertical cluster of points represents a calculation at a single temperature, beginning at 160 K in the lower left and decreasing by 10 K each point moving to the right.

et al. [82]). In this case, the values of p_3 depend quite sensitively on S^{id}, as this represents the fraction of $H_3^+ + H_2$ collisions that are nonreactive during the relatively short lifetime of H_3^+. Consequently with higher values of S^{id} (larger circles in Figure 4.6), the *p*-H_3^+ fraction in steady state is closer to the nascent fraction. For $S^{id} = 0.9$, which corresponds to a reactive rate coefficient of $k_{rc} = 1.9 \times 10^{-10}$ cm^3 s^{-1}, the calculated p_3 are in reasonable agreement with most of the observations. The upper range of the X Per uncertainty is consistent with $S^{id} = 0.7$.

In Figure 4.7, we instead consider the calculated DR rate coefficients for *ortho* and *para*-H_3^+ presented in [86]. Their prediction is that *p*-H_3^+ is destroyed considerably faster by electrons at low temperatures than *o*-H_3^+; consequently, even for large values of S^{id}, the steady state p_3 does not approach either the nascent or astronomically-observed values. In the absence of the $H_3^+ + H_2$ reaction ($S^{id} = 1$), p_3 would be governed by a steady state determined by the competition between the formation and the spin-dependent DR processes, and this is shown in Figure 4.8.

If the calculated rate coefficients of [86] are correct, it is difficult to explain the observed p_3. This is because, with the exception of X Per, the observed p_3 are higher than the curve resulting from the steady state of H_3^+ formation and destruction using these DR rate coefficients, and inclusion of the $H_3^+ + H_2$ reaction further drives p_3 toward the value expected for thermal equilibrium. Recent storage ring experiments by [28] and [87] both saw an increased DR cross-section when H_3^+ is produced from *p*-H_2; however, recent imaging results presented in [80] suggest that the ions in these experiments have been heated during extraction from the ion sources, and the difference between the *o*-H_3^+ and *p*-H_3^+ may therefore

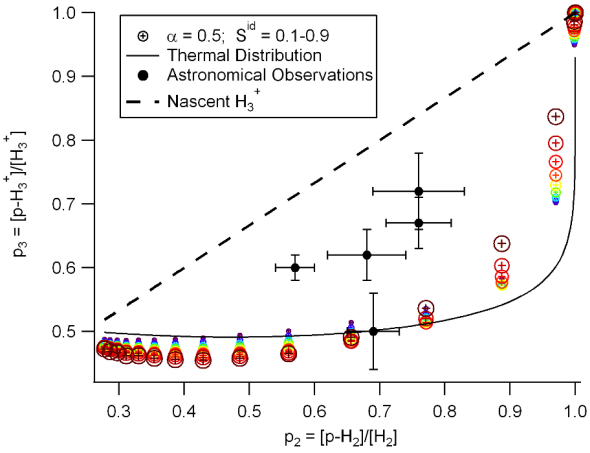

Figure 4.7: Same as Figure 4.6, except using the spin-dependent dissociative recombination rate coefficients from [86].

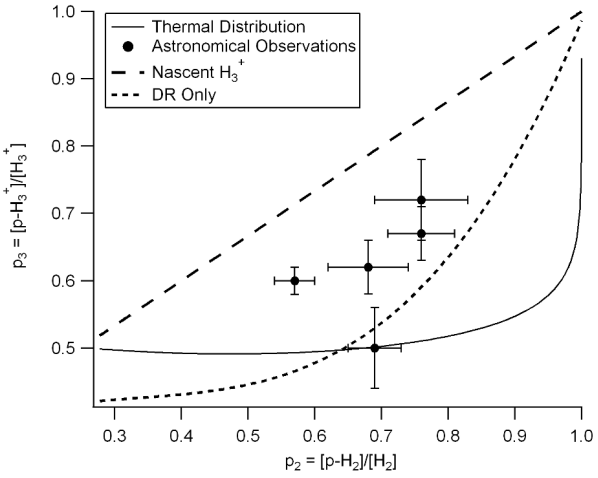

Figure 4.8: Steady state calculations of the *para*-H_3^+ fraction as a function of the *para*-H_2 fraction, under the influence of formation and dissociative recombination only. The solid line shows the thermal limit, and the dotted line represents the results of our calculations, where we have used the spin-dependent dissociative recombination rate coefficients from [86]. Also plotted are the nascent H_3^+ distribution (dashed line) and the astronomical observations.

have been overestimated. Further experimental work is clearly needed to pin down the enhancement (if any) in p-H_3^+ DR, and confirmation of the theoretical predictions would also be quite helpful.

To summarize, according to our models the reaction of H_3^+ with H_2 is expected to effectively thermalize the nuclear spin configurations of H_3^+ at steady-state, provided that sufficient collisions occur within the lifetime of an H_3^+. In diffuse molecular clouds, however, the average number of reactive collisions with H_2 suffered by an H_3^+ is small, indicating that the formation and destruction rates of the two nuclear spin species should be important. A more complete model which takes these factors into account reaches reasonable agreement with observations in 4 of 5 sight lines provided S^{id} is on the order of 0.9 and o-H_3^+ and p-H_3^+ are destroyed at equal rates owing to DR. Reconciling the observations with the spin-dependent theoretical rates of [86] is difficult, and accurate experimental measurements of the spin-dependent DR rates of H_3^+ at low temperature are needed.

4.5 Conclusions

While all evidence seems to suggest that T_{01} inferred from ultraviolet spectroscopy of H_2 accurately reflects the kinetic temperature of diffuse molecular clouds, the observed excitation temperature of H_3^+ is clearly non-thermal in 4 of the 5 measured sight lines. Based on the microcanonical model of [77], we have constructed a steady state model to predict the *para*-H_3^+ fraction (p_3) if reactive collisions between H_3^+ and H_2 control the spin modifications of H_3^+. Those results show p_3 slightly below the limit expected for full thermalization, and far from the observations. However, a steady state model that incorporates both the $H_3^+ + H_2$ reaction as well as the H_3^+ formation (following cosmic-ray ionization) and destruction (by electron recombination) can reproduce the observed p_3 if the reactive collision rate is somewhat slow and the dissociative recombination rates for *ortho* and *para* H_3^+ are comparable. Our interpretation, given the currently available data, is that H_3^+ suffers relatively few spin-changing collisions with H_2 in its lifetime, and is thus incompletely equilibrated by this reaction. The observed *para*-H_3^+ fraction therefore lies between the nascent fraction and the nearly-thermal fraction that would be reached with sufficient reactive collisions. If our model is correct (and the spin-dependent DR rates of H_3^+ are nearly equal at low temperature), this marks the first determination of the reactive rate coefficient of the $H_3^+ + H_2$ reaction, and suggests a value on the order of 10^{-10} cm^{-3} s^{-1}.

Fully quantum reactive scattering calculations of the $H_3^+ + H_2$ reaction would be highly desirable, as they would pin down the state-to-state rate coefficients needed to predict the interstellar *para*-H_3^+ fraction. Further experiments and theoretical calculations to elucidate the dependence (if any) of the dissociative recombination on the nuclear spin modification of H_3^+ are also urgently needed. Once the effects of the reac-

Number	Reaction	Rate	Comments
1	H_2 + CR $\rightarrow$ H_2^+ + e^- + CR´	$\zeta_2[H_2]$	Cosmic ray ionization
2	H_2 + H_2^+ $\rightarrow$ H_3^+ + H	$k_1[H_2][H_2^+]$	H_3^+ formation (see Table 4.1)
3	i-H_3^+ + j-H_2 $\rightarrow$ m-H_3^+ + n-H_2	$k_{ijmn}[i\text{-}H_3^+][j\text{-}H_2]$	Thermalization reaction for H_3^+
4	p-H_3^+ + e^- $\rightarrow$ H_2 + H (or) 3H	$k_{e,p}[p\text{-}H_3^+][e^-]$	p-H_3^+ DR
5	o-H_3^+ + e^- $\rightarrow$ H_2 + H (or) 3H	$k_{e,o}[o\text{-}H_3^+][e^-]$	o-H_3^+ DR

Table 4.5: The branching fractions for o-H_3^+ and p-H_3^+ in reaction 2 are assumed to be given by nuclear spin statistics. In reaction 3, i, j, m, and n represent the nuclear spin configurations of the respective species (o or p). Some of these 16 reactions are forbidden by nuclear spin selection rules, and others are not used directly in the derivation because they do not result in a change in the H_3^+ nuclear spin configuration. Square brackets refer to the number density of the species.

tive collisions and dissociative recombination are fully understood, the *para*-H_3^+ fraction in diffuse molecular clouds can be calculated as a function of the kinetic temperature and the ratio of the molecular fraction to the electron fraction. This, in turn, suggests that H_3^+ may become a useful "thermometer" for diffuse molecular clouds with high extinction, where ultraviolet measurements of H_2 are not feasible. However, the calibration of this thermometer will require further experimental and theoretical efforts.

The authors thank Brian L. Rachford for helpful discussions about the T_{01} determinations, Takeshi Oka for helpful conversations about *ortho* and *para*-H_3^+, Kisam Park for providing the code to determine the nuclear-spin-dependent rate coefficients for the H_3^+ + H_2 reaction, and the anonymous referee for helpful comments. This work has been supported by NSF grant PHY08-55633. This work is based in part on observations obtained at the Gemini Observatory, which is operated by the Association of Universities for Research in Astronomy, Inc., under a cooperative agreement with the NSF on behalf of the Gemini partnership: the National Science Foundation (United States), the Science and Technology Facilities Council (United Kingdom), the National Research Council (Canada), CONICYT (Chile), the Australian Research Council (Australia), Ministério da Ciência e Tecnologia (Brazil) and Ministerio de Ciencia, Tecnología e Innovación Productiva (Argentina). Gemini/Phoenix spectra were obtained through programs GS-2009B-Q-71 and GS-2010A-Q-60. This paper is also based in part on observations obtained with the Phoenix infrared spectrograph, developed and operated by the National Optical Astronomy Observatory.

4.6 Reactions And Rates

In this appendix, we derive the formulas for the bimolecular reactive equilibrium and steady-state *para*-H_3^+ fractions. We consider 4 processes: cosmic ray ionization of H_2, formation of H_3^+, the H_3^+ + H_2 reaction, and dissociative recombination of H_3^+. If all nuclear spin configurations are considered, this gives a total of

28 reactions. The chemical reactions used in the model and their rate expressions are summarized in Table 4.5. It should be noted that for this section, we employ the chemist's notation of using square brackets to refer to the number density of the respective species.

4.7 Derivation of Bimolecular Reactive Equilibrium Model

Consider the case that H_3^+ formation and destruction are slow compared with the $H_3^+ + H_2$ reaction. We can then ignore formation and destruction processes and write the rate equation for p-H_3^+ only in terms of the latter reaction:

$$\begin{aligned}\frac{\mathrm{d}}{\mathrm{d}t}[p\text{-}H_3^+] &= \{(k_{oopo}+k_{oopp})\,[o\text{-}H_2]+(k_{oppo}+k_{oppp})\,[p\text{-}H_2]\}\,[o\text{-}H_3^+] \\ &\quad -\{(k_{pooo}+k_{poop})\,[o\text{-}H_2]+(k_{ppoo}+k_{ppop})\,[p\text{-}H_2]\}\,[p\text{-}H_3^+]. \end{aligned} \tag{4.5}$$

Assuming steady state, equation 4.5 is equal to 0. The right side can then be divided by $[H_3^+][H_2]$ in order to express the rate in terms of p_2 and p_3 as follows:

$$\begin{aligned} 0 &= \{(k_{oopo}+k_{oopp})\,(1-p_2)+(k_{oppo}+k_{oppp})\,p_2\}\,(1-p_3) \\ &\quad -\{(k_{pooo}+k_{poop})\,(1-p_2)+(k_{ppoo}+k_{ppop})\,p_2\}\,p_3. \end{aligned} \tag{4.6}$$

The resultant equation can be solved for p_3:

$$p_3 = \frac{(k_{oopp}+k_{oopo})(1-p_2)+(k_{oppo}+k_{oppp})p_2}{(k_{oopp}+k_{oopo}+k_{poop}+k_{pooo})(1-p_2)+(k_{oppo}+k_{oppp}+k_{ppoo}+k_{ppop})p_2}. \tag{4.7}$$

Owing to nuclear spin selection rules, the rate coefficients k_{oppp} and k_{ppop} are rigorously 0. Removal of these terms gives the final result:

$$p_3 = \frac{(k_{oopp}+k_{oopo})(1-p_2)+k_{oppo}p_2}{(k_{oopp}+k_{oopo}+k_{poop}+k_{pooo})(1-p_2)+(k_{oppo}+k_{ppoo})p_2}. \tag{4.8}$$

4.8 Derivation of Steady State Models

Consider now the case in which H_3^+ formation and DR compete effectively with the $H_3^+ + H_2$ thermalization reaction. We make the assumption that formation of p-H_3^+ from $H_2^+ + H_2$ is governed only by the nuclear spin branching fractions presented in Table 4.4. Under these conditions, the full rate equation for p-$H_3^+$is:

$$\begin{aligned}\frac{\mathrm{d}}{\mathrm{d}t}[p\text{-}\mathrm{H}_3^+] &= k_1([p\text{-}\mathrm{H}_2][p\text{-}\mathrm{H}_2^+] + \frac{2}{3}[p\text{-}\mathrm{H}_2][o\text{-}\mathrm{H}_2^+] + \frac{2}{3}[o\text{-}\mathrm{H}_2][p\text{-}\mathrm{H}_2^+] + \frac{1}{3}[o\text{-}\mathrm{H}_2][o\text{-}\mathrm{H}_2^+]) \\ &+ \{(k_{oopo} + k_{oopp})\,[o\text{-}\mathrm{H}_2] + (k_{oppo} + k_{oppp})\,[p\text{-}\mathrm{H}_2]\}\,[o\text{-}\mathrm{H}_3^+] \\ &- \{(k_{pooo} + k_{poop})\,[o\text{-}\mathrm{H}_2] + (k_{ppoo} + k_{ppop})\,[p\text{-}\mathrm{H}_2]\}\,[p\text{-}\mathrm{H}_3^+] \\ &- k_{e,p}[e^-][p\text{-}\mathrm{H}_3^+]. \end{aligned} \tag{4.9}$$

From Table 4.4, we can reduce the first line in this equation to $k_1[\mathrm{H}_2][\mathrm{H}_2^+]\{(1/3) + (2/3)p_2\}$. We now invoke steady state arguments for all species. For H_2^+, $\zeta_2[\mathrm{H}_2] = k_1[\mathrm{H}_2][\mathrm{H}_2^+]$, therefore $k_1[\mathrm{H}_2^+]$ can be replaced by ζ_2. Setting the resultant equation equal to zero and dividing by $[\mathrm{H}_3^+][\mathrm{H}_2]$ as before gives:

$$\begin{aligned} 0 &= \frac{\zeta_2}{[\mathrm{H}_3^+]}(\frac{1}{3} + \frac{2}{3}p_2) \\ &+ \{(k_{oopo} + k_{oopp})\,(1 - p_2) + (k_{oppo} + k_{oppp})\,p_2\}\,(1 - p_3) \\ &- \{(k_{pooo} + k_{poop})\,(1 - p_2) + (k_{ppoo} + k_{ppop})\,p_2\}\,p_3 \\ &- k_{e,p}\frac{[e^-]}{[\mathrm{H}_2]}p_3. \end{aligned} \tag{4.10}$$

This equation can be further simplified by examining the steady state value of $[\mathrm{H}_3^+]$, which begins with the equation $\zeta_2[\mathrm{H}_2] = k_e[\mathrm{H}_3^+][e^-]$. More specifically, if we include the possibility for different DR rates for o-H_3^+ and p-H_3^+, we obtain the equation:

$$\zeta_2[\mathrm{H}_2] = [e^-](k_{e,p}[p\text{-}\mathrm{H}_3^+] + k_{e,o}[o\text{-}\mathrm{H}_3^+]). \tag{4.11}$$

Dividing both sides of equation 4.11 by $[\mathrm{H}_3^+][\mathrm{H}_2]$ results in an expression for $\zeta_2/[\mathrm{H}_3^+]$:

$$\frac{\zeta_2}{[\mathrm{H}_3^+]} = \frac{[e^-]}{[\mathrm{H}_2]}(k_{e,p}p_3 + k_{e,o}(1 - p_3)). \tag{4.12}$$

Substituting this relation into equation 4.10 gives:

$$
\begin{aligned}
0 &= \frac{[e^-]}{[\mathrm{H}_2]}(k_{e,p}p_3 + k_{e,o}(1-p_3))(\frac{1}{3}+\frac{2}{3}p_2) \\
&\quad + \{(k_{oopo}+k_{oopp})(1-p_2) + (k_{oppo}+k_{oppp})p_2\}(1-p_3) \\
&\quad - \{(k_{pooo}+k_{poop})(1-p_2) + (k_{ppoo}+k_{ppop})p_2\}p_3 \\
&\quad - k_{e,p}\frac{[e^-]}{[\mathrm{H}_2]}p_3. \qquad (4.13)
\end{aligned}
$$

Solving for p_3 and removing the k_{oppp} and k_{ppop} terms yields:

$$
p_3 = \frac{k_{e,o}\frac{[e^-]}{[\mathrm{H}_2]}\left(\frac{1}{3}+\frac{2}{3}p_2\right) + (k_{oopp}+k_{oopo})(1-p_2) + k_{oppo}p_2}{k_{e,p}\frac{[e^-]}{[\mathrm{H}_2]}\left(\frac{2}{3}-\frac{2}{3}p_2\right) + k_{e,o}\frac{[e^-]}{[\mathrm{H}_2]}\left(\frac{1}{3}+\frac{2}{3}p_2\right) + (k_{oopp}+k_{oopo}+k_{poop}+k_{pooo})(1-p_2) + (k_{oppo}+k_{ppoo})p_2}. \qquad (4.14)
$$

Finally, the ratio $[e^-]/[\mathrm{H}_2]$ can be replaced by $2x_e/f$, which results in equation 4.15:

$$
p_3 = \frac{k_{e,o}\frac{2x_e}{f}\left(\frac{1}{3}+\frac{2}{3}p_2\right) + (k_{oopp}+k_{oopo})(1-p_2) + k_{oppo}p_2}{k_{e,p}\frac{2x_e}{f}\left(\frac{2}{3}-\frac{2}{3}p_2\right) + k_{e,o}\frac{2x_e}{f}\left(\frac{1}{3}+\frac{2}{3}p_2\right) + (k_{oopp}+k_{oopo}+k_{poop}+k_{pooo})(1-p_2) + (k_{oppo}+k_{ppoo})p_2}. \qquad (4.15)
$$

Chapter 5

Modeling Nuclear Spin Effects in Hydrogenic Plasmas

5.1 Introduction

Symmetry and its associated selection rules have long been an integral component of spectroscopy. [88, 89] For high-resolution spectroscopy, the complete nuclear permutation-inversion (CNPI) group representation [90–92] has been useful for assigning symmetry labels to rotational energy levels and calculating nuclear spin statistical weights (NSSWs), in particular for nonrigid molecules. The symmetry rules are based on the fact that the molecular Hamiltonian is invariant under permutations of identical nuclei and spatial inversion of all particles through the molecular center-of-mass, in contrast to point group theory, which depends on the geometrical symmetry of a set of nuclei.

The formulation of the CNPI groups allows for an easy determination of the consequences of Bose-Einstein (for integer-spin nuclei) or Fermi-Dirac (for half-integer-spin nuclei) statistics. According to Dirac's formulation [93] of the Pauli exclusion principle, [94] a molecular wavefunction must be symmetric with respect to permutation of identical bosons, and antisymmetric with respect to permutation of identical fermions. When applied to H_2 and H_3^+, the consequence is that the nuclear spin configuration of each molecule is linked to its rotational manifold. For H_2, the *ortho* configuration (o-H_2, $I = 1$) exists only in rotational levels in which J is odd, and the *para* configuration (p-H_2, $I = 0$) exists only in the even-J levels. The symmetry of H_3^+ is a bit more complex, but it can be shown that in the vibrational ground state, the nuclear spin configurations are linked to the projection quantum number k: o-$H_3^+(I = 3/2) \rightarrow k = 3n$, p-$H_3^+(I = 1/2) \rightarrow k = 3n \pm 1$, where n is an integer. [95]

Because the nuclear magnetic interaction is rather weak, the nuclear spin configurations of H_2 and H_3^+ behave as independent chemical species, meaning that I is a good quantum number in these systems. Interconversion between nuclear spin configurations in each of these molecules can only be accomplished by means of interaction with a strong, local, inhomogeneous magnetic field (such as the surface of a ferromagnetic catalyst), or by means of reactive collisions that result in scrambling of nuclei. The thermoneutral reaction

This chapter is adapted with permission from K. N. Crabtree, B. A. Tom, and B. J. McCall, Journal of Chemical Physics 134 (2011) 194310, Copyright 2011, American Institute of Physics.

$H_3^+ + H_2 \rightarrow H_2 + H_3^+$ is a prime example of this type of reaction. However, because I is a good quantum number in each molecule, this reaction is subject to selection rules [69, 72] based on the conservation of the total nuclear spin of the system.

Beyond the fundamental interest of studying selection rules in chemical reactions, the reaction between H_3^+ and H_2 has practical application as well. Hydrogen is by far the most abundant element in the universe, and consequently H_2 and H_3^+ serve as useful probes of astrophysical or extraterrestrial conditions. In particular, H_3^+ has been used to image auroral activity in the atmospheres of Jupiter [23], Saturn, [25] and Uranus [24], to probe gas density and temperature in the galactic center, [96], and to estimate the interstellar cosmic-ray ionization rate. [22, 47] In molecular clouds, only the lowest states of o-H_3^+ and p-H_3^+ are populated, and the inferred *ortho*:*para* ratio of H_3^+ has been used to estimate interstellar cloud temperatures and dimensions. [47, 52, 53] In these environments, the $H_3^+ + H_2$ reaction is the dominant means by which the nuclear spin of H_3^+ can be changed, and the selection rules for this reaction have important implications for the use of H_3^+ as a temperature probe. [97]

To understand the $H_3^+ + H_2$ reaction, especially its role in the interstellar medium, laboratory measurements of its nuclear spin dependence are needed. Initial measurements of this reaction have been performed in a ∼400 K hydrogenic plasma, but the associated analysis was rather complex, and not readily applicable to experiments at lower temperatures. [74] Furthermore, in a laboratory plasma, the gas density may be sufficiently high to allow for three-body reactions to occur. If these exhibit nuclear spin dependence, then they will interfere with the measurement of the two-body process. These effects were not taken into account in the previous work.

In this paper, we present chemical models aimed at assessing the nuclear spin dependence of the $H_3^+ + H_2$ reaction. The paper is structured as follows. In Section 5.2, we examine in more detail the nuclear spin selection rules as they apply to reactions in laboratory plasmas. In Section 5.3, we derive models for nuclear spin dependence in a laboratory plasma at high temperature, and then we derive a model for a low-temperature plasma in Section 5.4. We summarize the work in Section 5.5. The models in this paper can be applied directly to experimental measurements, and are intended to serve as a framework for the interpretation of such measurements (see the following article in this issue [98]).

5.2 Nuclear Spin Selection Rules

The nuclear spin selection rules [69, 72] result in NSSWs for various nuclear spin reactant and product channels. If the energy available in a chemical reaction is sufficiently high, then these NSSWs describe the

(H_3^+,H_2)	Weight	$(\mathcal{D}_{3/2}, \mathcal{D}_1)$	$(\mathcal{D}_{3/2}, \mathcal{D}_0)$	$(\mathcal{D}_{1/2}, \mathcal{D}_1)$	$(\mathcal{D}_{1/2}, \mathcal{D}_0)$
$(\mathcal{D}_{3/2}, \mathcal{D}_1)$	12	37/5	1	14/5	4/5
$(\mathcal{D}_{3/2}, \mathcal{D}_0)$	4	1	1	2	0
$(\mathcal{D}_{1/2}, \mathcal{D}_1)$	12	14/5	2	28/5	8/5
$(\mathcal{D}_{1/2}, \mathcal{D}_0)$	4	4/5	0	8/5	8/5

Table 5.1: Total nuclear spin statistical weights for the $H_3^+ + H_2$ reaction. [69] The table rows correspond to the nuclear spin configuration of reactant (H_3^+,H_2) pairs, and the table columns correspond to the product pairs.

outcomes of the reaction in a statistical manner. We call this situation the "high temperature limit." The NSSWs have been derived for the $H_3^+ + H_2$ system by Oka [69] in terms of the rotation group representations of the nuclear spin angular momentum. For three-body collisions proceeding through a $(H_7^+)^*$ complex, the NSSWs for the seven-particle $H_5^+ + H_2$ system must be used. In this section, we review the NSSWs for the $H_3^+ + H_2$ system, and derive NSSWs for $H_5^+ + H_2$.

5.2.1 $H_3^+ + H_2$

The rotation group representation of the nuclear spin angular momentum of H_2 is $(\mathcal{D}_{1/2})^2 = \mathcal{D}_1 \oplus \mathcal{D}_0$, and that of H_3^+ is $(\mathcal{D}_{1/2})^3 = \mathcal{D}_{3/2} \oplus 2\mathcal{D}_{1/2}$. The correspondence between the representations and the nuclear spin states (with statistical weights in parentheses) is: $\mathcal{D}_1 \rightarrow o$-$H_2$ $(2 \times 1 + 1 = 3)$, $\mathcal{D}_0 \rightarrow p$-$H_2$ $(2 \times 0 + 1 = 1)$, $\mathcal{D}_{3/2} \rightarrow o$-$H_3^+$ $(2 \times 3/2 + 1 = 4)$, and $2\mathcal{D}_{1/2} \rightarrow p$-$H_3^+$ $(2[2 \times 1/2 + 1] = 4)$. Using the procedure described by Oka, [69] the NSSWs for the possible reactions between the nuclear spin configurations of H_3^+ and H_2 can be calculated, and these are shown for convenience in Table 5.1.

In the $H_3^+ + H_2$ reaction, proton scrambling may be incomplete, as has been experimentally demonstrated for this system [74] and for the $D_3^+ + H_2$ system. [75] Following Oka, we define the three statistical reaction pathways as follows:

$$\tilde{H}_3^+ + H_2 \rightarrow \tilde{H}_3^+ + H_2, \tag{5.1}$$

$$\tilde{H}_3^+ + H_2 \rightarrow H_2\tilde{H}^+ + \tilde{H}_2, \text{ and} \tag{5.2}$$

$$\tilde{H}_3^+ + H_2 \rightarrow H\tilde{H}_2^+ + H\tilde{H}. \tag{5.3}$$

These are the identity (5.1), proton hop (5.2), and hydrogen exchange (5.3) pathways, with branching fractions S^{id}, S^{hop}, and S^{exch} (1/10, 3/10, and 6/10 in the statistical limit, respectively). NSSWs can be calculated for each of these individually, and the results organized in matrix form. The ordering of rows and columns in these matrices correspond to the ordering in Table 5.1. The identity matrix is given by the

	Hop		Exchange	
(H_3^+,H_2)	o-H_3^+	p-H_3^+	o-H_3^+	p-H_3^+
$(\mathcal{D}_{3/2}, \mathcal{D}_1)$	2/3	1/3	2/3	1/3
$(\mathcal{D}_{3/2}, \mathcal{D}_0)$	0	1	2/3	1/3
$(\mathcal{D}_{1/2}, \mathcal{D}_1)$	2/3	1/3	1/3	2/3
$(\mathcal{D}_{1/2}, \mathcal{D}_0)$	0	1	1/3	2/3

Table 5.2: Mechanism-specific nuclear spin branching fractions for the formation of o-H_3^+ and p-H_3^+ from the $H_3^+ + H_2$ reaction with the (H_3^+,H_2) reactant nuclear spin configurations.

statistical weight of each channel multiplied by S^{id}; the hop matrix is calculated by representing a proton hop as the sequence $H_3^+ \rightarrow H_2 + H^+$, followed by $H^+ + \tilde{H}_2 \rightarrow H\tilde{H}_2^+$ and applying Oka's method. Finally, the exchange matrix is obtained by subtracting the identity and hop matrices from the total matrix shown in Table 5.1. These matrices are shown in equations 5.4-5.6, along with their values in the statistical limit.

$$\text{id} = S^{id} \begin{pmatrix} 12 & 0 & 0 & 0 \\ 0 & 4 & 0 & 0 \\ 0 & 0 & 12 & 0 \\ 0 & 0 & 0 & 4 \end{pmatrix} \rightarrow \begin{pmatrix} 6/5 & 0 & 0 & 0 \\ 0 & 2/5 & 0 & 0 \\ 0 & 0 & 6/5 & 0 \\ 0 & 0 & 0 & 2/5 \end{pmatrix} \tag{5.4}$$

$$\text{hop} = S^{hop} \begin{pmatrix} 8 & 0 & 4 & 0 \\ 0 & 0 & 4 & 0 \\ 4 & 4 & 2 & 2 \\ 0 & 0 & 2 & 2 \end{pmatrix} \rightarrow \begin{pmatrix} 12/5 & 0 & 6/5 & 0 \\ 0 & 0 & 6/5 & 0 \\ 6/5 & 6/5 & 3/5 & 3/5 \\ 0 & 0 & 3/5 & 3/5 \end{pmatrix} \tag{5.5}$$

$$\text{exch} = S^{exch} \begin{pmatrix} 19/3 & 5/3 & 8/3 & 4/3 \\ 5/3 & 1 & 4/3 & 0 \\ 8/3 & 4/3 & 19/3 & 5/3 \\ 4/3 & 0 & 5/3 & 1 \end{pmatrix} \rightarrow \begin{pmatrix} 19/5 & 1 & 8/5 & 4/5 \\ 1 & 3/5 & 4/5 & 0 \\ 8/5 & 4/5 & 19/5 & 1 \\ 4/5 & 0 & 1 & 3/5 \end{pmatrix} \tag{5.6}$$

It is often the case that H_2 is more abundant than H_3^+ by several orders of magnitude, such as in a laboratory plasma, and therefore the nuclear spin configuration of the product H_2 might not be important, especially if the plasma is pulsed. The number of $H_3^+ + H_2$ collisions will not be sufficient to significantly change the H_2 *ortho*:*para* ratio, so the branching fractions for the formation of o-H_3^+ and p-H_3^+ can be calculated ignoring the nuclear spin of the product H_2. This can be done separately for the hop and exchange reactions, and the results are summarized in Table 5.2.

5.2.2 $H_5^+ + H_2$

In a laboratory plasma, the collision rate may be high enough that during the lifetime of the $(H_5^+)^*$ complex formed by H_3^+ and H_2, the complex undergoes an additional collision with H_2. In such a three-body process, the excess energy of the complex may be drawn away, forming a stable H_5^+ species. Alternatively, the incoming H_2 may add to form an $(H_7^+)^*$ complex, where additional proton scrambling may occur, followed by the dissociation pathway $(H_7^+)^* \rightarrow (H_5^+)^* + H_2 \rightarrow H_3^+ + 2H_2$. To model this process, we must derive the NSSWs for the $H_5^+ + H_2$ system.

Following Oka's procedure, we first define the angular momentum representation of this reaction. H_5^+ is represented as $(\mathcal{D}_{1/2})^5 = \mathcal{D}_{5/2} \oplus 4\mathcal{D}_{3/2} \oplus 5\mathcal{D}_{1/2}$, and the reaction is represented by

$$\begin{aligned}
&(\mathcal{D}_{5/2} \oplus 4\mathcal{D}_{3/2} \oplus 5\mathcal{D}_{1/2}) \otimes (\mathcal{D}_1 \oplus \mathcal{D}_0) \rightarrow \\
&\mathcal{D}_{7/2} \oplus 6\mathcal{D}_{5/2} \oplus 14\mathcal{D}_{3/2} \oplus 14\mathcal{D}_{1/2} \rightarrow \\
&(\mathcal{D}_{5/2} \oplus 4\mathcal{D}_{3/2} \oplus 5\mathcal{D}_{1/2}) \otimes (\mathcal{D}_1 \oplus \mathcal{D}_0).
\end{aligned}$$

The reaction is then broken down into individual reactants. For this reaction, the forward and reverse reactions are identical, but to remain consistent with Oka's notation, the reverse reactions are

$$\begin{aligned}
\mathcal{D}_{7/2} \oplus \mathcal{D}_{5/2} \oplus \mathcal{D}_{3/2} &\leftarrow \mathcal{D}_{5/2} \otimes \mathcal{D}_1 \\
\mathcal{D}_{5/2} &\leftarrow \mathcal{D}_{5/2} \otimes \mathcal{D}_0 \\
4\mathcal{D}_{5/2} \oplus 4\mathcal{D}_{3/2} \oplus 4\mathcal{D}_{1/2} &\leftarrow 4\mathcal{D}_{3/2} \otimes \mathcal{D}_1 \\
4\mathcal{D}_{3/2} &\leftarrow 4\mathcal{D}_{3/2} \otimes \mathcal{D}_0 \\
5\mathcal{D}_{3/2} \oplus 5\mathcal{D}_{1/2} &\leftarrow 5\mathcal{D}_{1/2} \otimes \mathcal{D}_1 \\
5\mathcal{D}_{1/2} &\leftarrow 5\mathcal{D}_{1/2} \otimes \mathcal{D}_0.
\end{aligned}$$

(H_5^+,H_2)	Weight	$(\mathcal{D}_{5/2},\mathcal{D}_1)$	$(\mathcal{D}_{5/2},\mathcal{D}_0)$	$(\mathcal{D}_{3/2},\mathcal{D}_1)$	$(\mathcal{D}_{3/2},\mathcal{D}_0)$	$(\mathcal{D}_{1/2},\mathcal{D}_1)$	$(\mathcal{D}_{1/2},\mathcal{D}_0)$
$(\mathcal{D}_{5/2},\mathcal{D}_1)$	18	65/7	1	36/7	8/7	10/7	0
$(\mathcal{D}_{5/2},\mathcal{D}_0)$	6	1	1	4	0	0	0
$(\mathcal{D}_{3/2},\mathcal{D}_1)$	48	36/7	4	160/7	32/7	60/7	20/7
$(\mathcal{D}_{3/2},\mathcal{D}_0)$	16	8/7	0	32/7	32/7	40/7	0
$(\mathcal{D}_{1/2},\mathcal{D}_1)$	30	10/7	0	60/7	40/7	75/7	25/7
$(\mathcal{D}_{1/2},\mathcal{D}_0)$	10	0	0	20/7	0	25/7	25/7

Table 5.3: As Table 5.1, for the $H_5^+ + H_2$ reaction.

This leads to the normalized outcomes for the intermediates:

$$
\begin{aligned}
\mathcal{D}_{7/2} &\rightarrow 8(\mathcal{D}_{5/2}\otimes\mathcal{D}_1/18)\\
\mathcal{D}_{5/2} &\rightarrow (\mathcal{D}_{5/2}\otimes\mathcal{D}_1/18)\oplus(\mathcal{D}_{5/2}\otimes\mathcal{D}_0/6)\\
&\quad \oplus 4(\mathcal{D}_{3/2}\otimes\mathcal{D}_1/12)\\
\mathcal{D}_{3/2} &\rightarrow \frac{2}{7}(\mathcal{D}_{5/2}\otimes\mathcal{D}_1/18)\oplus\frac{8}{7}(\mathcal{D}_{3/2}\otimes\mathcal{D}_1/12)\\
&\quad \oplus\frac{8}{7}(\mathcal{D}_{3/2}\otimes\mathcal{D}_0/4)\oplus\frac{10}{7}(\mathcal{D}_{1/2}\otimes\mathcal{D}_1/6)\\
\mathcal{D}_{1/2} &\rightarrow \frac{4}{7}(\mathcal{D}_{3/2}\otimes\mathcal{D}_1/12)\oplus\frac{5}{7}(\mathcal{D}_{1/2}\otimes\mathcal{D}_1/6)\\
&\quad \oplus\frac{5}{7}(\mathcal{D}_{1/2}\otimes\mathcal{D}_0/2).
\end{aligned}
$$

From here, the calculation of the total NSSW matrix is possible, and an example will be given for completeness. To calculate a NSSW, the total weights of possible reaction pathways for a given reactant-product pair must be added. For reactant pair $(\mathcal{D}_{3/2},\mathcal{D}_1)$ and product pair $(\mathcal{D}_{5/2},\mathcal{D}_1)$, this proceeds as follows: the reactant $4(\mathcal{D}_{3/2}\otimes\mathcal{D}_1)$ gives the intermediates $4\mathcal{D}_{5/2}$, $4\mathcal{D}_{3/2}$, and $4\mathcal{D}_{1/2}$. For each intermediate, the normalized weight corresponding to the product $(\mathcal{D}_{5/2}\otimes\mathcal{D}_1)$ is its coefficient in the appropriate normalized outcome listed above. For the $4\mathcal{D}_{1/2}$ intermediates, the desired product is not obtained; for the $4\mathcal{D}_{5/2}$ and $4\mathcal{D}_{3/2}$ intermediates, the coefficients are 4×1 and $4\times 2/7$, respectively, giving a total weight of 36/7. The reverse reaction $(\mathcal{D}_{5/2},\mathcal{D}_1)\rightarrow(\mathcal{D}_{3/2},\mathcal{D}_1)$ has the same weight, as the reaction is symmetric. The NSSWs for all reactant and product pairs are listed in Table 5.3.

To calculate mechanism-specific NSSWs, the next step is to define the statistical mechanisms for the

p	$\mathcal{D}_{7/2}$	$\mathcal{D}_{5/2}$	$\mathcal{D}_{3/2}$	$\mathcal{D}_{1/2}$
$(\mathcal{D}_{5/2}, \mathcal{D}_1)$	8	6	4	0
$(\mathcal{D}_{5/2}, \mathcal{D}_0)$	0	6	0	0
$(\mathcal{D}_{3/2}, \mathcal{D}_1)$	0	6	4	2
$(\mathcal{D}_{3/2}, \mathcal{D}_0)$	0	0	4	0
$(\mathcal{D}_{1/2}, \mathcal{D}_1)$	0	0	4	2
$(\mathcal{D}_{1/2}, \mathcal{D}_0)$	0	0	0	2

Table 5.4: Values of g_{pI} for product pair p and intermediate angular momentum representation $\mathcal{D}_I$.

I_5	Substates (I_3, I_{ab}, I_{de})
5/2	(3/2,1,1)
3/2	(3/2,1,1), (3/2,1,0), (1/2,1,1), (1/2,0,1)
1/2	(3/2,1,1), (1/2,1,1), (1/2,0,1), (1/2,1,0), (1/2,0,0)

Table 5.5: Angular momentum substates for each I_5 state of H_5^+.

system:

$$H_5^+ + \tilde{H}_2 \rightarrow H_5^+ + \tilde{H}_2 \tag{5.7}$$

$$H_5^+ + \tilde{H}_2 \rightarrow H_3\tilde{H}_2^+ + H_2 \tag{5.8}$$

$$H_5^+ + \tilde{H}_2 \rightarrow H_4\tilde{H}^+ + \tilde{H}H. \tag{5.9}$$

Reaction 5.7 is the "identity" mechanism with statistical weight 1, 5.8 is the "H_3^+ hop" mechanism with statistical weight 10, and 5.9 is the "hydrogen exchange" mechanism with statistical weight 10. However, both the H_3^+ hop and hydrogen exchange pathways are complex, and application of Oka's method for calculating mechanism-specific NSSWs is nontrivial.

An alternative formulation for calculating the NSSWs of the $H_3^+ + H_2$ system has been demonstrated by Park and Light, [77] and this approach can be more readily applied to the $H_5^+ + H_2$ system. Using the statistical mechanisms (5.7), (5.8), and (5.9), the mechanism-specific NSSW (B_{pr}^M) for reactant pair r and product pair p through mechanism M can be calculated by

$$B_{pr}^M = S^M \sum_I g_{pI} P_{pIr}^M, \tag{5.10}$$

where g_{pI} is the statistical weight of the $\mathcal{D}_I$ representation of p, S^M is the statistical weight of the reaction pathway, and P_{pIr}^M is the cumulative spin modification probability for reactant r to product p through an intermediate with angular momentum I. The values of g_{pI} can be found in Table 5.4. In the statistical limit, S^{id} is 1/21, and S^{hop} and S^{exch} are 10/21.

Calculation of P_{pIr}^{M} requires construction of basis states for calculating transition matrix elements. The easiest basis set for defining the scrambling operators is that of proton nuclear spin angular momentum projections. This basis set is defined by the projection quantum number of the nuclear spin angular momentum of each proton in the $(H_aH_bH_cH_dH_e)^+ + (H_fH_g)$ system: $|m_a, m_b, m_c, m_d, m_e, m_f, m_g\rangle$ (as a general note on notation, m represents a projection quantum number, and I represents a total angular momentum quantum number). In this basis set, the scrambling operators take very simple forms: $O^{id} = \hat{I}, O^{hop} = \hat{p}_{af}\hat{p}_{bg}$, and $O^{exch} = \hat{p}_{ef}$, where $\hat{p}_{ab}$ is a permutation operator for nuclei a and b.

However, these 128 (2^7) orthonormal basis states do not directly map to the 128 reactant/product pair states, which are $18 \times (\mathcal{D}_{5/2}, \mathcal{D}_1)$, $6 \times (\mathcal{D}_{5/2}, \mathcal{D}_0)$, $12 \times 4(\mathcal{D}_{3/2}, \mathcal{D}_1)$, $4 \times 4(\mathcal{D}_{3/2}, \mathcal{D}_0)$, $6 \times 5(\mathcal{D}_{1/2}, \mathcal{D}_1)$, and $2 \times 5(\mathcal{D}_{1/2}, \mathcal{D}_0)$. Instead, these states are represented by the orthonormal total nuclear spin basis states $|I_7, m_7, I_5, I_3, I_{ab}, I_{de}, I_2\rangle$. In this form, I_5 and I_2 are the total nuclear spin angular momenta of H_5^+ and H_2, and I_7 and m_7 are the total nuclear spin angular momentum of the entire system and its projection. The quantities I_{ab} and I_{de} are the combined nuclear spin angular momenta of the (a, b) and (d, e) proton pairs in H_5^+, and I_3 is the combined angular momentum of I_{ab} and I_c. Together, I_3, I_{ab}, and I_{de} specify angular momentum substates of the I_5 state of H_5^+ (see Table 5.5). The elements of these substates can be compared to the elements of the basis states of Park and Light for the $H_3^+ + H_2$ system (our notation is slightly different): $I_5 \rightarrow I, m_5 \rightarrow I_z, I_3 \rightarrow I_3, I_{ab} \rightarrow i_2$, and $I_{de} \rightarrow I_2$.

The orthonormal nuclear spin angular momentum basis states $|I_7, m_7, I_5, I_3, I_{ab}, I_{de}, I_2\rangle$ can be constructed from linear combinations of the proton projection basis states $|m_a, m_b, m_c, m_d, m_e, m_f, m_g\rangle$; the weighting coefficients are products of Clebsch-Gordan coefficients as shown in Equation 5.11. The projections are defined explicitly as follows: $m_2 = m_f + m_g$, $m_{ab} = m_a + m_b$, $m_{de} = m_d + m_e$, $m_3 = m_{ab} + m_c$, and $m_5 = m_3 + m_{de}$.

$$
\begin{aligned}
|I_7, m_7, I_5, I_3, I_{ab}, I_{de}, I_2\rangle \quad = \quad & \sum_{m_a, m_b, m_c, m_d, m_e, m_f, m_g} \langle I_5, m_5; I_2, m_2 |\ I_7, m_7\rangle \, \langle I_3, m_3; I_{de}, m_{de} |\ I_5, m_5\rangle \\
& \times \langle I_{ab}, m_{ab}; I_c, m_c |\ I_3, m_3\rangle \, \langle I_d, m_d; I_e, m_e |\ I_{de}, m_{de}\rangle \, \langle I_a, m_a; I_b, m_b |\ I_{ab}, m_{ab}\rangle \\
& \times \langle I_f, m_f; I_g, m_g |\ I_2, m_2\rangle \, |m_a, m_b, m_c, m_d, m_e, m_f, m_g\rangle \qquad (5.11)
\end{aligned}
$$

Having defined the orthonormal total nuclear spin angular momentum basis states and the linear combinations of proton basis states that compose them, the mechanism-specific cumulative nuclear spin modification

probability P^M_{pIr} can be calculated (Equation 5.12).

$$P^M_{pIr} = \sum_{I^p_3, I^p_{ab}, I^p_{de}, I^r_3, I^r_{ab}, I^r_{de}} \left| \langle I_7, m_7, I^p_5, I^p_3, I^p_{ab}, I^p_{de}, I^p_2 | \, O^M \, | I_7, m_7, I^r_5, I^r_3, I^r_{ab}, I^r_{de}, I^r_2 \rangle \right|^2 \tag{5.12}$$

The summation takes into account the factors of 4 and 5 for $\mathcal{D}_{3/2}$ and $\mathcal{D}_{1/2}$ as seen in the rotation group representation of H_5^+ ($\mathcal{D}_{5/2} \oplus 4\mathcal{D}_{3/2} \oplus 5\mathcal{D}_{1/2}$). All values of P^M_{pIr} are shown in Table 5.6.

Using the P^M_{pIr} values in Table 5.6 with equation 5.10 allows calculation of the mechanism-specific NSSWs.

$$\text{id} = S^{id} \begin{pmatrix} 18 & 0 & 0 & 0 & 0 & 0 \\ 0 & 6 & 0 & 0 & 0 & 0 \\ 0 & 0 & 48 & 0 & 0 & 0 \\ 0 & 0 & 0 & 16 & 0 & 0 \\ 0 & 0 & 0 & 0 & 30 & 0 \\ 0 & 0 & 0 & 0 & 0 & 10 \end{pmatrix} \rightarrow \begin{pmatrix} 6/7 & 0 & 0 & 0 & 0 & 0 \\ 0 & 2/7 & 0 & 0 & 0 & 0 \\ 0 & 0 & 16/7 & 0 & 0 & 0 \\ 0 & 0 & 0 & 16/21 & 0 & 0 \\ 0 & 0 & 0 & 0 & 10/7 & 0 \\ 0 & 0 & 0 & 0 & 0 & 10/21 \end{pmatrix} \tag{5.13}$$

$$\text{hop} = S^{hop} \begin{pmatrix} 9 & 0 & 6 & 0 & 3 & 0 \\ 0 & 0 & 6 & 0 & 0 & 0 \\ 6 & 6 & 20 & 4 & 10 & 2 \\ 0 & 0 & 4 & 4 & 8 & 0 \\ 3 & 0 & 10 & 8 & 5 & 4 \\ 0 & 0 & 2 & 0 & 4 & 4 \end{pmatrix} \rightarrow \begin{pmatrix} 30/7 & 0 & 20/7 & 0 & 10/7 & 0 \\ 0 & 0 & 20/7 & 0 & 0 & 0 \\ 20/7 & 20/7 & 200/21 & 40/21 & 100/21 & 20/21 \\ 0 & 0 & 40/21 & 40/21 & 80/21 & 0 \\ 10/7 & 0 & 100/21 & 80/21 & 50/21 & 40/21 \\ 0 & 0 & 20/21 & 0 & 40/21 & 40/21 \end{pmatrix} \tag{5.14}$$

$$
\begin{aligned}
\text{exch} \quad &= \quad S^{exch} \begin{pmatrix} 87/10 & 21/10 & 24/5 & 12/5 & 0 & 0 \\ 21/10 & 3/2 & 12/5 & 0 & 0 & 0 \\ 24/5 & 12/5 & 116/5 & 28/5 & 8 & 4 \\ 12/5 & 0 & 28/5 & 4 & 4 & 0 \\ 0 & 0 & 8 & 4 & 29/2 & 7/2 \\ 0 & 0 & 4 & 0 & 7/2 & 5/2 \end{pmatrix} \\
&\rightarrow \begin{pmatrix} 29/7 & 1 & 16/7 & 8/7 & 0 & 0 \\ 1 & 5/7 & 8/7 & 0 & 0 & 0 \\ 16/7 & 8/7 & 232/21 & 56/21 & 80/21 & 40/21 \\ 8/7 & 0 & 56/21 & 40/21 & 40/21 & 0 \\ 0 & 0 & 80/21 & 40/21 & 145/21 & 35/21 \\ 0 & 0 & 40/21 & 0 & 35/21 & 25/21 \end{pmatrix}
\end{aligned} \tag{5.15}
$$

Equations 5.13, 5.14, and 5.15 show the branching fraction matrices as a function of S^M, and also show the matrices in the statistical limit ($S^{id} = 1/21$, $S^{hop} = 10/21$, and $S^{exch} = 10/21$). These matrices are ordered the same as Table 5.3.

Adding the statistical matrices for the identity, H_3^+ hop, and hydrogen exchange mechanisms gives the total NSSW matrix:

$$
\begin{pmatrix} 65/7 & 1 & 36/7 & 8/7 & 10/7 & 0 \\ 1 & 1 & 4 & 0 & 0 & 0 \\ 36/7 & 4 & 160/7 & 32/7 & 60/7 & 20/7 \\ 8/7 & 0 & 32/7 & 32/7 & 40/7 & 0 \\ 10/7 & 0 & 60/7 & 40/7 & 75/7 & 25/7 \\ 0 & 0 & 20/7 & 0 & 25/7 & 25/7 \end{pmatrix}.
$$

These are identical to the total NSSWs calculated using Oka's method (Table 5.3), which suggests that the calculation has been done properly. As with the $H_3^+ + H_2$ reaction, in a pulsed laboratory plasma the spin configuration of the product H_2 is not important, and the mechanism-specific branching fractions can be further reduced in terms of the branching fractions for the $\mathcal{D}_{5/2}$, $\mathcal{D}_{3/2}$, and $\mathcal{D}_{1/2}$ spin configurations of H_5^+. These results are in Table 5.7.

Reactant r	Total Spin I	Mechanism M	Product p (5/2,1)	(5/2,0)	(3/2,1)	(3/2,0)	(1/2,1)	(1/2,0)
		id	1	0	0	0	0	0
	7/2	hop	1	0	0	0	0	0
		exch	1	0	0	0	0	0
		id	1	0	0	0	0	0
(5/2,1)	5/2	hop	4/25	0	21/25	0	0	0
		exch	9/100	35/100	56/100	0	0	0
		id	1	0	0	0	0	0
	3/2	hop	1/100	0	24/100	0	75/100	0
		exch	1/25	0	9/25	15/25	0	0
		id	0	1	0	0	0	0
(5/2,0)	5/2	hop	0	0	1	0	0	0
		exch	7/20	5/20	8/20	0	0	0
		id	0	0	4	0	0	0
	5/2	hop	21/25	25/25	54/25	0	0	0
		exch	14/25	10/25	76/25	0	0	0
		id	0	0	4	0	0	0
(3/2,1)	3/2	hop	18/75	0	107/75	75/75	100/75	0
		exch	27/75	0	43/75	105/75	125/75	0
		id	0	0	4	0	0	0
	1/2	hop	0	0	2/3	0	7/3	3/3
		exch	0	0	4/3	0	2/3	6/3
		id	0	0	0	4	0	0
(1/2, 0)	3/2	hop	0	0	1	1	2	0
		exch	3/5	0	7/5	5/5	5/5	0
		id	0	0	0	0	5	0
	3/2	hop	9/12	0	16/12	24/12	11/12	0
		exch	0	0	5/3	3/3	7/3	0
(1/2,1)								
		id	0	0	0	0	5	0
	1/2	hop	0	0	7/3	0	2/3	6/3
		exch	0	0	2/3	0	31/12	7/4
		id	0	0	0	0	0	5
(1/2,0)	1/2	hop	0	0	1	0	2	2
		exch	0	0	8/4	0	7/4	5/4

Table 5.6: Mechanism-specific cumulative nuclear spin modification probabilities P^M_{pIr}.

Reactant Pair	Hop $\mathcal{D}_{5/2}$	Hop $\mathcal{D}_{3/2}$	Hop $\mathcal{D}_{1/2}$	Exchange $\mathcal{D}_{5/2}$	Exchange $\mathcal{D}_{3/2}$	Exchange $\mathcal{D}_{1/2}$
$(\mathcal{D}_{5/2}, \mathcal{D}_1)$	3/6	2/6	1/6	3/5	2/5	0
$(\mathcal{D}_{5/2}, \mathcal{D}_0)$	0	1	0	3/5	2/5	0
$(\mathcal{D}_{3/2}, \mathcal{D}_1)$	1/4	2/4	1/4	3/20	12/20	5/20
$(\mathcal{D}_{3/2}, \mathcal{D}_0)$	0	1/2	1/2	3/20	12/20	5/20
$(\mathcal{D}_{1/2}, \mathcal{D}_1)$	1/10	6/10	3/10	0	2/5	3/5
$(\mathcal{D}_{1/2}, \mathcal{D}_0)$	0	1/5	4/5	0	2/5	3/5

Table 5.7: Fractional H_5^+ spin product outcomes of the $H_5^+ + H_2$ reaction.

5.3 High Temperature Model

At sufficiently high temperature, the NSSWs calculated in the previous section can be exploited to determine the outcome of a large number of $H_3^+ + H_2$ collisions. In this section, we derive a model for the resultant p-H_3^+ fraction (p_3) at steady state in a plasma of a certain p-H_2 fraction (p_2), considering only two-body H_3^+-H_2 collisions. We then derive a model that takes into account the possibility of three-body collisions.

5.3.1 Two-Body High Temperature Model

In a laboratory plasma consisting only of hydrogen, the chemistry occurring is relatively simple compared to other plasmas. H_2 is ionized by electron impact to give predominantly H_2^+. H_2^+ is destroyed very rapidly by the reaction $H_2^+ + H_2 \rightarrow H_3^+ + H$, causing H_3^+ to typically be the dominant ion in the plasma. [99, 100] H_3^+ can undergo proton scrambling reactions with H_2, and can form larger H_{2n+1}^+ clusters through three-body reactions. H_3^+ and larger clusters are all destroyed either by further cluster formation, dissociative recombination, or ambipolar diffusion. Finally, hydrogen atoms can recombine in a three-body process to re-form H_2.

To study the $H_3^+ + H_2$ reaction, it is desirable to isolate the process as much as possible, which can be accomplished by tuning plasma conditions. If the *ortho*:*para* ratio of H_3^+ is established primarily by this reaction, as opposed to any other nuclear-spin-dependent processes, then the nuclear spin dependence can be directly inferred. Because H_3^+ formation [69] and destruction via dissociative recombination with electrons [28, 80, 87] exhibit spin dependence, the $H_3^+ + H_2$ reaction can control the *ortho*:*para* ratio of H_3^+ only if H_3^+ undergoes many collisions with H_2 prior to its destruction.

However, a more subtle effect is the H atom recombination to form H_2. The *ortho*:*para* ratio of H_2 in the plasma is equally as important as that of H_3^+. For instance, in a plasma of pure p-H_2 at room temperature, the H atom recombination on the walls of the containment vessel will produce normal-H_2 (n-H_2: 25% p-H_2, 75% o-H_2). Over time, this will cause a reduction in the p-H_2 fraction. This effect is in addition to the

change in p-H_2 fraction caused by the $H_3^+ + H_2$ reaction itself. An additional constraint, therefore, is that the plasma should be pulsed, and measurements taken as soon as possible after steady state is reached to avoid changes in the p-H_2 fraction. These conditions could be met in a pulsed hollow cathode discharge, or alternatively by storing H_3^+ in a radiofrequency ion trap with H_2 as a buffer gas.

Provided sufficient H_3^+-H_2 collisions occur, the *ortho*:*para* H_3^+ ratio can be modeled using the nuclear spin branching fractions from Table 5.2. To begin, we model $\mathrm{d}/\mathrm{d}t([p\text{-}H_3^+])$ in terms of the hop and exchange reactions involving all combinations of o-H_3^+, p-H_3^+, o-H_2, and p-H_2 (square brackets, such as $[p\text{-}H_3^+]$, denote number densities):

$$\begin{aligned}\frac{\mathrm{d}[p\text{-}H_3^+]}{\mathrm{d}t} &= \Big\{k^H\Big(\frac{1}{3}[o\text{-}H_2] + 1[p\text{-}H_2]\Big) + k^E\Big(\frac{1}{3}[o\text{-}H_2] + \frac{1}{3}[p\text{-}H_2]\Big)\Big\}[o\text{-}H_3^+] \\ &\quad -\Big\{k^H\Big(\frac{2}{3}[o\text{-}H_2] + 0[p\text{-}H_2]\Big) + k^E\Big(\frac{1}{3}[o\text{-}H_2] + \frac{1}{3}[p\text{-}H_2]\Big)\Big\}[p\text{-}H_3^+], \qquad (5.16)\end{aligned}$$

where k^H and k^E are the rates of the proton hop and hydrogen exchange reactions. The choice of using $\mathrm{d}/\mathrm{d}t([p\text{-}H_3^+])$ is arbitrary; the final result is the same if $\mathrm{d}/\mathrm{d}t([o\text{-}H_3^+])$ is used instead as a starting point. Invoking the steady state approximation, this equation is equal to 0.

Rather than working with absolute number densities, it is more convenient to work with spin state fractions. Because $[p\text{-}H_3^+] + [o\text{-}H_3^+] = [H_3^+]$ (and likewise for $[H_2]$), the number densities of the spin states can be expressed by a single parameter; in this case we choose the *para*-fractions $p_3 \equiv [p\text{-}H_3^+]/[H_3^+]$ and $p_2 \equiv [p\text{-}H_2]/[H_2]$. Dividing the equation by the product $[H_3^+][H_2]$ gives

$$\begin{aligned}0 &= \Big\{k^H\Big(\frac{1}{3}(1-p_2) + p_2\Big) + k^E\Big(\frac{1}{3}(1-p_2) + \frac{1}{3}p_2\Big)\Big\}(1-p_3) \\ &\quad -\Big\{k^H\Big(\frac{2}{3}(1-p_2)\Big) + k^E\Big(\frac{1}{3}(1-p_2) + \frac{1}{3}p_2\Big)\Big\}p_3.\end{aligned}$$

This can be solved for p_3 and simplified:

$$p_3 = \frac{k^H(\frac{1}{3} + \frac{2}{3}p_2) + \frac{1}{3}k^E}{k^H + \frac{2}{3}k^E}.$$

The quantity $k^E/3$ can be factored from both the numerator and denominator. Defining $\alpha \equiv k^H/k^E = S^{hop}/S^{exch}$ gives the final result:

$$p_3 = \frac{\alpha + 2\alpha p_2 + 1}{3\alpha + 2}. \qquad (5.17)$$

Equation 5.17 is a remarkably simple expression that allows for an experimental determination of the hop-to-exchange ratio α by measuring p_3 in a plasma of known p_2. As seen in Figure 5.1, this model suggests

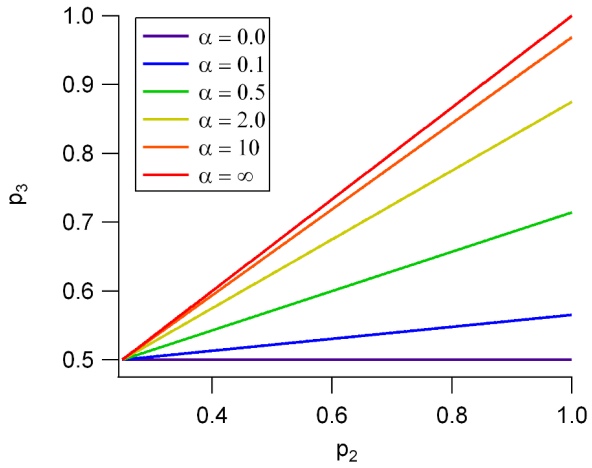

Figure 5.1: The two-body high temperature model (Equation 5.17) for values of α ranging from 0 (purple, horizontal) to ∞ (red, steepest slope).

that the relationship between p_3 and p_2 is linear, and that the slope should be related to α. It also suggests that no matter the value of α, a n-H_2 plasma ($p_2 = 0.25$) should produce n-H_3^+ (50% o-H_3^+, 50% p-H_3^+). The most sensitive probe of α would be an experiment performed with pure p-H_2. This has been done by Cordonnier *et al.* [74], who found that in a ~400 K p-H_2 pulsed hollow cathode plasma, p_3 was 0.89 or 0.91, depending on which spectroscopic transitions were observed. Using Equation 5.17, these give $\alpha = 2.4$ or 3.0, respectively, which are the same values they derived using a complex kinetic model including H_3^+ formation, dissociative recombination, and ambipolar diffusion. This gives some validation to the assumptions that went into the derivation of our simplified model.

An important question to consider is the timescale on which steady state is reached. Dividing Equation 5.16 by $[H_3^+]$ and integrating gives

$$p_3(t) = p_{3,\infty} - (p_{3,\infty} - p_{3,o}) \exp\left\{(k^H + \frac{2}{3}k^E)[H_2]t\right\},$$

where $p_{3,\infty}$ and $p_{3,o}$ are the values of p_3 at $t = \infty$ and $t = 0$, respectively. The argument in the exponential is an expression nearly equal to the reactive collision rate of H_3^+ and H_2. After a few reactive collisions, p_3 should already be at its steady state value.

This model is valid only if p_2 is constant, which is the case if H_2 has an independent means of thermalizing its spin temperature at a constant value, or at early stages of a cw discharge before H atom recombination and proton scrambling can lead to significant changes in p_2. In a cw p-H_2 plasma at room temperature, this model can still be applied, but p_2 will have to be replaced by a function $p_2(t)$ to include the long-term time dependence of p_2. There may be cases in which the $H_3^+ + H_2$ reaction is the only means by which the spin

of H_2 can be converted; in these cases it is possible to set up a pair of coupled differential equations that will give the steady state values of p_3 and p_2, but such a model is beyond the scope of this paper.

5.3.2 Three-Body High Temperature Model

The model derived in the previous section ignores the possibility of any three-body processes occurring in the plasma. This assumption is valid so long as the pressure is sufficiently low, or if three-body reactions do not exhibit any appreciable nuclear spin dependence on H_3^+. If these conditions are not met, then values of α derived from interpretations of laboratory data based on the two-body model may be inaccurate. Through more detailed modeling, it may be possible to detect and disentangle any three-body processes from the underlying two-body process. There are two three-body reactions to consider: H_5^+ formation via $H_3^+ + 2H_2 \rightarrow H_5^+ + H_2$, and proton scrambling through a $(H_7^+)^*$ collision complex via $H_3^+ + 2H_2 \rightarrow (H_5^+)^* + H_2 \rightarrow (H_7^+)^* \rightarrow H_3^+ + 2H_2$.

The H_5^+ formation reaction has been studied by Paul *et al.* [101] by introducing H_3^+ into a 10 K radiofrequency ion trap surrounded by a bath of H_2 with a known p-H_2 fraction. They observed that H_5^+ formation was much more rapid when p-H_2 was used instead of n-H_2. However, they did not investigate whether there was a dependence on the p-H_3^+ fraction; their experiments were performed with n-H_3^+. It is unknown whether the different nuclear spin configurations of the $(H_5^+)^*$ collision complex have different lifetimes (which would imply a dependence on the H_3^+ nuclear spin configuration), or if a subsequent collision with p-H_2 can more effectively stabilize the complex compared with an o-H_2 collision. It is also unclear whether this same effect would occur at higher temperatures, as these ternary association reactions become much slower. Because of this uncertainty, we assume that the rate of H_5^+ formation is independent of the spin configuration of H_3^+, and that the $(H_5^+)^*$ lifetime is independent of its spin configuration.

We instead treat the second of those processes: proton scrambling through $(H_7^+)^*$. A full treatment of this process is difficult, but we make the assumption that a given $(H_5^+)^*$ collision complex will undergo at most one reactive collision with H_2 during its lifetime, and this allows us to use the nuclear spin branching fractions in a similar manner as in the two-body case. The relevant reactions and their rates are listed in Table 5.8.

In order to use the nuclear spin branching fractions, the fraction of the $(H_5^+)^*$ complexes that undergo an additional collision with H_2 must be taken into account. First, it is important to note that any "identity" reaction is indistinguishable from a nonreactive collision. Because the two-body and three-body reaction channels may have different identity branching fractions (and different overall rates), we redefine all rates in terms of the rates of reactive collisions: those that result in a hop or exchange process. We will employ

Reaction	Rate
$H_3^+ + H_2 \rightarrow (H_5^+)^*$	$k_{3,2}^L[H_3^+][H_2]$
$(H_5^+)^* \rightarrow H_3^+ + H_2$	$k_5^u[(H_5^+)^*]$
$(H_5^+)^* + H_2 \rightarrow (H_7^+)^*$	$k_{5,2}^L[(H_5^+)^*][H_2]$
$(H_7^+)^* \rightarrow H_3^+ + 2H_2$	$k_7^u[(H_7^+)^*]$

Table 5.8: Reactions and rates used in the three-body high temperature model. The nuclear spin dependence of each reaction is not listed explicitly here. The final reaction is written so as to only allow for $(H_5^+)^*$ to undergo at most one collision with H_2. The superscript L refers to a Langevin rate coefficient, and the superscript u refers to a unimolecular dissociation rate coefficient.

subscripts 2 and 3 to refer to two-body ($H_3^+ + H_2$) and three-body [$(H_5^+)^* + H_2$] branching fractions, respectively:

$$
\begin{aligned}
&S_n^{id} + S_n^{hop} + S_n^{exch} = 1 (n = 2, 3), \\
&k_{3,2}^R = k_{3,2}^L (1 - S_2^{id}), \\
&k_{5,2}^R = k_{5,2}^L (1 - S_3^{id}), \\
&\alpha_n = \frac{S_n^{hop}}{S_n^{exch}} = \frac{\Sigma_n^H}{\Sigma_n^E}, \text{ and} \\
&\Sigma_n^H + \Sigma_n^E = 1.
\end{aligned}
$$

The coefficients k^R are the reactive rate coefficients; those with the identity reactions removed. We then define branching fractions Σ_n^M to refer to the branching fractions of only the reactive collisions. The ratio Σ_n^H / Σ_n^E is equal to S_n^{hop} / S_n^{exch}, so the change in how the overall rate coefficients is defined does not affect the ratio of the hop and exchange rates.

The utility of these redefinitions is that the branching fraction between two-body and three-body processes can now be expressed in terms of a single parameter. Once $(H_5^+)^*$ is formed, the fractions Φ_2 and Φ_3 for the two channels are:

$$
\begin{aligned}
&\Phi_2 = \frac{k_5^u}{k_5^u + k_{5,2}^R[H_2]}, \\
&\Phi_3 = \frac{k_{5,2}^R[H_2]}{k_5^u + k_{5,2}^R[H_2]}, \text{ and consequently} \\
&\Phi_2 + \Phi_3 = 1.
\end{aligned}
$$

As expected, these show that with increasing $[H_2]$, three-body processes become important, and that the density at which this happens depends on the lifetime of $(H_5^+)^*$ prior to unimolecular dissociation compared to the magnitude of $k_{5,2}^R[H_2]$.

(H_3^+,H_2)	$\mathcal{D}_{5/2}$	$\mathcal{D}_{3/2}$	$\mathcal{D}_{1/2}$
(o-H_3^+,o-H_2)	3/6	2/6	1/6
(o-H_3^+,p-H_2)	0	1	0
(p-H_3^+,o-H_2)	0	2/3	1/3
(p-H_3^+,p-H_2)	0	0	1

Table 5.9: Branching fractions for the spin configuration of $(H_5^+)^*$ formed in collisions of H_3^+ and H_2.

The final step before writing down steady state reaction rates is to calculate the final branching fractions for o-H_3^+ and p-H_3^+ through the three-body process. In Section 5.2.2, the branching fractions for reactant and product H_5^+ were derived. These must be combined with the branching fractions for the formation of nuclear spin states of $(H_5^+)^*$ through the $H_3^+ + H_2$ collision, as well as the branching fractions for formation of o-H_3^+ and p-H_3^+ resulting from the breakup of nuclear spin states of $(H_5^+)^*$. Using the angular momentum algebra of Oka, [69] this is straightforward.

For the formation of $(H_5^+)^*$, the branching fractions are obtained from the statistical weights of the angular momentum representations resulting from H_3^+ and H_2. We show them as coefficients for emphasis:

$$\begin{aligned}
\mathcal{D}_{3/2} \otimes \mathcal{D}_1 &\rightarrow 6(\mathcal{D}_{5/2}/6) \oplus 4(\mathcal{D}_{3/2}/4) \oplus 2(\mathcal{D}_{1/2}/2), \\
\mathcal{D}_{3/2} \otimes \mathcal{D}_0 &\rightarrow 4(\mathcal{D}_{3/2}/4), \\
2\mathcal{D}_{1/2} \otimes \mathcal{D}_1 &\rightarrow 8(\mathcal{D}_{3/2}/4) \oplus 4(\mathcal{D}_{1/2}/2), \text{ and} \\
2\mathcal{D}_{1/2} \otimes \mathcal{D}_0 &\rightarrow 4(\mathcal{D}_{1/2}/2).
\end{aligned}$$

For the destruction of $(H_5^+)^*$, the statistical weights are

$$\begin{aligned}
\mathcal{D}_{5/2} &\rightarrow 6(\mathcal{D}_{3/2} \otimes \mathcal{D}_1/12), \\
4\mathcal{D}_{3/2} &\rightarrow 4(\mathcal{D}_{3/2} \otimes \mathcal{D}_1/12) \oplus 4(\mathcal{D}_{3/2} \otimes \mathcal{D}_0/4) \\
&\quad \oplus 8(\mathcal{D}_{1/2} \otimes \mathcal{D}_1/6), \text{ and} \\
5\mathcal{D}_{1/2} &\rightarrow 2(\mathcal{D}_{3/2} \otimes \mathcal{D}_1/12) \oplus 4(\mathcal{D}_{1/2} \otimes \mathcal{D}_1/6) \\
&\quad \oplus 4(\mathcal{D}_{1/2} \otimes \mathcal{D}_0/2).
\end{aligned}$$

Keeping in mind that the spin configuration of the product H_2 is unimportant for a pulsed laboratory plasma, the branching fractions for the H_3^+ spin configurations can be obtained. These are listed explicitly in Tables 5.9 and 5.10. To obtain the overall o-H_3^+ and p-H_3^+ branching fractions for a the $H_3^+ + 2H_2$ process, Tables 5.9, 5.7, and 5.10 can be carefully treated with matrix multiplication. The results are listed in Table 5.11.

$(H_5^+)^*$	o-H_3^+	p-H_3^+
$\mathcal{D}_{5/2}$	1	0
$4\mathcal{D}_{3/2}$	1/2	1/2
$5\mathcal{D}_{1/2}$	1/5	4/5

Table 5.10: Branching fractions for the spin configuration of H_3^+ formed upon dissociation of $(H_5^+)^*$.

Reactants	Hop		Exchange	
(H_3^+,H_2,H_2')	o-H_3^+	p-H_3^+	o-H_3^+	p-H_3^+
(o-H_3^+,o-H_2,o-H_2')	61/100	39/100	31/50	39/50
(o-H_3^+,o-H_2,p-H_2')	41/100	59/100	31/50	31/50
(o-H_3^+,p-H_2,o-H_2')	11/20	9/20	1/2	1/2
(o-H_3^+,p-H_2,p-H_2')	7/20	13/20	1/2	1/2
(p-H_3^+,o-H_2,o-H_2')	13/25	12/25	11/25	14/25
(p-H_3^+,o-H_2,p-H_2')	8/25	17/25	11/25	14/25
(p-H_3^+,p-H_2,o-H_2')	23/50	27/50	8/25	17/25
(p-H_3^+,p-H_2,p-H_2')	13/50	37/50	8/25	17/25

Table 5.11: Mechanism-specific nuclear spin branching fractions for H_3^+ resulting from the three-body reaction $H_3^+ + 2H_2$. Reactant H_2' is the H_2 that collides with $(H_5^+)^*$.

Having calculated these branching fractions, it is now possible to write the equation for $\mathrm{d}/\mathrm{d}t([p\text{-}H_3^+])$.

$$\begin{aligned}
0 = \frac{\mathrm{d}[p\text{-}H_3^+]}{\mathrm{d}t} \quad = \quad & \Phi_2 \left(\left\{ \Sigma_2^H \left[\frac{1}{3}(1-p_2) + p_2 \right] + \Sigma_2^E \left[\frac{1}{3}(1-p_2) + \frac{1}{3}p_2 \right] \right\} (1-p_3) \right. \\
& \left. - \left\{ \Sigma_2^H \frac{2}{3}(1-p_2) + \Sigma_2^E \left[\frac{1}{3}(1-p_2) + \frac{1}{3}p_2 \right] \right\} p_3 \right) \\
& + \Phi_3 \left(\left\{ \Sigma_3^H \left[\frac{39}{100}(1-p_2)^2 + \frac{9}{20}p_2(1-p_2) + \frac{59}{100}(1-p_2)p_2 + \frac{13}{20}p_2^2 \right] \right. \right. \\
& \left. \left. + \Sigma_3^E \left[\frac{19}{50}(1-p_2)^2 + \frac{1}{2}p_2(1-p_2) + \frac{19}{50}(1-p_2)p_2 + \frac{1}{2}p_2^2 \right] \right\} (1-p_3) \right. \\
& \left. - \left\{ \Sigma_3^H \left[\frac{13}{25}(1-p_2)^2 + \frac{23}{50}p_2(1-p_2) + \frac{8}{25}(1-p_2)p_2 + \frac{13}{50}p_2^2 \right] \right. \right. \\
& \left. \left. + \Sigma_3^E \left[\frac{11}{25}(1-p_2)^2 + \frac{8}{25}p_2(1-p_2) + \frac{11}{25}(1-p_2)p_2 + \frac{8}{25}p_2^2 \right] \right\} p_3 \right)
\end{aligned} \tag{5.18}$$

Equation 5.18 shows the result, having applied the steady state approximation and divided by the product $[H_3^+][H_2]$, as was done in the derivation of the two-body model. Making the substitutions $\Phi_3 = 1 - \Phi_2$, $\Sigma_n^H = \alpha_n/(1+\alpha_n)$, and $\Sigma_n^E = 1/(1+\alpha_n)$, solving for p_3, and simplifying leads to Equation 5.19, the high temperature three-body model.

$$p_3 = \frac{\frac{\Phi_2}{1+\alpha_2}\left(\frac{1}{3}\alpha_2 + \frac{2}{3}\alpha_2 p_2 + \frac{1}{3}\right) + \frac{1-\Phi_2}{1+\alpha_3}\left(\frac{39}{100}\alpha_3 + \frac{13}{50}\alpha_3 p_2 + \frac{19}{50} + \frac{3}{25}p_2\right)}{\frac{\Phi_2}{1+\alpha_2}\left(\alpha_2 + \frac{2}{3}\right) + \frac{1-\Phi_2}{1+\alpha_3}\left(\frac{91}{100}\alpha_3 + \frac{41}{50}\right)} \tag{5.19}$$

The results of the model are plotted in Figure 5.2. As evident in Equation 5.19, when $\Phi_2 = 1$, the

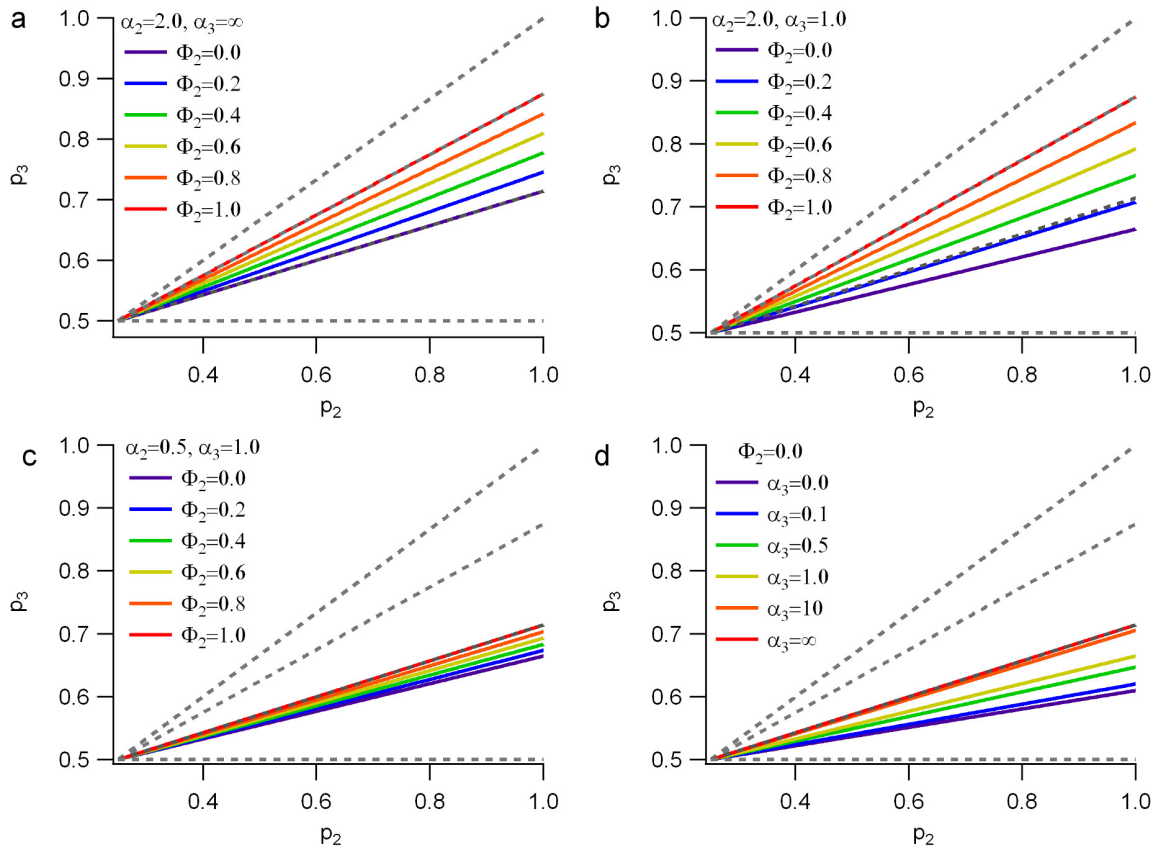

Figure 5.2: The three-body high temperature model (Equation 5.19) for various values of Φ_2, α_2, and α_3. For reference, the gray dotted lines are the two-body high temperature model (Equation 5.17) for $\alpha = \{0, 0.5, 2.0, \infty\}$ from shallowest to steepest slope.

three-body terms drop out of the equation and the two-body high temperature model (Equation 5.17) is obtained. This can be seen visually in panels a, b, and c of the figure as the red lines depicting $\Phi_2 = 1$ overlap with the corresponding α_2 value in the two-body model. When $\Phi_2 = 0$, the three-body process exclusively determines p_3, and this is shown in panel d for various values of α_3. When $\alpha_3 = \infty$, the results are identical to the two-body model with $\alpha_2 = 0.5$, and as α_3 decreases, the slope becomes more shallow. Panels a and b show the effects of an increasing effect of three-body reactions where $\alpha_2 = 2.0$, which is close to the value reported by Cordonnier and coworkers. [74] Three-body collisions effectively decrease the slope of the p_3 vs p_2 plot compared to the two-body model with the same α_2. If proton scrambling through the $(H_7^+)^*$ complex is influencing experimental measurements, a fit of the data to the two-body model would provide a lower limit on the value of α_2. Measurement at multiple pressures, however, would eliminate this ambiguity, because if three-body collisions are important, the slope should decrease with increasing pressure (and therefore decreasing Φ_2). Finally, Figure 5.2c shows the effect of decreasing Φ_2 if both hop/exchange ratios are at their statistical values ($\alpha_2 = 0.5$ and $\alpha_3 = 1.0$).

It is important to keep in mind that this model is constrained to allow only one three-body scrambling reaction to occur. Therefore, as Φ_2 decreases, the realism of this model might also decrease, as it could be possible for $(H_5^+)^*$ to experience multiple collisions with H_2 prior to dissociation. Also, this model does not treat nuclear spin dependence of the ternary association reaction $H_3^+ + 2H_2 \rightarrow H_5^+ + H_2$, which may have different rates for o-H_3^+ and p-H_3^+. The purpose of the model is to give a sense of what the experimental data may look like if three-body nuclear-spin-dependent processes begin to compete with the $H_3^+ + H_2$ nuclear spin dependence, not to serve as an accurate model for determining the full kinetics of the system.

5.4 Low Temperature Model

At lower temperatures, the assumption that many states are energetically accessible and populated breaks down, and the NSSWs cannot be used to determine the outcomes of many $H_3^+ + H_2$ reactions. [102] It is possible to account for the interplay of nuclear spin selection rules and energetic restrictions by employing a microcanonical statistical approach. Park and Light [77] have developed a microcanonical statistical model for the $H_3^+ + H_2$ system that conserves energy, angular momentum (both motional and nuclear spin), and parity, and also allows for incomplete proton scrambling. The output of their model gives rate coefficients k_{ijkl}, where the subscripts denote the nuclear spin configurations of the reactants and products: i-$H_3^+ + j$-$H_2 \rightarrow k$-$H_3^+ + l$-H_2. The rate coefficients depend on the reactants' total energy (based on their kinetic temperature T_{kin} and rotational temperature T_{rot}), as well as the branching fractions S^{id}, S^{hop}, and S^{exch}.

Because the rate coefficients themselves are not broken into identity, hop, and exchange components, another model must be derived. The derivation has been presented in detail elsewhere, [97] but will be summarized here. As with the high temperature models, we assume that the nuclear spin configuration is determined entirely by the $H_3^+ + H_2$ reaction, and ignore formation and destruction of H_3^+. We also ignore three-body processes, and invoke the steady state approximation:

$$\begin{aligned} 0 = \frac{\mathrm{d}[p\text{-}H_3^+]}{\mathrm{d}t} &= \Big\{(k_{oopo} + k_{oopp})\,[o\text{-}H_2] + (k_{oppo} + k_{oppp})\,[p\text{-}H_2]\Big\}[o\text{-}H_3^+] \\ &\quad -\Big\{(k_{pooo} + k_{poop})\,[o\text{-}H_2] + (k_{ppoo} + k_{ppop})\,[p\text{-}H_2]\Big\}[p\text{-}H_3^+]. \end{aligned}$$

From the nuclear spin selection rules, k_{oppp} and k_{ppop} are rigorously 0 (see Table 5.1). Dividing through by $[H_3^+][H_2]$ and solving for p_3 gives the final result:

$$p_3 = \frac{(k_{oopp} + k_{oopo})(1 - p_2) + k_{oppo}p_2}{(k_{oopp} + k_{oopo} + k_{poop} + k_{pooo})(1 - p_2) + (k_{oppo} + k_{ppoo})p_2}. \tag{5.20}$$

Equation 5.20 is the low temperature model, and it converges to equation 5.17 in the limit that $(k_{oopp} + k_{oopo}) = (k^H + k^E)/3$, $k_{oppo} = k^H + k^E/3$, and so on. This model can be more directly used with the low-temperature (10-160 K) rate coefficients k_{ijkl} calculated by the microcanonical statistical model of Park and Light. [77] This model has been previously applied to the conditions of diffuse molecular clouds in the interstellar medium, and it should be noted that although equation 5.20 is the same as that in [97], the conditions of a pulsed laboratory plasma are quite different than those in the diffuse molecular clouds. In the latter, the density is so low that the collision timescale (months) is longer than the spontaneous emission timescale (days) for most H_3^+ rotational levels. As a result, essentially all of the H_3^+ population lies in the lowest *ortho* and *para* rotational levels, and consequently the authors calculated rate coefficients at a "nonthermal" rotational temperature of 10 K, and kinetic temperatures from 10-160 K. In the laboratory, the collision rate is many orders of magnitude faster than the spontaneous emission rate, and "thermal" rotational temperatures are appropriate.

Results from the low temperature model are plotted in Figure 5.3. In general, the model shows that the p_3 vs p_2 traces are curved upwards; the curvature is greater at lower temperatures. As the temperature increases (panels a, b, c, and d; the blue shaded region), the results approach the high temperature model line for the same α. In panels a and b, $\alpha = 0.5$ and $S^{id} = 0.1$ and 0.9, respectively, and as T approaches 160 K, the curves approach the high temperature model $\alpha = 0.5$ line, especially at higher S^{id}, though it is interesting to note that p_3 is still expected to be less than 0.5 in a n-H_2 plasma. Panels c and d show the same effect for $\alpha = 2.0$. The implications of a nonthermal plasma ($T_{kin} \neq T_{rot}$) are shown in panels c and f

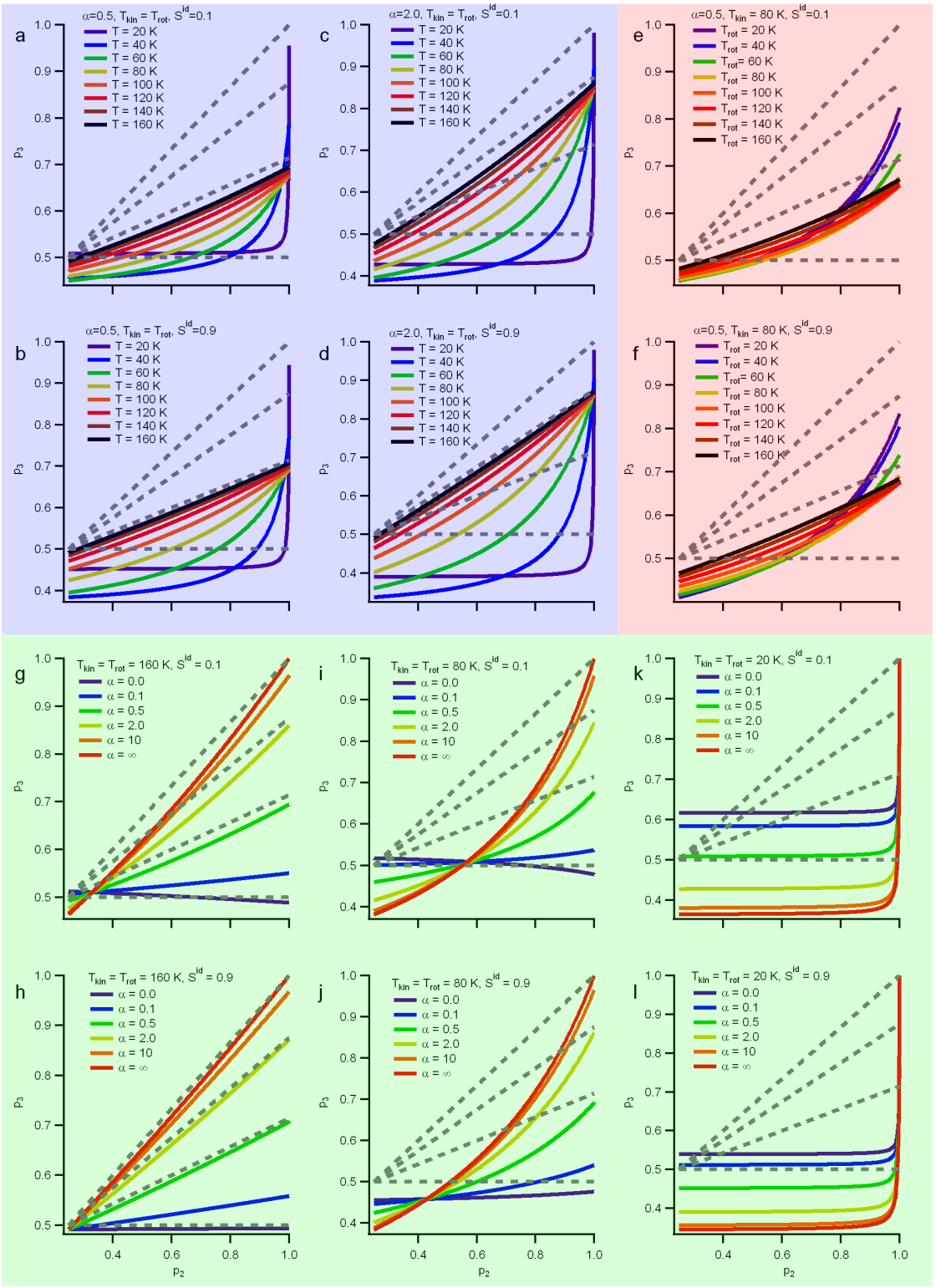

Figure 5.3: Low temperature model (Equation 5.20) results for a variety of temperatures and branching fractions. The gray dotted lines are the two-body high temperature model (Equation 5.17) for $\alpha = \{0, 0.5, 2.0, \infty\}$ from shallowest to steepest slope.

(the red shaded region; the effect is a subtle change in the curvature, particularly towards larger p_2.

The p_3 vs p_2 traces from the low temperature model are strongly dependent on α, as shown in panels g-l (the green shaded region). Depending on the temperature, the curves could be very close to those of the high temperature model (panels g and h), or dramatically different (panels k and l). Of particular interest are the results at the lowest temperatures. Generally, the differences in the curves due to a large change in S^{id} are subtle. But as seen in the panels k and l, if α is known, then according to this model S^{id} can be determined by the exact value of p_3 across the range of p_2 where the curve is nearly flat.

The low temperature model is only as good as the rate coefficients that are used with it. The rate coefficients used in this work are calculated using the microcanonical statistical model of Park and Light, [77] which is not a quantum mechanical model. If quantum effects become important at low temperatures, then the rate coefficients calculated using a statistical model may not be accurate. However, microcanonical statistical calculations of rate coefficients in other isotopic analogs of the $H_3^+ + H_2$ system have been found to agree well with ion trap measurements at 10-20 K, [78] which provides some support for the use of these rate coefficients in the purely hydrogenic system at similar temperatures. Reactive scattering calculations on the H_5^+ potential energy surface [73] are desirable, but still unfeasible. At more moderate temperatures, it would be unlikely for quantum effects to be important, and it is therefore likely that this model should perform well.

Extension of this model to include three-body scrambling is not straightforward. An analogous microcanonical statistical study of the $H_5^+ + H_2$ reaction would have to be carried out, and the complex formation rates compared with the complex lifetimes to determine the two-body:three-body ratio. Also, the nuclear spin dependence of ternary association reactions would also likely have to be taken into account, as these reactions are much faster at low temperatures. Such work is beyond the scope of this paper, and so the low temperature model that we have derived should only be employed at densities low enough to preclude three-body reactions.

5.5 Conclusions

In this paper, we have derived a series of models aimed at extracting the nuclear spin dependence of the $H_3^+ + H_2$ reaction from laboratory data. The appropriate experiment is to measure the p-H_3^+ fraction (p_3) formed in laboratory plasmas of varying p-H_2 fraction (p_2) at steady state. An important condition for using these models is that p_3 must be determined exclusively by the $H_3^+ + H_2$ reaction, not by other nuclear spin dependent processes like electron dissociative recombination of H_3^+. Another important condition is that the

p-H_2 fraction is constant, or at the very least, slowly changing, as is the case in the early stages of a pulsed plasma or in a plasma in which the H_2 has an external means of thermalizing its spin.

The nuclear spin dependence of the $H_3^+ + H_2$ reaction is influenced heavily by nuclear spin selection rules that arise as a consequence of exchange symmetry, and can be expressed in terms of the hop-to-exchange ratio α. At sufficiently high temperatures, the nuclear spin selection rules are expected to entirely determine the reaction outcome, and a steady state chemical model incorporating the resultant mechanism-specific product spin branching fractions (Equation 5.17) indicates that α can be determined from the slope of a plot of p_3 vs p_2.

However, in a laboratory plasma, there exists the possibility that the H_2 number density is sufficiently high to allow for three-body collisions to occur, resulting in processes such as ternary association to form H_5^+ or three-body scrambling in the $(H_7^+)^*$ collision complex. In Section 5.2.2 we derived mechanism-specific product spin branching fractions for the $H_5^+ + H_2$ reaction in an analogous manner to the $H_3^+ + H_2$ reaction, using the "H_3^+ hop" and "hydrogen exchange" mechanisms. These branching fractions are incorporated into a steady state kinetic model with the two-body branching fractions (Equation 5.19), where the p_3 vs p_2 plot then depends on the hop-to-exchange ratios for the two-body (α_2) and three-body (α_3) processes, and the relative rates of two-body reactive collisions to three-body reactive collisions. The model makes the assumption that ternary association reactions do not have significant nuclear spin dependence, and that a given $(H_5^+)^*$ complex suffers at most one reactive collision with H_2 during its lifetime.

Finally, we have considered lower temperature plasmas in which there is insufficient energy for the nuclear spin product branching fractions to accurately represent the reaction outcomes. Using rate coefficients calculated with a microcanonical statistical approach, we have developed a low temperature model (Equation 5.20) that predicts the p_3 vs p_2 behavior of the plasma in terms of the identity branching fraction S^{id}, α, and the kinetic and rotational temperatures of the plasma. This model has not been extended to include three-body processes. Fully quantum reactive scattering calculations may be required to accurately represent the behavior of this reaction at the lowest temperatures. It is hoped that these models, together with the appropriate experimental measurements, will allow for determination of the nuclear spin dependence of this important fundamental reaction, and will aid in the use of H_3^+ as a probe of astrophysical conditions.

The authors thank Kisam Park for providing code for calculating the rate coefficients used in our modeling work. This work has been supported by NSF PHY 08-55633.

Chapter 6

Experimental Measurements of Nuclear Spin Effects in Hydrogenic Plasmas

6.1 Introduction

The most abundant element in our universe is hydrogen, and consequently it can be argued that the chemistry and physics of hydrogenic species are the most important on a universal scale. Moreover, as the simplest of the elements, hydrogen has often been used as the benchmark species for testing computational techniques in quantum mechanics. Even with the impressive body of work accumulated about hydrogen, some areas are still undergoing active study.

One such area is the chemical physics of ion-molecule reactions. Hydrogenic ion-molecule reactions are excellent candidates for comparison of theoretical methods with experimental results. The simplest of these, the reaction of H^+ with H_2, has been extensively studied (see Jambrina *et al.* [103] and references therein), as has the simplest bimolecular reaction, $H_2^+ + H_2$. [104, 105] In each of these cases, fully quantum reactive scattering calculations are still quite challenging, but statistical models and/or semiclassical calculations have been shown to agree reasonably well with experimental measurements.

The next member in this series is the simplest bimolecular reaction involving a polyatomic, $H_3^+ + H_2$. H_3^+ has long been known to be an important player in interstellar chemistry, helping to initiate the ion-molecule reactions responsible for forming polyatomic molecules in space, [1, 2] and is also a useful probe of astrophysical conditions. [22, 106, 107] The $H_3^+ + H_2$ reaction has important implications for its use as an interstellar temperature probe, [97] and its deuterated variants are among the most important reactions involved in deuterium fractionation in the interstellar medium. [108]

While the deuterated forms of the $H_3^+ + H_2$ reaction have been studied extensively in the laboratory, [75, 76, 78, 102] the purely hydrogenic system has not been as well-studied experimentally. When H_3^+ reacts

This chapter is adapted with permission from K. N. Crabtree, C. A. Kauffman, B. A. Tom, E. Beçka, B. A. McGuire, and B. J. McCall, Journal of Chemical Physics 134 (2011) 194311, Copyright 2011, American Institute of Physics.

with H_2, there are three possible outcomes:

$$\tilde{H}_3^+ + H_2 \rightarrow \tilde{H}_3^+ + H_2, \tag{6.1}$$

$$\tilde{H}_3^+ + H_2 \rightarrow H_2\tilde{H}^+ + \tilde{H}_2, \text{and} \tag{6.2}$$

$$\tilde{H}_3^+ + H_2 \rightarrow H\tilde{H}_2^+ + H\tilde{H}. \tag{6.3}$$

These are defined as the identity (6.1), proton hop (6.2), and hydrogen exchange (6.3) processes, with statistical weights 1, 3, and 6, respectively. Each is subject to nuclear spin selection rules, [69, 72] and consequently the ratio of their rates ($\alpha \equiv k^H/k^E$, where k^H and k^E are the hop and exchange rate coefficients, respectively) can be inferred by observing the *ortho*:*para* ratio of H_3^+ in hydrogenic plasmas of varying *ortho*:*para* H_2 ratio (more details will be given in Section 6.4). The lone experimental study of this reaction found $\alpha = 2.4 \pm 0.6$ in a $\sim$400 K hollow cathode plasma, [74] well above the statistical limit of $\alpha = 3/6 = 0.5$. This is roughly consistent with a study of the $D_3^+ + H_2$ system, [75] which found that α increased well above its statistical limit with increasing collision energy.

As a consequence of the dearth of experimental data available for this reaction, theoretical efforts have been limited. Full dimensional potential energy surfaces for H_5^+ are available, [73, 109] but no quasiclassical trajectory calculations have been published to our knowledge. The only efforts at calculating rate coefficients for these processes have been microcanonical statistical calculations. [77, 78] Experimental measurements of the $H_3^+ + H_2$ system, especially at low temperature, are necessary for validating these models and providing data against which future theoretical calculations can be judged.

The structure of this paper is as follows. Section 6.2 describes the experimental approach for our study of this reaction. Section 6.3 presents the experimental results. The data are analyzed and discussed within the context of the modeling work presented in the previous article in this issue [110] in Section 6.4, and conclusions/perspectives summarized in Section 6.5. Finally, throughout this paper *o*-H_2, *p*-H_2, *o*-H_3^+, and *p*-H_3^+ will be used to refer to *ortho*- and *para*-H_2 and H_3^+.

6.2 Experimental Details

The objective of this experiment is to spectroscopically measure transitions arising from several of the lowest-energy rotational levels of H_3^+ in a plasma of a known *ortho*:*para* H_2 ratio. Doing so allows determination of the *ortho*:*para* H_3^+ ratio, the plasma kinetic temperature, and the H_3^+ rotational temperature. The target transitions are within the H_3^+ ν_2 fundamental band, and are listed in Table 6.1. This experiment has three

Rotational Level (J,K)	Type	Energy (cm^{-1})	Transition	Frequency (cm^{-1})	$\|\mu\|^2$ (D^2)
(1,1)	*para*	64.121	$R(1,1)^u$	2726.219	0.0158
(1,0)	*ortho*	86.960	$R(1,0)$	2725.898	0.0259
(2,2)	*para*	169.295	$R(2,2)^l$	2762.070	0.0177
(2,1)	*para*	237.356	$R(2,1)^u$	2826.117	0.0182
(3,3)	*ortho*	315.342	$R(3,3)^l$	2829.922	0.0191
(3,2)	*para*	428.009	$R(3,2)^u$	2923.344	0.0143
(3,1)	*para*	494.753	$R(3,1)^u$	2928.317	0.0180
(3,0)	*ortho*	516.867	$R(3,0)$	2930.145	0.0191

Table 6.1: The rotational levels used in this work and their target transitions. Energies are relative to the forbidden $(J, K) = (0, 0)$ level. Energies and transition frequencies are taken from literature values. [19] Transition dipole moments are calculated from the Einstein A coefficients. [111]

main components: a p-H_2 production system, a hollow cathode plasma cell, and a mid-infrared spectrometer.

6.2.1 p-H_2 Production

Normal hydrogen gas (n-H_2, 25% p-H_2) is produced at a purity of 99.99999% by a hydrogen generator (Parker Balsten H2-1200). To produce $> 99.9\%$ p-H_2, the n-H_2 from the generator is passed over an Fe_2O_3 catalyst held at 15 K. Full details about this p-H_2 converter are given elsewhere. [112] Mixtures of 40%, 50%, 66%, and 83% p-H_2 are obtained by combining appropriate partial pressures of p-H_2 and n-H_2 in a 1 gallon cylinder, which is lined with Teflon to minimize back-conversion of p-H_2 to o-H_2. The uncertainties on the p-H_2 fractions for these mixtures are 1.0%, 1.1%, 1.2%, and 1.4%, respectively.

6.2.2 Hollow Cathode Cell

A hollow cathode cell based on the design of Amano [113] was used to produce pulsed hydrogenic plasmas, and is illustrated in Figure 6.1. The cathode consists of a 1.4 m long, 1.5 in. diameter cylindrical copper tube wrapped in 1/4 in. diameter copper tubing used for cooling the cathode, all encased in a 4 in. diameter glass tube. The water-cooled anode is situated in an extended glass tube above a 1 in. diameter hole located at the midpoint of the cathode. A pulsed electrical discharge is generated by applying a 200 μs, 1 kV pulse to the anode at $\sim$1 Hz while grounding the cathode. The current during the pulse is uniformly 1.25 A in nearly all cases, though subtle differences are observed under different cell temperature and pressure conditions (Figure 6.2).

At each end of the glass tube are stainless steel flanges with 1 in. apertures cut into the centers, sealed to the cell with silicone o-rings. Into these apertures, a glass section with tubing for sample introduction/evacuation is placed. The ends of these tubes are connected with Ultra-Torr fittings to metal pieces cut at Brewster's angle, and BaF_2 windows are epoxied to the ends. This allows a laser to pass unimpeded

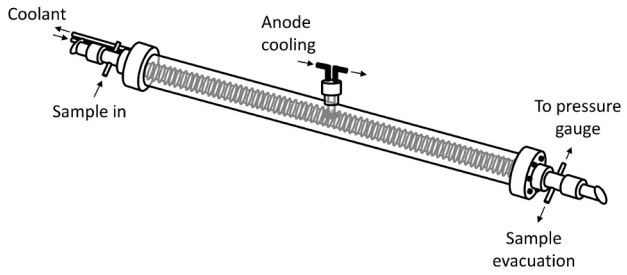

Figure 6.1: Schematic drawing of the hollow cathode cell used in this study.

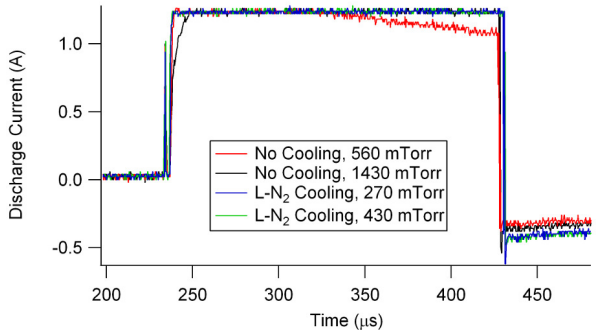

Figure 6.2: Current during the discharge pulse for the four main sets of conditions used in this study. The discharge is started at $t \sim 230$ μs, and is cut off at $t \sim 430$ μs. Details about the choice of conditions are discussed in Sections 6.3.2 and 6.3.3. The negative current after the discharge pulse is an artifact of the current monitor setup, which sees the pulser box recharging.

through the center of the hollow cathode. One of the two stainless steel flanges is connected to the inner coiled tubing to pass coolant into the vacuum cell. The cell is evacuated with a Welch pump (DuoSeal 1374, 10 L/s), and the cell pressure is monitored with a capacitance manometer.

6.2.3 Spectrometer

The plasma was probed by multipass direct absorption spectroscopy using a tunable difference frequency generation laser (DFG), which has been described previously. [114] The outputs of a 532 nm Nd:YVO_4 laser (Coherent Verdi V-10) and 622 nm tunable dye laser (Coherent 899-29, rhodamine 640 dye) are combined in a MgO-doped periodically-poled $LiNbO_3$ crystal, producing $\sim$500 μW of tunable radiation around 2800 cm^{-1}. The DFG light was sent through the hollow cathode in a White-type multipass configuration, collected with a dc InSb detector, and the resultant signal stored on a computer for analysis. The InSb signal was ratioed with the signal from a silicon photodiode monitoring the dye laser to remove pump laser amplitude noise.

6.2.4 Analysis Procedure

When a discharge pulse occurred, the InSb detector signal was recorded and split into two 750 μs intervals: a signal interval centered around the pulse, and a pretrigger interval for recording the background laser intensity. The latter interval was averaged over time, and the former binned and averaged into 150 5 μs intervals. Each of these was used to calculate a time-dependent absorbance signal: $-\ln(I/I_0)$, where I is the average laser intensity in the bin, and I_0 is the averaged background laser intensity. The binned absorbances were averaged over 10 consecutive discharge pulses, and the laser was then stepped by $\sim$0.002 cm^{-1}. This process was repeated until the absorption line was fully scanned, yielding a three-dimensional data set representing the spectrum as a function of time during the discharge pulse. Each transition was recorded three times for each set of conditions. A sample scan over a single transition is shown in Figure 6.3.

The spectrum at each point in time for each individual scan is then fit to a Gaussian function to determine the integrated intensity and linewidth as a function of time. For each transition, the integrated intensity and inferred kinetic temperature (as determined from the measured linewidth) over time are averaged over the three scans, and the standard deviation of each quantity used as an estimate of the uncertainty. The plasma kinetic temperature is inferred from the average of all scans, and the rotational temperature is inferred from the relative intensities of the $R(1,1)^u$ and $R(2,1)^u$ transitions (the reasons for this are explained in Section 6.3.1).

As will be seen in Section 6.4, it is most convenient to express the *ortho*:*para* ratio of H_3^+ in terms of the

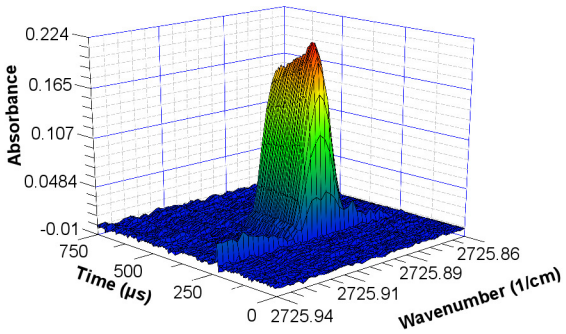

Figure 6.3: A sample scan of the $R(1,0)$ transition of H_3^+ in a n-H_2 plasma produced by a liquid-nitrogen-cooled hollow cathode. The plot has been slightly modified for clarity by eliminating artifacts at the beginning and end of the discharge pulse resulting from electrical pickup.

fraction of p-H_3^+(p_3). To calculate this quantity from the experimental data, we use the inferred rotational temperature to calculate separate Boltzmann distributions for the first 15 rotational levels of o-H_3^+ and p-H_3^+, using the forbidden (0,0) level energy as a common reference energy. The o-H_3^+ distribution is scaled to the population of the (1,0) level inferred from the $R(1,0)$ transition intensity, and likewise for p-H_3^+ with the (1,1) level population. For each subsequent level that was spectroscopically measured, the calculated population is replaced by the experimentally-determined population. Finally, p_3 is calculated by dividing the sum of all *para* level populations by the sum of all level populations. An example of the results of the final calculation is shown in Fig. 6.4.

6.3 Experimental Results

In this section, the results of a series of experimental measurements aimed at determining the value of α as a function of temperature are presented. First, we show measurements pertaining to the rotational thermalization of H_3^+ in the hollow cathode plasma. We then present parallel sections detailing measurements when the cell is uncooled, and when it is cooled with liquid nitrogen. Within each of these sections, measurements of the pressure dependence of the plasma chemistry and measurements of p_3 as a function of the p-H_2 fraction (p_2) at two different pressures are shown.

6.3.1 Thermalization Measurements

To assess the degree of thermalization of the rotational levels of H_3^+ formed in the plasma and to validate the calculation of p_3, all eight transitions listed in Table 6.1 were recorded in an uncooled p-H_2 plasma. A time slice of the data at 300 μs was taken and was subjected to a Boltzmann analysis, shown in Figure 6.5. The kinetic temperature for this data set was found to be 319 $\pm$ 33 K, in good agreement with the inferred

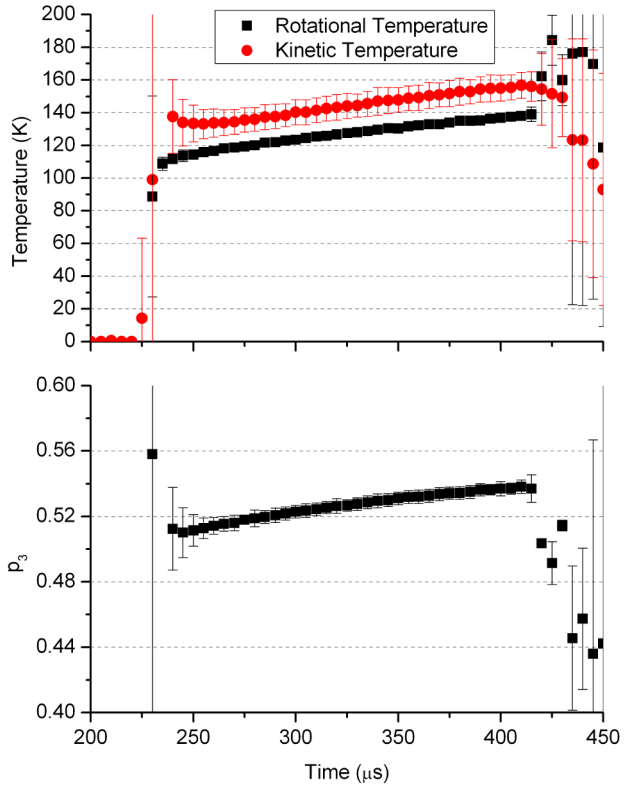

Figure 6.4: Kinetic and rotational temperatures and p-H_3^+ fraction (p_3) inferred from measurements of the $R(1,0)$, $R(1,1)^u$, $R(2,2)^l$, and $R(2,1)^u$ transitions of H_3^+ in a liquid-nitrogen-cooled hollow cathode plasma consisting of 50% p-H_2. The discharge is started at $t \sim 220$ μs and is cut off at $t \sim 410$ μs.

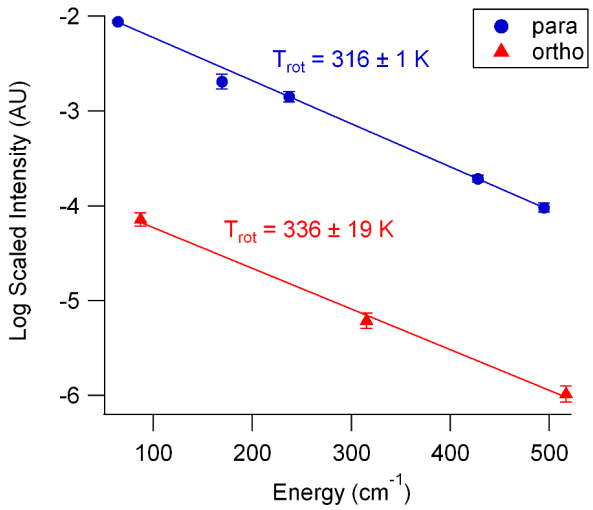

Figure 6.5: Boltzmann plot of the first eight transitions of H_3^+ formed in a p-H_2 plasma. The data are taken at $t = 300$ μs, about 70 μs after the start of the discharge pulse. Because of systematic underpopulation, the population of the (2,2) level is not taken into account for the rotational temperature calculation of p-H_3^+.

rotational temperatures for *ortho* (336 ± 19 K) and *para* (316 ± 1 K) H_3^+. A time slice taken at $t = 370$ μs gives similar results with slightly elevated temperatures: a kinetic temperature of 337 ± 29 K, o-H_3^+ rotational temperature of 339 ± 24 K, and p-H_3^+ temperature of 327 ± 1 K.

A noticeable feature in the plot is the underpopulation of the (2,2) level relative to all other *para* levels; this is a feature common to all data sets discussed in this work. Also, the o-H_3^+ rotational level distribution is thermal and consistent with the p-H_3^+ rotational temperature. Under liquid nitrogen conditions, only the $R(1,0)$ and $R(3,3)^l$ transitions of o-H_3^+ can be observed, and the signal-to-noise ratio of the $R(3,3)^l$ transition is low. Nevertheless, the o-H_3^+ rotational temperature, as inferred from the relative populations of the (1,0) and (3,3) levels, is consistent with the p-H_3^+ temperature. For these reasons, the relative populations of the (2,1) and (1,1) levels are used to calculate the rotational temperature of both o-H_3^+ and p-H_3^+ in the remainder of the data sets.

6.3.2 Uncooled Measurements

Pressure Dependence

As the goal of this work is to measure the hop:exchange ratio α in the reaction of H_3^+ with H_2, it is important to evaluate to what extent three-body collisions ($H_3^+ + 2H_2$) may influence the experimental measurements. As a first-order assessment, the intensity of the $R(1,0)$ transition was recorded as a function of cell pressure in a n-H_2 plasma. Because p_3, and temperature do not change greatly with changing pressure in a n-H_2 plasma (see Section 6.3.2), this measurement serves as a proxy for the H_3^+ number density in the cell.

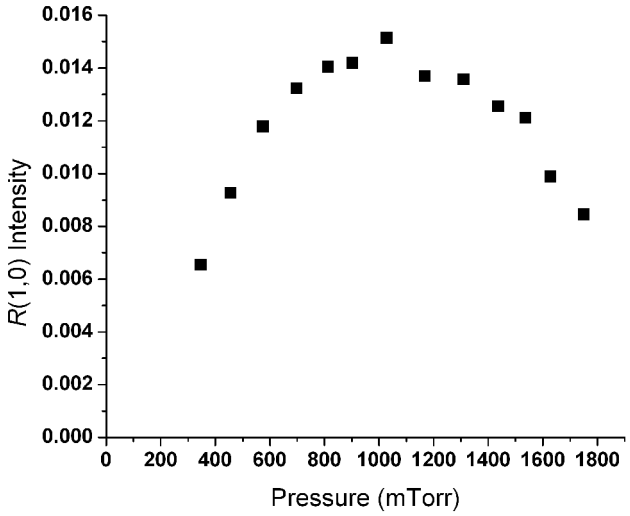

Figure 6.6: $R(1,0)$ integrated intensity as a function of cell pressure in an uncooled n-H_2 plasma. The plotted data are selected at $t = 300$ μs. No error bars are shown, as only one scan was performed at each pressure.

The measurements are shown in Figure 6.6. The $R(1,0)$ transition intensity initially increases with pressure, owing to the decreasing electron mobility (and therefore increasing charge density) with increasing cell pressure at constant electric current. However, at ∼1000 mTorr, the trend begins to reverse, and the transition intensity decreases. Because the electron mobility should decrease monotonically with increasing pressure, the total ion density (equal to the electron density) must still be increasing, and therefore H_3^+ must be consumed by a chemical process leading to the formation of another stable ion. While not absolutely conclusive, it is likely that the reaction $H_3^+ + 2H_2 \rightarrow H_5^+ + H_2$ is responsible, [101, 115] and this indicates that three-body effects may be present at some pressures.

In light of the pressure dependence observed in Fig. 6.6, measurements to determine the value of α are taken at two pressures. The lower pressure (560 mTorr) is chosen to be on the rising edge of the pressure curve, where it is likely that H_3^+ is the dominant ionic species in the plasma. The higher pressure (1430 mTorr) is chosen on the falling edge, where it is suspected that three-body collisions are occurring. A comparison of these data will assist in estimating the influence of three-body effects on the determination of α.

p-H_3^+ Fraction

The $R(1,1)^u$, $R(1,0)$, $R(2,2)^l$, and $R(2,1)^u$ transitions of H_3^+ were recorded to determine the value of p_3 in plasmas with known p_2. For n-H_2 ($p_2 = 0.25$), the hydrogen gas was used continuously from the hydrogen generator, and for $p_2 = 0.999$, gas was used continuously from the p-H_2 converter. All other mixtures were prepared in advance. Measurements at both pressures (560 mTorr and 1430 mTorr) were performed in

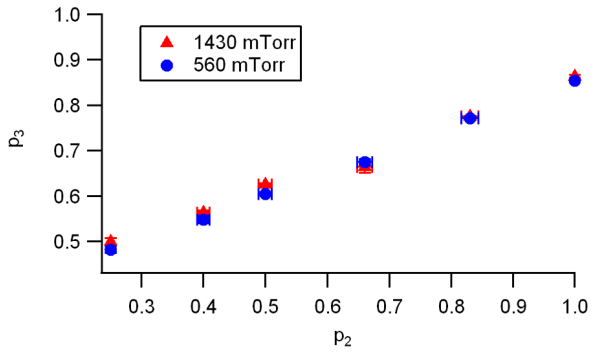

Figure 6.7: Experimental measurements of p-H_3^+ fraction plotted against p-H_2 fraction for an uncooled plasma at 560 and 1430 mTorr.

succession on the same day with the same gas mixture.

The observed transition intensities, inferred temperatures and p_3 values are presented in Table 6.2, and p_3 is plotted as a function of p_2 in Figure 6.7. Differences between the inferred values of p_3 between the two pressures are minor. The cell pressure does not seem to affect the p_3 vs p_2 distribution to any significant degree despite the pressure dependence seen in Figure 6.6.

The inferred temperatures are plotted in Figure 6.8. As mentioned in Section 6.2.4, the rotational temperatures reported in Table 6.2 are derived from the relative intensities of the $R(1,1)^u$ and $R(2,1)^u$ transitions. The quantity $T(2,2)$ in the plots is the inferred rotational temperature inferred from the $R(1,1)^u$ and $R(2,2)^l$ transitions, and it is consistently lower than the kinetic and rotational temperatures. This is due to the underpopulation of the (2,2) level alluded to in Figure 6.5. The variance weighted means of T_{kin}, T_{rot}, and $T(2,2)$ are (351 ± 10) K, (310 ± 8) K, and (187 ± 5) K respectively for the low pressure data, and (336 ± 8) K, (320 ± 6) K, and (259 ± 5) K for the data set at 1430 mTorr.

6.3.3 Liquid-Nitrogen-Cooled "Low Temperature" Measurements

Pressure Dependence

The same experiment described in Section 6.3.2 for the uncooled plasma was carried out in a liquid-nitrogen-cooled n-H_2 plasma. The results are qualitatively similar to the high-temperature data, albeit shifted toward lower pressures, and are plotted in Figure 6.9. The kinetic temperature was determined to be (128 ± 11) K for this data set. For the same purposes described earlier, a lower pressure of 270 mTorr and a higher pressure of 430 mTorr were chosen for the p_3 vs p_2 measurements.

Pressure (mTorr)	p_2	$R(1,1)^u$ cm^{-1}	$R(1,0)$ cm^{-1}	$R(2,2)^l$ cm^{-1}	$R(2,1)^u$ cm^{-1}	T_{kin} (K)	T_{rot} (K)	p_3
560	0.25	$4.92(46) \times 10^{-3}$	$1.52(4) \times 10^{-2}$	$5.11(21) \times 10^{-3}$	$4.79(24) \times 10^{-3}$	354(45)	367(57)	0.483(7)
	0.40	$7.87(65) \times 10^{-3}$	$1.73(8) \times 10^{-2}$	$5.69(39) \times 10^{-3}$	$6.11(47) \times 10^{-3}$	362(44)	275(34)	0.548(8)
	0.50	$4.73(16) \times 10^{-3}$	$9.22(35) \times 10^{-3}$	$5.86(28) \times 10^{-3}$	$4.45(3) \times 10^{-3}$	343(14)	349(17)	0.605(4)
	0.66	$9.79(40) \times 10^{-3}$	$1.30(7) \times 10^{-2}$	$8.52(28) \times 10^{-3}$	$7.44(71) \times 10^{-3}$	359(25)	269(30)	0.676(7)
	0.83	$6.46(18) \times 10^{-3}$	$5.41(41) \times 10^{-3}$	$6.18(13) \times 10^{-3}$	$5.67(7) \times 10^{-3}$	358(25)	318(12)	0.772(1)
	0.999	$9.93(20) \times 10^{-3}$	$4.58(27) \times 10^{-3}$	$7.73(18) \times 10^{-3}$	$7.91(32) \times 10^{-3}$	359(27)	283(15)	0.855(2)
1430	0.25	$5.18(55) \times 10^{-3}$	$1.47(5) \times 10^{-2}$	$5.13(46) \times 10^{-3}$	$4.11(16) \times 10^{-3}$	346(33)	282(36)	0.501(7)
	0.40	$7.08(48) \times 10^{-3}$	$1.51(13) \times 10^{-2}$	$6.17(28) \times 10^{-3}$	$5.70(39) \times 10^{-3}$	343(36)	287(32)	0.564(4)
	0.50	$5.97(3) \times 10^{-3}$	$1.04(6) \times 10^{-2}$	$6.46(8) \times 10^{-3}$	$5.17(29) \times 10^{-3}$	336(12)	313(22)	0.626(2)
	0.66	$8.18(87) \times 10^{-3}$	$1.13(5) \times 10^{-2}$	$6.79(68) \times 10^{-3}$	$6.55(68) \times 10^{-3}$	339(20)	285(48)	0.665(14)
	0.83	$7.87(10) \times 10^{-3}$	$6.57(7) \times 10^{-3}$	$8.21(18) \times 10^{-3}$	$7.06(5) \times 10^{-3}$	332(22)	327(7)	0.775(2)
	0.999	$1.01(3) \times 10^{-2}$	$4.41(30) \times 10^{-3}$	$8.58(53) \times 10^{-3}$	$8.22(43) \times 10^{-3}$	329(26)	290(20)	0.863(3)

Table 6.2: Integrated intensities of transitions from the lowest four rotational levels of H_3^+ in uncooled plasmas of varying p_2, with inferred kinetic and rotational temperatures and p_3 values. Numbers in parentheses represent 1σ uncertanties in the final digit(s).

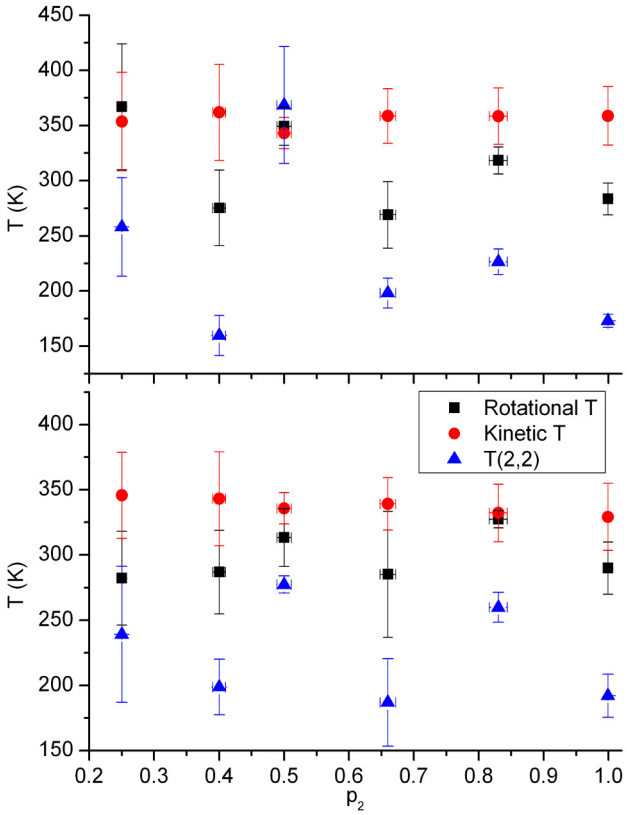

Figure 6.8: Kinetic and rotational temperatures as a function of p-H_2 fraction in an uncooled plasma. Also plotted is the rotational temperature derived from comparison of the (2,2) and (1,1) levels, as an illustration of the underpopulation of the (2,2) level. Top: 560 mTorr. Bottom: 1430 mTorr.

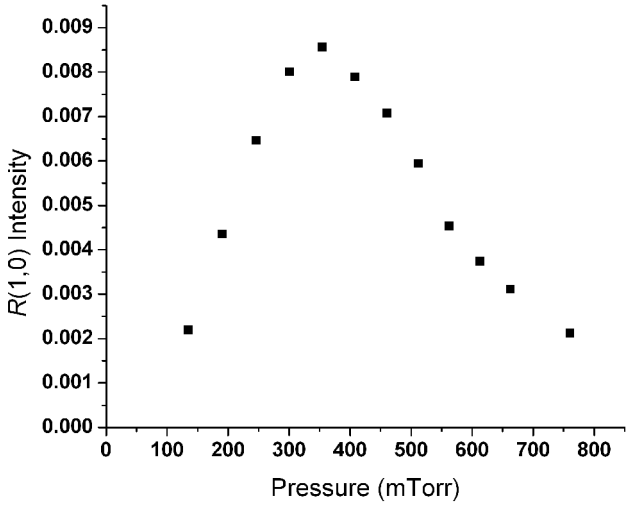

Figure 6.9: $R(1,0)$ integrated intensity as a function of cell pressure in a liquid-nitrogen-cooled n-H_2 plasma. The plotted data are selected at $t = 300$ μs.

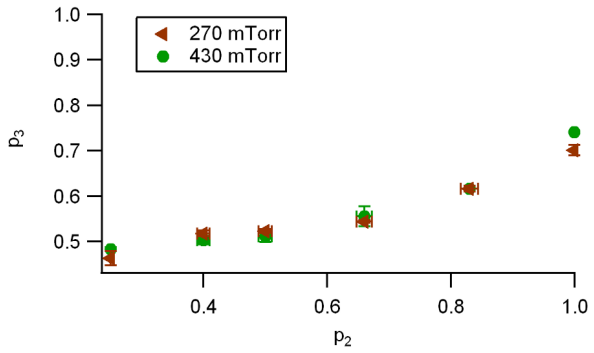

Figure 6.10: Experimental measurements of p-H_3^+ fraction plotted against p-H_2 fraction for a liquid nitrogen cooled plasma at 270 and 430 mTorr.

p-H_3^+ Fraction

Experiments analogous to those described in Section 6.3.2 were performed in a liquid nitrogen cooled hollow cathode. The results are summarized in Table 6.3, and plotted in Figure 6.10. At the lower temperature, there is a noticeable difference between the 270 and 430 mTorr data sets. In particular, the data point at $p_2 = 0.999$ is significantly higher than the corresponding point at low pressure, although the remainder of the data points are quite similar. The inferred temperatures are plotted in Figure 6.11. While T_{kin} remains constant with increasing p_2, T_{rot} and $T(2,2)$ markedly decrease, with the latter generally being lower. The variance-weighted mean of the kinetic temperature is (139 ± 4) K for the 270 mTorr data set, and (136 ± 5) K for the 430 mTorr set.

6.4 Analysis and Discussion

6.4.1 Steady State Modeling

In order to extract the value of α from the experimental data, we have constructed steady state models that calculate p_3 as a function of p_2 and α. The full details of these models are presented in the previous article in this issue, [110] and the results are briefly summarized here.

The key assumption in these models is that the *ortho*:*para* ratio of H_3^+ in the hollow cathode plasma is predominantly determined by the reaction of H_3^+ with H_2. As a check of this assumption, we estimate the number of H_3^+-H_2 collisions that occur prior to destruction of H_3^+ by electron recombination (ambipolar diffusion is not a significant loss mechanism in a hydrogenic hollow cathode plasma [100]). In the uncooled n-H_2 plasma at 570 mTorr, we observe an H_3^+ ion density of $\sim 2 \times 10^{12}$ cm^{-3} with H_2 number density $\sim 1.5 \times 10^{16}$ cm^{-3}. Because H_3^+ is the dominant ion at this pressure, the electron density is also $\sim 2 \times 10^{12}$

Pressure (mTorr)	p_2	$R(1,1)^u$ cm^{-1}	$R(1,0)$ cm^{-1}	$R(2,2)^l$ cm^{-1}	$R(2,1)^u$ cm^{-1}	T_{kin} (K)	T_{rot} (K)	p_3
270	0.25	$9.11(82) \times 10^{-3}$	$2.71(9) \times 10^{-2}$	$5.81(15) \times 10^{-3}$	$2.82(15) \times 10^{-3}$	136(15)	136(8)	0.464(16)
	0.40	$1.38(4) \times 10^{-2}$	$3.16(5) \times 10^{-2}$	$7.36(12) \times 10^{-3}$	$3.48(12) \times 10^{-3}$	140(6)	123(3)	0.518(6)
	0.50	$1.52(5) \times 10^{-2}$	$3.27(11) \times 10^{-2}$	$7.04(28) \times 10^{-3}$	$3.86(7) \times 10^{-3}$	140(8)	123(2)	0.523(4)
	0.66	$1.42(5) \times 10^{-2}$	$2.75(14) \times 10^{-2}$	$6.03(13) \times 10^{-3}$	$2.80(8) \times 10^{-3}$	134(13)	110(2)	0.544(3)
	0.83	$1.82(5) \times 10^{-2}$	$2.43(5) \times 10^{-2}$	$5.39(26) \times 10^{-3}$	$3.23(20) \times 10^{-3}$	135(14)	105(3)	0.616(6)
	0.999	$2.02(9) \times 10^{-2}$	$1.83(2) \times 10^{-2}$	$5.77(56) \times 10^{-3}$	$2.88(10) \times 10^{-3}$	138(13)	96(2)	0.701(11)
430	0.25	$9.82(25) \times 10^{-3}$	$2.52(6) \times 10^{-2}$	$4.77(18) \times 10^{-3}$	$2.57(9) \times 10^{-3}$	136(10)	125(3)	0.483(4)
	0.40	$8.78(21) \times 10^{-3}$	$2.09(12) \times 10^{-2}$	$4.39(11) \times 10^{-3}$	$2.27(17) \times 10^{-3}$	138(10)	124(5)	0.503(9)
	0.50	$9.77(46) \times 10^{-3}$	$2.08(6) \times 10^{-2}$	$3.46(40) \times 10^{-3}$	$2.64(13) \times 10^{-3}$	141(16)	127(5)	0.512(13)
	0.66	$1.06(8) \times 10^{-2}$	$1.80(8) \times 10^{-2}$	$3.01(31) \times 10^{-3}$	$1.82(19) \times 10^{-3}$	132(22)	103(6)	0.556(22)
	0.83	$9.31(8) \times 10^{-3}$	$1.26(3) \times 10^{-2}$	$3.06(16) \times 10^{-3}$	$1.59(5) \times 10^{-3}$	129(14)	103(1)	0.617(1)
	0.999	$1.04(4) \times 10^{-2}$	$7.63(65) \times 10^{-3}$	$2.80(27) \times 10^{-3}$	$1.57(10) \times 10^{-3}$	137(13)	98(3)	0.741(1)

Table 6.3: Integrated intensities of transitions from the lowest four rotational levels of H_3^+ in liquid-nitrogen cooled plasmas of varying p_2, with inferred kinetic and rotational temperatures and p_3 values. Numbers in parentheses represent 1σ uncertanties in the final digit(s).

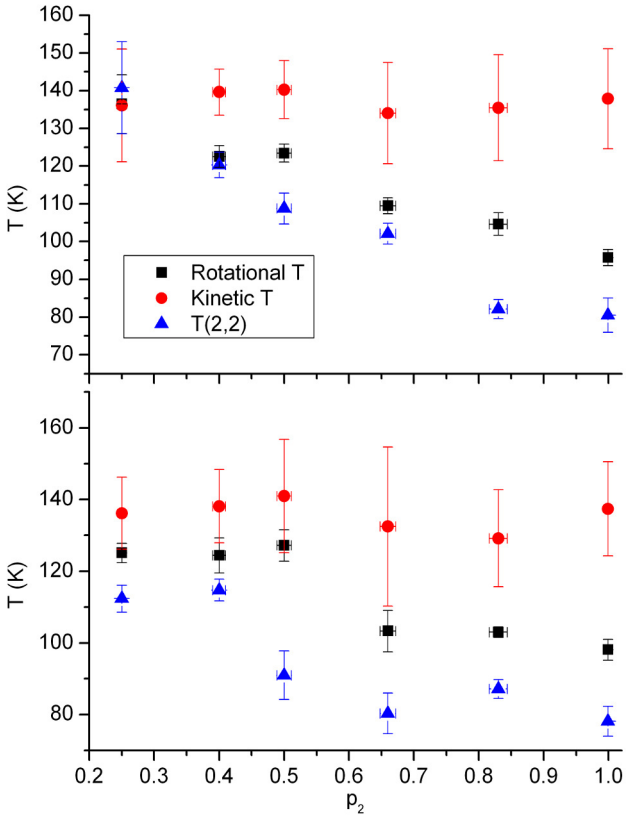

Figure 6.11: Inferred temperatures as a function of p-H_2 fraction in a liquid nitrogen cooled plasma. Top: 270 mTorr. Bottom: 430 mTorr.

cm^{-3}. The majority of these electrons are expected to be so-called "ultimate electrons," with a temperature on the order of 5000 K. [116, 117] Using the H_3^+ electron recombination rate coefficient temperature scaling from storage ring measurements, [82] we estimate a dissociative recombination rate coefficient of $\sim 1 \times 10^{-8}$ cm^3 s^{-1}, and the rate coefficient for the $H_3^+ + H_2$ reaction is assumed to be the Langevin rate of $\sim 2 \times 10^{-9}$ cm^3 s^{-1}. Using these rate coefficients and densities, a single H_3^+ ion is expected to experience around 750 collisions with H_2 prior to its destruction by electron dissociative recombination. As steady state is expected to be reached in fewer than 10 collisions, [110] this assumption should be valid.

For the uncooled plasma, we make a further assumption that the outcomes of the hop and exchange reactions are determined entirely by nuclear spin branching fractions. [69] This assumption is valid so long as sufficient energy is available for many reactant and product states to be populated. The result, which we shall refer to as the "high temperature model," is:

$$p_3 = \frac{\alpha + 2\alpha p_2 + 1}{3\alpha + 2}, \tag{6.4}$$

where p_3 is the p-H_3^+ fraction, p_2 is the p-H_2 fraction, and $\alpha \equiv k^H/k^E$ is the hop-to-exchange reaction rate ratio. This equation is a straight line that passes through $(p_3, p_2) = (0.5, 0.25)$ (n-H_3^+ and n-H_2, respectively) and whose slope is related to α.

Because of the pressure dependence discussed in Section 6.3.2, we have also constructed a high temperature model that includes the possibility of three-body spin-changing collisions of the form $H_3^+ + 2H_2 \rightarrow H_3^+ + 2H_2$. We assume that reactions leading to the formation of stable H_5^+ do not affect the p-H_3^+ fraction. In this case, p_3 is given by Equation 6.5 (the "three-body high temperature model"), where α_2 is the same α from Equation 6.4, α_3 is the three-body hop-to-exchange ratio, and Φ_2 is the branching fraction for reactive two body collisions compared to reactive three-body collisions.

$$p_3 = \frac{\frac{\Phi_2}{1+\alpha_2}\left(\frac{1}{3}\alpha_2 + \frac{2}{3}\alpha_2 p_2 + \frac{1}{3}\right) + \frac{1-\Phi_2}{1+\alpha_3}\left(\frac{39}{100}\alpha_3 + \frac{13}{50}\alpha_3 p_2 + \frac{19}{50} + \frac{3}{25}p_2\right)}{\frac{\Phi_2}{1+\alpha_2}\left(\alpha_2 + \frac{2}{3}\right) + \frac{1-\Phi_2}{1+\alpha_3}\left(\frac{91}{100}\alpha_3 + \frac{41}{50}\right)} \tag{6.5}$$

At the lower temperatures of the liquid-nitrogen-cooled plasma, energetic considerations may inhibit some reaction channels. For instance, conversion of p-H_2 to o-H_2 requires $E/k_B = 170$ K of energy, and so such processes might be expected to proceed more slowly in a colder plasma. In order to take this into account, a different derivation is employed, and Equation 6.6 (the "low temperature model") results. In this equation, the rate coefficients k_{ijkl} represent the rates of reactions of the form i-$H_3^+ + j$-$H_2 \rightarrow k$-$H_3^+ + l$-H_2 (for instance, k_{oppo} is the rate coefficient for the reaction o-$H_3^+ + p$-$H_2 \rightarrow p$-$H_3^+ + o$-H_2). The rate coefficients are dependent on T_{kin}, T_{rot}, and the branching fractions for the identity, proton hop, and

hydrogen exchange reactions (S^{id}, S^{hop}, and S^{exch}, where $\alpha \equiv S^{hop}/S^{exch}$), and they are calculated using a microcanonical statistical model. [77] Inclusion of three-body effects into this model is unfeasible owing to large numbers of unknown rate coefficients.

$$p_3 = \frac{(k_{oopp} + k_{oopo})(1 - p_2) + k_{oppo}p_2}{(k_{oopp} + k_{oopo} + k_{poop} + k_{pooo})(1 - p_2) + (k_{oppo} + k_{ppoo})p_2} \tag{6.6}$$

6.4.2 Uncooled Plasma

By comparing the results of the high pressure and low pressure measurements in the context of Equations 6.4 and 6.5, the extent to which three-body collisions affect the determination of α can be assessed. The three-body high temperature model (Equation 6.5) reveals that for a given α_2, any three-body effects will cause the slope of a plot of p_3 vs p_2 to become more shallow (see Figure 2 from previous article [110]). Therefore, if three-body effects are important, then a fit to the high temperature model (Equation 6.4) will underestimate α.

The term Φ_2 in the three-body high temperature model becomes smaller as the H_2 number density increases. If three-body proton-scrambling processes are important, a p_3 vs p_2 plot should give a shallower slope for measurements taken at a higher cell pressure (at the same temperature) compared to a lower pressure. As can be seen in Figure 6.7, this was not observed in our data sets. We conclude that while there is evidence for H_5^+ formation in the cell, and therefore three-body collisions, these processes do not exhibit significant nuclear spin dependence under our experimental conditions, and therefore do not influence the value of α inferred from measurements in our uncooled plasma.

The data from the uncooled plasma are plotted in Figure 6.12 along with fits to the high temperature model. The high pressure data fit reasonably well to the model, but the low pressure data are consistently below the model fit, especially at low p_2. This discrepancy is not due to three-body effects, but appears similar to curves produced by the low temperature model (Equation 6.6). It is possible that even at a temperature of ~ 350 K, energetic effects may still restrict some of the possible reaction channels. Another possibility is that significant variation in state-to-state reaction cross sections causes the use of nuclear spin statistical weights to be inaccurate. Nevertheless, the data set at 560 mTorr gives $\alpha = 1.58$, and the set at 1430 mTorr gives $\alpha = 1.69$. We regard these as being within the overall experimental uncertainty, although the uncertainty in the fits are only 0.02 and 0.03, respectively.

Cordonnier *et al.* [74] performed a similar measurement in a pulsed hollow cathode plasma. They measured the ratio of the transition intensities of the $R(1,0)$ and $R(1,1)^u$ transitions in n-H_2 and p-H_2 plasmas at a pressure of 1.85 Torr and temperature of ~ 400 K. Using a detailed chemical model of their plasma

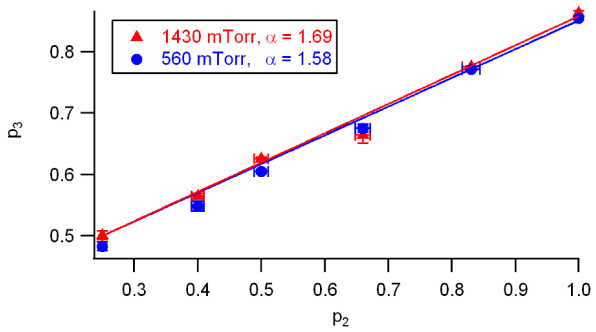

Figure 6.12: High temperature model fits to experimental measurements in an uncooled plasma.

together with their measurements ($p_3 = 0.893$ at $p_2 = 0.999$), they derived $\alpha = 2.4$, with an uncertainty of at least 0.6. As validation, inserting their results into Equation 6.4 gives $\alpha = 2.46$.

An issue discussed in their work is the back-conversion of p-H_2 to o-H_2 in their plasma over the course of a discharge pulse. This is illustrated in their Figure 2. For comparison, our results are plotted in a similar format in Figure 6.13. The time dependence of our signals most closely resembles theirs for the 1430 mTorr data set. Note the relatively slow rise of H_3^+ absorption, and the slight increase in the $R(1,0)$ integrated intensity over time in the p-H_2 measurement at 1430 mTorr. This effect is not observed in the 560 mTorr data set. We suspect that the higher ion density in the 1430 mTorr data set results in more H atom recombination on the walls of the cathode, which forms H_2 in the "normal" 3:1 *ortho*:*para* ratio in quantities large enough to significantly affect the overall p-H_2 fraction. The higher pressure and discharge current (2.8 A) reported by Cordonnier *et al.* likely caused more back-conversion in their experiment than in ours. For our calculation of α, we have chosen data points early on in the discharge pulse when these effects are minimal.

Our derived values for α around 1.6 fall just below the lower limit of the estimated uncertainty of the results of Cordonnier *et al.* Our temperature of $\sim$ 350 K is lower than theirs, and a decrease of α with temperature is in line with expectations from statistical arguments. The value of α inferred from measurements of the $D_3^+ + H_2$ isotopic system by Gerlich [75] is ~ 1.6 at a collision energy of $\sim$ 44 meV, which corresponds roughly to a temperature $T = (2/3)(E/k_B) = 340$ K, in excellent agreement with our results.

6.4.3 Liquid-Nitrogen-Cooled Plasma

Unlike the case of high temperature, with our current models we are unable to make predictions about the change in a plot of p_3 vs p_2 with pressure (hence, three-body interactions) at low temperature. It has been

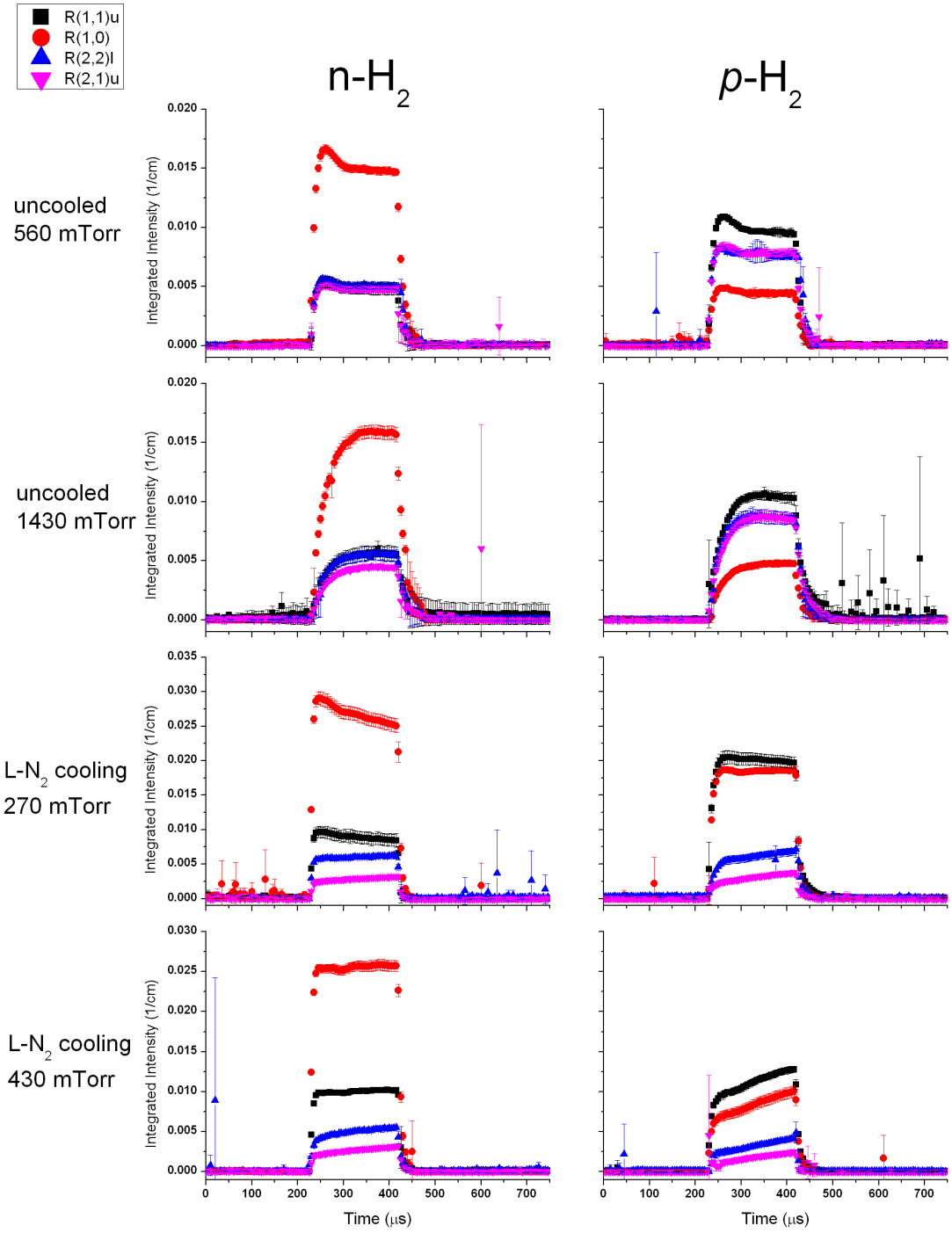

Figure 6.13: Time dependence of integrated intensities of all four observed transitions in n-H_2 ($p_2 = 0.25$, left) and p-H_2 ($p_2 = 0.999$, right) plasmas under the different temperature and pressure conditions explored in this work. The integrated intensities are averaged over three scans of each transition. Nonzero intensities outside of the pulse are the result of a blind Gaussian fit to a noise feature within a spectrum with no absorption, resulting in a spurious "integrated intensity."

observed that the rates of ternary association reactions leading to the formation of H_{2n+1}^+ clusters increase with decreasing temperature. [101, 115] However, it is unclear whether this process is dependent on the nuclear spin configuration of H_3^+. It is, however, dependent on the nuclear spin of H_2; the rate coefficient for ternary association of H_3^+ with p-H_2 at 10 K is over an order of magnitude faster than with n-H_2. [101] This may account for the differences in the time traces in the lowest pair of plots in Figure 6.13.

At both pressures, the temperatures plotted in Figure 6.11 suggest that higher energy levels of p-H_3^+ are being selectively destroyed at a faster rate as the p-H_2 fraction increases. Although since the (3,3) level of o-H_3^+ was not observed during these measurements, our thermalization measurements (see Section 6.3.1) suggest that the behavior of o-H_3^+ is the same as p-H_3^+. Also, the time traces within individual conditions in Figure 6.13 do not display significantly different time dependence between o-H_3^+ and p-H_3^+, after considering the increasing temperature and possibly a small amount of p-H_2-to-o-H_2 back-conversion.

To model the p_3 vs p_2 curves, rate coefficients k_{ijkl} were calculated with $S^{id} = 0.1$ (the statistical value), $\alpha = \{0, 0.1, 0.5, 2, 10, \infty\}$, $T_{kin} = 135$ K, and $T_{rot} = \{85 - 145\}$ K in steps of 15 K. Several of these curves are plotted along with the experimental results for comparison in Figure 6.14. For the data set at 270 mTorr, the data agree well with rate coefficients calculated with $\alpha = 0.5$, no matter the rotational temperature used. Because the apparent rotational temperature decreases with increasing p_2, the most appropriate comparison would involve multiple low temperature model curves, but these only differ by a small amount. A more important effect is the change of the shape in the p_3 vs p_2 curve as a function of α (Figure 6.14, lower panel).

The higher pressure data do not fit as well with the calculated curves. This might be due to a greater influence of nuclear-spin-dependent three-body processes not taken into account by our model. As mentioned before, H_5^+ formation has been observed to be faster in a p-H_2 plasma, and this may have some effect on the p-H_3^+ fraction at high pressure and high p-H_2 fraction. Because of the uncertainties here, we do not attempt to express a value of α for the 430 mTorr data set. We conclude that in our 139 ± 4 K plasma, the value of α is 0.5 ± 0.1. This suggests that even at this relatively modest temperature, the $(H_5^+)^*$ collision complex has a lifetime sufficient to allow for full scrambling.

Recently, Crabtree *et al.* have used a modified version of the low-temperature model to study the *ortho*:*para* ratio of H_3^+ in diffuse molecular clouds. [110] While their usage of the model includes some parameters related to interstellar chemistry, they found that their best match to astronomical observations required the value of S^{id} to be large, on the order of 0.9. To see if this value is consistent with our data, we have calculated rate coefficients for $S^{id} = 0.9$, $T_{kin} = 135$ K, $T_{rot} = 85$ K, and a range of α values. The results are plotted in Figure 6.15. Each of the curves is shifted upwards slightly at higher p_2 relative to the corresponding curve in Figure 6.14 (lower), but the curve at $\alpha = 0.5$ still agrees with the data reasonably

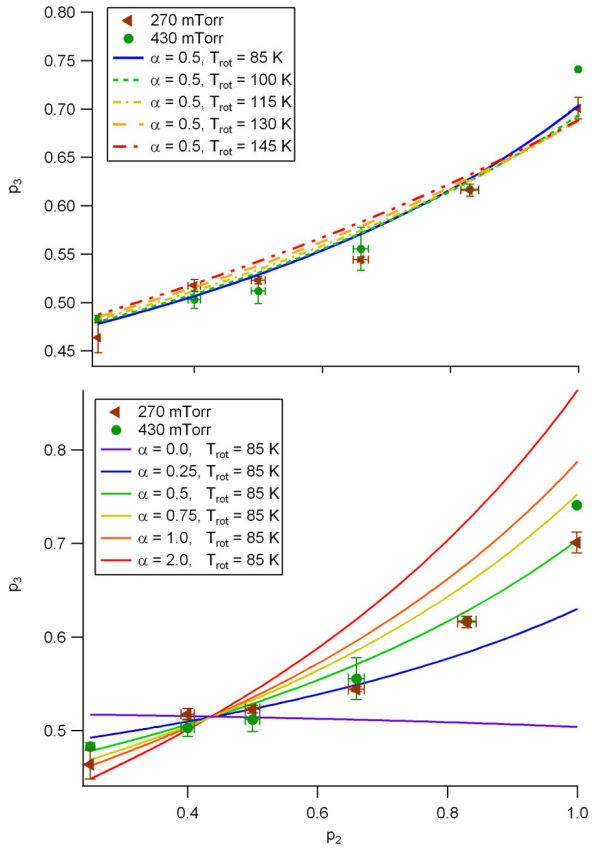

Figure 6.14: Comparison of the data from the liquid nitrogen cooled hollow cathode with calculations from the low temperature model (Equation 6.6). For all curves shown, $T_{kin} = 135$ K and $S^{id} = 0.1$.

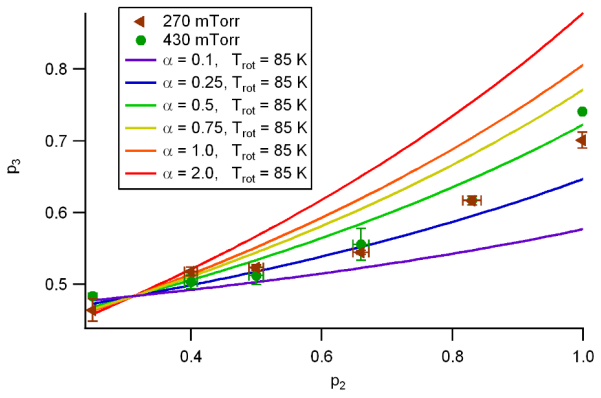

Figure 6.15: Comparison of the data from the liquid nitrogen cooled hollow cathode with calculations from the low temperature model (Equation 6.6). For all curves shown, $T_{kin} = 135$ K and $S^{id} = 0.9$.

well. It is possible that a lower value of α would provide a more optimal agreement, but this difference is likely within our total experimental uncertainty. It is not surprising that changing the value of S^{id} by such a large amount has a relatively small influence on the calculated p_3 values. This is because all of the rate coefficients in the low temperature model are reactive rate coefficients (i.e., none of them involve the identity pathway). The effect of increasing S^{id} is essentially just to scale all of the rate coefficients down by a roughly constant factor.

Comparison of the liquid nitrogen cooled data with the uncooled data indicate that, as observed in the $D_3^+ + H_2$ system, [75] α decreases with temperature, as illustrated in Figure 6.16. Even without the use of models, the decrease in α is evident by looking at the p-H_3^+ fraction formed in a plasma of pure p-H_2. In such a plasma, the H_3^+ produced by the $H_2^+ + H_2$ reaction is entirely p-H_3^+, and the formation of o-H_3^+ proceeds only through the $H_3^+ + H_2$ reaction. The nuclear spin selection rules for $H_3^+ + H_2$ show that for p-$H_3^+ + p$-H_2, the only way for o-H_3^+ to be formed is via the exchange process. Therefore, the decrease in p_3 at $p_2 \sim 1$ from high temperature to low temperature suggests that the exchange reaction becomes more dominant.

To further confirm this trend, we used a fluid circulator to pass heated ethylene glycol at 100 °C through the cathode. We then performed measurements of the $R(1,0)$, $R(1,1)^u$, $R(2,2)^l$, and $R(2,1)^u$ transitions in a 99.9% p-H_2 plasma at 560 mTorr. The kinetic temperature obtained was 450 ± 75 K, and the inferred p_3 value was 0.883 ± 0.007, corresponding to $\alpha = 2.2 \pm 0.3$. While this measurement is only at one value of p_2, the p_3 value is significantly higher than the corresponding value in the 350 K plasma, which is consistent with a higher hop:exchange ratio at higher temperature.

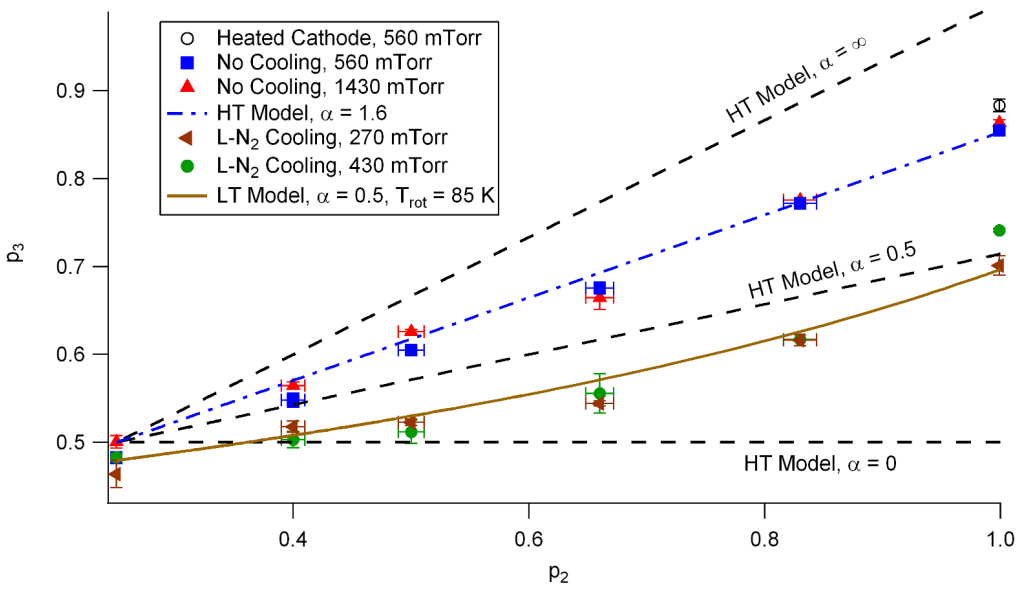

Figure 6.16: Summary of all experimental data and the best estimates for α for each temperature. Also shown for reference are high temperature model traces for $\alpha = \{0, 0.5, \infty\}$.

6.5 Conclusions

We have studied the nuclear spin dependence of the reaction of H_3^+ with H_2 by monitoring the populations of the four lowest rotational levels of H_3^+ formed in plasmas of varying p-H_2 enrichment. For the first time, this reaction has been studied at low temperature by cooling a hollow cathode discharge cell, resulting in a plasma temperature of 135 K. Using steady-state chemical models, the ratio of the rates of the proton hop and hydrogen exchange reactions (α) has been inferred at two different temperatures: 1.6 ± 0.1 at 350 K, and 0.5 ± 0.1 at 135 K. These values can be compared favorably with previous studies of this reaction at $\sim$400 K ($\alpha = 2.4 \pm 0.6$), [74] preliminary measurements at 450 K ($\alpha = 2.2 \pm 0.3$), and measurements of the analogous $D_3^+ + H_2$ system. [75]

In spite of the good agreement between the experimental data and steady state models, some of the results hint at a greater level of complexity than treated here. The (2,2) level of p-H_3^+ is consistently underpopulated relative to the kinetic temperature of the gas in our plasmas, and the rotational temperature of H_3^+ decreases with increasing p-H_2 fraction in our liquid nitrogen cooled cell. It is unclear whether the origin of these effects is ternary association reactions to form H_5^+, or state-to-state processes not accounted for in our models.

To remove any ambiguity in these results, it will be necessary to perform similar measurements in the carefully-controlled conditions of an ion trap. In such an environment, the gas density can be kept low enough to preclude three-body processes, and the temperature can be lowered beyond the 135 K achieved in this work. Fully quantum reactive scattering calculations on the H_5^+ potential energy surface, combined

with our results and ion trap measurements, would help greatly in furthering our understanding of this fundamental process.

The authors would like to thank Takayoshi Amano for providing designs and helpful suggestions for the hollow cathode cell used in this work. We thank Kisam Park for providing a computer program for calculating the rate coefficients used in our low temperature model. This work was supported by NSF PHY 08-55633.

Appendix A

Dissociative Recombination of Highly Enriched para-H_3^+

Dissociative recombination of highly enriched para-H_3^+

Brian A. Tom,[1] Vitali Zhaunerchyk,[2] Michael B. Wiczer,[1,a)] Andrew A. Mills,[1] Kyle N. Crabtree,[1] Magdalena Kaminska,[2,3] Wolf D. Geppert,[2] Mathias Hamberg,[2] Magnus af Ugglas,[2] Erik Vigren,[2] Wim J. van der Zande,[4] Mats Larsson,[2] Richard D. Thomas,[2] and Benjamin J. McCall[1,5,b)]

[1]*Department of Chemistry, University of Illinois at Urbana-Champaign, Urbana, Illinois 61801, USA*
[2]*Department of Physics, Stockholm University, Alba Nova, S-106 91 Stockholm, Sweden*
[3]*Institute of Physics, Jan Kochanowski University, Swietokrzyska 15, PL-25406 Kielce, Poland*
[4]*Department of Physics, Radboud University, NL-6500 GL Nijmegen, The Netherlands*
[5]*Department of Astronomy, University of Illinois at Urbana-Champaign, Urbana, Illinois 61801, USA*

(Received 11 September 2008; accepted 15 December 2008; published online 16 January 2009)

The determination of the dissociative recombination rate coefficient of H_3^+ has had a turbulent history, but both experiment and theory have recently converged to a common value. Despite this convergence, it has not been clear if there should be a difference between the rate coefficients for ortho-H_3^+ and para-H_3^+. A difference has been predicted theoretically and could conceivably impact the ortho:para ratio of H_3^+ in the diffuse interstellar medium, where H_3^+ has been widely observed. We present the results of an experiment at the CRYRING ion storage ring in which we investigated the dissociative recombination of highly enriched (~83.6%) para-H_3^+ using a supersonic expansion source that produced ions with $T_{rot} \sim 60-100$ K. We observed an increase in the low energy recombination rate coefficient of the enriched para-H_3^+ by a factor of ~1.25 in comparison to H_3^+ produced from normal H_2 (ortho:para=3:1). The ratio of the rate coefficients of pure para-H_3^+ to that of pure ortho-H_3^+ is inferred to be ~2 at low collision energies; the corresponding ratio of the thermal rate coefficients is ~1.5 at electron temperatures from 60 to 1000 K. We conclude that this difference is unlikely to have an impact on the interstellar ortho:para ratio of H_3^+. © *2009 American Institute of Physics*. [DOI: 10.1063/1.3065970]

H_3^+, the simplest polyatomic molecule, plays a central role in the chemistry of the interstellar medium because it easily protonates most atoms and molecules.[1,2] Consequently, understanding the formation and destruction pathways for this molecular ion under astrophysical conditions is of great importance. Dissociative recombination (DR), the recombination of molecular ions with electrons that leads to dissociation into neutral fragments, is the primary mechanism by which H_3^+ is destroyed in diffuse interstellar clouds.[3] The search for the H_3^+ DR rate coefficient has had a somewhat turbulent history, with values that varied by orders of magnitude.[4,5] The measurement of rotationally cold H_3^+ at CRYRING in 2002,[6] together with complete dimensionality quantum mechanical calculations,[7] has finally brought some level of closure to the debate. In fact, the CRYRING data were recently used to observationally determine the cosmic ray ionization rate in diffuse clouds.[8] Theory[7] also predicted that ground-state ortho-H_3^+ recombines faster than the ground state of para-H_3^+ at low collision energies. To probe this difference, Kreckel *et al.*[9] studied H_3^+ produced from both normal and highly enriched para-H_2, and found that para-H_3^+ had a higher DR rate coefficient (although the exact ortho:para ratio of H_3^+ in their source is unknown). A subsequent theoretical refinement[10] was consistent with this observation. Unfortunately, recent experiments performed at TSR have not been able to replicate this difference.[11] Confirming and characterizing the difference in the DR rate coefficients of ortho- and para-H_3^+ are of great importance, not only because of the impact such knowledge can have on our ability to more precisely model astrophysical processes but also because of the basic physical insight we can gain regarding this simple yet pivotal molecular ion.

In the present experiment, the DR of highly enriched para-H_3^+ was studied at the CRYRING ion storage ring using a pulsed supersonic expansion ion source. This approach was motivated by the spin selection rules derived by Quack[12] and Oka,[13] which imply that para-H_2^+ reacting with para-H_2 can only form para-H_3^+. We sought to enrich the fraction of para-H_3^+ as much as possible and furthermore to precisely measure this fraction in order to characterize the rate coefficient difference between ortho- and para-H_3^+.

An enriched >99.9% para-H_2 gas was produced using a modified closed-cycle ^{4}He cryostat. The enrichment of the para-H_2 gas was measured using thermal conductivity[14,15] and NMR. The gas was shipped to the experimental facility at the Manne Siegbahn Laboratory at Stockholm University in a Teflon-lined sample vessel. Tests indicated that the highly enriched para-H_2 gas stored in this vessel converted back to ortho-H_2 at a rate of ~1.7% per week. Therefore, the gas was ≥97% enriched in para-H_2 at the time of the experimental runs.

a)Present address: Department of Physics, Massachusetts Institute of Technology, Cambridge, MA 02139.
b)Electronic mail: bjmccall@illinois.edu.

The design and operation of the source have been covered in detail elsewhere.[6] In short, the gas emerging from the source pinhole underwent collisional cooling in a supersonic expansion, and was ionized when passing an electrode held at approximately −350 V. About 1500 Torr of backing pressure was used to feed the source, which was pulsed for 400–800 μs. The source was spectroscopically characterized at the University of Illinois before and after the experiment at CRYRING. This was done in order to verify that our test gas and source conditions produced a plasma that was highly enriched in para-H_3^+, and at rotationally cold temperatures. We used continuous-wave (CW) cavity ring-down spectroscopy with a difference frequency laser to probe the ortho-H_3^+ $R(1,0)$ and the para-H_3^+ $R(1,1)^u$ ground-state rovibrational transitions near 3.67 μm. Details regarding the difference frequency laser, the integration of the pulsed source with CW ring-down, as well as the source characterization itself will be presented elsewhere. The measured fraction of para-H_3^+ was ~49.1% for normal H_2 and ~74.7% for 97% para-H_2 enriched samples. Because we were seeking the highest fraction of para-H_3^+ possible, we experimented with dilutions in argon to reduce the number of $H_3^+ + H_2$ collisions, thereby reducing back-conversion from para- to ortho-H_3^+ in the plasma (see Ref. 16). We obtained the highest enrichment using a 1% dilution of para-enriched hydrogen in argon (by pressure), with a para-H_3^+ fraction of ~83.6%. The rotational temperature of the ions was measured to be ~60–100 K for all enrichments and dilutions.

Details regarding the experimental method at CRYRING are thoroughly discussed in Ref. 6 but a brief description is provided here for continuity. After exiting the source, the H_3^+ ions were mass selected, focused through ion optics floated at 30 kV, accelerated to 900 keV using a radio frequency quadrupole, and finally injected into the ring and accelerated to 13 MeV. The ions, having been rotationally cooled in the expansion, were stored in the ring for up to 5.6 s to allow vibrational relaxation to occur. During this relaxation period, the ions periodically passed through an electron cooler where they interacted with electrons at velocity matching conditions, leading to the translational cooling of the ions. As such, the electron cooler served the dual purpose of reducing the energy distribution of the ions, as well as providing a location where the DR could occur. The electron cooler cathode voltage was linearly ramped from 2965 to 1892 V over a 1 s interval, which covered the interaction energy range from ~0 to ~30 eV. The neutral DR products, no longer subject to the magnetic forces of the ring's bending magnets, emerged tangentially from the ring and were counted by an ion-implanted silicon detector. Measurements were taken such that the rate coefficient, α_{DR}, was measured as a function of the detuning energy, E_d, defined as the electron energy in the ion frame not including the electron thermal spread. The background contribution, originating from the interaction of the ion beam with residual gas in the ring, was corrected by subtracting counts until the relative difference between the trough centered at 2 eV and the peak at 10 eV was the same as that observed in the 2002 data. It is worth noting that this correction did not affect the rate coefficients at small interaction energies because of the magnitude of the DR signal in these regimes. In addition, the measured rate coefficients were corrected for the space charge of the electrons and the noncoaxial nature of the beams in the toroidal regions of the electron cooler.[17,18]

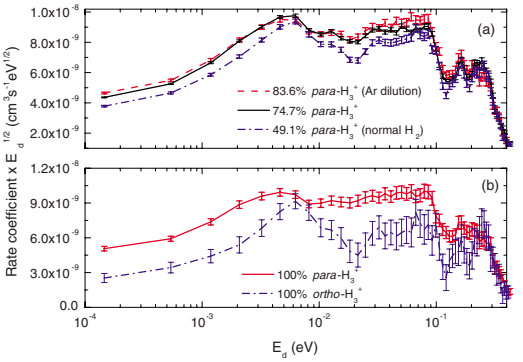

FIG. 1. (Color online) (a) Comparison of the DR rate coefficients for different para-H_3^+ fractions. Log scaling is avoided by applying the $E_d^{1/2}$ factor. (b) Extrapolated rate coefficients for pure ortho- and para-H_3^+. Uncertainties are statistical.

We performed three experiments using three different sample gases. The first experiment used the 1% dilution of enriched para-H_2 in argon. The second experiment was run with normal H_2 gas in order to compare the performance of both the supersonic expansion source and the storage ring with the results from Ref. 6. The final experimental measurements were taken using the enriched para-H_2 with no argon dilution. The respective ion currents after acceleration were 8.16, 54, and 48 nA.

The results of these three runs are presented in Fig. 1(a). We do not include systematic uncertainty (~16%) in our analysis because it did not change from experiment to experiment, and our focus is on the differences between the measurements. It is evident that the DR rate coefficient has a dependence on the spin modification of H_3^+. We observed the enriched para-H_3^+ produced from 97% para-H_2 to have a higher rate coefficient than that of the normal-H_2 at small E_d. The differences continue up to ~100 meV, with a region of much smaller differences centered around 6 meV. The measurement using argon-diluted para-H_2, with a para-H_3^+ fraction of ~83.6%, shows a slight increase over that of the undiluted para-H_2 sample. Figure 1(b) shows the extrapolated rate coefficients for hypothetical pure ortho- and para-H_3^+ derived using the 83.6% and 49.1% para-H_3^+ results. The same extrapolated rate coefficients can be derived using the data from the 74.7% para-H_3^+ experiment.

The 2007 rate coefficients for normal hydrogen were larger for all E_d than observed in the 2002 data, which might be due to inaccuracies in the ion current measurement during our experiment. Great care was taken in making the ring current measurements for the 2002 run. Consequently, we multiplied our data by a normalization factor of 0.65 which was based on a comparison of the 10 eV peak heights of the 2007 and 2002 experiments. Our objective was to observe relative differences in the DR rate between para-enriched H_3^+ and less enriched para-H_3^+ samples; therefore, the consistent

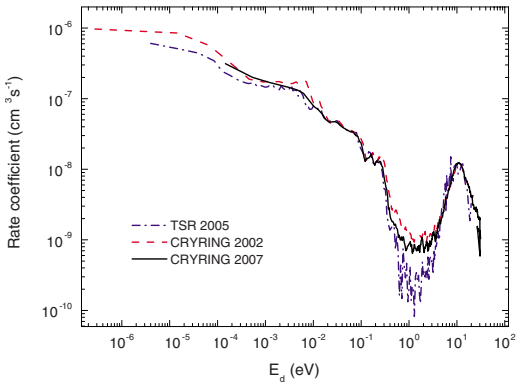

FIG. 2. (Color online) Comparison of the normal H_2-fed H_3^+ DR rate coefficients using the supersonic expansion source in 2007 and 2002; both experiments were performed with a transverse electron thermal spread ($kT_{e\perp}$) of 2 meV. Also included is a spectrum from TSR using the thermal cathode electron target with $kT_{e\perp}=4$ meV (Ref. 9). Uncertainty bars are removed to facilitate comparison of 2002 and 2007 spectra.

application of a multiplication factor to all of our data does not detract from our conclusions. A comparison with past experiments is presented in Fig. 2, and most structures above 10^{-2} eV are in good agreement.[6,9]

The 2007 spectrum is structurally smoother below 10^{-2} eV compared with the 2002 data. The rate coefficient curve at low electron energy could show less structure due to the presence of rotationally hotter ions. The indirect DR mechanism, proceeding through intermediate Rydberg states, gives rise to resonant structure in the rate coefficient. An increase in the population of excited rotational states will increase the number of resonances, resulting in a smoother curve.[10]

Our supersonic expansion source produced ions with $T_{\rm rot}\sim 60-100$ K based on the spectroscopic characterization, which was slightly higher than the value of 20–60 K obtained with the same source in 2002. Perhaps this higher $T_{\rm rot}$, combined with heating due to interactions with residual neutral molecules in the ring, led to the observed lack of structure in the cross section. That being said, experiments at TSR demonstrated that residual gas heating does not raise $T_{\rm rot}$ by more than 100–200 K.[19] It is important to note that although some excited rotational states may have contributed to our measurement, these states retain the para- to ortho-H_3^+ distribution as measured spectroscopically; therefore, the comparison between DR reaction rate coefficients remains valid. Para-H_3^+ cannot be converted to ortho-H_3^+ by reactive collisions in the ring, as the only likely spin-changing reaction with residual H_2 molecules at these high collision energies is a proton hop. Any H_3^+ ions formed by this process would not be at an energy that could circulate in the ring and contribute to the measurement. Additionally, we determined that the uneven depletion of spin modifications due to the different rate coefficients would not significantly affect the ortho/para ratio over our storage timescales.

The thermal rate coefficients, $\alpha(T_e)$, were calculated by integrating the energy dependent DR cross section over a Maxwellian distribution of electrons (see Ref. 6) at a given electron temperature, T_e. To derive the absolute cross section from the measured rate coefficient, the deconvolution procedure described in Ref. 20 was used. Table I presents the values of $\alpha(T_e)$, normalized as described above. The thermal rate coefficient at 300 K for normal H_2 (49.1% para-H_3^+) of the current experiment is in excellent agreement with that of 2002; however, the higher $T_{\rm rot}$ described earlier likely resulted in less agreement at lower electron temperatures [Fig. 3(a)]. Figure 3(b) shows the extrapolated values for 100% para-H_3^+ and 100% ortho-H_3^+. The ratio of these rate coefficients [dashed black line in Fig. 3(b)] increases as the electron temperature decreases.

TABLE I. Thermal rate coefficients, $\alpha(T_e)$, measured in the current experiment for $T_{\rm rot}=80\pm 20$ K and $T_e=300$ K. These data are derived from the measured rate coefficients, normalized to the 2002 data by a factor of 0.65. The $\alpha(T_e)$ for n-H_2 is in good agreement with Ref. 6, 0.68×10^{-7} cm^3 s^{-1}.

% para-H_2 feed	% para-H_3^+ [a]	$\alpha(T_e)$ (10^{-8} cm^3 s^{-1}) [b]
⋯	0	5.52 ± 0.77 [c]
25.0 (normal-H_2)	49.1 ± 2.4	6.79 ± 0.14
97.0 ± 0.8	74.7 ± 2.1	7.48 ± 0.10
97.0 ± 0.8 (Ar dilution)	83.6 ± 1.9	7.65 ± 0.16
⋯	100	8.12 ± 0.36 [c]

[a]Spectroscopically determined after CRYRING measurements. Reported errors are 1σ.
[b]Uncertainty is statistical.
[c]Extrapolated values for pure ortho- and para-H_3^+.

Both the E_d-dependent rate coefficients and the thermal rate coefficients indicate that the DR of H_3^+ has a nuclear spin state dependence, with that of the para spin modification proceeding at a more rapid rate. The para-H_3^+ has a rate coefficient almost two times larger than ortho-H_3^+ at low electron temperatures, with a smaller difference ($\sim$1.5) at higher temperatures. Theory predicts differences that range from more than a factor of 10 down to unity between electron temperatures of $\sim$0 and 300 K.[10]

The relatively modest (by astrophysical standards) difference in the rate coefficients of ortho- and para-H_3^+ sug-

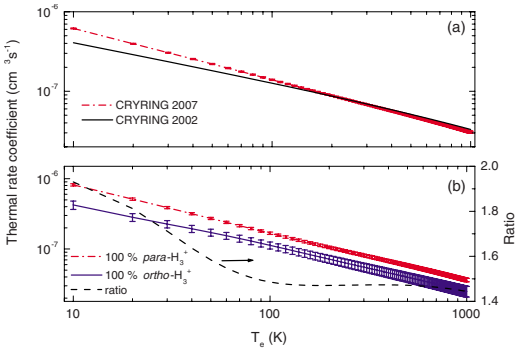

FIG. 3. (Color online) Thermal rate coefficients calculated for (a) normal H_2 (49.1% para-H_3^+) and for (b) the extrapolated 100% ortho- and para-H_3^+ results. Uncertainties are statistical. The dashed line represents the ratio of the thermal rate coefficients (para-H_3^+/ortho-H_3^+), with an arrow directing the reader to the appropriate axis.

gests that DR is unlikely to be the dominant process in determining the ortho:para ratio of H_3^+ in the diffuse interstellar medium. An even more convincing argument is the fact that para-H_3^+ is more abundant than ortho-H_3^+ in diffuse clouds;[8] yet we observe that para-H_3^+ has the higher DR rate coefficient. It is likely that the explanation for the interstellar ortho:para-H_3^+ ratio lies instead with the proton exchange reaction $H_3^+ + H_2 \rightarrow H_2 + H_3^+$. Although this reaction has a rate coefficient roughly two orders of magnitude lower than DR, the reaction partner (H_2) is some four orders of magnitude more abundant than electrons in diffuse clouds.

Preparations are underway to refine our supersonic expansion source design in order to consistently achieve rotationally colder ions. In addition, work is scheduled at CRYRING to minimize residual gas heating so we can better observe structural details in the DR cross section. Together, these improvements should permit a more definitive measurement of the absolute α_{DR} for highly enriched para-H_3^+.

We would like to thank the staff of the Manne Siegbahn Laboratory for valuable help during the experiment. The University of Illinois team acknowledges NSF Grant No. PHY 05-55486 for providing support, as well as a Hewlett International Travel Award. The Stockholm-based team would like to acknowledge support from the Swedish Research Council. M.K. acknowledges support from the Polish Ministry of Science and Higher Education Grant No. N202 111 31/1194, and the Swedish Institute.

[1] W. D. Watson, Astrophys. J. **183**, L17 (1973).
[2] E. Herbst and W. Klemperer, Astrophys. J. **185**, 505 (1973).
[3] T. Oka, in *Dissociative Recombination of Molecular Ions With Electrons*, edited by S. L. Guberman (Kluwer, New York, 2003), pp. 209–220.
[4] M. Larsson, Philos. Trans. R. Soc. London, Ser. A **358**, 2433 (2000).
[5] M. Larsson, B. J. McCall, and A. E. Orel, Chem. Phys. Lett. **462**, 145 (2008).
[6] B. J. McCall, A. J. Huneycutt, R. J. Saykally, N. Djuric, G. H. Dunn, J. Semaniak, O. Novotny, A. Al-Khalili, A. Ehlerding, F. Hellberg, S. Kalhori, A. Neau, R. D. Thomas, A. Paal, F. Österdahl, and M. Larsson, Phys. Rev. A **70**, 052716 (2004).
[7] V. Kokoouline and C. H. Greene, Phys. Rev. A **68**, 012703 (2003).
[8] N. Indriolo, T. R. Geballe, T. Oka, and B. J. McCall, Astrophys. J. **671**, 1736 (2007).
[9] H. Kreckel, M. Motsch, J. Mikosch, J. Glosík, R. Plašil, S. Altevogt, V. Andrianarijaona, H. Buhr, J. Hoffmann, L. Lammich, M. Lestinsky, I. Nevo, S. Novotny, D. A. Orlov, H. B. Pedersen, F. Sprenger, A. S. Terekhov, J. Toker, R. Wester, D. Gerlich, D. Schwalm, A. Wolf, and D. Zajfman, Phys. Rev. Lett. **95**, 263201 (2005).
[10] S. F. dos Santos, V. Kokoouline, and C. H. Greene, J. Chem. Phys. **127**, 124309 (2007).
[11] A. Petrignani, H. Kreckel, M. H. Berg, S. Altevogt, D. Bing, H. Buhr, M. Froese, J. Hoffmann, B. Jordon-Thaden, C. Krantz, M. B. Mendes, O. Novotný, S. Novotny, D. A. Orlov, S. Reinhardt, and A. Wolf, e-print arXiv:0810.0405.
[12] M. Quack, Mol. Phys. **34**, 477 (1977).
[13] T. Oka, J. Mol. Spectrosc. **228**, 635 (2004).
[14] A. Farkas, *Orthohydrogen, Parahydrogen, and Heavy Hydrogen* (Cambridge University Press, Cambridge, 1935), pp. 20–28.
[15] A. T. Stewart and G. L. Squires, J. Sci. Instrum. **32**, 26 (1955).
[16] M. Cordonnier, D. Uy, R. M. Dickson, K. E. Kerr, Y. Zhang, and T. Oka, J. Chem. Phys. **113**, 3181 (2000).
[17] D. R. DeWitt, R. Schuch, H. Gao, W. Zong, S. Asp, C. Biedermann, M. H. Chen, and N. R. Badnell, Phys. Rev. A **53**, 2327 (1996).
[18] A. Lampert, A. Wolf, D. Habs, J. Kenntner, G. Kilgus, D. Schwalm, M. S. Pindzola, and N. R. Badnell, Phys. Rev. A **53**, 1413 (1996).
[19] H. Kreckel, A. Petrignani, M. Berg, D. Bing, S. Reinhardt, S. Altevogt, H. Buhr, M. Froese, J. Hoffmann, B. Jordon-Thaden, C. Krantz, M. Lestinksy, M. Mendes, O. Novotný, S. Novotny, H. B. Pedersen, D. A. Orlov, J. Mikosch, R. Wester, R. Plašil, J. Glosík, D. Schwalm, D. Zajfman, and A. Wolf, J. Phys.: Conf. Ser. **88**, 012064 (2007).
[20] J. R. Mowat, H. Danared, G. Sundström, M. Carlson, L. H. Andersen, and L. Vejby-Christensen, M. af Ugglas, and M. Larsson, Phys. Rev. Lett. **74**, 50 (1995).

Appendix B

Development and Characterization of a Source of Rotationally Cold, Enriched para-H_3^+

Communications: Development and characterization of a source of rotationally cold, enriched para-H_3^+

Brian A. Tom,[1,a)] Andrew A. Mills,[1] Michael B. Wiczer,[1,b)] Kyle N. Crabtree,[1] and Benjamin J. McCall[1,2,c)]
[1]*Department of Chemistry, University of Illinois at Urbana-Champaign, Urbana, Illinois 61801, USA*
[2]*Department of Astronomy, University of Illinois at Urbana-Champaign, Urbana, Illinois 61801, USA*

(Received 3 October 2009; accepted 26 January 2010; published online 25 February 2010)

In an effort to develop a source of H_3^+ that is almost entirely in a single quantum state ($J=K=1$), we have successfully generated a plasma that is enriched to ~83% in para-H_3^+ at a rotational temperature of 80 K. This enrichment is a result of the nuclear spin selection rules at work in hydrogenic plasmas, which dictate that only para-H_3^+ will form from para-H_2, and that para-H_3^+ can be converted to ortho-H_3^+ by subsequent reaction with H_2. This is the first experimental study in which the H_2 and H_3^+ nuclear spin selection rules have been observed at cold temperatures. The ions were produced from a pulsed solenoid valve source, cooled by supersonic expansion, and interrogated via continuous-wave cavity ringdown spectroscopy. © *2010 American Institute of Physics*. [doi:10.1063/1.3322827]

In 1911, Thomson[1] made the first experimental observation of the simplest polyatomic molecular ion, H_3^+. Within 20 years, the existence of two species of molecular hydrogen, defined by the intrinsic spins of their protons, was predicted by Heisenberg and Hund.[2,3] Shortly thereafter, Bonhoeffer and Harteck[4] were able to experimentally prepare parahydrogen, in which the nuclear spins are antisymmetrically combined ($I=0$).

Hogness and Lunn[5] discovered that H_3^+ is the dominant species in hydrogenic plasmas, formed by

$$H_2 + H_2^+ \rightarrow H_3^+ + H \tag{1}$$

(exothermicity of ~1.7 eV and Langevin rate constant, $k_L \sim 10^{-9}$ cm^3 s^{-1}).[6] The relationship between the ortho and para spin modifications of molecular hydrogen and the ortho- and para-H_3^+ products, however, was not studied for another 50 years. New insight was gained when spin selection rules were derived by Quack using group theoretical methods,[7] and later (using an angular momentum formalism) by Oka,[8] for reaction (1) and for the reaction

$$H_3^+ + H_2 \rightarrow H_2 + H_3^+. \tag{2}$$

Reaction (2) occurs in one out of three ways: identity (2i), proton hop (2h), or hydrogen exchange (2e),

$$H_3^+ + \tilde{H}_2 \rightarrow H_3^+ + \tilde{H}_2, \tag{2i}$$

$$H_3^+ + \tilde{H}_2 \rightarrow H\tilde{H}_2^+ + H_2, \tag{2h}$$

$$H_3^+ + \tilde{H}_2 \rightarrow H_2\tilde{H}^+ + H\tilde{H}. \tag{2e}$$

Here, the hydrogens originally in the H_2 reactant are designated as $\tilde{H}$ in order to illustrate the differences between the three reactions.

As discussed by Cordonnier *et al.*,[9] each of these pathways must obey strict selection rules imposed by the conservation of nuclear spin angular momentum. The effects of these selection rules have been experimentally observed by Uy *et al.*[10] and Cordonnier *et al.*[9] in hot (300–500 K) plasmas. In addition, Gerlich[11] studied the closely related D_3^+ and H_2 system at much colder temperatures.

The selection rules for reaction (1) dictate that only para-H_3^+ will form from pure para-H_2. However, in a hydrogenic plasma (where H_2 is several orders of magnitude more abundant than H_3^+), reaction (2) will occur immediately following the formation of H_3^+ and will affect its ortho:para ratio. This process has been considered in detail by Cordonnier *et al.*;[9] their Table IV presents the nuclear spin branching ratios for this reaction. The identity reaction (2i) clearly has no effect on the H_3^+ nuclear spin modification. If para-H_3^+ combines with para-H_2 in the proton hop reaction (2h), the product H_3^+ also emerges without spin conversion. The exchange reaction (2e) is the only mechanism that converts para-H_3^+ to ortho-H_3^+ in pure para-H_2. If ortho-H_2 is present, then para-H_3^+ can also be converted to ortho-H_3^+ via reaction (2h).

In a high-temperature discharge of normal-H_2 (ortho:para=3:1), one would expect an H_3^+ ortho:para ratio of 1:1, as discussed by Cordonnier *et al.*[9] These authors also

a)Present address: Department of Chemistry, United States Air Force Academy, CO 80840. Electronic address: brian.tom@usafa.edu.
b)Present address: Department of Physics, Massachusetts Institute of Technology, Cambridge, MA 02139.
c)Electronic address: bjmccall@illinois.edu.

TABLE I. Excitation and rotational temperatures measured using normal- and para-H_2. The "a" and "b" designations identify temperatures measured in close succession. The absorbance values are given in 10^{-6} cm^{-1}.

		Absorbance			Temperature (K)	
	Feed gas	$R(1,1)^u$	$R(1,0)$	$R(2,2)^\ell$	T_{ex}	T_{rot}
1	normal-H_2	0.35	0.84	⋯	105	⋯
2	para-H_2	0.41	⋯	0.07	⋯	62
3a	normal-H_2	1.32	2.83	⋯	77	⋯
3b	normal-H_2	1.32	⋯	0.43	⋯	85
4	normal-H_2	0.25	0.56	⋯	86	⋯
5a	normal-H_2	0.98	2.1	⋯	77	⋯
5b	normal-H_2	0.98	⋯	0.28	⋯	79

calculated the expected ortho:para ratio of H_3^+ for a para-enriched H_2 discharge and found an enhancement in para-H_3^+, in agreement with their experiments. These calculations took a statistical approach, assuming that product states will be formed from combinations of reactant states according only to the constraints imposed by nuclear spin conservation. While this assumption is reasonable at high temperatures, it will break down at lower temperatures where (for example) there may be insufficient thermal energy to convert $J=0$ para-H_2 to $J=1$ ortho-H_2. New approaches to solving this problem have recently been proposed[12,13] and will need to be taken into account in plasma modeling.

The present study was motivated by a dissociative recombination experiment requiring a cold, highly enriched para-H_3^+ plasma.[14] The work described in this Communication measured the para-H_3^+ enrichment obtained when using an enriched para-H_2 feed gas along with dilutions intended to minimize the frequency of the hop (2h) and exchange (2e) reactions in the plasma. The experimental setup consisted of a closed-cycle helium cryostat capable of producing highly enriched para-H_2 (~99.99%) and a system for testing the level of enrichment.[15] The plasma was generated by a pulsed solenoid source, and the para-H_3^+ enrichment was measured using a continuous-wave cavity ringdown spectrometer built around a mid-IR difference frequency generation laser. Software was developed in order to synchronize the ringdown events with the pulsed source. The spectrometer was capable of probing transitions from the lowest H_3^+ states: $R(1,1)^u$, $R(1,0)$, and $R(2,2)^\ell$ (see Ref. 16 for a description of the notation). A detailed discussion of the spectrometer, pulsed source hardware, and synchronization software can be found in an online supplement[17] and in Ref. 18.

The experimental measurements had the following three objectives: (1) to determine the temperature of the expansion, (2) to measure the para-H_3^+ enrichment that resulted from using highly enriched para-H_2, and (3) to observe the effect of dilution in an inert carrier gas on the fraction of para-H_3^+ in the expansion.

The temperature of the expansion was measured by comparing the relative abundances of the para and ortho spin modifications of H_3^+ formed from a normal-H_2 precursor gas (where ortho:para=3:1). This so-called excitation temperature (T_{ex}) has often been used as a proxy for the rotational temperature (T_{rot}).[19–21] The excitation temperature can be calculated using the equation

$$\frac{N_{(1,0)}}{N_{(1,1)}} = \frac{g_{(1,0)}}{g_{(1,1)}} e^{-\Delta E_{1,0-1,1}/k_B T_{ex}}, \tag{3}$$

where the ratio of nuclear spin degeneracy $g_{(1,0)}/g_{(1,1)}=4/2=2$ and $\Delta E_{1,0-1,1}=22.84$ cm^{-1}.[16] In place of $N_{(1,0)}$ and $N_{(1,1)}$, we used the normalized peak absorbances of the rovibrational transitions $R(1,0)$ and $R(1,1)^u$ for ortho- and para-H_3^+, respectively, divided by the squares of their transition dipole moments, $\mu^2_{R(1,0)}=0.0259$ D^2 and $\mu^2_{R(1,1)^u}=0.0158$ D^2. These transitions are separated by only 0.32 cm^{-1}, which made it easy to measure the peaks in quick succession. The results are presented in Table I.

In some instances, the rotational temperature itself was measured using transitions from the two lowest para-H_3^+ rotational states: $R(1,1)^u$ and $R(2,2)^\ell$. T_{rot} was calculated using an equation similar to Eq. (3), with $\Delta E_{(2,2)-(1,1)}=105.2$ cm^{-1} (Ref. 16) and applicable degeneracy terms, along with Einstein A coefficients.[22] In all cases there was good agreement between T_{rot} and T_{ex}.

The temperature of the expansion was sensitive to the condition of the poppet as well as how tightly the poppet was seated in the source pinhole. The probe region was approximately 3.8 cm downstream of the electrode and about 4 mm in front of a skimmer. Measurements of the temperature were taken throughout the experiment. If the temperature was too hot (>100 K), the poppet would be "tuned" or replaced before proceeding. As can be seen from Table I, the typical temperature in the expansion was between 60 and 100 K, and the variations were likely due to the changing conditions of the poppet.

It is unclear why we did not observe temperatures colder than 60–100 K in our expansion. This same source produced ions at $T_{ex}=20-60$ K a few years earlier.[19] One possible cause was the gas-pulse/discharge-pulse sequencing. In the present experiment the gas pulse was embedded in a longer voltage pulse, which could have resulted in additional heating.

The intensities of the $R(1,0)$ ortho-H_3^+ and the $R(1,1)^u$ para-H_3^+ peaks were measured for normal and highly enriched (99.99%) para-H_2 precursor gases. The purpose of

TABLE II. The para-H_3^+ fraction observed with two different para-H_2 enrichments, including argon dilution results for the higher enrichment. A Boltzmann distribution for $T_{rot}=80$ K has been applied.

Starting para-H_2 (%)	Percent H_2[a]	para-H_3^+[b] (%)
25	100	49.1 ± 2.4
99.99	100	78.5 ± 2.2
	15	78.0 ± 1.8
	5	70.9 ± 2.2
	0.8	83.3 ± 1.8

[a]The dilution was carried out using pressure $(P_{H_2}/(P_{H_2}+P_{Ar}))$.
[b]The reported errors are calculated from the standard deviation (1σ) of multiple measurements at a particular point and a temperature uncertainty of ± 20 K.

these measurements was to quantitatively characterize the dependence of the para-H_3^+ fraction in the plasma on the para enrichment of the precursor gas. The simple equation,

$$\% \text{ para-}H_3^+ = \frac{\Sigma N_{\text{para}}}{\Sigma N_{\text{para}} + \Sigma N_{\text{ortho}}}, \quad (4)$$

was used to derive the para-H_3^+ percentage, where the ΣN values were calculated using the measured intensities of the para- and ortho-H_3^+ ground state transitions. To go from the ground state intensities to the various ΣN, it was assumed that the rotational states within the para and ortho manifolds were thermally populated. Boltzmann distributions were applied assuming $T_{rot}=80 \pm 20$ K (based on the temperature measurements described above). At 80 K, almost 25% of para-H_3^+ ions are in rotationally excited states, whereas only 4% of ortho-H_3^+ are excited out of the ground state. The derived para-H_3^+ percentages are shown in Table II.

As expected, a discharge of normal-H_2 (25% para-H_2) gave results consistent with "normal-H_3^+" (50% para). However, using a highly enriched sample of para-H_2 in the discharge resulted in a plasma with $\sim 78.5 \pm 2.2\%$ para-H_3^+. Figure 1 depicts the changes in peak heights of $R(1,0)$ and $R(1,1)^u$ as the enrichment of the para-H_2 precursor gas was increased from that of normal-H_2 to 99.99%.

Measurements were also taken using dilutions of para-H_2 in a nonhydrogenic gas to reduce the number of

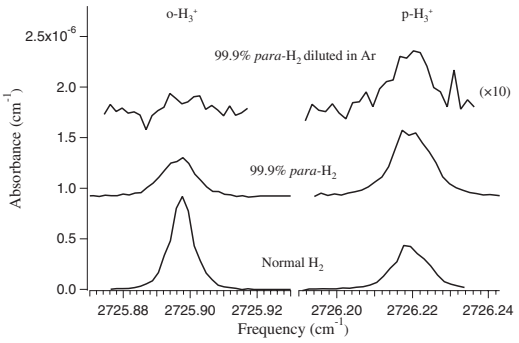

FIG. 1. Comparison of the spectra for H_3^+ for various precursor gases. Increasing the para-H_2 enrichment of the feed gas resulted in a higher enrichment of para-H_3^+. The plots are shifted vertically for clarity.

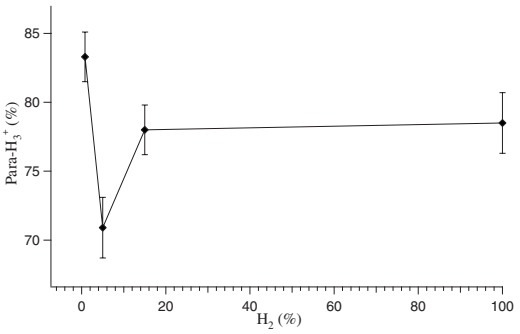

FIG. 2. The para-H_3^+ fraction vs argon dilution for 99.99% para-H_2. Uncertainties are 1σ.

reactions between the para-H_3^+ ions and H_2. The rate of reaction (2) for a given H_3^+ ion goes as $k[H_2]$, where k is the rate constant and $[H_2]$ is the number density of H_2. If the overall number of molecules in the expansion remains the same, but $[H_2]$ is reduced by dilution in an inert gas, then the number of interactions between H_3^+ and H_2 will decrease. Thus, dilution will reduce the deleterious effect of the exchange reaction (2e) on the para-H_3^+ enrichment of the plasma. As discussed earlier, the exchange is the primary mechanism by which para-H_3^+ is converted to ortho-H_3^+ in para-enriched plasmas.

The dilutions were carried out by premixing the desired pressures of H_2 and argon or neon in order to provide 2 atm of backing pressure for the source. In all cases, the H_3^+ signal was substantially attenuated (by one or two orders of magnitude) by the dilution, as can be seen in Fig. 1. Not surprisingly, the results of the dilution experiments, graphically depicted in Fig. 2, show that the para-H_3^+ fraction has a dependence on the extent of the dilution. When the hydrogen was diluted between 5% and 15% in argon, an unexpected decrease in the fraction of $[\text{para-}H_3^+]/[\text{total } H_3^+]$ in the plasma was observed. The reason for this decrease is not understood at present but could have an impact on $Ar-H_3^+$ action spectroscopy schemes.[23–25] Despite this, there was an increase in the para-H_3^+ fraction when H_2 was diluted to $\sim 1\%$ in argon.

The para-H_3^+ fraction was also measured in a neon carrier gas. The 10% dilutions in neon resulted in a signal similar to that of the 15% dilution in argon; however, when an $\sim 1\%$ dilution was analyzed, the H_3^+ signal was almost completely quenched.

In conclusion, we have observed for the first time the effects of the nuclear spin selection rules on the reaction between H_3^+ and H_2 at low temperature and exploited them to produce a source of rotationally cold and highly para-enriched H_3^+. By diluting 99.99% para-H_2 in argon to $\sim 1\%$ by pressure, we have achieved a further enrichment to 83.3% para-H_3^+. We have also observed unexpected behavior in the derived para-H_3^+ fraction at intermediate argon dilutions, which warrants further investigation, perhaps by simultaneous laser and mass spectroscopic measurements. Such a source can be used for reaction dynamics experiments be-

tween H_2 and H_3^+, along with experiments that measure properties of para-H_3^+ enriched plasmas at astrophysically relevant temperatures.

We are presently in the process of extending these measurements to a wider range of both temperature and para-H_3^+ enrichment using a more reliable source based on a piezo valve[26] as well as a cryogenically cooled hollow cathode discharge. These measurements should provide more insight into the dynamics of reaction (2) and, in particular, into the branching ratio of reactions (2i), (2h), and (2e), and will be presented in a future publication.

We would like to thank Takeshi Oka for valuable discussions on the dynamics of the hop and exchange reactions, Dana Dlott for the loan of equipment, and Jim Wentz for his assistance in building many of the electronic devices used in this experiment. This research was funded by the National Science Foundation AMO Physics under Grant No. PHY-08-55633.

[1] J. J. Thomson, Philos. Mag. **21**, 225 (1911).
[2] W. Heisenberg, Z. Phys. **41**, 239 (1927).
[3] F. Hund, Z. Phys. **42**, 93 (1927).
[4] K. F. Bonhoeffer and P. Harteck, Z. Phys. Chem. **B4**, 113 (1929).
[5] T. R. Hogness and E. G. Lunn, Phys. Rev. **26**, 44 (1925).
[6] T. Oka, Rev. Mod. Phys. **64**, 1141 (1992).
[7] M. Quack, Mol. Phys. **34**, 477 (1977).
[8] T. Oka, J. Mol. Spectrosc. **228**, 635 (2004).
[9] M. Cordonnier, D. Uy, R. M. Dickson, K. E. Kerr, Y. Zhang, and T. Oka, J. Chem. Phys. **113**, 3181 (2000).
[10] D. Uy, M. Cordonnier, and T. Oka, Phys. Rev. Lett. **78**, 3844 (1997).
[11] D. Gerlich, J. Chem. Soc., Faraday Trans. **89**, 2199 (1993).
[12] K. Park and J. C. Light, J. Chem. Phys. **126**, 044305 (2007).
[13] E. Hugo, O. Asvany, and S. Schlemmer, J. Chem. Phys. **130**, 164302 (2009).
[14] B. A. Tom, V. Zhaunerchyk, M. B. Wiczer, A. A. Mills, K. N. Crabtree, M. Kaminska, W. D. Geppert, M. Hamberg, M. af Ugglas, E. Vigren, W. J. van der Zande, M. Larsson, R. D. Thomas, and B. J. McCall, J. Chem. Phys. **130**, 031101 (2009).
[15] B. A. Tom, Y. Miyamoto, S. Bhasker, T. Momose, and B. J. McCall, Rev. Sci. Instrum. **80**, 016108 (2009).
[16] C. M. Lindsay and B. J. McCall, J. Mol. Spectrosc. **210**, 60 (2001).
[17] See supplementary material at http://dx.doi.org/10.1063/1.3322827 for a detailed description of the experimental method.
[18] B. A. Tom, "Nuclear spin dependence in reactions of H_3^+ in the laboratory and the interstellar medium," Ph.D. thesis, University of Illinois at Urbana-Champaign, 2009.
[19] B. J. McCall, A. J. Huneycutt, R. J. Saykally, N. Djuric, G. H. Dunn, J. Semaniak, O. Novotny, A. Al-Khalili, A. Ehlerding, F. Hellberg, S. Kalhori, A. Neau, R. D. Thomas, A. Paal, F. Österdahl, and M. Larsson, Phys. Rev. A **70**, 052716 (2004).
[20] T. Oka, Proc. Natl. Acad. Sci. U.S.A. **103**, 12235 (2006).
[21] N. Indriolo, T. R. Geballe, T. Oka, and B. J. McCall, Astrophys. J. **671**, 1736 (2007).
[22] L. Neale, S. Miller, and J. Tennyson, Astrophys. J. **464**, 516 (1996).
[23] H. Kreckel, A. Petrignani, M. Berg, D. Bing, S. Reinhardt, S. Altevogt, H. Buhr, M. Froese, J. Hoffmann, B. Jordon-Thaden, C. Krantz, M. Lestinksy, M. Mendes, O. Novotný, S. Novotny, H. B. Pedersen, D. A. Orlov, J. Mikosch, R. Wester, R. Plašil, J. Glosík, D. Schwalm, D. Zajfman, and A. Wolf, J. Phys.: Conf. Ser. **88**, 012064 (2007).
[24] A. Petrignani, H. Kreckel, M. H. Berg, S. Altevogt, D. Bing, H. Buhr, M. Froese, M. Grieser, J. Hoffmann, B. Jordon-Thaden, C. Krantz, M. B. Mendes, O. Novotný, S. Novotny, D. A. Orlov, S. Reinhardt, and A. Wolf, J. Phys.: Conf. Ser. **192**, 012022 (2009).
[25] H. Kreckel, D. Bing, S. Reinhardt, A. Petrignani, M. Berg, and A. Wolf, J. Chem. Phys. **129**, 164312 (2008).
[26] D. Proch and T. Trickl, Rev. Sci. Instrum. **60**, 713 (1989).

Appendix C

Measurements of the Dissociative Recombination of H_3^+ at the Test Storage Ring

High-resolution storage-ring measurements of the dissociative recombination of H_3^+ using a supersonic expansion ion source

Holger Kreckel,[1,*] Oldřich Novotný,[2] Kyle N. Crabtree,[1] Henrik Buhr,[4,3] Annemieke Petrignani,[3] Brian A. Tom,[1,†] Richard D. Thomas,[5] Max H. Berg,[3] Dennis Bing,[3] Manfred Grieser,[3] Claude Krantz,[3] Michael Lestinsky,[2] Mario B. Mendes,[3] Christian Nordhorn,[3] Roland Repnow,[3] Julia Stützel,[3] Andreas Wolf,[3] and Benjamin J. McCall[1,6]

[1]*Department of Chemistry, University of Illinois at Urbana-Champaign, Urbana, Illinois 61801, USA*

[2]*Columbia Astrophysics Laboratory, 550 West 120th Street, New York, New York 10027, USA*

[3]*Max-Planck-Institut für Kernphysik, Saupfercheckweg 1, D-69117 Heidelberg, Germany*

[4]*Faculty of Physics, Weizmann Institute of Science, Rehovot 76100, Israel*

[5]*Department of Physics, Stockholm University, Alba Nova, S-106 91 Stockholm, Sweden*

[6]*Department of Astronomy, University of Illinois at Urbana-Champaign, Urbana, Illinois 61801, USA*

(Received 14 July 2010; published 25 October 2010)

We have performed measurements of the dissociative electron recombination (DR) of H_3^+ at the ion storage ring TSR utilizing a supersonic expansion ion source. The ion source has been characterized by continuous wave cavity ring-down spectroscopy. We present high-resolution DR rate coefficients for different nuclear spin modifications of H_3^+ combined with precise fragment imaging studies of the internal excitation of the H_3^+ ions inside the storage ring. The measurements resolve changes in the energy dependence between the ortho-H_3^+ and para-H_3^+ rate coefficients at low center-of-mass collision energies. Analysis of the imaging data indicates that the stored H_3^+ ions may have higher rotational temperatures than previously assumed, most likely due to collisional heating during the extraction of the ions from the ion source. Simulations of the ion extraction shed light on possible origins of the heating process and how to avoid it in future experiments.

DOI: 10.1103/PhysRevA.82.042715 PACS number(s): 34.80.Ht, 34.80.Lx, 33.20.Ea

I. INTRODUCTION

The dissociative electron recombination (DR) of H_3^+ has received a good deal of attention in recent decades. As it is acknowledged as one of the key reactions of interstellar chemistry [1], many groups around the world have invested considerable effort into the determination of the DR rate coefficient at low temperatures. More than 30 experimental studies of the DR of H_3^+ have been published. It is beyond the scope of this article to list all the references; a review can be found in [2]. In brief, early H_3^+ DR measurements in the seventies resulted in rate coefficients on the order of 10^{-7} cm^3 s^{-1}. In the eighties there was a period of time when the H_3^+ DR reaction was believed to be much slower, based on flowing afterglow experiments giving upper limits for the rate coefficient of 10^{-8} cm^3 s^{-1} [3] and 10^{-11} cm^3 s^{-1} [4]. These conclusions were drawn in accordance with contemporary theory [5], predicting a very small DR rate coefficient. A few years later spectroscopic measurements carried out by Amano [6] and the storage-ring measurements of Larsson *et al.* [7] again supported a faster DR process.

The last decade has seen the storage-ring community striving for better control of the internal temperature of the H_3^+ ions. While it could be shown that the spontaneous decay of vibrationally excited states is fast enough to yield vibrationally cold ions within 2 s of storage [8], it was also found that rotational relaxation proceeds much more slowly [8,9]. In fact, the existence of metastable rotational states of H_3^+ with lifetimes exceeding months [10] makes it impractical to rely on spontaneous decay alone. Therefore, dedicated ion sources that precool the H_3^+ ions prior to injection into the storage ring were employed. McCall *et al.* carried out measurements at CRYRING using a supersonic expansion source for rotational cooling [11,12]. Kreckel *et al.* developed a cryogenic 22-pole ion trap to produce cold ions for DR measurements at TSR [13,14]. Both measurements showed excellent agreement. In the meantime the storage-ring rate coefficient has become the accepted reference.

In order to understand the discrepancies between the storage-ring results and afterglow measurements, detailed studies of hydrogen plasmas have been conducted by Glosík *et al.* [15,16]. They show that at the high pressures necessary to establish a continuous gas flow in afterglow setups, ternary collisions influence the outcome of the measurements. These findings and appropriate corrections may finally remove the disagreements between afterglow and storage-ring experiments [16].

For H_3^+, electron recombination can result in either two or three neutral fragments,

$$H_3^+ + e^- \rightarrow \begin{cases} H(1s) + H(1s) + H(1s), \\ H_2(X^1\Sigma_g^+) + H(1s). \end{cases} \quad (1)$$

While the total rate coefficient is the primary goal of most studies, the branching ratio between the two- and three-body channels has also been determined experimentally [17], as well as the vibrational excitation of the product H_2 molecules in the two-body case and the momentum sharing in the three-body case [9].

On the theoretical frontier a lot of progress has been made in the last decade. Early studies that predicted a very low recombination rate were born in the spirit that a curve crossing between the ionic state and a repulsive neutral state represents

*hkreckel@illinois.edu

†Present address: Department of Chemistry, United States Air Force Academy, CO 80840, USA.

the only effective DR mechanism [5]. This notion has been abandoned and the mechanism driving H_3^+ DR at low energies has been identified [18]. Modern calculations agree well with the storage-ring measurements on the absolute scale of the rate coefficient, while distinct discrepancies still remain for the exact shape of the cross section [19–21].

More recently, storage-ring measurements have been carried out that manipulate the nuclear spin of H_3^+. It has been shown that at low electron energies the rate coefficient of para-H_3^+ is faster than the one for ortho-H_3^+ [13,22] (from here on we will denote ortho-H_3^+ and para-H_3^+ by o-H_3^+ and p-H_3^+, and normal H_2 and para-H_2 by n-H_2 and p-H_2, respectively). Kreckel *et al.* measured the difference of the DR rate coefficient of H_3^+ created from n-H_2 and p-H_2, respectively, using a cryogenic 22-pole trap as an ion injector at TSR [13]. Tom *et al.* used a supersonic expansion ion source that was characterized by cavity ring-down spectroscopy for a DR experiment at CRYRING [22]. Both measurements remain somewhat incomplete, however, since Kreckel *et al.* did not determine the p-H_3^+ fraction, and since both studies are impeded by low electron energy resolution.

In this work we present high-resolution DR measurements with a spectroscopically characterized supersonic expansion ion source using p-H_2 and n-H_2 as a precursor gas. Furthermore, we have carried out DR fragment imaging measurements with this ion source in order to determine the rotational temperature of the H_3^+ ions inside the storage ring.

The paper is organized as follows: the next section gives a brief overview of the storage-ring technique and the supersonic ion source. Section III describes the spectroscopic characterization of the ion source. In Sec. IV the results of the DR rate coefficient and fragment imaging measurements are presented. Section V outlines a possible collisional heating mechanism and in Sec. VI a summary is given and perspectives for future experiments are described.

II. EXPERIMENT

A. Storage-ring technique

The DR measurements were carried out at the TSR storage ring of the Max-Planck-Institut für Kernphysik in Heidelberg, Germany [23]. The storage ring consists of an octagon-shaped ion orbit surrounded by an ultra-high-vacuum chamber of 55.4 m circumference with a base pressure of $\sim 10^{-11}$ mbar, providing a clean environment for electron collision experiments. Dipole and quadrupole magnets direct the ions on their revolving course inside the vacuum tube.

Two independent cold electron beam facilities are located in two of the straight sections of the storage ring. Both of them were used for the present work. The first one (the electron cooler) is equipped with a thermal cathode limiting the transverse electron temperature to ~12.5 meV. In the second one (the electron target [24]) the electrons are extracted from a photocathode [25], thus allowing for much lower electron temperatures. In the present study the parallel and transverse electron temperatures were $kT_{||} \sim 40$ μeV and $kT_{\perp} \sim 1$ meV, respectively.

A strong pilot H_3^+ ion beam was produced from a Penning ion source in order to facilitate the initial setting of the storage-ring magnets. The ions were accelerated to an energy of $E_{\text{beam}} \sim 4.08$ MeV by a radiofrequency quadrupole accelerator (RFQ) followed by an RF linear accelerator and injected into the storage ring. Once all the settings had been optimized, the ion source port was switched to the supersonic expansion source which emitted one ion pulse per injection.

The electron densities in the cooler and target were set to 1.4×10^7 cm^{-3} and 1.34×10^6 cm^{-3}, respectively. The overlap length of the electrons with the ion beam in the electron cooler amounts to ~1.5 m while the electron target length is ~1.1 m. This exposes the ions to electron cooling for an effective fraction of $\eta_c \sim 2.7\%$ of the 55.4 m storage-ring circumference in the electron cooler, and $\eta_t \sim 2.0\%$ in the electron target. The voltage required to match the velocity of the electron target beam to the ion beam (cooling voltage) was $V_{\text{cool}} = 740.9$ V.

After injection into the storage ring the ions are merged with the velocity-matched electron beams of both the electron cooler and the electron target for a 2 s-long precooling period. In this phase the translational temperature of the ions is reduced dramatically in interactions with the mono-energetic electrons and the diameter of the stored ion beam shrinks to ~1 mm. After precooling, the energy of the electron target beam is scanned over the desired collision energy range while the electron cooler stays at the initial cooling energy. During the measurements the electron target energy is "wobbled" repeatedly in cycles consisting of three steps with lengths of 40, 40, and 80 ms, respectively. For the first step—the so-called cooling step—the beam is set to the nominal cooling energy in order to avoid beam dragging effects. The second step is the measurement step. Here the energy is changed for each injection, according to the desired scanning region. The final step is called the reference step. This step is included as a cross-check and for normalization. The energy in this step is set to a value where the spectrum is believed to be independent of the internal energy of the ions and where the cross section exhibits no sharp features. For the present experiment the reference energy was held at a center-of-mass collision energy of 11.5 eV for all runs, corresponding to the maximum of the broad direct DR peak at higher energies. Between each of the wobble steps a 5-ms delay is enforced before the data taking commences in order to make sure that the power supplies have reached their designated values. The ion beam is kept inside the storage ring for a total of ~10 s before it is removed by kicker magnets and the next ion pulse is injected.

1. Rate coefficient measurements

For rate coefficient measurements the neutral fragments resulting from the recombination process are counted by a Si surface barrier detector located ~12 m downstream of the electron target. The detector has an area of 10×10 cm^2 and the beam energy was chosen such that all neutral particles resulting from DR hit the detector, even for the most extreme momentum sharing possible. Neutral events for which an energy equivalent to three atomic mass units is deposited in the detector are counted as DR events. The measured rate R_{DR} is proportional to the DR rate coefficient α, the electron density n_e, and the number of ions in the interaction region N_i,

$$R_{\text{DR}} \propto \alpha n_e N_i. \quad (2)$$

Test measurements without the electron beam show that the number of mass 3 events produced by dissociative charge transfer in collisions with residual gas atoms and molecules is negligible. On the other hand, interactions with residual gas *do* lead to collision-induced dissociation (CID) of H_3^+, resulting in either neutral H or H_2 fragments and events with correspondingly lower energies deposited in the detector. The rate of these events $R_{\rm CID}$ is proportional to the ion current and the residual gas pressure. We use the CID rate during the cooling step as a measure of the ion current to normalize the energy bins within one run of data taking (typically 1–2h). The proportionality between the CID rate and the ion current is warranted, as long as the residual gas pressure does not change significantly. The pressure at various locations in the storage ring is monitored and recorded continuously for verification.

In order to average the data from separate runs taken at different times we cannot rely on constant pressure, however. Therefore, the DR rate at the reference energy step of 11.5 eV is used to normalize and co-add the data from individual runs. Substituting the number of ions N_i by $R_{\rm CID}$ we can express the relative DR rate coefficient as a function of the electron-ion center-of-mass collision energy by

$$\alpha_{\rm rel}(E_{\rm c.m.}) = \frac{R_{\rm DR}(E_{\rm c.m.})}{n_e(E_{\rm c.m.})R_{\rm CID}(E_{\rm beam})}. \quad (3)$$

The electron density $n_e(E_{\rm c.m.})$ can be derived from the electron beam current measured in the electron target. To normalize the rate coefficient measurement on an absolute scale we have calibrated the absolute rate coefficient for velocity-matched ion and electron target beams (corresponding to $E_{\rm c.m.} \sim 0$). These results will be presented in Sec. IV B.

2. Imaging measurements

We have performed two-dimensional (2D) DR fragment imaging studies to determine the internal energy of the stored H_3^+ ions. A microchannel plate (MCP) detector is used in combination with a phosphor screen and a CCD camera to measure the relative distance of particle impacts. The imaging detector is located in the straight section downstream of the electron target at a distance of 12.24 m from the center of the target. Only the three-body decay of H_3^+ was considered here, as the outgoing ground-state H atoms in this case have no internal excitation, which greatly simplifies the analysis. For H_3^+ in the rovibrational ground state ~4.8 eV of kinetic energy are released in the three-body DR process. This kinetic energy release is transformed into particle distances of millimeters to centimeters at the end of the ~12 m flight path to the detector. We record the two-dimensional impact distances at the detector for one DR event at a time. By comparing the measured distance distribution with simulated distributions assuming different degrees of rotational excitation, we can infer the average rotational energy stored in the H_3^+ molecules prior to the DR process. The DR fragment imaging method has been used extensively in the past [9,26–28], however, recently we tried to extend the technique to lower rotational temperatures (see, e.g. [29]). For H_3^+ this ultimately leads to a situation where the temperature derivation is limited by the uncertainty in the H_3^+ binding energy. A detailed description of the temperature analysis can be found in Sec. IV A.

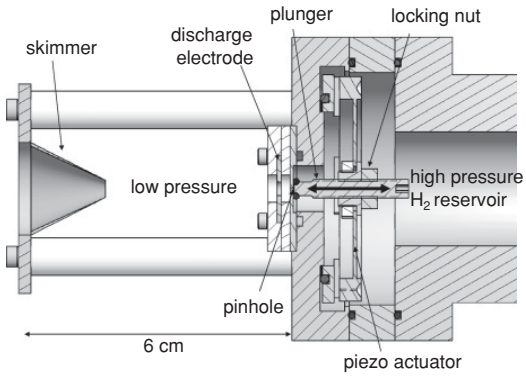

FIG. 1. Schematic of the supersonic expansion ion source. For the spectroscopy measurements, the laser beam crossed between the nozzle and the skimmer, at a distance of ~1 cm upstream of the skimmer.

For the imaging measurements, the electron beam of the target remained velocity matched with the ion beam during the entire storage time. The effect of the electron beam of the cooler on the internal temperature of the H_3^+ ions was investigated through measurements with the cooler turned on and with the cooler turned off.

B. Supersonic expansion source and spectroscopy setup

Schematics of the supersonic expansion source are given in Fig. 1. A piezoelectric actuator valve is used to produce short gas pulses from a high-pressure reservoir into a low-pressure vacuum chamber. The valve design follows the description given by Proch and Trickl [30]. We have added a stainless steel ring in front of the nozzle that serves as a discharge electrode. The piezo is activated by 300 μs-long pulses of −400 V. By applying a potential of −900 V a discharge is initiated between the electrode and the nozzle. The discharge pulse has a length of 1 ms. The gas pulse is delayed with respect to the discharge pulse by 200 μs, hence the gas pulse is embedded in the discharge pulse. Spectroscopic measurements of the rotational temperature of H_3^+ with this source showed no difference for variations of the length and delay of the gas pulse or the order with which the pulses are applied. For the TSR measurements we used backing pressures of 2 bar and either pure n-H_2 or mixtures of argon with n-H_2 and p-H_2, respectively.

The ion source was characterized spectroscopically at the University of Illinois. For this purpose it was connected to a vacuum chamber evacuated to a base pressure of 10 mtorr by a Leybold WS-2001 roots blower backed by a rotary vane pump. The spectroscopy setup is similar to the one described in [31]. It consists of a continuous wave difference frequency laser (DFG) and a continuous wave cavity ring-down spectrometer. We use the DFG laser to produce tunable infrared light (2.2–4.8 μm) at the wavelength difference between two pump laser beams. We split the output of a Nd:YVO_4 laser at 532 nm (Coherent Verdi V-10) into two beams. The first beam is used to pump a continuous wave dye laser (Coherent 899-29)

using Rhodamine 640 to produce laser light at ~622 nm. The second beam from the Nd:YVO_4 laser is passed through an acousto-optic modulator (AOM) and the first-order output is superimposed with the dye laser beam in a MgO-doped periodically poled $LiNbO_3$ crystal. For the present work the difference frequency generation resulted in ~500 μW of light around ~ 3.67 μm. The wavelength of the DFG light is tuned by tuning the dye laser frequency.

The heart of the cavity ring-down spectrometer is a high-finesse cavity that is made from two high-reflectivity mirrors (~99.98%) which are attached directly to the vacuum chamber. The DFG light is coupled into the cavity through the backside of one of the mirrors. A piezoelectric transducer dithers the mirror, effectively altering the cavity length. When the resonance frequency of the cavity and the DFG laser frequency coincide, power builds up inside the cavity. The light leaking out of the backside of the second mirror is recorded by a liquid-nitrogen cooled InSb detector. Once the observed power level exceeds an adjustable threshold, the AOM is switched off and the light intensity ring-down in the cavity is recorded by a high-speed digitizer. Typical ring-down time constants were on the order of 10 μs.

The ion source was mounted such that the laser cavity probed the ions at a distance around 1 cm upstream of the skimmer. Moving the ion source up or down by several millimeters did not result in a change of the measured temperatures.

To combine a pulsed ion source with a continuous wave cavity ring-down setup, it is necessary to synchronize the source pulses with respect to the ring-down occurences. We used a ring-down prediction scheme similar to the one described in [32]. In addition, we implemented a hardware signal derived from the actual discharge current that allows us to distinguish unambiguously between events where the ring-down occurred during a source pulse and ring-downs without ion sample present.

III. SPECTROSCOPIC CHARACTERIZATION OF THE SUPERSONIC ION SOURCE

To characterize the rotational temperature and nuclear spin distribution of the H_3^+ ions produced by the supersonic expansion source, we have measured transitions starting from the five lowest-lying rotational levels to the bending mode fundamental band $(v_1, v_2^l) = (0, 1^1)$. Figure 2 shows the observed transitions and the corresponding energy levels. A review on H_3^+ spectroscopy and notation can be found in [33]. Figure 3 shows a Boltzmann plot for all five transitions measured with a gas mixture of 1:5 n-H_2:Ar at 2 bar. The plot shows that the rotational levels can be fitted very well with a thermal distribution at a temperature of (180 ± 10) K. The level populations observed in pure n-H_2 (no argon admixture) are equally well fit with a thermal distribution, however, they result in a significantly lower temperature of (120 ± 10) K. Although the addition of argon increases the rotational temperature observed at the ion source, the argon-diluted gas mixtures were used for the storage-ring measurements in order to determine the difference in the rate coefficient between o-H_3^+ and p-H_3^+. As the para-hydrogen generator that was used for the DR measurements was not

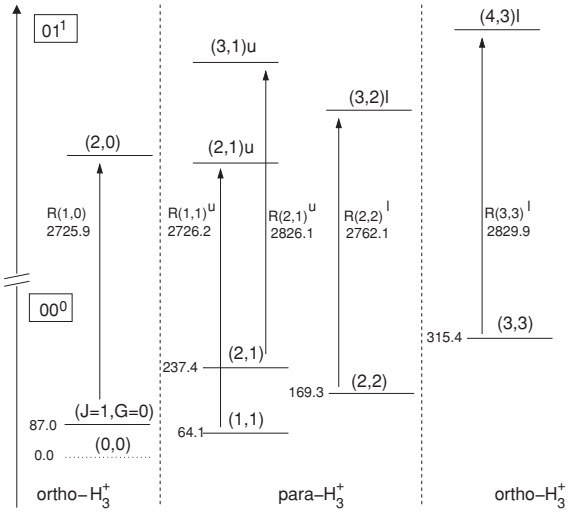

FIG. 2. Diagram of the H_3^+ levels and transitions that were probed for the characterization of the supersonic expansion source. The numbers in parentheses denote the level and transitions labels. The small numeric labels at the left-hand side of the individual levels give the level energy with respect to the symmetry-forbidden rotational ground state ($J = 0, G = 0$) of H_3^+ (plotted as a dotted line). Likewise the transition frequencies are given below the transition labels. All energies and frequencies are in cm^{-1}.

able to provide high enough p-H_2 pressure for pure hydrogen expansions, the gas had to be diluted with argon.

Figure 4 compares the $(1,0)$, $(1,1)^u$, and $(2,2)^l$ lines observed in 1:5 n-H_2:Ar and 1:5 p-H_2:Ar mixtures. Since comparative measurements using n-H_2:Ar and p-H_2:Ar mixtures were rather time-consuming, routinely only three lines were measured. Special care was taken to ensure that the spectra were taken under the same source conditions, with the only change being the nuclear spin mixtures of the precursor gas. The p-H_2 used for the spectroscopy measurements

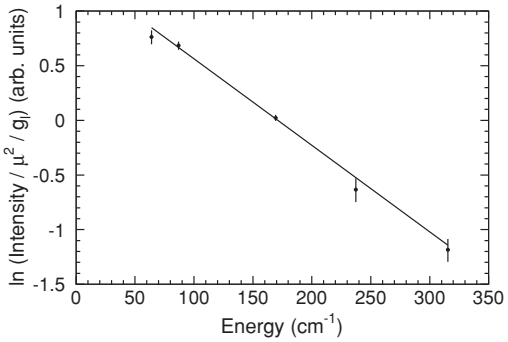

FIG. 3. Boltzmann plot derived from transitions starting at the five lowest-lying rotational levels of H_3^+ observed with the supersonic expansion source at a backing pressure of 2 bar. The gas mixture was 1:5 n-H_2:Ar. The fit results in a temperature of (180 ± 10) K. The transition intensities have been divided by the transition dipole moment μ^2 as given in [35] and by the multiplicity of the lower level g_l.

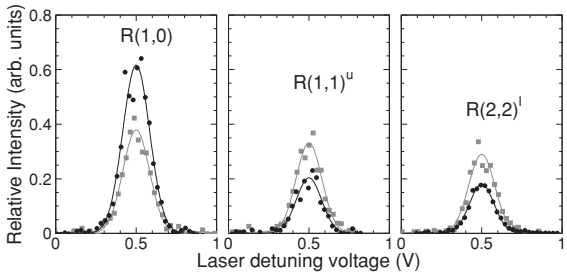

FIG. 4. Comparison of transitions starting from the three lowest rotational levels of H_3^+ measured in the supersonic expansion source with a 1:5 n-H_2:Ar gas mixture (black dots) and a 1:5 p-H_2:Ar gas mixture (gray squares). Calculating the rotational temperature from the two para-lines [R(1,1)^u and R(2,2)^l] results in rotational temperatures of (204 ± 30) K for the n-H_2 mixture and (200 ± 30) K for the p-H_2 mixture. The p-H_3^+ fraction is (47.9 ± 2)% for the n-H_2 mixture and (70.8 ± 2)% for the p-H_2 mixture.

was produced by a dedicated para-hydrogen converter [34] that was calibrated by nuclear magnetic resonance (NMR) measurements. The p-H_2 had a purity of >99%. The relative line strengths of the two para-lines (1,1)^u and (2,2)^l indicates a rotational temperature of (205 ± 30) K in the n-H_2:Ar mixture and (201 ± 30) K in the p-H_2:Ar mixture, respectively. These temperatures are slightly higher than those derived from the fit of the Boltzmann plot, but both methods agree within the uncertainties. Comparison to the intensity of the (1,0) ortho-line allows us to calculate the p-H_3^+ fraction which is (47.9 ± 2)% for the n-H_2:Ar mixture and (70.8 ± 2)% for the p-H_2:Ar mixture, respectively.

It has been shown that vibrational excitations of H_3^+ decay within 2 s of storage [8] and will therefore not survive the precooling phase in storage-ring experiments. On the other hand, the decay of these states could repopulate rotational excitations in steps of $\Delta J = \pm 1$ and thus alter the observed temperatures in the first seconds of storage. In order to constrain the vibrational excitation produced by the ion source, we have carried out a search for the R(1,1) $02^2 \leftarrow 01^1$ transition which has a transition dipole moment that is comparable to the fundamental band. We tried to find the R(1,1) $02^2 \leftarrow 01^1$ line in both pure p-H_2 gas and in a 1:5 p-H_2:Ar mixture, with no success. From the nondetection of this line we establish an upper limit for the fraction of vibrationally excited H_3^+ ions of <2% in the case of pure hydrogen precursor gas—assuming that the rotational excitation would be thermalized in the vibrationally excited levels. The absence of vibrationally excited states seems surprising at first glance, since vibrational excitations typically are cooled much less efficiently by inelastic collisions in supersonic expansion sources, compared to translational and rotational degrees of freedom. The case of H_3^+ may be special, however, since here every collision with a neutral H_2 molecule must be regarded as a chemical reaction, which can lead to proton-hop reactions or even total scrambling of the nuclei. As the H_3^+ molecules undergo many collisions with H_2 during the expansion process, the outcome of this chemical reaction may dominate the excitation pattern rather than inelastic collisions or the vibrational level spacing.

IV. STORAGE-RING RESULTS

A. H_3^+ rotational energy by DR fragment imaging

We have used the kinetic energy release (KER) that is set free in the three-body DR channel to infer the internal excitation of the stored H_3^+ ions inside the storage ring. The amount of energy released for ground-state H_3^+ molecules at zero center-of-mass collision energy can be derived by consideration of the sequence,

$$\begin{aligned} H_3^+ + e &\xrightarrow{-E_b(H_3^+)} H_2 + H^+ + e, \\ H_2 + H^+ + e &\xrightarrow{-E_b(H_2)} H + H + H^+ + e, \\ H + H + H^+ + e &\xrightarrow{+I_p(H)} H + H + H, \end{aligned} \tag{4}$$

where $E_b(H_3^+)$ denotes the binding energy of H_3^+, $E_b(H_2)$ the binding energy of the hydrogen molecule, and $I_p(H)$ the ionization potential of the hydrogen atom. The expected KER for ground-state H_3^+ thus can be calculated as

$$E_{\mathrm{KER}} = I_p(H) - E_b(H_2) - E_b(H_3^+). \tag{5}$$

The hydrogen ionization potential $I_p(H) = 13.5984$ eV [36] and the H_2 binding energy $E_b(H_2) = 4.4781$ eV [37] have been determined with high precision, while the binding energy of H_3^+ is not known as precisely as the other parameters. The experiment of Cosby and Helm [38] resulted in a binding energy of (4.373 ± 0.021) eV. Increasingly accurate theoretical calculations, however, disagree with this value and converge at 4.3300 eV (see, e.g. [39] for an overview). Furthermore, more recent photodissociation data [40] indicate a somewhat lower value of 4.337 eV for the H_3^+ binding energy [41], closer to the theoretical results. Based on the accuracy that calculations of the H_3^+ potential surface have reached and the agreement among the published values, we use the theoretical value as our reference. The expected kinetic energy release for three-body DR from the ($J = 1$, $G = 1$) ground state is $E_{\mathrm{KER}} = 4.7903$ eV.

For the temperature analysis we use the sum of the transverse interparticle distances $R^2 = R_1^2 + R_2^2 + R_3^2$ measured by the imaging detector. As the relative distances R_i are proportional to the relative transverse velocities $v_i^\perp$, R^2 is proportional to the total transverse kinetic energy release $E_{\mathrm{KER}}^\perp$,

$$E_{\mathrm{KER}}^\perp = \frac{1}{3\,s^2} E_{\mathrm{beam}} R^2, \tag{6}$$

with s being the flight distance to the detector. To infer the amount of excess energy, we compare the measured distributions of $E_{\mathrm{KER}}^\perp$ to a Monte Carlo simulation of the dissociation process assuming various degrees of internal excitation. In order to simulate the expected distances at the detector precisely, the ion beam energy has to be known to better than 0.5%. Since electron cooling leads to a near-perfect match between the velocities of the electron and ion beams, we use the well-defined velocity of the electrons in the electron target to obtain the energy of the ion beam in the laboratory frame, which results in $E_{\mathrm{beam}} = (4.0784 \pm 0.0017)$ MeV. The simulation includes the effective target overlap length and the dissociation anisotropy as determined in previous measurements [42]. We assume Boltzmann distributions for the rotational excitations in the simulation, which allows us

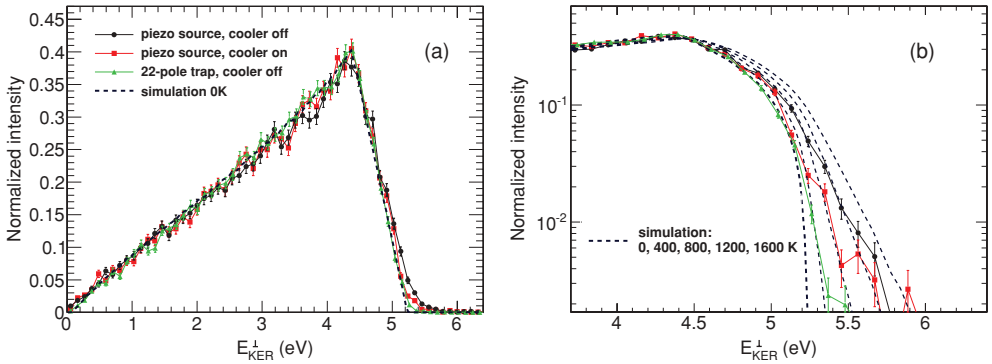

FIG. 5. (Color online) Transverse kinetic energy release distributions resulting from DR fragment imaging measurements. In (a) the measured distributions taken with the piezo expansion source and the electron cooler off are shown as black dots. The supersonic expansion data measured with the electron cooler on are plotted as red squares. Also shown are the results obtained with a cryogenic 22-pole ion injector (green triangles) taken with the electron cooler off. The dashed line represents the simulated distribution for 0 K rotational temperature. In (b) the higher energy region of the same experimental distributions is plotted on a logarithmic scale. Here, the dashed lines represent simulations with (from left to right) 0 K, 400 K, 800 K, 1200 K, and 1600 K rotational temperature. For the data plotted here 1:5 p-H_2:Ar was used as a precursor gas for the supersonic expansion source and pure p-H_2 for the 22-pole injector.

to assign a temperature to each individual simulation run. This choice is motivated by simplicity rather than an exact knowledge of the underlying populations. Furthermore, in the simulation we also assume that the DR rate coefficient is independent of the rotational state.

Figure 5 shows the measured kinetic energy release derived from the 2D particle distance distributions. Here, we plot experimental data for the present work and, for comparison, a TSR measurement performed with the cryogenic 22-pole ion trap in 2007 for which preliminary results were given in [42,43] and whose full analysis has recently been completed [44]. Also plotted are a series of simulated distributions assuming different rotational temperatures. All experimental data plotted in Fig. 5 were obtained using p-H_2 (1:5 p-H_2:Ar in the case of the expansion source) as a precursor gas. The transverse kinetic energy distributions measured using n-H_2 did not show a significant difference in temperatures.

Regarding Figs. 5(a) and 5(b), it is important to note that a visual comparison between experiment and theory becomes most meaningful when it is not done at the tails of the distributions where the statistics are poor. The statistically significant portion of the distribution lies at transverse kinetic energies of <5.2 eV. The fact that the extreme tails of the distributions seem to indicate higher rotational temperatures implies that the population of rotational states is probably not thermal.

We have derived temperature estimates for the respective experimental data sets by minimizing the χ^2 between the experimental and the simulated distributions using the rotational temperature in the simulation as a free parameter. With this method the supersonic expansion data (with the electron beam in the electron cooler being switched off) are best approximated by a simulation with (950 ± 100) K rotational temperature. The quoted uncertainty estimate corresponds to a 90% confidence level for the fit. When the high-density beam of the electron cooler is used in combination with the electron target, the internal temperature of the H_3^+ ions drops significantly to (450 ± 100) K. This electron-induced rotational cooling effect can be seen as a consequence of the tenfold higher electron density present in the electron cooler than in the electron target. The effect has been observed previously for the dissociative recombination of D_2H^+ [45] and can be either assigned to collisional cooling by superelastic electron collisions or to selective depletion of highly excited states in collisions with electrons. It has also been observed for HD^+ ions [29] where it could be clearly assigned to collisional cooling by superelastic electron collisions.

While the 22-pole measurement appears colder than the supersonic expansion data [Fig. 5(b)], it is difficult to get a temperature estimate as there is no significant difference in the χ^2 for simulations with rotational temperatures <300 K [44]. For this measurement the electron cooler beam was switched off after 0.5 s of storage while the electron beam of the electron target interacted with the ions over the whole storage time period.

It should be noted that the imaging results shown here are pushing the technique to its limits. The quoted uncertainties are purely statistical in nature and independent of the approximations that have to be made for the simulation. Furthermore, systematic uncertainties have to be taken into account. For example, a change in the H_3^+ binding energy by 20 meV induces a shift in the simulated curves corresponding to a temperature of $\sim$100 K. An even larger uncertainty is imposed by the determination of the actual overlap length of the electron and ion beams inside the electron target. The uncertainty range of this parameter translates into an uncertainty of $\sim$130 K for the rotational temperature; the length used in the analysis was set as to rather overestimate the derived temperatures within this uncertainty.

The supersonic expansion data reveal a large discrepancy between the spectroscopically determined temperature at the ion source ($\sim$200 K) and the rotational temperature of the stored ions without electron cooling ($\sim$950 K). This difference is indicative of a heating process occurring between ion

production and injection into the storage ring. This heating process is currently not fully understood; however, a possible explanation is given in Sec. V.

For the 22-pole trap measurements the ions were buffer-gas cooled to a nominal temperature of 13 K prior to injection [13,42]. The combined statistical and systematic uncertainties of the imaging method do not permit a definitive statement whether this temperature is maintained throughout acceleration and storage. The deviation of the experimental data from the zero rotational temperature curve at the upper end point of the distribution may also be indicative of a heating process, yielding a small nonthermal population in high-J levels. The above analysis of the 22-pole data applies only for the imaging results which are presented here for comparison of the initial temperatures of the ion sources. Rate coefficient measurements with the 22-pole trap were usually carried out using both electron beams; a discussion of the resulting temperatures and detailed rate coefficient studies will be presented elsewhere [44].

B. Absolute DR rate coefficient measurement

Absolute measurements of the H_3^+ DR rate coefficient were carried out in the CRYRING experiment in 2002 [11]. Subsequent studies at TSR [13] were normalized to these measurements at the high-energy direct DR peak. Recent studies at CRYRING, however, had to be scaled by a factor of 0.65 to be brought into agreement with the 2002 data [22]. To calibrate the absolute scale of the rate coefficient independently, we have analyzed lifetime measurements of the stored ion beam with and without the electron target beam (a similar method has been used in [46]). Figure 6 shows a plot of the intensity of the stored H_3^+ beam as a function of the storage time, as measured with a scintillation detector situated in the dipole magnet chamber downstream of the electron target. The events recorded in this detector correspond to charged particles resulting from interactions of the H_3^+ beam with the residual gas. For the measurement shown in Fig. 6 the electron target beam was set to the nominal cooling energy ($E_{\mathrm{c.m.}} \sim 0$) initially and after 12 s of storage it was switched off. The electron cooler beam remained off for

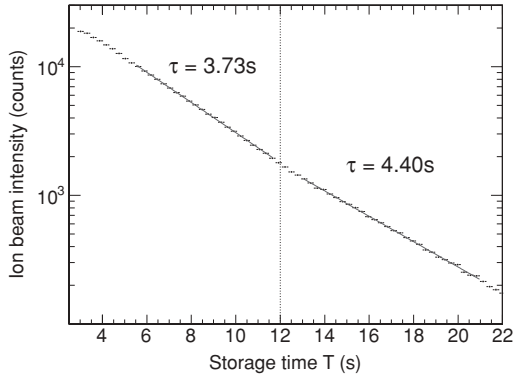

FIG. 6. Plot of the intensity of the H_3^+ ion beam as a function of the storage time. For the first 12 s of storage the electron target beam is switched on and set to the nominal cooling energy. At a storage time of $T = 12$ s the electron beam is switched off.

the entire lifetime measurement. The decay curve at storage times $T > 12$ s is fitted by an exponential decay with a decay constant $\tau_{\mathrm{off}} = 4.40$ s. We attribute this decay to an effective loss rate inflicted by residual gas and described by

$$R_{\mathrm{eff}}^{\mathrm{res}} = \frac{1}{\tau_{\mathrm{off}}}. \tag{7}$$

At storage times smaller than 12 s, the decay is due to both residual gas and electron interactions in the electron target. It can be fitted by an exponential decay with $\tau_{\mathrm{on}} = 3.73$ s. Assuming that the dominating loss process induced by the electron target beam is DR, we can write

$$R_{\mathrm{eff}}^{\mathrm{res}} + R_{\mathrm{DR}} = \frac{1}{\tau_{\mathrm{on}}}. \tag{8}$$

Substituting Eq. (7) in Eq. (8) and solving for R_{DR} yields

$$R_{\mathrm{DR}} = \frac{1}{\tau_{\mathrm{on}}} - \frac{1}{\tau_{\mathrm{off}}}, \tag{9}$$

which can be converted into the DR rate coefficient by

$$\alpha_{\mathrm{DR}} = \frac{1}{n_e \eta_t}\left(\frac{1}{\tau_{\mathrm{on}}} - \frac{1}{\tau_{\mathrm{off}}}\right), \tag{10}$$

where n_e denotes the electron density in the target overlap region and η_t the ratio of the effective electron target length and the storage-ring circumference. With $n_e = 1.34 \times 10^6$ cm^{-3} and $\eta_t = 0.0199$ we calculate an H_3^+ DR rate coefficient of $\alpha_{\mathrm{DR}} = 1.53 \times 10^{-6}$ cm^3 s^{-1} at cooling energy. Note that this value is used to calibrate the measured rate coefficient before corrections for the toroidal regions of the electron target are applied. The toroid correction procedure [47] then accounts for the effective target length much more precisely and makes the final result almost independent of the exact value of η_t. We estimate an uncertainty of 30% for the calibration method of the absolute scale described above.

Figure 7 shows a comparison of the rate coefficient from the present work (1:5 n-H_2:Ar mixture) normalized to the lifetime measurement, and the 2002 CRYRING data. For the present work the electron cooler was switched on during the measurement and set to zero center-of-mass collision energy, while the electron target energy was scanned as described in Sec. II A 1. The comparison shows that the rate coefficient measured with the piezo expansion source and n-H_2:Ar is practically identical on an absolute scale with the rate coefficient measured at CRYRING with n-H_2 and a similar type of ion source. The fact that the rate coefficient can be reproduced in such detail at a different storage ring with different beam energies and measurement schemes confirms the stability and reproducibility of the storage-ring technique.

C. Dependence of the DR rate coefficient on the nuclear spin

To examine the dependence of the DR rate coefficient on the nuclear spin of H_3^+, we carried out measurements utilizing the supersonic expansion source with n-H_2:Ar and p-H_2:Ar gas mixtures, respectively. At center-of-mass collision energies >0.3 eV the measured rate showed no dependence on the nuclear spin of the precursor gas, in agreement with previous experiments [13,22]. In the following, we focus on the low energy region.

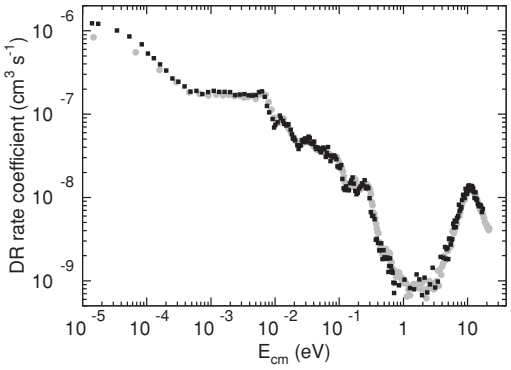

FIG. 7. DR rate coefficient as a function of the center-of-mass collision energy $E_{c.m.}$. The black squares depict the results of the present measurement obtained using the supersonic expansion source with a 1:5 n-H_2:Ar gas mixture. The data are independently normalized to the absolute rate measurement described in Sec. IV B. The gray dots represent the 2002 CRYRING measurement [11].

Figure 8(a) shows a comparison of the rate coefficient at low energies obtained with 1:5 n-H_2:Ar and 1:5 p-H_2:Ar mixtures, respectively. The rate coefficient has been multiplied by $\sqrt{E_{c.m.}}$ in all cases to eliminate the inherent $1/v$ dependence for clarity of presentation. The data obtained using p-H_2 show a slightly higher rate coefficient at low collision energies. While this general trend is consistent with previous measurements, we observe structural details in the rate coefficients that were not visible in either of the previous studies. The higher

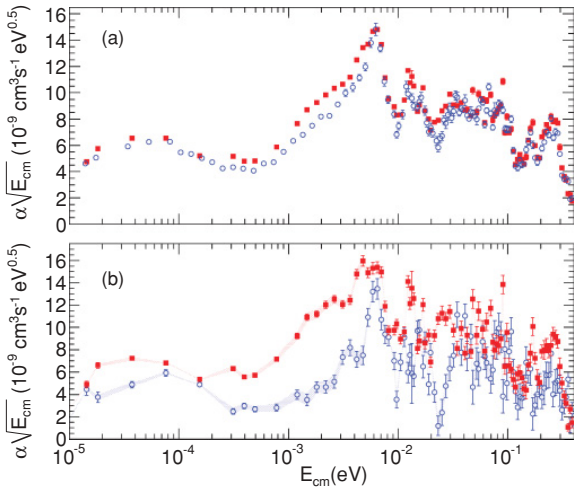

FIG. 8. (Color online) Comparison of the DR rate coefficient for different nuclear spin modifications of H_3^+. The upper panel (a) shows the results obtained with the supersonic expansion source and 1:5 n-H_2:Ar (blue circles) and 1:5 p-H_2:Ar (red squares) mixtures. The lower panel (b) shows the extrapolated results for "pure" p-H_3^+ (red squares) and "pure" o-H_3^+ (blue circles). For the extrapolation we assume a p-H_3^+ fraction of (47.9 ± 2)% for n-H_2:Ar and (70.8 ± 2)% for p-H_2:Ar (see discussion in the text). The error bands in the lower panel represent the effect of the 2% uncertainty in the spectroscopic determination of the p-H_3^+ fractions.

transverse electron temperature of ~4 meV in the experiment of Kreckel *et al.* [13] and ~2 meV for Tom *et al.* [22], as compared to ~1 meV for the present work, might be partly responsible for the absence of structure in those measurements. On the other hand, the 2002 CRYRING measurements [11] that were performed with the same ~2 meV transverse electron temperature as those of Tom *et al.* display distinctly more structure at low energy. Tom *et al.* suggest that the presence of excited rotational states, perhaps due to residual gas collisions in CRYRING, might have smoothed out the rate coefficient curve [22].

Figure 8(b) shows the rate coefficients of o-H_3^+ and p-H_3^+ extrapolated from the present measurements using n-H_2:Ar and p-H_2:Ar mixtures. For the extrapolation we assumed that the n-H_2:Ar mixture results in a p-H_3^+ fraction of 47.9% and the p-H_2:Ar mixture results in a p-H_3^+ fraction of 70.8%, as inferred from the cavity ring-down spectra. This procedure can be questioned, since the rotational temperature derived from DR fragment imaging is much higher than the rotational temperature of the ion source in the spectroscopic measurements. Hence, a heating process must exist that changes the rotational level populations. It is not clear whether this process will also influence the p-H_3^+ fraction, but since the initial 200 K temperature of the ion source is not too far from room temperature, here we assume that the measured nuclear spin distribution is a result of the high-temperature equilibrium as established in H_3^+-H_2 collisions and that further collisions with the same buffer gas at higher collision energies will not alter the p-H_3^+ fraction.

It should be mentioned, however, that experiments with isotopically substituted species suggest that $H_3^+ + H_2$ collisions at increased temperatures [48] proceed predominantly via the proton-hop channel. As the proton-hop reaction favors para-enrichment of H_3^+ in p-H_2 gas (see [49,50] for nuclear spin selection rules in $H_3^+ + H_2$ collisions), this could lead to an increase of the p-H_3^+ fractions when the ions are extracted through p-H_2 gas in the present case. Effectively, this would lead us to overestimate the differences between the o-H_3^+ and p-H_3^+ rate coefficients extrapolated for Fig. 8(b).

With that being said, the comparison in Fig. 8(b) shows differences between the rate coefficients for o-H_3^+ and p-H_3^+ at narrow structures in their energy dependence. At energies between 10^{-3} eV and 5×10^{-3} eV the p-H_3^+ rate coefficient is higher than the o-H_3^+ rate coefficient by roughly a factor of two. Below 10^{-3} eV the results must be considered less informative as the transverse electron temperature will dominate the measured rates. Above 10^{-2} eV there are distinct regions where the rate coefficients for the two nuclear spin modifications exhibit counterpropagating trends, resulting in rather large differences in the rate coefficients. Most notably is the region around 2.5×10^{-2} eV where the o-H_3^+ rate coefficient almost tends toward zero. Comparison to theory will reveal whether these energies can be matched with resonances in the DR cross section.

V. ION EXTRACTION

The fragment imaging results confront us with the fact that the rotational temperatures of the stored H_3^+ ions are much higher than the spectroscopically measured temperatures. On

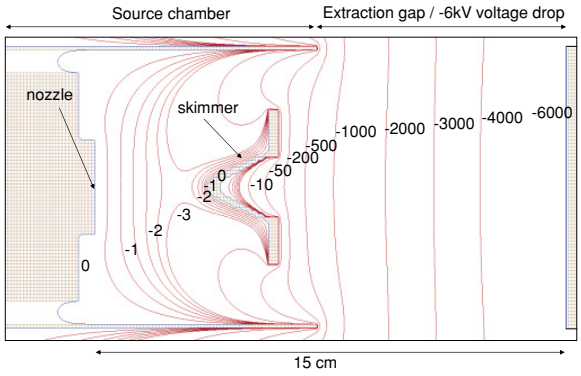

FIG. 9. (Color online) SIMION simulation of the extraction region for the supersonic ion source. The equipotential lines show the voltage difference with respect to the nozzle unit (in volt).

the other hand, the temperature of the stored ions *does* depend on the ion source that is used, which signifies that we are not dealing with a universal heating process inside the storage ring. Therefore, the acceleration process that takes place between the ion formation in the ion source and the DR measurements is the primary suspect for inducing rotational heating.

We have simulated the electric fields in the acceleration region for the supersonic expansion ion source with the SIMION 3D program suite [51,52]. Prior to injection into the accelerator of the TSR facility, the ions are extracted from the source and preaccelerated to 12 keV in two steps of 6 kV. Figure 9 shows the equipotential lines for the first extraction stage. It can be seen that besides the intended potential drop between the skimmer and the extraction electrode, the field lines also penetrate slightly into the region between skimmer and nozzle where the pressure is still high. Potentials up to 3 eV are reached in this region, possibly disturbing the expansion process.

Figure 10 shows various parameters in the region downstream of the nozzle for a pure hydrogen expansion. The upper panel shows the H_2 number density $n(H_2)$ on the axis going through the midpoint of the nozzle and the center of the skimmer. The number density was estimated using a simple $1/r^2$ scaling law [53]. The middle panel shows the electric field strength and the lower panel the estimated mean free path d of the H_3^+ ions. The mean free path is calculated using the following assumptions: (i) the rate coefficient for $H_3^+ + H_2$ collisions is constant with a value $\alpha_{\mathrm{col}} = 1.3 \times 10^{-9}$ cm^3 s^{-1} [54]; (ii) the energy and thus the velocity $v(H_3^+)$ of the H_3^+ ions is determined by the electrostatic potential alone. With these assumptions the energy-dependent collision cross section can be approximated by

$$\sigma_{\mathrm{col}} = \frac{\alpha_{\mathrm{col}}}{v(H_3^+)}, \tag{11}$$

and the mean free path is given by

$$d = \frac{1}{\sigma n(H_2)}. \tag{12}$$

The plots show that the ions are likely to undergo many collisions while being accelerated away from the nozzle. The skimmer extends from distances of ∼3.7 cm to ∼5.7 cm after

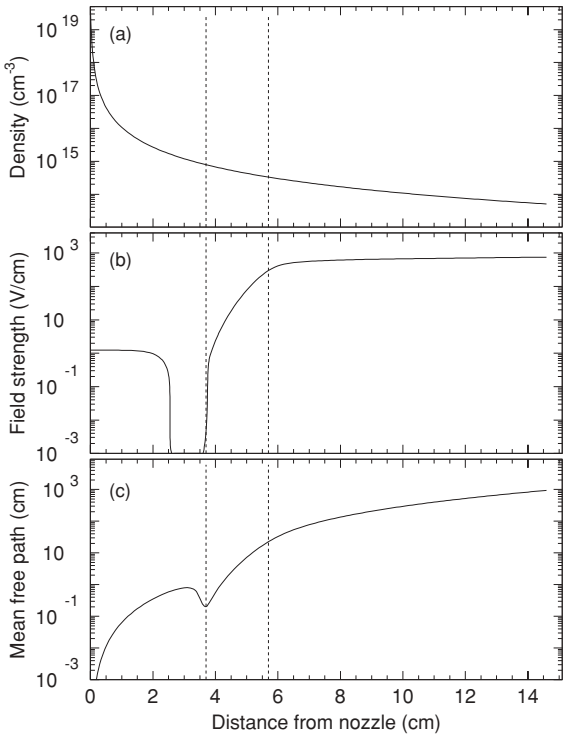

FIG. 10. Plots of the density (a), electric field strength (b), and the estimated mean free path (c) in the extraction region of the supersonic expansion source for pure H_2 gas. Details on the mean free path approximation are given in the text. The dashed lines mark the beginning and the end of the skimmer.

the nozzle. The mean free path in this region ranges from 10^{-3} cm to 1 cm, while electric field strengths are on the order of 0.1 V/cm. This indicates that the ions undergo many collisions while being accelerated through the gas before they reach the skimmer. After the skimmer the mean free path increases but the ions are still likely to interact with the expanding gas. It is possible that these nonthermal collisions are responsible for the elevated temperatures observed in the DR measurements. In order to avoid collisions during the ion extraction a longer undisturbed flight path before acceleration would be required.

VI. SUMMARY AND PERSPECTIVES

We have performed high-resolution measurements of the dissociative recombination of H_3^+ utilizing a spectroscopically calibrated supersonic expansion source. The line intensities obtained by cavity ring-down spectroscopy at the ion source indicate a rotational temperature of ∼200 K with 1:5 H_2:Ar gas mixtures. A comparison of the rate coefficient obtained using n-H_2 to a previous DR experiment with a similar type of ion source at CRYRING [11] shows a very strong agreement.

Measurements with n-H_2 and p-H_2 precursor gas show detailed differences in the rate coefficients for o-H_3^+ and p-H_3^+ at low energies.

While the spectroscopic measurements with the piezo ion source result in rotational temperatures on the order of 200 K, fragment imaging of the stored ions inside the storage ring reveal temperatures around ∼950 K and ∼450 K, respectively, where the lower value is reached during the interaction with cold electrons at the elevated density of the electron cooler. The large discrepancy between the spectroscopy results and the fragment imaging data is indicative of a heating process between ion production and electron recombination.

The apparent difference in temperature between the 22-pole trap ion source and the supersonic expansion seen in the fragment imaging data suggests that the heating is not a universal property of storage-ring measurements but is more likely to occur during the ion extraction. For future measurements a careful analysis of the electric fields and pressure profile in the ion extraction section is called for.

Previous and present comparisons between different storage rings exhibit a remarkable degree of reproducibilty for H_3^+ as well as for other molecular ions (see, e.g. [55]). The H_3^+ DR rate coefficient has been measured at heavy-ion storage rings with a multitude of different ion sources, ranging in temperature between 10 and 4000 K; still the rate coefficient never changed by more than 40%. The work presented here shows, however, that in order to reliably determine the rotational temperature of the stored ions, it has to be measured *in situ*, inside the storage ring. The fact that previous measurements with supersonic ion sources were done with similar ion extraction geometries and that the rate coefficient obtained in these measurements agrees with the present measurement in all details, suggests that these measurements were affected by the same heating mechanism. Unfortunately, no imaging data exist for these experiments to determine the rotational temperature.

Additional studies with optimized extraction geometries to reach lower rotational temperatures, as well as measurement schemes that would allow for a direct spectroscopic determination of the populated H_3^+ rotational levels inside the storage ring [56], are foreseen in the near future.

ACKNOWLEDGMENTS

H.K., K.N.C., B.A.T., and B.J.M. were supported by National Science Foundation (NSF) Grant No. PHY08-55633. O.N. was supported by NSF Astronomy and Astrophysics Grant No. AST-0807436. M.L. was supported by Astronomy and Physics Research and Analysis Grant No. NNX09AF74G. We thank Daniel W. Savin as the principal investigator of both these grants for partial support of the present project. H.B. acknowledges partial support from the German-Israeli Foundation for Scientific Research and Development (G.I.F.) under Grant No. I-900-231.7/2005 and from the European Project ITS LEIF (Grant No. HRPI-CT-2005-026015). We thank P. Buscay for assistance with the mechanical drawings for the supersonic expansion source. We thank M. König and the accelerator staff at MPI-K for their excellent support during the beam time. Support from the Max-Planck Society is acknowledged.

[1] A. Dalgarno, Adv. At. Mol. Opt. Phys. **32**, 57 (1994).
[2] M. Larsson and A. E. Orel, *Dissociative Recombination of Molecular Ions* (University Press, Cambridge, 2008).
[3] N. G. Adams, D. Smith, and E. Alge, J. Chem. Phys. **81**, 1778 (1984).
[4] D. Smith and N. G. Adams, J. Chem. Soc., Faraday Trans. 2 **83**, 149 (1987).
[5] H. H. Michels and R. H. Hobbs, Astrophys. J. Lett. **286**, L27 (1984).
[6] T. Amano, Astrophys. J. Lett. **329**, L121 (1988).
[7] M. Larsson *et al.*, Phys. Rev. Lett. **70**, 430 (1993).
[8] H. Kreckel *et al.*, Phys. Rev. A **66**, 052509 (2002).
[9] D. Strasser *et al.*, Phys. Rev. Lett. **86**, 779 (2001).
[10] H. Kreckel, J. Tennyson, D. Schwalm, D. Zajfman, and A. Wolf, New J. Phys. **6**, 151 (2004).
[11] B. J. McCall *et al.*, Nature (London) **422**, 500 (2003).
[12] B. J. McCall *et al.*, Phys. Rev. A **70**, 052716 (2004).
[13] H. Kreckel *et al.*, Phys. Rev. Lett. **95**, 263201 (2005).
[14] H. Kreckel, J. Mikosch, R. Wester, J. Glosík, R. Plašil, M. Motsch, D. Gerlich, D. Schwalm, D. Zajfman, and A. Wolf, J. Phys.: Conf. Ser. **4**, 126 (2005).
[15] J. Glosík, I. Korolov, R. Plašil, O. Novotný, T. Kotrík, P. Hlavenka, J. Varju, I. A. Mikhailov, V. Kokoouline, and C. H. Greene, J. Phys. B: At. Mol. Opt. Phys. **41**, 191001 (2008).
[16] J. Glosík, R. Plašil, I. Korolov, T. Kotrík, O. Novotný, P. Hlavenka, P. Dohnal, J. Varju, V. Kokoouline, and C. H. Greene, Phys. Rev. A **79**, 052707 (2009).
[17] S. Datz, G. Sundström, C. Biedermann, L. Broström, H. Danared, S. Mannervik, J. R. Mowat, and M. Larsson, Phys. Rev. Lett. **74**, 896 (1995).
[18] V. Kokoouline, C. H. Greene, and B. D. Esry, Nature (London) **412**, 891 (2001).
[19] V. Kokoouline and C. H. Greene, Phys. Rev. A **68**, 012703 (2003).
[20] V. Kokoouline and C. H. Greene, Phys. Rev. Lett. **90**, 133201 (2003).
[21] S. F. Dos Santos, V. Kokoouline, and C. H. Greene, J. Chem. Phys. **127**, 124309 (2007).
[22] B. A. Tom *et al.*, J. Chem. Phys. **130**, 031101 (2009).
[23] D. Habs *et al.*, Nucl. Instr. Meth. Phys. Res. B **43**, 390 (1989).
[24] F. Sprenger, M. Lestinsky, D. A. Orlov, D. Schwalm, and A. Wolf, Nucl. Instr. Meth. Phys. Res. A **532**, 298 (2004).
[25] D. A. Orlov, U. Weigel, D. Schwalm, A. S. Terekhov, and A. Wolf, Nucl. Instr. Meth. Phys. Res. A **532**, 418 (2004).
[26] D. Strasser, L. Lammich, H. Kreckel, M. Lange, S. Krohn, D. Schwalm, A. Wolf, and D. Zajfman, Phys. Rev. A **69**, 064702 (2004).
[27] D. Zajfman, Z. Amitay, C. Broude, P. Forck, B. Seidel, M. Grieser, D. Habs, D. Schwalm, and A. Wolf, Phys. Rev. Lett. **75**, 814 (1995).
[28] Z. Amitay *et al.*, Science **281**, 75 (1998).
[29] D. Shafir *et al.*, Phys. Rev. Lett. **102**, 223202 (2009).
[30] D. Proch and T. Trickl, Rev. Sci. Instrum. **60**, 713 (1989).

[31] B. A. Tom, A. A. Mills, M. B. Wiczer, K. N. Crabtree, and B. J. McCall, J. Chem. Phys. **132**, 081103 (2010).
[32] P. Birza, T. Motylewski, D. Khoroshev, A. Chirokolave, H. Linnartz, and J. P. Maier, Chem. Phys. **283**, 119 (2002).
[33] C. M. Lindsay and B. J. McCall, J. Mol. Spectrosc. **210**, 60 (2001).
[34] B. A. Tom, S. Bhasker, Y. Miyamoto, T. Momose, and B. J. McCall, Rev. Sci. Instrum. **80**, 016108 (2009).
[35] M. Goto, B. J. McCall, T. R. Geballe, T. Usuda, N. Kobayashi, H. Terada, and T. Oka, Publ. Astron. Soc. Japan **54**, 951 (2002).
[36] W. R. Johnson and G. Soff, At. Data Nucl. Data Tables **33**, 405 (1985).
[37] A. Balakrishnan, V. Smith, and B. P. Stoicheff, Phys. Rev. Lett. **68**, 2149 (1992).
[38] P. C. Cosby and H. Helm, Chem. Phys. Lett. **152**, 71 (1988).
[39] W. Kutzelnigg and R. Jaquet, Phil. Trans. R. Soc. A **364**, 2855 (2006).
[40] U. Galster, P. Kaminski, M. Beckert, H. Helm, and U. Müller, Eur. Phys. J. D **17**, 307 (2001).
[41] H. P. Helm (private communication).
[42] A. Petrignani *et al.*, J. Phys.: Conf. Ser. **192**, 012022 (2009).
[43] H. Kreckel *et al.*, J. Phys.: Conf. Ser. **88**, 012064 (2007).
[44] A. Petrignani *et al.* (in preparation).
[45] L. Lammich *et al.*, Phys. Rev. Lett. **91**, 143201 (2003).
[46] H. B. Pedersen *et al.*, Phys. Rev. A **72**, 012712 (2005).
[47] Z. Amitay, D. Zajfman, P. Forck, U. Hechtfischer, B. Seidel, M. Grieser, D. Habs, R. Repnow, D. Schwalm, and A. Wolf, Phys. Rev. A **54**, 4032 (1996).
[48] D. Gerlich, J. Chem. Soc., Faraday Trans. **89**, 2199 (1993).
[49] M. Cordonnier, D. Uy, R. M. Dickson, K. E. Kerr, Y. Zhang, and T. Oka, J. Chem. Phys. **113**, 3181 (2000).
[50] T. Oka, J. Mol. Spectrosc. **228**, 635 (2004).
[51] Computer code SIMION 3D 8.0, Scientific Instrument Services, Ringoes, NJ, 2008 [http://www.simion.com].
[52] D. A. Dahl, Int. J. Mass Spectrom. **200**, 3 (2000).
[53] H. C. W. Beijerinck, R. J. F. V. Gerwen, E. R. T. Kerstel, J. F. M. Martens, E. J. W. V. Vliembergen, M. r. Th. Smits, and G. H. Kaashoek, Chem. Phys. **96**, 153 (1985).
[54] N. G. Adams and D. Smith, Astrophys. J. **248**, 373 (1981).
[55] A. Al Khalili *et al.*, Phys. Rev. A **68**, 042702 (2003).
[56] A. Petrignani *et al.*, J. Phys.: Conf. Ser. **194**, 022101 (2009).

Appendix D

The ortho/para Ratio of H_3^+ in Laboratory and Astrophysical Plasmas

This appendix is a preprint of a manuscript in press at Philosophical Transactions of the Royal Society of London, Series A, published by Royal Society Publishing.

The ortho/para ratio of H_3^+ in laboratory and astrophysical plasmas

Kyle N. Crabtree and Benjamin J. McCall

Department of Chemistry, Astronomy, and Physics, University of Illinois, Urbana, IL, 61801, USA

In diffuse molecular clouds, the nuclear spin temperature of H_3^+ (∼30 K) is much lower than the cloud kinetic temperature (∼ 70 K). To understand this temperature discrepancy, we have measured the ratio of the hop to exchange pathways (α) in the $H_3^+ + H_2 \rightarrow H_2 + H_3^+$ reaction (which interconverts *ortho*- and *para*-H_3^+) using high resolution spectroscopy of the ν_2 fundamental band of H_3^+ in a hydrogenic plasma. We find that α decreases from 1.6 ± 0.1 at 350 K down to its statistical value of 0.5 ± 0.1 at 135 K. We use this result to model the steady-state chemistry of diffuse molecular clouds, finding good agreement with astronomical data provided the dissociative recombination rates of *ortho*- and *para*-H_3^+ are equal and the identity branching fraction for the $H_3^+ + H_2$ reaction is large. Our results highlight the need for further studies of the $H_3^+ + H_2$ reaction as well as state-selective measurements of H_3^+ dissociative recombination.

Key words: hydrogen, nuclear spin, spectroscopy, interstellar clouds.

1. Introduction

H_3^+ is the simplest polyatomic molecule, and has been of interest since its discovery by J. J. Thomson in 1911 [1]. At this time, little was known about molecular structure, as the tenets of quantum mechanics had not yet been fully developed. Considerable debate over the existence of the molecule (and the neutral molecule H_3) ensued, and it was not until the 1930s that H_3^+ was recognized as a "stable" species [2]. Over the next few decades, it was proposed that H_3^+ could be present in space, as it could be produced via cosmic ray ionization of H_2, followed by the reaction $H_2^+ + H_2 \rightarrow H_3^+ + H$. By the early 1970s, H_3^+ was recognized as the initiator of ion-molecule chemistry in the interstellar medium [3, 4]. Since its infrared spectrum was measured in the laboratory by Oka in 1980 [5], its astronomical importance has been confirmed by its detection in a variety of environments, such as interstellar clouds [6, 7], the Galactic Center [8, 9], and planetary atmospheres [10–12].

In addition to its astronomical significance, H_3^+ is of fundamental importance. As the simplest polyatomic molecule, it serves as a critical benchmark species for ab initio calculations [13]. Its molecular symmetry is also interesting, and can be of pedagogical significance. Its equilibrium geometry is that of an equilateral triangle belonging to the D_{3h} point group. To treat H_3^+ with group theory [14] is a straightforward exercise that could be taught in a classroom, and the results have

Phil. Trans. A 1–13; doi: 10.1098/rspa.00000000

a practical impact on its spectroscopic properties. Owing to the Pauli exclusion principle, in its vibrational ground state, the $(J,K)=(0,0)$ rotational level is forbidden, and spectroscopic transitions arising from that level are not observed experimentally. Another consequence of the Pauli principle is that the nuclear spin configurations [$I=3/2$ (*ortho*) and $I=1/2$ (*para*)] are linked to the rotational manifold, similar to H_2. Also like H_2, interconversion between *ortho*- and *para*-H_3^+ (o-H_3^+ and p-H_3^+) can only be accomplished by interaction with a strong, inhomogeneous magnetic field or by a chemical reaction.

The primary chemical reaction that can interconvert the nuclear spin configuration of H_3^+ is the reaction $H_3^+ + H_2 \rightarrow H_3^+ + H_2$. On the surface, this would not appear to be a chemical reaction in the traditional sense, as the reactants and products are the same, but upon closer examination bonds are broken and formed, as can be seen from the possible outcomes of the reaction:

$$\begin{aligned} \tilde{H}_3^+ + H_2 &\rightarrow \tilde{H}_3^+ + H_2 \\ \tilde{H}_3^+ + H_2 &\rightarrow H_2\tilde{H}^+ + \tilde{H}_2 \\ \tilde{H}_3^+ + H_2 &\rightarrow \tilde{H}_2H^+ + H\tilde{H} \end{aligned}$$

These are called the "identity," "hop," and "exchange" pathways; they represent how the hydrogen atoms can be rearranged after scrambling via an $(H_5^+)^*$ collision complex. However, these scrambling processes must obey selection rules based on conservation of nuclear spin angular momentum [15, 16]. These three processes can be expressed in terms of their branching fractions S^{id}, S^{hop}, and S^{exch}, with $S^{id}+S^{hop}+S^{exch}=1$. The ratio of the rates of the hop and exchange reactions ($\alpha \equiv S^{hop}/S^{exch}$) is the critical parameter that governs how exactly this reaction interconverts the nuclear spin configurations of both H_3^+ and H_2, while S^{id} represents the fraction of collisions that do not result in hydrogen scrambling.

Prior to this work, the only study of the $H_3^+ + H_2$ scrambling reaction was done by the Oka group [17]. In that work, they probed a hydrogenic plasma with high resolution infrared spectroscopy to measure transitions arising from various o-H_3^+ and p-H_3^+ rotational levels, thereby measuring the *ortho*:*para* ratio. They did this with "normal" hydrogen gas (75% o-H_2, 25% p-H_2), and also with nearly pure p-H_2, and they found an enhancement in the p-H_3^+ abundance in the plasma enriched with p-H_2. This was the first observation of nuclear spin selection rules in a chemical reaction, and from the p-H_3^+ enhancement they derived $\alpha = 2.4 \pm 0.6$ at an estimated temperature of 400 K.

In this contribution, we will discuss our work on measuring the hop:exchange ratio α at lower temperatures using a liquid nitrogen cooled plasma cell, and its implications for chemistry in interstellar space. In Section 2, we describe our experiment, and in Section 3 we discuss the results of the measurements. Section 4 covers the chemistry of diffuse molecular clouds, and how our measurements of the $H_3^+ + H_2$ reaction factor into the hydrogenic chemistry. We conclude in Section 5 with some closing thoughts and future directions on the study of nuclear spin effects in the $H_3^+ + H_2$ system.

2. Experimental Details

The details of this experiment have been presented previously [18], and will be summarized briefly here. The goal of the experiment is to measure the *ortho*:*para* ratio of H_3^+ (rather, the p-H_3^+ fraction p_3) in a hydrogenic plasma of known p-H_2 fraction (p_2) at a known temperature. Hydrogen gas with a known p-H_2 fraction was prepared by combining appropriate amounts of high purity normal hydrogen and $> 99.9\%$ pure p-H_2 (produced with a p-H_2 converter [19]) to give mixtures of 25%, 40%, 50%, 66%, 83%, and $> 99.9\%$ p-H_2. This gas flowed into a hollow cathode plasma cell made from a ~ 1.4 m cylindrical copper tube encased in a glass cell evacuated with a mechanical pump. At each end were Brewster windows to allow a laser to traverse the cell, and the copper tube was wrapped in additional small tubing to allow coolant circulation. A plasma was generated throughout the length of the cell by applying a 1 kV pulse 200 μs in duration to a stainless steel anode located a few inches above a hole in the center of the copper cathode, which was grounded.

To measure the p-H_3^+ fraction generated in the plasma pulse, several low-J rovibrational transitions in the ν_2 fundamental band of H_3^+ were recorded with multipass direct absorption laser spectroscopy. Tunable mid-infrared light was produced by a difference frequency generation laser, and was passed through the hollow cathode cell 4-8 times in a White configuration. After exiting the cell, the light was measured with a DC InSb detector and sent to a computer for digitization. The transitions were recorded in a step-scan mode, in which multiple pulses were averaged at each laser frequency. After processing, the integrated intensity and linewidth of each transition were recorded as a function of time. After recording a series of transitions, the linewidths were averaged to calculate the kinetic temperature of the plasma, and the integrated intensities were used to calculate the rotational temperature and p-H_3^+ fraction. For each gas mixture, measurements were taken with the cell uncooled and also with liquid nitrogen cooling, and at each temperature measurements were taken at two different cell pressures.

3. Results and Discussion

The results of the experiment in both the uncooled cell ($T \sim 350$ K) and in the liquid nitrogen cooled cell ($T \sim 135$ K) are plotted in Figure 1. From the data, a few observations are readily apparent:

- The cell pressure has little influence on the observed p-H_3^+ fraction.
- The p-H_3^+ fraction generally is greater in plasmas enriched in p-H_2.
- At higher temperatures, the degree of p-H_3^+ enrichment is greater at larger p-H_2 fraction compared to the low temperature data.
- The p_3 vs. p_2 trend at high temperature is nearly linear, but not at low temperature.

These observations can be understood through use of modeling based on nuclear spin statistics and steady state kinetics. The $H_3^+ + H_2$ reaction is

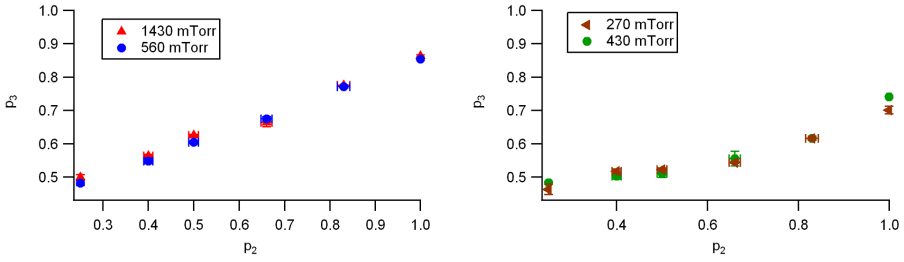

Figure 1. p-H_3^+ fraction vs. p-H_2 fraction in the hollow cathode plasma. (left) Uncooled cell. (right) Liquid nitrogen cooled cell. Graphs reproduced from Ref. [18] with permission of AIP Publishing.

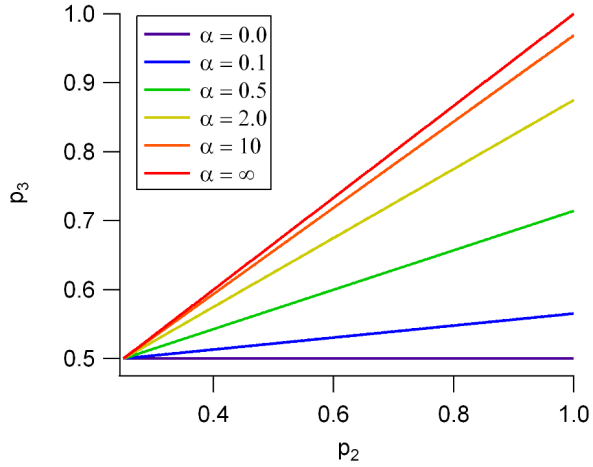

Figure 2. Plot of Equation 3.1 for values of α ranging from 0 (purple, horizontal) to ∞ (red, top). Figure reproduced from Ref. [20] with permission of AIP Publishing.

assumed to proceed through an $(H_5^+)^*$ collision complex in which hydrogen scrambling occurs. Under the assumption that the complex contains sufficient energy to populate any of a large number of H_3^+/H_2 product rotational states, the probability of any particular reaction outcome is proportional to its statistical weight. In the case of the $H_3^+ + H_2$ reaction, the statistical weights for each reaction channel can be calculated for each reaction "mechanism:" whether a hop or exchange pathway is followed [16]. By combining these mechanism-specific statistical weights into a steady state model for the p-H_3^+ fraction [20], the relationship between p_3 and p_2 at steady state is:

$$p_3 = \frac{\alpha + 2\alpha p_2 + 1}{3\alpha + 2} \tag{3.1}$$

Equation 3.1 shows that the relationship between p_3 and p_2 is linear, and the slope of the line is related to α (see Figure 2).

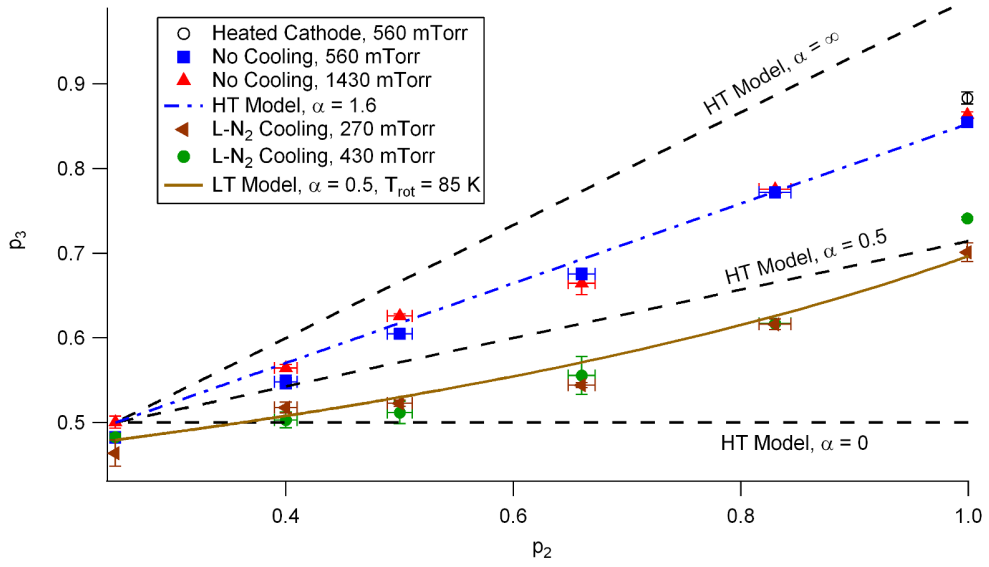

Figure 3. Summary of all data acquired in the hollow cathode, along with modeling results. Figure reproduced from Ref. [18] with permission of AIP Publishing.

The high temperature data are fit well by this equation, yielding $\alpha = 1.6 \pm 0.1$ at a temperature of 350 K. This is slightly lower than the value of 2.4 ± 0.6 reported previously at a temperature of 400 K. However, the data obtained in the liquid nitrogen cooled cell are clearly nonlinear, and are not well fit by Equation 3.1. At the lower temperature (~ 135 K), the assumption that any of a large number of product rotational states may be populated is less valid, as the energy level spacing of H_2 is > 170 K. Thus, because of energetic effects, the relative probability of a particular outcome may not be proportional to its statistical weight. To model the steady state chemistry at low temperature, nuclear spin dependent rate coefficients for the $H_3^+ + H_2$ reaction are calculated using a microcanonical statistical model [21], taking temperature, S^{id}, and α as parameters. Using these rate coefficients, at steady state

$$p_3 = \frac{(k_{oopp} + k_{oopo})(1 - p_2) + k_{oppo}p_2}{(k_{oopp} + k_{oopo} + k_{poop} + k_{pooo})(1 - p_2) + (k_{oppo} + k_{ppoo})p_2}, \tag{3.2}$$

where, for example, k_{oppo} is the rate coefficient for the reaction o-$H_3^+ + p$-$H_2 \rightarrow p$-$H_3^+ + o$-H_2.

The experimental results are shown together with the modeling results in Figure 3. The low temperature data are well-described by Equation 3.2 using rate coefficients calculated with $\alpha = 0.5$ and $T = 135$ K. Overall, the observed trend is that α increases with increasing temperature. To test this, the hollow cathode cell was heated to 450 K by flowing hot ethylene glycol through the coils, and the p-H_3^+ fraction was measured in a pure p-H_2 plasma. As can be seen in Figure 3, the observed p_3 value is even greater than that at 350 K, suggesting a larger value of α. This single point is consistent with $\alpha = 2.2 \pm 0.3$, consistent

with the overall trend of increasing α with temperature, and also in line with the measurements from Oka's laboratory [17].

Physically, the results suggest that the hop-to-exchange ratio α is determined by the lifetime of the $(H_5^+)^*$ complex formed in the collision between H_3^+ and H_2. The lifetime is important because, semiclassically, the hop pathway only requires that a single hydrogen move from H_3^+ to H_2, while in order for an exchange to occur, the complex must at least undergo a hop, and internal rotation, and another hop. At higher temperatures, the average complex lifetime is shorter owing to the higher collision energy, and the hop pathway is favored simply because fewer complexes exist for sufficient time to allow the exchange to occur. When the complex lifetime is sufficiently long, the complex can fully scramble, leading to the statistical outcome $\alpha = 0.5$. At 135 K, the statistical value of 0.5 is already observed, so, barring any quantum effects at extremely low temperatures, we would expect that α will remain at that value at even lower temperatures.

4. Diffuse Cloud Modeling

The $H_3^+ + H_2$ reaction is of particular importance in interstellar clouds, where it is responsible for thermalizing the *ortho*:*para* ratio of H_3^+. Of particular interest are diffuse molecular clouds, because the chemistry is very simple and yet the *ortho*:*para* ratio of H_3^+ is not well understood. Diffuse molecular clouds are regions of space with densities around 10^2 cm^{-3}, most hydrogen in molecular form, and most carbon in the form of C^+ [22]. Temperature in these environments is generally determined by measuring the *ortho*:*para* ratio of H_2 (called T_{01}), which is very rapidly thermalized through collisions with abundant protons [23]. A survey of diffuse molecular clouds yields $\langle T_{01} \rangle \sim 70$ K [24–26], but $\langle T(H_3^+) \rangle$, the temperature derived from observations of the *ortho*:*para* ratio of H_3^+, is ~ 30 K [27].

Recent observations[1] [23] provide a total of 6 clouds in which *ortho*:*para* ratios of both H_3^+ and H_2 have been measured. For H_3^+, spontaneous emission brings all p-H_3^+ into its lowest (J,K)=(1,1) rotational state faster than the collisional timescale. In the case of o-H_3^+, its lowest-energy (1,0) state is the only state significantly populated at diffuse cloud temperatures, so measurement of the ratio of column densities $N(1,0)/N(1,1)$ gives the *ortho*:*para* ratio of H_3^+ directly. The ratios observed in diffuse clouds are plotted in Figure 4 in terms of their *para* fractions, and the data are shown in Table 1. From the observations, it can be seen that the p-H_3^+ fraction is not in thermodynamic equilibrium with its environment, as measured by the p-H_2 fraction.

The chemistry of H_3^+ in diffuse molecular clouds is simple. As discussed in the introduction, it is formed from cosmic ray ionization of H_2, followed by the reaction $H_2^+ + H_2 \rightarrow H_3^+ + H$, and is destroyed primarily through dissociative recombination (DR) with electrons. Because the nuclear spin configurations of H_2 are rapidly brought into thermodynamic equilibrium, the p-H_2 fraction can

[1] The data presented in this paper differ from those in Ref. [23]. The raw data have been re-reduced to correct some recently discovered errors, and one additional H_3^+ detection has been added. Further details are available in Ref. [28].

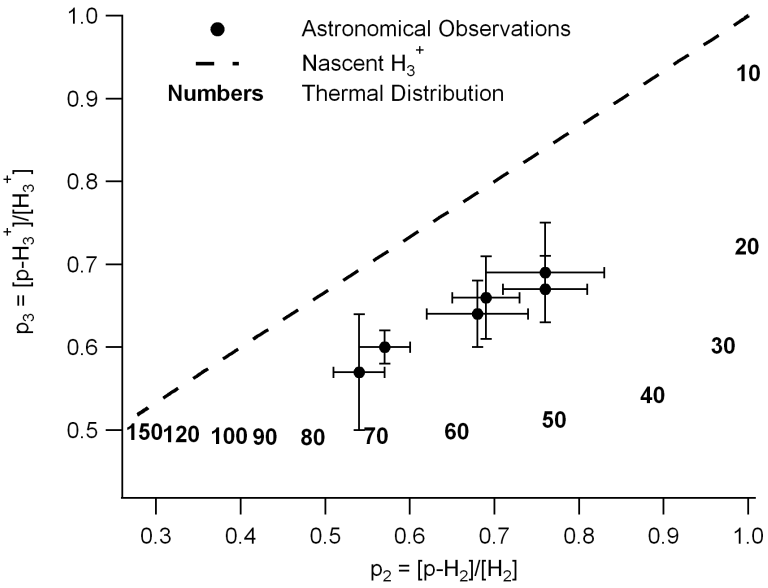

Figure 4. Observed *para* fractions of H_3^+ and H_2 in diffuse molecular clouds. The dotted line shows the *p*-H_3^+ fraction formed from the $H_2^+ + H_2$ reaction, and the numbers show the *para* fractions at thermodynamic equilibrium for the temperature given by the number at that point. Figure adapted from Ref [23] with permission of the American Astronomical Society.

Target	p_2	p_3	T_{01}	$T(H_3^+)$
ζ Per	$0.68 \pm .06$	$0.65 \pm .04$	58 ± 6	25 ± 3
X Per	$0.69 \pm .03$	$0.66 \pm .06$	57 ± 3	25 ± 5
HD 73882	$0.76 \pm .05$	$0.68 \pm .05$	51 ± 4	23 ± 4
HD 110432	$0.57 \pm .03$	$0.59 \pm .03$	69 ± 3	31 ± 4
HD 154368	$0.76 \pm .07$	$0.69 \pm .07$	51 ± 6	22 ± 5
λ Cep	$0.54 \pm .03$	$0.57 \pm .09$	72 ± 4	34 ± 13

Table 1. Diffuse molecular cloud sight lines, observed *para* fractions, and temperatures. All H_3^+ data are from Ref. [28] and references therein. All H_2 data are from Ref. [25] except those of ζ Per, which are from Ref. [24].

Reaction	Collision Fraction	Branching Fraction	p-H_3^+ Fraction
p-H_2^+ + p-H_2	$(p_2)^2$	1	p_2^2
p-H_2^+ + o-H_2	$p_2(1-p_2)$	2/3	$(2/3)(1-p_2)p_2$
o-H_2^+ + p-H_2	$(1-p_2)p_2$	2/3	$(2/3)(1-p_2)p_2$
o-H_2^+ + o-H_2	$(1-p_2)^2$	1/3	$(1/3)(1-p_2)^2$
Total	–	–	$(1/3)+(2/3)p_2$

Table 2. This table presents the calculation of the nascent p-H_3^+ fraction formed in diffuse molecular clouds from the $H_2^+ + H_2$ reaction, assuming that cosmic ray ionization of H_2 to form H_2^+ does not affect its nuclear spin configuration. The collision fraction represents the fraction of total $H_2^+ + H_2$ collisions with the specified nuclear spin configurations. The branching fractions are for p-H_3^+ formation, and are derived from nuclear spin selection rules [15, 16]. The final column presents the calculation of the nascent p-H_3^+ fraction. Table adapted from Ref. [23] with permission of the American Astronomical Society.

be treated as a constant, and it is straightforward to calculate the nascent p-H_3^+ fraction as it is formed from H_2 (see Table 2 and the dotted line in Figure 4). The observed p-H_3^+ fractions fall between their nascent values and their equilibrium values, implying that H_3^+ does not undergo sufficient collisions with H_2 during its lifetime to thermalize its nuclear spin prior to its destruction via DR.

To model the chemistry occurring in diffuse molecular clouds, we have built a steady state chemical model that takes into account the nuclear spin dependence of the relevant reactions involving H_3^+. [23] The result is

$$\begin{aligned} p_3 &= \left[k_{e,o}\frac{2x_e}{f}\left(\frac{1}{3}+\frac{2}{3}p_2\right)+(k_{oopp}+k_{oopo})(1-p_2)+k_{oppo}p_2\right] \\ &\quad \Bigg/\left[k_{e,p}\frac{2x_e}{f}\left(\frac{2}{3}-\frac{2}{3}p_2\right)+k_{e,o}\frac{2x_e}{f}\left(\frac{1}{3}+\frac{2}{3}p_2\right)+\right. \\ &\quad \left.(k_{oopp}+k_{oopo}+k_{poop}+k_{pooo})(1-p_2)+(k_{oppo}+k_{ppoo})p_2\right], \quad (4.1) \end{aligned}$$

where $k_{e,o}$ and $k_{e,p}$ are the DR rate coefficients for o-H_3^+ and p-H_3^+, respectively, x_e is the fractional abundance of electrons (typically $\sim 1.5\times10^{-4}$), and f is the local molecular fraction $(2n(H_2)/[n(H)+2n(H_2)]$; we adopt a value of 0.9 as the gas is thought to be highly molecular in these regions). Equation 4.1 is similar to Equation 3.2, with the addition of terms related to H_3^+ formation and destruction particular to diffuse molecular clouds. The k_{xxxx} rate coefficients are calculated using the aforementioned microcanonical statistical model [21]. Because of the low temperatures in these environments (< 130 K), we compute these rate coefficients using $\alpha = 0.5$. The kinetic temperature at which they are calculated is determined by the value of p_2, as the p-H_2 fraction is in thermodynamic equilibrium with the environment. Finally, the k_{xxxx} rate coefficients are calculated assuming a rotational temperature of 10 K because H_3^+ undergoes spontaneous emission faster than the collisional timescale at such low densities. By doing this, we ensure that the rate coefficients we compute have all p-H_3^+ in the (1,1) state and all o-H_3^+

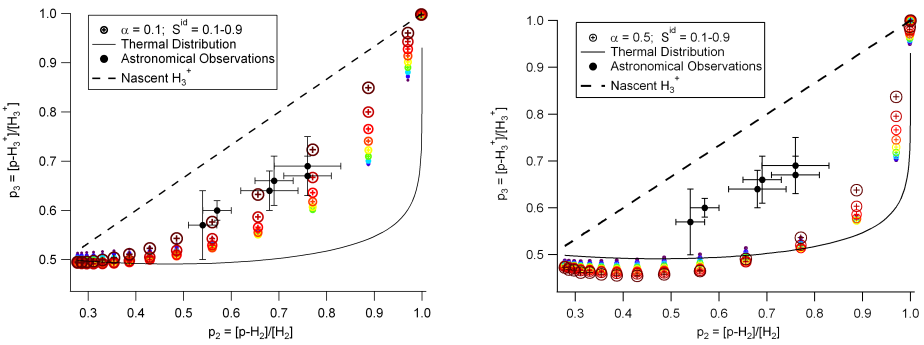

Figure 5. Results of Equation 4.1. (a) Results using dissociative rate coefficients from Ref. [29]. The clusters of points are calculated from 10-160 K in steps of 10 K from right to left. Within each cluster, the identity branching fraction S^{id} varies from 0.1 (small purple symbols) to 0.9 (large brown symbols). (b) Results using the theoretical dissociative rate coefficients from Ref. [33]. If S^{id} is set to 1, the model still does not come into agreement with the astronomical data. Graphs adapted from Ref. [23] with permission of the American Astronomical Society.

in the (1,0) state, so the extra rotational energy of (2,2) and (2,1) (which decay spontaneously between collisions) is not included.

Using spin-independent low-temperature dissociative rate coefficients measured using the storage ring technique [29], we obtain the results plotted in Figure 5(a). The agreement with the astronomical observations is particularly good for $S^{id} \sim 0.9$. The identity branching fraction is not well-constrained from current experimental data, as only the hop:exchange ratio α could be determined. If S^{id} really is 0.9, that would imply that a large fraction of collisions included in the total collisional rate coefficient (the Langevin rate 1.91×10^{-9} cm^3 s^{-1}) do not form scrambling complexes. However, more recent storage ring measurements of the H_3^+ DR rate have shown that the o-H_3^+ and p-H_3^+ rates are not equal, but differ by a factor of 2 ($k_{e,p} \approx 2k_{e,o}$) [30, 31]. However, the latest storage ring measurements call into question the results of the prior studies [32]. Recent theory agrees with this general trend, but predicts that for the lowest states of H_3^+ $k_{e,p} \approx 10k_{e,o}$ [33], and recent flowing afterglow measurements [34] are consistent with the theoretical results. In all, the uncertainty in the DR rate coefficients is just as large a problem as the uncertainty in S^{id} (see Figure 5(b)), highlighting the need for further experimental studies of these reactions before the diffuse cloud chemistry can completely be understood.

5. Perspectives

We have measured the hop-to-exchange ratio α of the $H_3^+ + H_2$ reaction for the first time at low temperature, and found that at 135 K, it is at its statistical value of 0.5. The value of α increases with temperature because the $(H_5^+)^*$ collision complex has a shorter lifetime, favoring the hop pathway over the exchange. We would expect α to remain at its statistical value at even lower temperatures, but

further experimental work is needed for verification. One way of performing such measurements is to use the ion trap/laser-induced reaction method [35], which has the potential of reaching temperatures as low as 10-20 K. Such measurements may also provide absolute rate coefficients, thereby determining the value of S^{id}.

Our experimental results have guided efforts at understanding the H_3^+-H_2 temperature discrepancy in diffuse molecular clouds. Using steady state modeling, we are able to explain this discrepancy provided that o-H_3^+ and p-H_3^+ have nearly equal DR rates, and that the value of S^{id} is on the order of 0.9. However, there is no experimental justification for $S^{id} = 0.9$, and equal o-H_3^+ and p-H_3^+ DR rates would contradict the most recent experimental and theoretical results, so at present the model only represents an early step towards understanding the observed temperature discrepancy. Further experimental measurements of the H_3^+ + H_2 reaction as well as state-specific H_3^+ DR rates would help validate or falsify our model. On the astronomical front, we are in the process of searching for H_3^+ in eight more diffuse molecular cloud sight lines in which H_2 measurements are available. Additional H_3^+ detections would provide additional data points to more firmly establish the relationship between the *ortho*:*para* ratios of H_3^+ and H_2.

The *ortho*:*para* ratio of H_2 is also a critical parameter in deuterium fractionation because o-H_2 acts as an energy reservoir capable of reversing fractionation reactions involving H_3^+. Deuterium fractionation is most commonly observed in cold, dense molecular clouds, where the visual extinction is too high to allow for UV measurements of the H_2 *ortho*:*para* ratio as is done in diffuse clouds. H_3^+, on the other hand, is readily observed in these environments. Given that a simple relationship between the H_3^+ and H_2 *ortho*:*para* ratios in diffuse clouds exists, it is possible that such a relationship also exists in dense clouds. The chemistry in dense clouds is much more complicated, and the steady state assumption may not be valid because the p-H_2 fraction can no longer be assumed constant, so modeling is comparatively more difficult. Nevertheless, with some additional modeling work it may be possible to infer the H_2 *ortho*:*para* ratio from measurements of H_3^+.

The authors would like to thank Kisam Park for providing software for calculating H_3^+ + H_2 nuclear spin dependent rate coefficients, as well as Brian Tom, Carrie Kauffman, Holger Kreckel, Nick Indirolo, Brett McGuire, and Eftalda Beçka for their contributions. This work has been supported by NSF PHY 08-55633. KNC has been supported by a NASA Earth and Space Science Fellowship.

References

[1] Thomson, J. J., 1911 Rays of positive electricity. *Phil. Mag.*, **21**, 225–249.

[2] Kragh, H., 2010 The childhood of H_3 and H_3^+. *Astron. Geophys.*, **51**(6), 6.25–6.27, doi:10.1111/j.1468-4004.2010.51625.x.

[3] Herbst, E. & Klemperer, W., 1973 The formation and depletion of molecules in dense interstellar clouds. *Astrophys. J.*, **185**, 505–534.

[4] Watson, W. D., 1973 The rate of formation of interstellar molecules by ion-molecule reactions. *Astrophys. J.*, **183**, L17.

[5] Oka, T., 1980 Observation of the infrared spectrum of H_3^+. *Phys. Rev. Lett.*, **45**(7), 531–534.

[6] Geballe, T. R. & Oka, T., 1996 Detection of H_3^+ in interstellar space. *Nature*, **384**, 334–335.

[7] McCall, B. J., Geballe, T. R., Hinkle, K. H. & Oka, T., 1998 Detection of H_3^+ in the diffuse interstellar medium toward Cygnus OB2 No. 12. *Science*, **279**, 1910–1913.

[8] Goto, M., McCall, B. J., Geballe, T. R., Usuda, T., Kobayashi, N., Terada, H. & Oka, T., 2002 Absorption line survey of H_3^+ toward the galactic center sources I. GCS 3-2 and GC IRS3. *Pub. Astron. Soc. Japan*, **54**, 951–961.

[9] Goto, M., Usuda, T., Nagata, T., Geballe, T. R., McCall, B. J., Indriolo, N., Suto, H., Henning, T., Morong, C. P. & Oka, T., 2008 Absorption line survey of H_3^+ toward the galactic center sources. II. Eight infrared sources within 30 pc of the galactic center. *Astrophys. J.*, **688**, 306–319.

[10] Drossart, P., Maillard, J.-P., Caldwell, J., Kim, S. J., Watson, J. K. G., Majewski, W. A., Tennyson, J., Miller, S., Atreya, S. K., Clarke, J. T. *et al.*, 1989 Detection of H_3^+ on Jupiter. *Nature*, **340**(6234), 539–541.

[11] Trafton, L. M., Geballe, T. R., Miller, S., Tennyson, J. & Ballester, G. E., 1993 Detection of H_3^+ from Uranus. *Astrophys. J.*, **405**, 761–766.

[12] Geballe, T. R., Jagod, M.-F. & Oka, T., 1993 Detection of H_3^+ infrared emission lines in Saturn. *Astrophys. J.*, **408**, L109–L112.

[13] Morong, C. P., Gottfried, J. L. & Oka, T., 2009 H_3^+ as the benchmark for rigorous ab initio theory. *J. Mol. Spectrosc.*, **255**(1), 13–23.

[14] McCall, B. J., 2001 *Spectroscopy of H_3^+ in laboratory and astrophysical plasmas*. Ph.D. thesis, University of Chicago.

[15] Quack, M., 1977 Detailed symmetry selection rules for reactive collisions. *Mol. Phys.*, **34**(2), 477–504.

[16] Oka, T., 2004 Nuclear spin selection rules in chemical reactions by angular momentum algebra. *J. Mol. Spectrosc.*, **228**(2), 635–639.

[17] Cordonnier, M., Uy, D., Dickson, R. M., Kerr, K. E., Zhang, Y. & Oka, T., 2000 Selection rules for nuclear spin modifications in ion-neutral reactions involving H_3^+. *J. Chem. Phys.*, **113**(8), 3181–3193.

[18] Crabtree, K. N., Kauffman, C. A., Tom, B. A., Beçka, E., McGuire, B. A. & McCall, B. J., 2011 Nuclear spin dependence of the reaction of H_3^+ with H_2 II. Experimental measurements. *J. Chem. Phys.*, **134**, 194 311.

[19] Tom, B. A., Bhasker, S., Miyamoto, Y., Momose, T. & McCall, B. J., 2009 Producing and quantifying enriched para-H_2. *Rev. Sci. Instrum.*, **80**(1), 016 108–3.

[20] Crabtree, K. N., Tom, B. A. & McCall, B. J., 2011 Nuclear spin dependence of the reaction of H_3^+ with H_2 I. Kinetics and modeling. *J. Chem. Phys.*, **134**, 194 310.

[21] Park, K. & Light, J. C., 2007 Microcanonical statistical study of ortho-para conversion in the reaction $H_3^+ + H_2 \rightarrow (H_5^+)^* \rightarrow H_3^+ + H_2$ at very low energies. *J. Chem. Phys.*, **126**(4), 044 305–19.

[22] Snow, T. P. & McCall, B. J., 2006 Diffuse atomic and molecular clouds. *Annu. Rev. Astron. Astrophys.*, **44**, 367–414.

[23] Crabtree, K. N., Indriolo, N., Kreckel, H., Tom, B. A. & McCall, B. J., 2011 On the *ortho:para* ratio of H_3^+ in diffuse molecular clouds. *Astrophys. J.*, **729**, 15.

[24] Savage, B. D., Bohlin, R. C., Drake, J. F. & Budich, W., 1977 A survey of interstellar molecular hydrogen. I. *Astrophys. J.*, **216**, 291–307.

[25] Rachford, B. L., Snow, T. P., Tumlinson, J., Shull, J. M., Blair, W. P., Ferlet, R., Friedman, S. D., Gry, C., Jenkins, E. B., Morton, D. C. *et al.*, 2002 A far ultraviolet spectroscopic explorer survey of interstellar molecular hydrogen in translucent clouds. *Astrophys. J.*, **577**, 221–244.

[26] Rachford, B. L., Snow, T. P., Destree, J. D., Ross, T. L., Ferlet, R., Friedman, S. D., Gry, C., Jenkins, E. B., Morton, D. C., Savage, B. D. *et al.*, 2009 Molecular hydrogen in the far ultraviolet spectroscopic explorer translucent lines of sight: The full sample. *Astrophys. J. Suppl. Ser.*, **180**, 125–137.

[27] Indriolo, N., Geballe, T. R., Oka, T. & McCall, B. J., 2007 H_3^+ in diffuse interstellar clouds: A tracer for the cosmic-ray ionization rate. *Astrophys. J.*, **671**(2), 1736–1747.

[28] Indriolo, N. & McCall, B. J., 2012 Investigating the cosmic-ray ionization rate in the galactic diffuse interstellar medium through observations of H_3^+. *Astrophys. J.*, **745**, 91, doi:10.1088/0004-637X/745/1/91.

[29] McCall, B. J., Huneycutt, A. J., Saykally, R. J., Djuric, N., Dunn, G. H., Semaniak, J., Novotny, O., Al-Khalili, A., Ehlerding, A., Hellberg, F. *et al.*, 2004 Dissociative recombination of rotationally cold H_3^+. *Phys. Rev. A*, **70**(5), 052 716.

[30] Kreckel, H., Motsch, M., Mikosch, J., Glosik, J., Plasil, R., Altevogt, S., Andrianarijaona, V., Buhr, H., Hoffmann, J., Lammich, L. *et al.*, 2005 High-resolution dissociative recombination of cold H_3^+ and first evidence for nuclear spin effects. *Phys. Rev. Lett.*, **95**(26), 263 201–4.

[31] Tom, B. A., Zhaunerchyk, V., Wiczer, M. B., Mills, A. A., Crabtree, K. N., Kaminska, M., Geppert, W. D., Hamberg, M., af Ugglas, M., Vigren, E. *et al.*, 2009 Dissociative recombination of highly enriched para-H_3^+. *J. Chem. Phys.*, **130**(3), 031101.

[32] Kreckel, H., Novotný, O., Crabtree, K. N., Buhr, H., Petrignani, A., Tom, B. A., Thomas, R. D., Berg, M. H., Bing, D., Grieser, M. *et al.*, 2010 Storage ring measurements of the dissociative recombination of H_3^+: A closer look. *Phys. Rev. A*, **82**, 042 715.

[33] dos Santos, S. F., Kokoouline, V. & Greene, C. H., 2007 Dissociative recombination of H_3^+ in the ground and excited vibrational states. *J. Chem. Phys.*, **127**(12), 124 309–8.

[34] Varju, J., Hejduk, M., Dohnal, P., Jílek, M., Kotrík, T., Plašil, R., Gerlich, D. & Glosík, J., 2011 Nuclear spin effect on recombination of H_3^+ ions with electrons at 77 K. *Phys. Rev. Lett.*, **106**(20), 203201, doi:10.1103/PhysRevLett.106.203201.

[35] Kreckel, H., Petrignani, A., Berg, M., Bing, D., Reinhardt, S., Altevogt, S., Buhr, H., Froese, M., Hoffmann, J., Jordon-Thaden, B. *et al.*, 2007 Electron collisions and rovibrational action spectroscopy of cold H_3^+ molecules. *J. Phys.: Conf. Ser.*, **88**(1), 012 064.

Appendix E

Notes on Nuclear Spin Statistics and the Degeneracy of para-H_3^+

The purpose of this Appendix is to highlight some aspects of the nuclear spin statistics and degeneracy of p-H_3^+ that are not clearly explained elsewhere in the literature. The first point to make is about the nature of the nuclear spin wavefunctions themselves. As discussed elsewhere in this dissertation, H_3^+ exists in two nuclear spin modifications: o-H_3^+ and p-H_3^+, with total nuclear spin angular momentum of 3/2 and 1/2, respectively. It is commonly stated, especially in conference talks, that o-H_3^+ has all three proton nuclear spins aligned, and p-H_3^+ has one proton anti-aligned with respect to the other two (see, for instance, [95]). While this is a simple intuitive picture, it is not accurate, primarily because a basis of individual proton spins is not symmetry-adapted to the S_3^* permutation-inversion group. Using the individual proton spin basis, one would derive that there exist two possible *ortho* configurations ($|\uparrow\uparrow\uparrow\rangle$ and $|\downarrow\downarrow\downarrow\rangle$), and six *para* configurations. A proper analysis [95] quickly reveals that there are in fact 4 *ortho* and 4 *para* configurations, with symmetries $4A_1'$ and $2E'$. In the symmetry-adapted total nuclear spin angular momentum basis, these wavefunctions are expressed as $|I_3, m_3, I_2\rangle$, where I_3 and m_3 are the total nuclear spin angular momentum of H_3^+ and its projection, and I_2 is the total nuclear spin angular momentum of two of the three protons in H_3^+. These wavefunctions can be calculated according to the formula

$$|I_3, m_3, I_2\rangle = \sum_{m_a, m_b, m_c} \langle I_c, m_c; I_2, m_2 |\ I_3, m_3\rangle \langle I_a, m_a; I_b, m_b |\ I_2, m_2\rangle |m_a, m_b, m_c\rangle \tag{E.1}$$

where m_a, m_b, and m_c are the projections of the individual proton spins ($\pm 1/2$), $m_2 = m_a + m_b$, and $\langle I_x, m_x; I_y, m_y |\ I_z, m_z\rangle$ represents a Clebsch Gordan coefficient. The results of this calculation are shown in Table E.1, and it can be seen that while it is true that two of the *ortho* wavefunctions do in fact correspond to the situations in which all three individual proton spins are aligned, the other two are linear combinations of multiple proton basis functions, and all *para* wavefunctions are linear combinations.

Because of the fact that p-H_3^+ has $2E'$ nuclear spin symmetry, is is commonly stated that p-H_3^+ has a statistical weight of 2, while o-H_3^+ has a statistical weight of 4 ($4A_1'$). [95, 118] However, such a statement is incorrect, because it neglects that an E' representation has a dimension of 2, and this brings the statistical

Symmetry	I Basis	Proton Basis
A_1	$\left\|\frac{3}{2},\frac{3}{2},1\right\rangle$	$\left\|\uparrow\uparrow\uparrow\right\rangle$
A_1	$\left\|\frac{3}{2},\frac{1}{2},1\right\rangle$	$\frac{1}{\sqrt{3}}\left(\left\|\uparrow\uparrow\downarrow\right\rangle+\left\|\uparrow\downarrow\uparrow\right\rangle+\left\|\downarrow\uparrow\uparrow\right\rangle\right)$
A_1	$\left\|\frac{3}{2},-\frac{1}{2},1\right\rangle$	$\frac{1}{\sqrt{3}}\left(\left\|\uparrow\downarrow\downarrow\right\rangle+\left\|\downarrow\uparrow\downarrow\right\rangle+\left\|\downarrow\downarrow\uparrow\right\rangle\right)$
A_1	$\left\|\frac{3}{2},-\frac{3}{2},1\right\rangle$	$\left\|\downarrow\downarrow\downarrow\right\rangle$
E	$\left\|\frac{1}{2},\frac{1}{2},1\right\rangle$	$\frac{1}{\sqrt{6}}\left(\left\|\downarrow\uparrow\uparrow\right\rangle+\left\|\uparrow\downarrow\uparrow\right\rangle-2\left\|\uparrow\uparrow\downarrow\right\rangle\right)$
	$\left\|\frac{1}{2},\frac{1}{2},0\right\rangle$	$\frac{1}{\sqrt{2}}\left(\left\|\uparrow\downarrow\uparrow\right\rangle-\left\|\downarrow\uparrow\uparrow\right\rangle\right)$
E	$\left\|\frac{1}{2},-\frac{1}{2},1\right\rangle$	$\frac{1}{\sqrt{6}}\left(2\left\|\downarrow\downarrow\uparrow\right\rangle-\left\|\downarrow\uparrow\downarrow\right\rangle-\left\|\uparrow\downarrow\downarrow\right\rangle\right)$
	$\left\|\frac{1}{2},-\frac{1}{2},0\right\rangle$	$\frac{1}{\sqrt{2}}\left(\left\|\uparrow\downarrow\downarrow\right\rangle-\left\|\downarrow\uparrow\downarrow\right\rangle\right)$

Table E.1: H_3^+ nuclear spin wavefunctions in terms of the proton spin basis.

S_3^*	A_1'	A_2'	E'	A_1''	A_2''	E''
A_1'	A_1'	A_2'	E'	A_1''	A_2''	E''
A_2'	A_2'	A_1'	E'	A_2''	A_1''	E''
E'	E'	E'	$A_1'\oplus A_2'\oplus E'$	E''	E''	$A_1''\oplus A_2''\oplus E''$
A_1''	A_1''	A_2''	E''	A_1'	A_2'	E'
A_2''	A_2''	A_1''	E''	A_2'	A_1'	E'
E''	E''	E''	$A_1''\oplus A_2''\oplus E''$	E'	E'	$A_1'\oplus A_2'\oplus E'$

Table E.2: S_3^* multiplication table

weight of p-H_3^+ to 4, as expected from Table E.1, and in accordance with other publications. [69, 78] Nevertheless, when considering an individual rotational level of p-H_3^+, the nuclear spin degeneracy is in fact 2, not 4. Such a situation is encountered, for instance, in calculating the excitation temperature T_{ex} for H_3^+ (see Chapter 4 and [70, 106] for examples), or when converting an absorption intensity into a number density as in Chapter 6. To understand why this is, it is important to note that the Pauli exclusion principle places restrictions on the total molecular wavefunction: it must be antisymmetric with respect to identical fermions. In terms of the S_3^* group, this means that $\Gamma=\Gamma_{elec}\otimes\Gamma_{vib}\otimes\Gamma_{rot}\otimes\Gamma_{ns}\subset\{A_2',A_2''\}$, where Γ is the irreducible representation of a wavefunction in the S_3^* group. In the vibronic ground state, $\Gamma_{elec}=\Gamma_{vib}=A_1'$, and therefore $\Gamma_{rot}\otimes\Gamma_{ns}\subset\{A_2',A_2''\}$. The multiplication table for S_3^* is shown in Table E.2.

The rotational wavefunction symmetry Γ_{rot} depends on the projection quantum number K in the vibrational ground state (for a more detailed discussion of the symmetry of H_3^+, see [95]), and the possibilities are listed in Table E.3. As a consequence of these symmetries, the nuclear spin wavefunctions listed in Table E.1 can only combine with certain rotational wavefunctions. For instance, *para* wavefunctions can only combine with rotational wavefunctions with $K=3n\pm1$, and *ortho* wavefunctions can only combine with

	K even	K odd
$K = 3n$	$A_1' \oplus A_2'$	$A_1'' \oplus A_2''$
$K = 3n \pm 1$	E'	E''
	J even	J odd
$K = 0$	A_1'	A_2'

Table E.3: Irreducible representations of H_3^+ rotational wavefunctions in the vibrational ground state (see [95]).

$K = 3n$ rotational wavefunctions. These selection rules also result in the fact that the $(J, K) = (0, 0)$ state is forbidden, because neither A_1' nor E' give A_2' or A_2'' when multiplied by A_1' (this applies to all states with J =even, $K = 0$ in the vibrational ground state). When considering a *para* level of H_3^+ (using $J = 1$,$K = 1$ as an example), the initial combination of rotational and nuclear spin wavefunction has a degeneracy of 8: $\Gamma_{rot} \otimes \Gamma_{ns} = E' \otimes 2E'$ (recall that each E representation has a degeneracy of 2). Of those 8 degenerate states, only two satisfy the Pauli exclusion principle, because $E' \otimes 2E' = 2A_1' \oplus 2A_2' \oplus 2E'$, and only the $2A_2$ states obey the appropriate exchange symmetry. It is important to note that the degeneracy of 2 comes from the nuclear spin portion of the wavefunction, not the rotational part as would be expected for a standard symmetric top in which the two $k = \pm K$ states are degenerate. It is not strictly true that one of the two k states is forbidden; rather, only two linear combinations of rotation/nuclear spin product wavefunctions satisfy exchange symmetry, and the origin of the 2 comes from the fact that there are two pairs of degenerate *para* wavefunctions. The same type of analysis holds for all other rotational levels of H_3^+, including levels that couple to *ortho* nuclear spin wavefunctions, as can be easily verified.

Why, then, is the statistical weight of 4 used for p-H_3^+ in Chapter 5 and in [69, 77, 78]? The reason is that in the high temperature limit, when considering proton scrambling in the $(H_5^+)^*$ complex, each of the 4 *para* and 4 *ortho* nuclear spin wavefunctions can combine with energetically accessible rotational levels in a symmetry-allowed manner. Thus, p-H_3^+ and o-H_3^+ have equal statistical weights when considered as a whole. However, as the temperature decreases this assumption begins to break down. Consider temperatures sufficiently low that only the (1,0) and (1,1) rotational levels of H_3^+ are energetically allowed. All 4 *ortho* nuclear spin wavefunctions can combine with the (1,0) level ($\Gamma_{rot} \otimes \Gamma_{ns} = A_2' \otimes 4A_1' = 4A_2'$), while only two of the *para* nuclear spin wavefunctions can combine with (1,1) as demonstrated above. As a result, at the lowest temperatures, under some circumstances it is possible to enrich the o-H_3^+ fraction above its statistical value of 1/2 (up to a maximum of 2/3), as has been observed in extremely low temperature plasmas in an ion trap (o-H_3^+ fraction = 0.6). [81]

References

[1] E. Herbst, W. Klemperer, Astrophys. J. 185 (1973) 505–534.

[2] W. D. Watson, Astrophys. J. 183 (1973) L17–L20.

[3] A. A. Mills, B. M. Siller, M. W. Porambo, M. Perera, H. Kreckel, B. J. McCall, J. Chem. Phys. 135 (2011) 224201.

[4] H. C. W. Beijerinck, R. J. F. Van Gerwen, E. R. T. Kerstel, J. F. M. Martens, E. J. W. Van Vliembergen, M. r. T. Smits, G. H. Kaashoek, Chem. Phys. 96 (1985) 153–173.

[5] D. C. Jordan, R. Barling, R. B. Doak, Rev. Sci. Instrum. 70 (1999) 1640–1648.

[6] J. Varju, M. Hejduk, P. Dohnal, M. Jílek, T. Kotrík, R. Plašil, D. Gerlich, J. Glosík, Phys. Rev. Lett. 106 (2011) 203201.

[7] P. Dohnal, M. Hejduk, J. Varju, P. Rubovič, v. Roučka, T. Kotrík, R. Plašil, J. Glosik, R. Johnsen, J. Chem. Phys. 136 (2012) 244304.

[8] C. P. Morong, J. L. Gottfried, T. Oka, J. Mol. Spectrosc. 255 (2009) 13–23.

[9] R. C. Woods, Rev. Sci. Instrum. 44 (1973) 282–288.

[10] S. Stephenson, R. Saykally, Chem. Rev. 105 (2005) 3220–3234.

[11] T. Amano, Phil. Trans. R. Soc. Lond. Ser. A 324 (1988) 163–178.

[12] C. M. Gabrys, D. Uy, M.-F. Jagod, T. Oka, T. Amano, J. Phys. Chem. 99 (1995) 15611–15623.

[13] S. Mohamed, M. C. McCarthy, A. L. Cooksy, C. Hinton, P. Thaddeus, J. Chem. Phys. 123 (2005) 234301.

[14] P. C. Engelking, Rev. Sci. Instrum. 57 (1986) 2274–2277.

[15] S. K. Lee, Chem. Phys. Lett. 358 (2002) 110–114.

[16] D. T. Anderson, S. Davis, T. S. Zwier, D. J. Nesbitt, Chem. Phys. Lett. 258 (1996) 207–212.

[17] M. C. McCarthy, W. Chen, M. J. Travers, P. Thaddeus, Astrophys. J. Suppl. Ser. 129 (2000) 611–623.

[18] T. Oka, Phys. Rev. Lett. 45 (1980) 531–534.

[19] C. M. Lindsay, B. J. McCall, J. Mol. Spectrosc. 210 (2001) 60–83.

[20] T. R. Geballe, T. Oka, Nature 384 (1996) 334–335.

[21] B. J. McCall, T. R. Geballe, K. H. Hinkle, T. Oka, Science 279 (1998) 1910–1913.

[22] N. Indriolo, T. R. Geballe, T. Oka, B. J. McCall, Astrophys. J. 671 (2007) 1736–1747.

[23] P. Drossart, J.-P. Maillard, J. Caldwell, S. J. Kim, J. K. G. Watson, W. A. Majewski, J. Tennyson, S. Miller, S. K. Atreya, J. T. Clarke, J. H. Waite, R. Wagener, Nature 340 (1989) 539–541.

[24] L. M. Trafton, T. R. Geballe, S. Miller, J. Tennyson, G. E. Ballester, Astrophys. J. 405 (1993) 761–766.

[25] T. R. Geballe, M.-F. Jagod, T. Oka, Astrophys. J. 408 (1993) L109–L112.

[26] T. R. Geballe, B. J. McCall, K. H. Hinkle, T. Oka, Astrophys. J. 510 (1999) 251–257.

[27] S. L. Widicus Weaver, M. B. Wiczer, B. Negru, J. P. DiGangi, B. A. Tom, B. J. McCall, J. Molec. Spectrosc. 249 (2008) 14–22.

[28] B. A. Tom, V. Zhaunerchyk, M. B. Wiczer, A. A. Mills, K. N. Crabtree, M. Kaminska, W. D. Geppert, M. Hamberg, M. af Ugglas, E. Vigren, W. J. van der Zande, M. Larsson, R. D. Thomas, B. J. McCall, J. Chem. Phys. 130 (2009) 031101.

[29] Y. Xu, M. Fukushima, T. Amano, A. R. W. McKellar, Chem. Phys. Lett. 242 (1995) 126–131.

[30] C. S. Gudeman, M. H. Begemann, J. Pfaff, R. J. Saykally, J. Chem. Phys. 78 (1983) 5837–5838.

[31] S. Davis, M. Fárník, D. Uy, D. J. Nesbitt, Chem. Phys. Lett. 344 (2001) 23–30.

[32] H. Linnartz, D. Verdes, T. Speck, Rev. Sci. Inst. 71 (2000) 1811–1815.

[33] C. S. Gudeman, M. H. Begemann, J. Pfaff, R. J. Saykally, Phys. Rev. Lett. 50 (1983) 727–731.

[34] B. M. Siller, A. A. Mills, B. J. McCall, Opt. Lett. 35 (2010) 1266–1268.

[35] A. A. Mills, B. M. Siller, B. J. McCall, Chem. Phys. Lett. 501 (2010) 1–5.

[36] L. C. Sinclair, K. C. Cossel, T. Coffey, J. Ye, E. A. Cornell, Phys. Rev. Lett. 107 (2011) 093002.

[37] J. Ye, L.-S. Ma, J. L. Hall, J. Opt. Soc. Am. B 15 (1998) 6–15.

[38] A. Foltynowicz, F. Schmidt, W. Ma, O. Axner, Appl. Phys. B 92 (2008) 313–326.

[39] B. M. Siller, M. W. Porambo, A. A. Mills, B. J. McCall, Opt. Exp. 19 (2011) 24822–24827.

[40] M. S. Taubman, T. L. Myers, B. D. Cannon, R. M. Williams, Spectrochim. Acta 60 (2004) 3457–3468.

[41] C. Lindsay, E. T. White, T. Oka, Chem. Phys. Lett. 328 (2000) 129–134.

[42] A. Foltynowicz, W. Ma, O. Axner, Opt. Express 16 (2008) 14689–14702.

[43] O. Axner, W. Ma, A. Foltynowicz, J. Opt. Soc. Am. B 25 (2008) 1166–1177.

[44] L. Velilla, B. Lepetit, A. Aguado, J. A. Beswick, M. Paniagua, J. Chem. Phys. 129 (2008) 084307–11.

[45] I. Silander, P. Ehlers, J. Wang, O. Axner, J. Opt. Soc. Am. B 29 (2012) 916–923.

[46] T. P. Snow, B. J. McCall, Annu. Rev. Astron. Astrophys. 44 (2006) 367–414.

[47] B. J. McCall, A. J. Huneycutt, R. J. Saykally, T. R. Geballe, N. Djuric, G. H. Dunn, J. Semaniak, O. Novotny, A. Al-Khalili, A. Ehlerding, F. Hellberg, S. Kalhori, A. Neau, R. Thomas, F. Österdahl, M. Larsson, Nature 422 (2003) 500–502.

[48] B. D. Savage, R. C. Bohlin, J. F. Drake, W. Budich, Astrophys. J. 216 (1977) 291–307.

[49] B. L. Rachford, T. P. Snow, J. Tumlinson, J. M. Shull, W. P. Blair, R. Ferlet, S. D. Friedman, C. Gry, E. B. Jenkins, D. C. Morton, B. D. Savage, P. Sonnentrucker, A. Vidal-Madjar, D. E. Welty, D. G. York, Astrophys. J. 577 (2002) 221–244.

[50] B. L. Rachford, T. P. Snow, J. D. Destree, T. L. Ross, R. Ferlet, S. D. Friedman, C. Gry, E. B. Jenkins, D. C. Morton, B. D. Savage, J. M. Shull, P. Sonnentrucker, J. Tumlinson, A. Vidal-Madjar, D. E. Welty, D. G. York, Astrophys J. Suppl. Ser. 180 (2009) 125–137.

[51] A. Dalgarno, J. H. Black, J. C. Weisheit, Astrophys. Lett. 14 (1973) 77–79.

[52] B. J. McCall, K. H. Hinkle, T. R. Geballe, T. Oka, Faraday Discuss. 109 (1998) 267–280.

[53] E. L. Gibb, S. D. Brittain, T. W. Rettig, M. Troutman, T. Simon, C. Kulesa, Astrophys. J. 715 (2010) 757–766.

[54] K. H. Hinkle, R. D. Blum, R. R. Joyce, N. Sharp, S. T. Ridgway, P. Bouchet, N. S. van der Bliek, J. Najita, C. Winge, Proc. SPIE 4834 (2003) 353–363.

[55] H. Käufl, P. Ballester, P. Biereichel, B. Delabre, R. Donaldson, R. Dorn, E. Fedrigo, G. Finger, G. Fischer, F. Franza, D. Gojak, G. Huster, Y. Jung, J. Lizon, L. Mehrgan, M. Meyer, A. Moorwood, J. Pirard, J. Paufique, E. Pozna, R. Siebenmorgen, A. Silber, J. Stegmeier, S. Wegerer, Proc. SPIE 5492 (2004) 1218–1227.

[56] M. Goto, B. J. McCall, T. R. Geballe, T. Usuda, N. Kobayashi, H. Terada, T. Oka, Pub. Astron. Soc. Japan 54 (2002) 951–961.

[57] I. A. Crawford, Mon. Not. Royal Acad. Sci. 277 (1995) 458–470.

[58] J. Takahashi, Astrophys. J. 561 (2001) 254–263.

[59] L. Spitzer, Jr., Physical Processes in the Interstellar Medium, New York Wiley-Interscience, 1978.

[60] C. Gry, F. Boulanger, C. Nehmé, G. Pineau des Forêts, E. Habart, E. Falgarone, Astron. Astrophys. 391 (2002) 675–680.

[61] A. E. Glassgold, W. D. Langer, Astrophys. J. 193 (1974) 73–91.

[62] J. Woodall, M. Agúndez, A. J. Markwick-Kemper, T. J. Millar, Astron. Astrophys. 466 (2007) 1197–1204.

[63] D. Gerlich, J. Chem. Phys. 92 (1990) 2377–2388.

[64] S. I. B. Cartledge, J. T. Lauroesch, D. M. Meyer, U. J. Sofia, Astrophys. J. 613 (2004) 1037–1048.

[65] A. G. Jensen, B. L. Rachford, T. P. Snow, Astrophys. J. 619 (2005) 891–913.

[66] E. B. Jenkins, M. Jura, M. Loewenstein, Astrophys. J. 270 (1983) 88–104.

[67] D. A. Neufeld, M. G. Wolfire, P. Schilke, Astrophys. J. 628 (2005) 260–274.

[68] K. Gillmon, J. M. Shull, Astrophys. J. 636 (2006) 908–915.

[69] T. Oka, J. Mol. Spectrosc. 228 (2004) 635–639.

[70] T. Oka, E. Epp, Astrophys. J. 613 (2004) 349–354.

[71] T. Oka, T. R. Geballe, M. Goto, T. Usuda, B. J. McCall, Astrophys. J. 632 (2005) 882–893.

[72] M. Quack, Mol. Phys. 34 (1977) 477–504.

[73] Z. Xie, B. J. Braams, J. M. Bowman, J. Chem. Phys. 122 (2005) 224307.

[74] M. Cordonnier, D. Uy, R. M. Dickson, K. E. Kerr, Y. Zhang, T. Oka, J. Chem. Phys. 113 (2000) 3181–3193.

[75] D. Gerlich, J. Chem. Soc., Faraday Trans. 89 (1993) 2199–2208.

[76] D. Gerlich, E. Herbst, E. Roueff, Planet. Space Sci. 50 (2002) 1275–1285.

[77] K. Park, J. C. Light, J. Chem. Phys. 126 (2007) 044305.

[78] E. Hugo, O. Asvany, S. Schlemmer, J. Chem. Phys. 130 (2009) 164302.

[79] B. A. Tom, A. A. Mills, M. B. Wiczer, K. N. Crabtree, B. J. McCall, J. Chem. Phys. 132 (2010) 081103.

[80] H. Kreckel, O. Novotný, K. N. Crabtree, H. Buhr, A. Petrignani, B. A. Tom, R. D. Thomas, M. H. Berg, D. Bing, M. Grieser, C. Krantz, M. Lestinsky, M. B. Mendes, C. Nordhorn, R. Repnow, J. Stützel, A. Wolf, B. J. McCall, Phys. Rev. A 82 (2010) 042715.

[81] H. Kreckel, A. Petrignani, M. Berg, D. Bing, S. Reinhardt, S. Altevogt, H. Buhr, M. Froese, J. Hoffmann, B. Jordon-Thaden, C. Krantz, M. Lestinsky, M. Mendes, O. Novotny, S. Novotny, H. B. Pedersen, D. A. Orlov, J. Mikosch, R. Wester, R. Plail, J. Glosk, D. Schwalm, D. Zajfman, A. Wolf, J. Phys.: Conf. Ser. 88 (2007) 012064.

[82] B. J. McCall, A. J. Huneycutt, R. J. Saykally, N. Djuric, G. H. Dunn, J. Semaniak, O. Novotny, A. Al-Khalili, A. Ehlerding, F. Hellberg, S. Kalhori, A. Neau, R. D. Thomas, A. Paal, F. sterdahl, M. Larsson, Phys. Rev. A 70 (2004) 052716.

[83] J. A. Cardelli, D. M. Meyer, M. Jura, B. D. Savage, Astrophys. J. 467 (1996) 334–340.

[84] U. J. Sofia, J. T. Lauroesch, D. M. Meyer, S. I. B. Cartledge, Astrophys. J. 605 (2004) 272–277.

[85] N. G. Adams, D. Smith, in: M. S. Vardya, S. P. Tarafdar (Eds.), Astrochemistry, volume 120 of *IAU Symposium*, pp. 1–18.

[86] S. F. dos Santos, V. Kokoouline, C. H. Greene, J. Chem. Phys. 127 (2007) 124309.

[87] H. Kreckel, M. Motsch, J. Mikosch, J. Glosik, R. Plasil, S. Altevogt, V. Andrianarijaona, H. Buhr, J. Hoffmann, L. Lammich, M. Lestinsky, I. Nevo, S. Novotny, D. A. Orlov, H. B. Pedersen, F. Sprenger, A. S. Terekhov, J. Toker, R. Wester, D. Gerlich, D. Schwalm, A. Wolf, D. Zajfman, Phys. Rev. Lett. 95 (2005) 263201.

[88] E. B. Wilson, J. C. Decius, P. C. Cross, Molecular Vibrations: The Theory of Infrared and Raman Vibrational Spectra, McGraw-Hill Book Company, Inc., 1955.

[89] D. C. Harris, M. D. Bertolucci, Symmetry and Spectroscopy: An Introduction to Vibrational and Electronic Spectroscopy, Oxford University Press, New York, 1978.

[90] R. S. Mulliken, Phys. Rev. 59 (1941) 873–889.

[91] J. T. Hougen, J. Chem. Phys 37 (1962) 1433–1441.

[92] H. C. Longuet-Higgins, Mol. Phys. 6 (1963) 445–460.

[93] P. A. M. Dirac, Proc. Royal Soc. London A 112 (1926) 661–677.

[94] W. Pauli, Z. Phys. 31 (1925) 765–783.

[95] B. J. McCall, Spectroscopy of H_3^+ in laboratory and astrophysical plasmas, Ph.D. thesis, University of Chicago, 2001.

[96] M. Goto, T. Usuda, T. Nagata, T. R. Geballe, B. J. McCall, N. Indriolo, H. Suto, T. Henning, C. P. Morong, T. Oka, Astrophys. J. 688 (2008) 306–319.

[97] K. N. Crabtree, N. Indriolo, H. Kreckel, B. A. Tom, B. J. McCall, Astrophys. J. 729 (2011) 15.

[98] K. N. Crabtree, C. A. Kauffman, B. A. Tom, E. Beçka, B. A. McGuire, B. J. McCall, J. Chem. Phys. 134 (2011) 194311.

[99] M. Saporoschenko, Phys. Rev. 139 (1965) A349–A351.

[100] T. Amano, J. Chem. Phys. 92 (1990) 6492–6501.

[101] W. Paul, B. Lücke, S. Schlemmer, D. Gerlich, Int. J. Mass Spec. Ion Proc. 149-150 (1995) 373–387.

[102] D. Gerlich, F. Windisch, P. Hlavenka, R. Plašil, J. Glosik, Phil. Trans. Royal Soc. A 364 (2006) 3007–3034.

[103] P. G. Jambrina, F. J. Aoiz, C. J. Eyles, V. J. Herrero, V. S. Rabanos, J. Chem. Phys. 130 (2009) 184303.

[104] C. W. Eaker, G. C. Schatz, J. Phys. Chem. 89 (1985) 2612–2620.

[105] J. E. Pollard, L. K. Johnson, D. A. Lichtin, R. B. Cohen, J. Chem. Phys. 95 (1991) 4877–4893.

[106] B. J. McCall, T. R. Geballe, K. H. Hinkle, T. Oka, Astrophys. J. 522 (1999) 338–348.

[107] B. J. McCall, K. H. Hinkle, T. R. Geballe, G. H. Moriarty-Schieven, N. J. Evans, II, K. Kawaguchi, S. Takano, V. V. Smith, T. Oka, Astrophys. J. 567 (2002) 391–406.

[108] T. J. Millar, A. Bennett, E. Herbst, Astrophys. J. 340 (1989) 906–920.

[109] A. Aguado, P. Barragán, R. Prosmiti, G. Delgado-Barrio, P. Villarreal, O. Roncero, J. Chem. Phys. 133 (2010) 024306.

[110] K. N. Crabtree, B. A. Tom, B. J. McCall, J. Chem. Phys. 134 (2011) 194310.

[111] L. Neale, S. Miller, J. Tennyson, Astrophys. J. 464 (1996) 516–520.

[112] B. A. Tom, S. Bhasker, Y. Miyamoto, T. Momose, B. J. McCall, Rev. Sci. Instrum. 80 (2009) 016108.

[113] T. Amano, J. Opt. Soc. Am. B 2 (1985) 790–793.

[114] K. N. Crabtree, C. A. Kauffman, B. J. McCall, Rev. Sci. Instrum. 81 (2010) 086103.

[115] R. Johnsen, C.-M. Huang, M. A. Biondi, J. Chem. Phys. 65 (1976) 1539–1541.

[116] J. S. Dobrosavljević, D. S. Pešić, Appl. Spectrosc. 35 (1981) 57–59.

[117] P. A. Büger, W. Fink, Z. Phys. 236 (1970) 314–320.

[118] D. Uy, M. Cordonnier, T. Oka, Phys. Rev. Lett. 78 (1997) 3844–3847.